Green Catalysts for Energy Transformation and Emission Control

ACS SYMPOSIUM SERIES **1184**

Green Catalysts for Energy Transformation and Emission Control

Virender K. Sharma, Editor
Texas A&M University, College Station, Texas

Sue-min Chang, Editor
National Chiao Tung University, Hsinchu, Taiwan

Ruey-an Doong, Editor
National Tsing Hua University, Hsinchu, Taiwan

Chien-Hou Wu, Editor
National Tsing Hua University, Hsinchu, Taiwan

The paper used in this publication meets the minimum requirements of American National Standard for Information Sciences—Permanence of Paper for Printed Library Materials, ANSI Z39.48n1984.

Foreword

The ACS Symposium Series was first published in 1974 to provide a mechanism for publishing symposia quickly in book form. The purpose of the series is to publish timely, comprehensive books developed from the ACS sponsored symposia based on current scientific research. Occasionally, books are developed from symposia sponsored by other organizations when the topic is of keen interest to the chemistry audience.

Before agreeing to publish a book, the proposed table of contents is reviewed for appropriate and comprehensive coverage and for interest to the audience. Some papers may be excluded to better focus the book; others may be added to provide comprehensiveness. When appropriate, overview or introductory chapters are added. Drafts of chapters are peer-reviewed prior to final acceptance or rejection, and manuscripts are prepared in camera-ready format.

As a rule, only original research papers and original review papers are included in the volumes. Verbatim reproductions of previous published papers are not accepted.

ACS Books Department

Preface

The development of alternative energy for transportation and the reduction of pollution emission from vehicles are the major challenge for environmental sustainability. Green catalysis is at the heart of industrial and environmental challenges on energy, health, and sustainable development. For example, the use of petroleum-based fuels produces air pollutants and catalysts are needed for reduction of the emission of gaseous pollutants as well as for carbon sequestration. Green catalytic processes are also used to produce biofuels and renewable energies. To meet these challenges, an interdisciplinary chemical approach from molecules to materials and processes from homogeneous, heterogeneous, and enzymatic catalysis are needed. This book addresses the most advanced research topics in the fabrication and application of environmentally friendly catalysts for energy conversion and emission control. The topics that are covered in this book include fabrication and characterization of environmentally benign catalysts, catalytic process for reduction, chemistry and catalysis of particulate and gaseous pollutants, water splitting for hydrogen production.

This book is derived from the symposium "Green Catalysts for Energy Transformation and Emission Control" at the 246th ACS National Meeting in Indianapolis, Indiana during the fall of 2013 sponsored by the American Chemical Society 9ACS) division of Environmental Chemistry. Many presentations, addressing the topics of roles of green catalysts in energy production and pollution control (gaseous and aquatic), were given in this symposium and they constitute the main content of this book.

This book contains 12 peer-reviewed chapters that cover various aspects of green catalysts with main emphasis on energy and depollution of air. Chapter 1 gives the overall view of catalysis that define green chemistry for synthesis and decontamination of a wide range of pollutants. Chapter 2 evaluates the approach used to improve energy security and mitigate greenhouse gas emissions. Chapter 3 shows the application of naphthalimide derivatives as fluorogenic chemosensors for Hg^{2+} detection. Chapter 4 has iron-containing glass as photocatalysts for decontamination under visisble light. Chapters 5, 6, and 7 discusses synthesis of titanium dioxide and zinc oxides as photocatalysts for use in energy and environmental remediation. Basically, these chapters discuss enhanced photocatalytical activity through improving surfaces and doping of catalysts. Chapter 8 presents preparation of titanium dioxide nanotubes for water splitting to generate hydrogen gas. Chapter 9 describes the Ag-BiOI photoactivated fuel cell that can be applied to efficient electricity generation and to degrade organic pollutants. The last three chapters (10, 11, and 12) are iron-based green compounds for various environmental applications. Chapter 10

gives an overview of iron-enriched mineral oxides as sustainable oxygenation catalysts for water decontamination. Chapter 11 demonstrates the combination of zero-valent iron and iron(III) oxides as efficient photocatalysts for remediating organic contaminants. Finally, Chapter 12 presents text on high-valent iron oxide compound, ferrate(VI) as emerging oxidant to clean the gas from pollutants.

We hope this book will be beneficial to graduate students who are engaged in research and development of the field of green chemistry for nanotechnology and environmental science and technology. We wish to thank anonymous reviewers for their invaluable time to review chapters of this book. We are also very thankful to Aimee Greene and Timothy Marney of the editorial department of ACS for their assistance in preparing this volume. We greatly appreciate their efforts to publish this volume on scheduled time.

Virender K. Sharma
Department of Environmental and Occupational Health
School of Rural Public Health
Texas A&M University, 1266 TAMU, College Station, Texas 77845
vsharma@srph.tamhsc.edu (e-mail)

Sue-min Chang
Institute of Environmental Engineering
National Chiao Tung University, Hsinchu, Taiwan
chang@mail.nctu.edu.tw (e-mail)

Ruey-an Doong
Department of Biomedical Engineering and Environmental Sciences
National Tsing Hua University, Hsinchu, Taiwan
radoong@mx.nthu.edu.tw (e-mail)

Chien-Hou Wu
Department of Biomedical Engineering and Environmental Sciences
National Tsing Hua University, Hsinchu, Taiwan
chwu@mx.nthu.edu.tw (e-mail)

Editors' Biographies

Virender K. Sharma

Virender K. Sharma received his Ph.D. in Marine and Atmospheric Chemistry at the University of Miami after graduating from the Indian Institute of Technology in New Delhi, India with the Master in Technology. In January 2014, he has joined School of Public Health (SPH) at Texas A&M University, College Station, Texas as a full Professor. Currently, he is serving as an Interim Head of the Department of Environmental and Occupational Health, SPH. He was a visiting research scholar at Stanford University under the advisory of Professor Ed Solomon and won both the Florida Tech Faculty of the Year award in 2008 and the ACS Orlando Section Outstanding Chemist Award. He is highly active in pursuing chemistry and environmental applications of high-valent iron species. His other interests include nanoparticles in aquatic environment and in remediation of contaminated water. He has published more than 300 reviewed journal articles, book chapters, and proceedings. His books authorship and editing include *Ferrates: Synthesis, Properties, and Applications in Water and Wastewater Treatment"*, *Sustainable Nanotechnology and the Environment: Advances and Achievements*, and Interactions of Nanomaterials with Emerging Environmental Contaminants; published by Oxford University Press.

Sue-min Chang

Sue-min Chang received her B.S. degree in Chemistry in June 1997 and Ph.D. degree in Atomic Science in November 2004 from National Tsing Hua University, Taiwan. After a short-term postdoctoral training, she joined Institute of Environmental Engineering at National Chiao Tung University, Taiwan, as an Assistant Professor in August 2005, and has been promoted to Associate Professor since 2010. Professor Chang cuts into environmental engineering from the angle of material chemistry. She devotes her efforts to develop advanced materials for environmental and energy applications. She is currently working on nanofabrication and surface modification of photocatalysts, sensing materials, and solid acids. She aims to improve the performance of conventional materials for efficient environmental treatments and invent new functional materials for the demand of ultra-clean technology.

Ruey-an Doong

Ruey-an Doong received his Ph.D. in Environmental Engineering at National Taiwan University, Taiwan after graduation from the National Chung-Hsing University in Taichung, Taiwan. Currently, he is the Dean of College of Nuclear Science and a full professor in the Department of Biomedical Engineering and Environmental Sciences, National Tsing Hua University, Taiwan. He is serving as an editorial member of several reputed journals like *Journal of Environmental Chemical Engineering*, *Sustainable Environmental Research*, and *Journal of Biosensors and Bioelectronics*. He has authored more than 200 journal article, book chapters and Proceedings. He was also honored as fellow of the Alexander von Humboldt Foundation of Germany in 2000.

Chien-Hou Wu

Chien-Hou Wu received his B.S. in 1989 and M.S. in 1993 under the supervision of Professor Wann-Yin Lin, both in Chemistry from National Taiwan University, Taiwan. He went on to obtain his Ph.D. in Civil and Environmental Engineering from the University of California, Los Angeles in 1999 under the guidance of Professor Bruce C. Faust and Professor Janet G. Hering. He then spent one year as a postdoctoral fellow in the Power, Environmental and Energy Research Institute at California Institute of Technology under the advisory of Professor Yongchun Tang. He joined the faculty of National Tsing Hua University as an Assistant Professor of Biomedical Engineering and Environmental Sciences in 2000 and became Associate Professor in 2005. His research interests lie within the broad field of environmental chemistry and analytical chemistry. Current topics include photochemistry of copper-organic complexes in aquatic systems, synthesis of highly water-dispersible titanium dioxide nanoparticles and their photocatalysis, and development of methods for trace analysis of environmental pollutants such as ammonia, amines, and aldehydes.

Chapter 1

Greener and Sustainable Remediation Using Iron Nanomaterials

Jurate Virkutyte[1] and Rajender S. Varma*,[2]

[1]Hammontree and Associates Ltd, North Canton, Ohio
[2]U.S. Environmental Protection Agency, NRMRL, Cincinnati, Ohio
*E-mail: Varma.Rajender@epa.org.

The main goal of remediation is to protect humans and the environment. Unfortunately, many remedial actions in the past concentrated more on site-specific environmental risks and conditions completely ignoring external social and economic impacts. Thus, new approach called green sustainable remediation (GSR) has to be adopted throughout industry. One of the significant factors that make remedial actions successful is green and sustainable catalyst that makes remediation process implementation cheaper and effective. Nanoparticles (e.g. Zero Valent Iron, ZVI) has a potential to not only reduce the costs of the cleanup but also significantly reduce remediation time, eliminate or at least significantly minimize the need for treatment and disposal of dredged soil due to applications *in situ*. This chapter presents information on GSR, provides examples of catalyst preparation and real scale applications with details.

Introduction

Environmental remediation can generally be summarized as the removal or destruction of contaminants from a media through physical, chemical or biological processes. The main goal of remediation is to protect humans and the environment. Unfortunately, many remedial actions in the past concentrated more on site-specific environmental risks and conditions completely ignoring external social and economic impacts.

Furthermore, traditional risk-based site remedial approach is based on (*1*):

1) The effectiveness and appropriateness of the particular remediation method to meet the remedial goals;
2) Ease of implementation;
3) Remediation costs; and
4) Remediation duration.

Unfortunately, such may not be sustainable because it does not account for broader environmental impacts such as generated waste, extraction and use of natural resources, and energy use for on and off-site operations. Therefore, general even "green approach" does not account for the net environmental benefit when all relevant environmental factors are considered. Over the past several years Green and Sustainable Remediation (GSR) has earned its place as a beneficial approach to optimize all phases of site remediation, from site investigation to project closeout taking into account environmental, social and economic aspects.

GSR maximizes the social and economic benefits associated with the remedial action. GSR goals include (*2*):

1) Minimizing total energy use and promoting the use of renewable energy for operations and transportation;
2) Preserving natural resources;
3) Minimizing waste generation while maximizing materials recycling;
4) Maximizing future reuse options for remediated land.

Definitions

To effectively address the pollution and develop sustainable solution, one needs to understand the key concepts and terms associated with it.

Sustainability

Sustainability is based on understanding that "Everything we need for our survival and well-being depends, either directly or indirectly, on our natural environment". According to the U.S. EPA (http://www.epa.gov/sustainability/basicinfo.htm), sustainability creates and maintains the conditions under which humans and nature can exist in productive harmony, that permit fulfilling the social, economic and other requirements of present and future generations. Sustainability postulates that resources are finite, and should be used conservatively and wisely with a view to long-term priorities and consequences of the ways in which resources are used. Sustainability ensures that we have and will continue to have, the water, materials, and resources to protect human health and our environment (Figure 1).
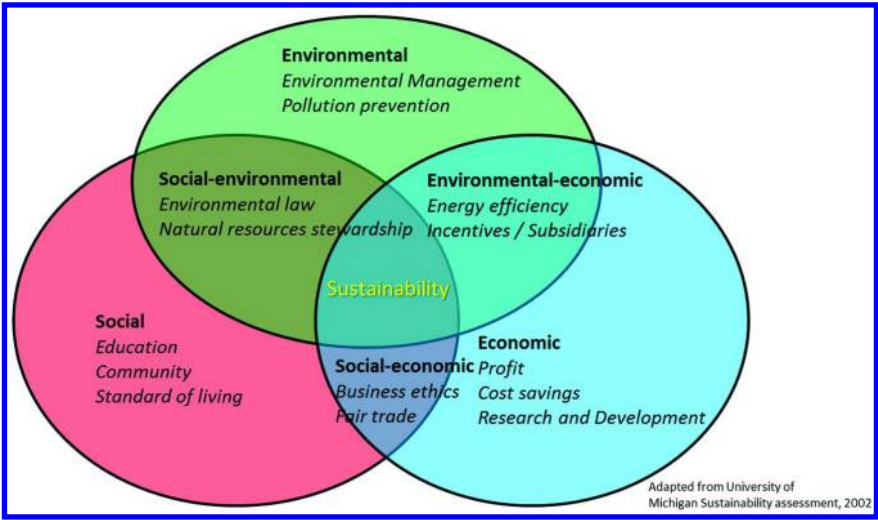
Figure 1. Sustainability schematics.
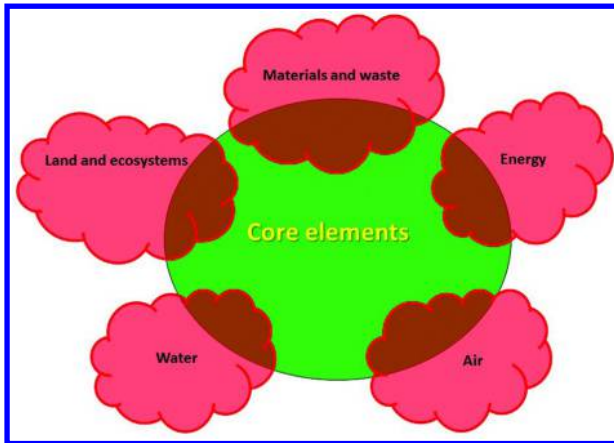
Figure 2. Core elements of green remediation.

Green Remediation

Green remediation considers all the environmental aspects and effects of remediation while incorporating options to minimize the environmental footprints of cleanup (EPA. 2011a. "Green Remediation Focus." Office of Superfund Remediation and Technology Innovation. www.clu-in.org/greenremediation). Assessment of environmental footprint has five core elements (Figure 2):

Conventional and renewable energy use – increasing the use of renewable energy;

Atmospheric and air pollutants and greenhouse emissions – reducing contaminants and green house emissions;

Water use and impact on water resources – reducing water use;

Waste reduction and materials management – improving waste management approaches and techniques;

Land management – protecting ecosystems during site cleanup.

Green and Sustainable Remediation

By nature, a remediation, if properly administered, is sustainable. It improves the environment, land value, and public trust. However, not all remedies are equivalent in terms of sustainability. Remediation of contaminated sites is necessary, but the process can be energy and resource-intensive, and result in numerous unwanted impacts. Growing awareness to decrease greenhouse gas emissions and use less energy, water and other resources has led to increased demand for green technologies and integrating sustainability into the site remediation process. Green and sustainable remediation is not only remedial activities that take into account environmental stressors and factors but also employment of processes, products, approaches and technologies that mitigate contamination risks, adverse economic and social impacts (Figure 3).
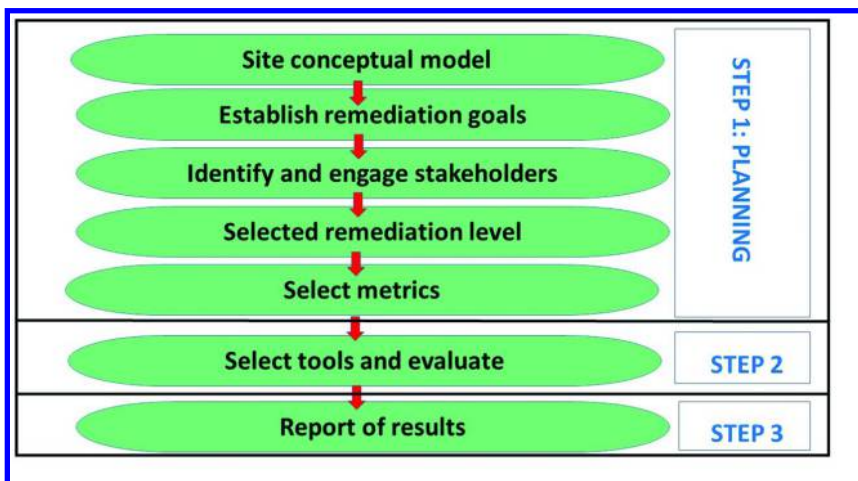

Figure 3. Green and sustainable remediation.

Contaminated Sites

Remediation of contaminated sites in the United States may be grouped into seven major cleanup programs implemented under different federal or state statues. Principles of Best Management Practices (BMPs) of green remediation can be applied at sites, although administrative, institutional, and remedy-selection decision criteria may vary across programs (*3*):

RCRA Sites: U.S. EPA estimates that more than 3,800 regulated hazardous waste treatment, storage, and disposal facilities are expected to need corrective action under the RCRA Corrective Action Program by 2020.

Underground Storage Tank (UST) Sites: currently there are over 575,000 releases of hazardous substances have been reported at sites with underground storage tanks. The greatest potential threat from a leaking UST is contamination of groundwater, the source of drinking water for nearly half of all Americans.

Department of Defense Sites: The U.S. Department of Defense (DOD) estimates that investigations and/or cleanups are undergoing at nearly 8,000 areas. These areas are located on hundreds of active and inactive installations and formerly used defense sites.

Department of Energy Sites: The U.S. Department of Energy (DOE) has identified approximately 4,000 contaminated or potentially contaminated areas on 22 installations and other locations. Most of DOE's remediated areas will require ground water treatment and monitoring or other long-term stewardship efforts.

Other Federal Agency Sites: U.S. EPA estimates that there are more than 3,000 contaminated sites, located on 700 federal facilities, potentially requiring remediation. These facilities are distributed among 17 federal agencies. These estimates do not include an estimated 8,000-31,000 abandoned mine sites, most of which are located on federal lands.

State, Brownfields, and Private Sites: U.S. EPA estimates that more than 5,000 cleanups are completed annually under brownfields and mandatory or voluntary state programs.

Sustainability Principles and Criteria

Principles

There are five sustainability principles that are defined by their direct ethical and social impacts on the environment, society, and the economy (Figure 4):

- Accountability
- Compliance
- Ethical behavior
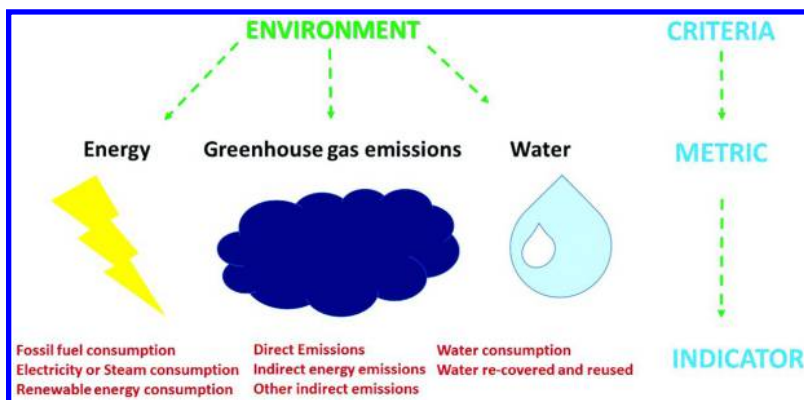- Stakeholder interests
- Transparency

Figure 4. Sustainability principles and criteria. (adapted from 2014 Tavares group consulting Inc)

Criteria

The four Criteria are the high-level categories that are applicable when developing a sustainability strategy:

- Environment
- Operating Practices
- Products and Services
- Community

Indicators

Indicators are the specific measurements that will be used for monitoring a performance at managing relevant metrics. Several indicators can be defined for a single sustainability metric.

Metrics

Metrics are the sustainability variables impacted by actions. The materiality (relevancy) of metrics is determined using a risk-based approach that considers stakeholder priorities and benchmarking. Metrics that are considered will have linkages to identified significant economic, environmental, and social impacts. Material metrics need to be identified for each of the four sustainability Criteria.

Unfortunately, there are no standardized metrics for GSR performance yet. Traditional remediation metrics include remediated area (m² or sq. ft.), mass of treated contaminants (kg or tons), and mass of treated soil (kg or tons). In addition, performance of GSR should be evaluated by:

- Energy consumption (kWh or BTU)
- Water consumption (m^3 or gallons)
- Waste generation (kg or tons)
- Greenhouse gas emissions (carbon dioxide equivalents or tons)
- Air pollutants (kg or tons)

Other metrics include but not limited to the amount of renewable energy used, materials recycling, preserved natural resources, redevelopment and re-use of the site, ecological restoration, etc. However, environmental intensity indicators may better serve as metrics:

- Energy per unit treated mass (kWh/kg)
- Water used per unit treated soil mass (m^3/kg)
- Carbon dioxide emissions per unit treated soil mass (t/kg).

The associated environmental costs may be expressed by cost per unit remediated area (\$/m^2), cost per unit treated contaminant mass (\$/kg), and cost per unit treated soil mass (\$/kg).

GSR Technologies

GSR should be incorporated during all the phases of remedial action:

1. Site investigation
2. Remedial system design, construction and operation
3. Monitoring
4. Site closure

Relevant sustainability principles can be incorporated into site characterization activities. For instance, direct push technologies, geophysical techniques, and passive sampling and monitoring techniques can reduce waste generation, consume less energy, and minimize land and ecosystem disturbance. The use of green catalysts can significantly increase the efficiency of the treatment without producing hazardous by-products and shortening the treatment time. The use of electricity to remediate the soil can diminish noise and dust pollution and lower the overall treatment costs.

Thus, an ideal remediation technology should aim to (*4*):

- Minimize the risk to public health and the environment in a cost-effective manner and a reasonable time period.
- Eliminate the potential for secondary waste and prevent uncontrolled contaminant mass transfer from one phase to another.
- Provide an effective, long-term solution.
- Minimize the impacts to land and ecosystem.
- Facilitate appropriate and beneficial land use.

- Minimize or eliminate energy input. If required, renewable energy sources (e.g., solar, wind, etc.) should be used.
- Minimize the emissions of air pollutants and greenhouse gases.
- Eliminate fresh water usage while encouraging the use of recycled, reclaimed, and storm water. Further, the remedial action should minimize impact to natural hydraulics water bodies.
- Minimize material use while facilitating recycling and/or the use of recycled materials.

It is important to point out that those technologies or approaches that encourage uncontrolled contaminant partitioning between media (i.e., from soil to liquid or from liquid to air) or those generate significant secondary wastes/effluents are not sustainable. Among generally accepted sustainable technologies that destroy contaminants are bioremediation, advanced oxidation and reduction, electrokinetics. These technologies minimize energy input, minimize air emissions and produce limited amount or no wastes. *In situ* techniques are favored due to minimal greenhouse gas emissions, low carbon footprint and minimal disturbance to ground surface and the overlaying soils.

In most cases, a single remediation technology cannot effectively address the challenges that occur in contaminated site. Based on various factors and site-specific conditions, several approaches and technologies may have to be combined to develop a truly sustainable remedian program.

Remediation Process Optimization

Remediation Process Optimization (RPO) is a systematic approach to evaluate and improve site remediation processes while maximizing risk reduction for cost expenditure. Generally, RPO is a proven, field-tested approach that can bring significant savings to site remediation programs. RPO focuses on three areas:

1. Optimization of the remedial strategy and technology upgrades

   - Conceptual site model refinement (review of existing data to identify data gaps and other problems)
   - Performance evaluations (review data for existing remediation options)
   - Regulatory strategy review (optimize remediation strategy accepted by regulatory agencies)
   - Remediation technology selection and implementation (selection of the most appropriate technology for a given site)

2. Optimization of ongoing remediation practices

   - Evaluation of labor, equipment, energy, materials, water use
   - Modifications of treatment systems to reduce chemicals or adsorbent costs

- More efficient use of automation upgrades to reduce labor requirements
- Reduce the outside services for repairs

3. Optimization of long-term groundwater monitoring and reporting

- Reducing costs for samples and analyses, evaluating data and reporting
- Optimization of monitoring techniques and approaches (less analytical parameters and reduced reporting)
- Use of statistical tools to evaluate data

Table 1 provides background information on remediation descriptions from various regulatory agencies.

Table 1. Remediation Descriptions for Different Regulatory Agencies(*5*)

Remediation	*RCRA*	*CERCLA*	*State level programs*	*Underground storage tanks (USTs)*
Investigation	RCRA facility investigation	Remediation investigation	Site assessment (e.g. Voluntary Action Programs)	Remediation investigation
Remediation approach evaluation and selection	General statements, basic ideas, corrective measures study	Feasibility study, proposed action plan, record of decision	Remediation alternative selection and evaluation	Corrective action plan design and implementation
Remediation design	Correctives measures design and implementation, work plan	Remediation design	Remedial action plan, interim source removal plan	Investigation, detailed corrective action design
Remediation construction	Corrective measures implementation	Remediation and construction completion	Construction completion report, interim source removal report	Corrective action implementation

Continued on next page.

Table 1. (Continued). Remediation Descriptions for Different Regulatory Agencies(5)

Remediation	RCRA	CERCLA	State level programs	Underground storage tanks (USTs)
Operation, maintenance and monitoring	Corrective measures implementation and reports	Post-construction completion, five year review	Remedial action status report	Corrective action O&M (system performance evaluation and post-shutdown monitoring
Remediation optimization	Corrective measures implementation	Five year review, record of decision amendment	Remedial action plan addendum	
Remediation completion	Corrective action completion determination, final report	National priorities list deletion	No further action proposal	Closure

Thus, based on aforementioned information, one of the vital tools for successful green and sustainable remediation is effective and "green" catalyst to ensure that degradation of hazardous chemicals during advanced oxidation processes is achieved.

Remediation Using Microscale and Nanoparticles

Nearly 10 years ago, U.S. Environmental Protection Agency (6) estimated that will take 30 to 35 years and up to $250 billion to clean up the nation's hazardous waste sites. U.S. EPA anticipated that high costs would provide incentive to create and implement cleanup approaches that would be cost effective, scientifically and technically sound as well as sustainable. Thus, over the next several decades, federal, state, and local governments and private industry will commit billions of dollars annually to clean up sites contaminated with hazardous waste and petroleum products from a variety of industrial sources.

Nanoparticles has a potential to not only reduce the costs of the cleanup but also significantly reduce remediation time, eliminate or at least significantly minimize the need for treatment and disposal of dredged soil due to applications *in situ* (7). These *in situ* methods provide significant monetary and time savings because no groundwater needs to be pumped out for above ground treatment and no soil has to be transported to other places for treatment and disposal (8). Furthermore, nanoparticles (e.g. calcium) have already demonstrated capacity to reduce the presence of non-aqueous phase liquids (NAPL). The majority of sites that use calcium nanoparticles are in New Jersey and cleanup is conducted in consultation with the New Jersey Department of Environmental Protection (NJDEP). Unfortunately, the risks associated with the use of nanomaterials for

sites remediation are still poorly understood. The factors affecting ecotoxicity are very complex and current knowledge of the potential impacts of nanomaterials on environment and human health is still rather limited.

Despite the risks, nanoparticles posses many desirable properties that could be successfully utilized for environmental remediation. Their small size and various shapes equipped them with dispersability and tuned reactivity. Synthesis methods (using capping stabilizing agents) provide nanoparticles with increased mobility in soils and sediments that could be used as advantage in remediation. Therefore, nanoparticles can be manufactured in such a way that their physicochemical properties, such as higher surface area per unit of volume, or increased affinity towards target contaminant or organism through surface functionalization are utilized at the most. Also, their small size allows them to travel further in groundwater attaining wider distribution. Despite all the latest developments, synthesis of nanoparticles that are used for environmental remediation should still be further improved. For instance monometallic or bimetallic nanoparticles and nano zero valent iron (nZVI) in particular demonstrated capacity to destroy or transform organic and inorganic contaminants into less harmful compounds. Unfortunately, nZVI is excessively reactive and tends to oxidize when reaches environment, thus losing its destructive powers. Therefore, stabilizing or capping agents and other metallic or non-metallic species should be coated or placed on the surface of nZVI to sustain its reactivity.

Similar to nanoparticles, microscale ZVI has the ability to dehalogenate chlorinated compounds by chemical reduction and has been used for years as a granular material in permeable reactive barriers for the treatment of contaminated groundwater (*9*). Due to the high specific surface area, nano- and micro-sized ZVI-particles are more reactive than granular materials. Thus, both ZVI particles can be injected into the soil matrix, thus allowing for active treatment of source and plume areas, even at greater depth.

Synthesis of Iron Nanoparticles

Numerous nanoscale metals and metal oxides such as silver, iron, gold, titanium oxides and iron oxides are used in environmental remediation (*7*). For instance, silver nanoparticles can destroy bacteria, viruses and fungi in wastewater. Pure and doped titanium dioxide can destroy organic contaminants, kill bacteria and disinfect water upon activation with UV or visible / solar light. Gold nanoparticles can remove chlorinated organic compounds, pesticides and inorganic mercury from water. When combined with titanium dioxide, gold nanoparticles are able to convert the toxic air pollutant sulphur dioxide to sulphur. Carbon nanotubes are able to adsorb bacteria and plethora of organic contaminants from water. Furthermore, zinc oxide placed on carbon or polymer support can destroy organochlorine pesticides, halogenated herbicides and azo dyes. Despite the variety of available nanomaterials, ZVI is still considered the most reliable and stable nano- and microscale particle capable of destroying a wide array of hazardous materials.

Iron (ZVI) Nanoparticles

ZVI is a reactive metal with standard redox potential ($E^o = -0.44$ V). Due to its properties, ZVI is an effective reductant when in contact with oxidized contaminants such as Cr(VI). The removal mechanism of contaminants by ZVI concerns the directional transfer of electrons from ZVI to the contaminants which transforms the latter into non-toxic or less toxic species. On the contrary, ZVI can degrade and oxidize a series of organic compounds in the presence of dissolved oxygen (DO) since ZVI transfers two electrons to O_2 to produce H_2O_2, which can be reduced to water by another two-electron transfer from ZVI (*10*). More details on ZVI applications, unfortunately mostly on the laboratory scale can be found in this review (*10*).

Conventionally, iron nanoparticles (e.g. ZVI) are synthesized using sodium borohydride (*11*, *12*) with aggregation, which is a high cost process and environmentally toxic (*9*). Other energy intensive and high pressure requiring methods include thermal decomposition (*13*), ultraviolet irradiation (*14*). ZVI can be used alone (*15–26*), immobilized on various supports (*27–39*), doped with various materials (*40–43*), combinted with Fenton and Fenton-like chemistry (*44–49*) and in permeable reactive barriers (*50–61*).

However, to address the green and sustainable remediation requirements, this process can be significantly improved and made "greener" by, for instance, using green, oolong and black teas with significant amount of polyphenols that act as capping and reducing agents (*12*, *62–65*). Varma and his group pioneered green synthesis of zero valent iron using green and black tea extracts (*7*, *12*, *62*) During a typical synthesis, 4 g of dry green tea leafs were placed into in boiling water (200 mL) for 30 min, then the liquid was filtered using a filter paper and a 200 nm microfiltration (regenerated cellulose) membrane. Solution was mixed with 0.1 M $FeSO_4$ and left for 12 hours at room temperature.

Huang et al. (*9*), Kuang et al. (*66*) and Weng et al. (*67*) developed similar synthesis method where 60 g L^{-1} of green, oolong and black tea extracts (heated at 80°C for 1 hour) were prepared and subsequently vacuum filtered. Then 0.10 mol L^{-1} $FeSO_4$ solution was added to the extract at a ratio of 1:2. The highest degradation (81.5%) of a target contaminant malachite green was achieved with green tea due to the hhighest amount of polyphenols/caffeine content in that type of tea. In addition, oxidation of monochlorobenzene and the removal of COD were 81.15% and 31.01%, respectively. Also, 96% of malachite was removed with a 50 mg L^{-1} at room temperature (*67*).

In addition to green tea, eucalyptus leaves were used to synthesize stable and effective nZVI (*68*, *69*). Prior to the synthesis, eucalyptus leaves were washed with DI water to eliminate dust on the surface and dried at a room temperature. Then the extracts were prepared by boiling 15 g of dry material at 80 °C for 1 hour, vacuum-filtered and stored in the fridge until the further use. nZVI were prepared by adding extract to 0.1 M $FeSO_4$ with a volume ratio of 2:1 at room temperature and stirring for 30 min. Immediately, black color appeared indicating the reduction of Fe^{2+} ions and formation of ZVI. Formed particles were collected by vacuum filtration, rinsed three times with ethanol and vacuum dried at 50°C for 12 hours. As prepared ZVI was capable of removing 86.7% of NO_3^- from water.

However, when swine wastewater was used as a experimental mediumonly 35.6% of total N was removed indicating that such a complex medium may need further improval of the catalyst. In addition, nZVI was able to eliminate 71.7% of total N and 84.5% of COD from euthrophic wastewater.

Food waste can also be used to manufacturer ZVI nanoparticles. For instance, Machado et al. (70) used orange (Newhall orange, *Citrus sinensis* (L.) Osbeck), lime (sweet lime, Citrus limettioides Tan), lemon (frost Lisbon lemon, Citrus limon (L.) Burm. f. Rutaceae), and mandarin (encore mandarin, Citrus reticulata) to synthesize nZVI. Procedure included gentle mixing of 1 mL of extracts from citrus fruits with 250 µL (0.1 mol L^{-1}) Fe(III) solution until the solution became dark. The reactivity of nZVI was tested against reduction of Cr(VI) in water. The green nZVIs exhibited distinct reactivities, with degradation efficiencies ranging from 12% up to 37%. Comparing the fruits, the nZVIs produced using lemon waste extracts were the most reactive, while nZVIs produced using orange waste extracts were the least efficient.

Bimetallic Iron Nanoparticles

Bimetallic nanoparticles exhibit new functions because of the synergistic rather than merely additive effects of the metals. Compared with monometallic ZVI, bimetallic nanoparticles have markedly enhanced physical and chemical properties, including magnetism and reducing ability. However, bimetallic nanoparticles with controlled morphology, size, composition, and structure are often difficult to synthesize (71).

According to Ferrando et al. (72) bimetallic nanoparticles generally have complicated structures that can be classified into four based on their mixing mode, i.e., core–shell segregated, heterostructure, intermetallic or alloyed structure, and multishell structure. In the core–shell segregated structure, a shell of one type of atom surrounds a core of the other atom. In the formation of a core–shell segregated structure, Type A metal ions are initially reduced to form a metallic inner core, and then Type B metal atoms grow around the core to form a shell. In the heterostructure, two different subclusters share a mixed interface or have only a small number of A–B bonds. The heterostructure usually forms by a process of independent nucleation and growth of two kinds of metal atoms (71, 72).

Synthesis methods include radiolysis (from 100 W power / 3 min to 600 W / 10 min and 160 W / 60 min applying 20 kHz ultrasound as well as 300 W / 3 min to 900 W/4 min using microwave irradiation of 2.45 GHz) (73–75), alloying (76–82), chemical reduction (H$_2$ at 500-600°C, glycol and microwave irradiation at 30 seconds, ascorbic acid at room temeprature) (83–89).

If sucessfuly prepared, bimetallic nanoparticles can be used to degrade plethora of organic contaminants. For instance, Liu and co-workers (90) synthesized functional kaolin-supported bimetallic Fe/Ni nanoparticles using the liquid-phase reduction method and NaBH$_4$ as a reducing agent. Shortly, ferric chloride hexa-hydrate (FeCl$_3$ x 6H$_2$O) (4.84 g) and nickel sulphate hexa-hydrate (NiSO$_4$ x 6H$_2$O) (0.45 g) was dissolved in 50 mL of miscible liquids (distilled water and absolute ethanol at a volume ratio of 1:4), and 1.0 g of kaolin. Mixture

was dried and rinsed three times with absolute ethanol prior to experiments. Bimetallic nanoparticle (1.05 g of nanoparticle was added to 1000 mL wastewater) was tested againts Direct Black G die and was able to destroy 99.97% of it in wastewater from textile printing and dyeing company based in Fuzhou, China.

Real Scale Remediation Examples Using Iron Microscale and Nanoparticles

Soil and Groundwater

Naval Air Engineering Station performed numerous full scale applications in 2004-2007, where nanomaterials (e.g. bimetallic nanoparticles, BNP) were used to treat various organic contaminants. Most of the sites were under CERLA and/or RCRA program.

For instance, aircraft launch facility site in New Jersey (*91*) (coastal plain aquifer consisting of mostly sand and gravel) that was contaminated with PCE, TCE, TCA, c-DCE and VC had average initial VOC concentration of 900 μg L^{-1}. The average decrease in total VOCs was 74% at the end of the treatment. A total of 300 lbs of BNP slurry was used for the treatment with concentration of 2 g L^{-1}. The BNP iron slurry was injected (treatment depth of 70 ft bgs) into the ground (Geoprobe) at 15 various locations over 13 days. At each injection point, 20 lbs of BNP were mixed with 1,200 gallons of water and a total of 300 lbs were mixed with 18,000 gallons of water. The total cost of the treatment was $255,500 (*92*).

Former underground storage tank (UST) site (groundwater) in Florida was mainly contaminated with PCE (4,360 μg kg^{-1}), TCE (60,100 μg kg^{-1}), DCE (6,700 μg kg^{-1}) and TCA (25,300 μg kg^{-1}). Unsaturated zone at the site was composed of uniform fine to medium grained sand and sandy fill. After the treatment with BNP (4.5 to 10 g L^{-1} of iron slurry), reduction in contaminants concentrations from 65% to 99% was observed. The total treatment costs were $412,000 (*93*).

Cape Canaveral Air Force Station Launch Complexes in Florida were treated in 2002-2011 under RCRA with emulsified zero valent iron (EZVI). The soil and groundwater (Upper Sand Unit, Middle-Fine-Grained Unit and Lower Sand Unit Upper) were contaminated with TCEs ranging from 439,000 μg L^{-1} to 1,180,000 μg L^{-1}. After the 90 day treatment was over, 65 % to 85 % reduction was observed in soil. Significant TCE reduction (57 to 100 %) was observed in groundwater at all depths tested. 670 gallons of EZVI was injected using high pressure, pneumatic and pressure pulse enhanced injection at depths ranging from 16 to 24 ft bgs. The EZVI consisted of 44.3% water, 37.2% oil, 1.5% surfactant, and 17.0% iron by weight. The cost of the sites treatment was approx. $1,000,000 including vendor costs, assessments and monitoring (*94*).

Hunters Point Shipyard in San Francisco, California (Navy site), contaminated with TCE, PCE, cis-1,2-DCE, vinyl chloride, total chlorinated ethenes, chloroform, and carbon tetrachloride has been treated with zero valent iron (ZVI) in 2010. Maximum concentrations of 88,000 μg L^{-1} in groundwater has been detected. The source of contamination was the leakage from an underground storage tank (UST) and the associated floor drain and underground piping, a grease trap and associated cleanout and underground piping and five steel dip tanks from a former paint shop. Two ZVI injections has been performed, one in

the source area and another one directly into the contaminated plume. Source area was injected with 16,000 lbs of micron-sized ZVI mixed with tap water to produce 265 g L^{-1} iron slurry by pneumatic fracturing using nitrogen gas as a carrer. Contaminated plume was treated with 72,650 lbs of micron-sized ZVI mixed with tap water to produce 300 g L^{-1} iron slurry also by pneumatic fracturing. After the treatment, total concentrations of VOC 1,530 μg L^{-1} to 21,100 μg L^{-1} have been detected. The total costs for the source area treatment was $289,300 which included costs for ZVI ($32,500), equipment, labor, sampling and analysis, waste disposal and drilling. Total contaminated plume treatment costs were $1,390,000 including materials, waste characterization, project management, reporting, equipment, field labor and waste disposal costs.

Another fulls scale attempt was made in the industrial site targeting both, soil and groundwater in New Jersey (former Adhesive manufacturer site) contaminated with TCA, TCE, DCA, DCE, chloroethane, VC with concentrations ranging from 170,000 - 1,200,000 ppb in the shallow zone and 13,000 ppb - 190,000 ppb in the deeper zone in 2005. The industrial site consisted of mostly fractured bedrock, specifically Brunswick Shale. Over the bedrock, there was 4 to 6 feet of silty and clayey soil. Remediation using 3,000 and 7,013 gallons of nano zero valent iron (nZVI, Z-loy from OnMaterials Inc) in shallow target and deeper zones, respectively was performed for 13 months. Remedial injection included nZVI, emulsified vegetable oil (from NewmanZone) and filtered potable water. Concentrations decreased within the shallow target zone to less than 700 ppb and to as low as to non-detect in deeper zone (95).

Several private and industrial full scale applications have been reported using other nanoparticles as well (96). For instance, groundwater in residential area in New Jersey, contaminated with PCE (1.1 μg L^{-1}), Bis(2-Ethylhexyl)phthalate (9.8 μg L^{-1}) and Benzo[a]Anthracene (0.14 μgL^{-1}) was treated with Nanoscale calcium ions with noble metal catalyst (Nano-Ox™) in 2007 for 3 months. Treatment was performed with 825 lbs of NanoOx™ mixed with tap water to form a slurry which was injected into the impacted area using a direct-push (Geoprobe) technology. After the treatment, PCE, Bis(2-Ethylhexyl)phthalate and Benzo[a]Anthracene concentrations dropped to below NJDEP standards.

Permeable Reactive Barriers (PRB)

ZVI has been used to remove heavy metals and radionuclids using PRB (97):
Several PRBs have been installed in Bodo Canyon Disposal Site, La Plata County, Colorado from 1999 to 2004 to treat arsenic, molybdenium, selenium, uranium, vanadium and zinc. The PRB consisted of ZVI, copper and steel wool and after the treatment, less than 0.01 mg L^{-1} of contaminants was detected.

ZVI PRB was used to treat molybdenium and uranium at Cotter Corporation Uranium mill in Canon City, Colorado. Unfortunately, after some time, ZVI became clogged with mineral precipitants and remediation was significantly impaired. Modifications included the addition of pre-treatment zone composed of coarse gravel mixed with ZVI. It was still unsuccessful for molybdenium but at the end of the treatment, uranium concentration was less than 0.006 mg L^{-1}.

The mixture of ZVI, amorphous ferric oxide and phosphate rock was used to treat uranium in Canyon site, Fry Canyon, Utah. The ZVI barrier successfully removed 99% of uranium.

PRB that contained ZVI and shredded cast iron was used to treat uranium in Mescek Ore site, Pecs, Hungary in 2003. Treatment resulted in 99% uranium removal from groundwater.

Another PRB containing ZVI was used to treat uranium, arsenic, manganese, molybdenium, selenium, vanadium and nitrates in Monticello Mill Tailings site, Monticello, Utah in 2000. Nearly all the concentrations were below the detection limits after the treatment was over.

A PRB with ZVI and wood chips were used to treat nitrates and uranium in Rocky Flats environmental technology site in Golden, Colorado. Initial concentration of uranium was as high as 20-28 pCi L^{-1} and treatment reduced it to as low as 10 pCi L^{-1} as required by regulatory agencies.

Summary

Despite the latest developments in nanoscience, still ZVI nanoparticles are the mostly used in pilot and full scale remediation applications. The use of microscale ZVI in subsurface PRBs is gaining importance with every successfully implemented project due to sound science, cost effectiveness and non-toxical nature of the treatment. ZVI nanoparticles utilize exactly the same chemistry, but take advantage of large surface area and the rheological ability to flow in the subsurface where contaminants may be found. In case where there are mixed contaminants, such as chlorinated organics and toxic heavy metals, ZVI nanoparticles is able to remove both types of contaminants through a combination of adsorption and reduction processes. Furthermore, the capacity of ZVI to act as a reducing agent offers a significant potential to remove radionuclides, where the reduced form is much less toxic and soluble and can be subsequently removed from solution. Furthermore, nZVI can be combined with other nanoparticles to increase treatment effectivity. Risk issues associated with ZVI toxicity are not significant, since data to date indicate that ZVI does not cause toxicity, does not travel extensively through the medium and iron oxides to which nanoparticles eventually transform are naturally present in groundwater.

References

1. Agency, U. S. E. P. *Green Remediation: Incorporating Sustainable Environmental Practices into Remediation of Contaminated Sites*; Washington DC, 2008.
2. Ellis, D. E.; Hadley, P. W. *Sustainable Remediation White Paper- Integrating Sustainable Principles, Practices, and Metrics Into Remediation Projects. Remediation*; Wiley: Hoboken, NJ, 2008.
3. Response, U. S. E. P. A. O. o. S. W. a. E. *Green Remediation: Incorporating Sustainable Environmental Practices into Remediation of Contaminated Sites*; 2008.

4. Sharma, H. D.; Reddy, K. R. *Geoenvironmental Engineering: Site Remediation, Waste Containment, and Emerging Waste Management Technologies*; John Wiley: Hoboken, NJ, 2004.

5. ITRC, T. I. T. R. C. G. a. S. R. T. *Green and Sustainable Remediation: A Practical Framework*; Washington DC, 2011.

6. Agency, U. S. E. P. *Cleaning Up the Nation's Waste Sites: Markets and Technology Trends*; Washington DC, 2004.

7. Virkutyte, J.; Varma, R. S. *Chem. Sci.* **2011**, *2*, 837–846.

8. Zhang, W. *J. Nanopart. Res.* **2003**, *5*, 323–332.

9. Huang, L.; Weng, X.; Chen, Z.; Megharaj, M.; Naidu, R. *Spectrochim. Acta, Part A* **2014**, *130,* 295–301.

10. Fu, F.; Dionysiou, D. D.; Liu, H. *J. Hazard. Mater.* **2014**, *267*, 194–205.

11. Sun, Y.-P.; Li, X.-q.; Cao, J.; Zhang, W.-x.; Wang, H. P. *Adv. Colloid Interface Sci.* **2006**, *120*, 47–56.

12. Nadagouda, M. N.; Castle, A. B.; Murdock, R. C.; Hussain, S. M.; Varma, R. S. *Green Chem.* **2010**, *12*, 114–122.

13. Wang, Y.; Maksimuk, S.; Shen, R.; Yang, H. *Green Chem.* **2007**, *9*, 1051–1056.

14. Parsons, J. G.; Peralta-Videa, J. R.; Gardea-Torresdey, J. L. Use of plants in biotechnology: Synthesis of metal nanoparticles by inactivated plant tissues, plant extracts, and living plants. In *Developments in Environmental Science*; Dibyendu Sarkar, R. D., Robyn, H., Eds.; Elsevier: New York, 2007; Vol. 5, Chapter 21, pp 463−485.

15. Genuino, H. C.; Mazrui, N.; Seraji, M. S.; Luo, Z.; Hoag, G. E. Green Synthesis of Iron Nanomaterials for Oxidative Catalysis of Organic Environmental Pollutants. In *New and Future Developments in Catalysis*; Suib, S. L., Ed.; Elsevier: Amsterdam, 2013; Chapter 3, pp 41−61.

16. Tosco, T.; Petrangeli Papini, M.; Cruz Viggi, C.; Sethi, R. *J. Cleaner Prod.* **2014**, *77*, 10–21.

17. Greenlee, L. F.; Torrey, J. D.; Amaro, R. L.; Shaw, J. M. *Environ. Sci. Technol.* **2012**, *46*, 12913–12920.

18. Kharisov, B. I.; Rasika Dias, H. V.; Kharissova, O. V.; Manuel Jimenez-Perez, V.; Olvera Perez, B.; Munoz Flores, B. *RSC Adv.* **2012**, *2*, 9325–9358.

19. Crane, R. A.; Scott, T. B. *J. Hazard. Mater.* **2012**, *211–212*, 112–125.

20. Grieger, K. D.; Fjordbøge, A.; Hartmann, N. B.; Eriksson, E.; Bjerg, P. L.; Baun, A. *J. Contam. Hydrol.* **2010**, *118*, 165–183.

21. Chang, D.; Chen, T.; Liu, H.; Xi, Y.; Qing, C.; Xie, Q.; Frost, R. L. *Chem. Eng. J.* **2014**, *244*, 264–272.

22. Cohen, E. L.; Patterson, B. M.; McKinley, A. J.; Prommer, H. *J. Contam. Hydrol.* **2009**, *103*, 109–118.

23. Fjordbøge, A. S.; Baun, A.; Vastrup, T.; Kjeldsen, P. *Chemosphere* **2013**, *90*, 627–633.

24. Kowalski, K. P.; Søgaard, E. G. *Chemosphere* **2014**, *117*, 108–114.

25. Rangsivek, R.; Jekel, M. R. *Water Res.* **2005**, *39*, 4153–4163.

26. Wanaratna, P.; Christodoulatos, C.; Sidhoum, M. *J. Hazard. Mater.* **2006**, *136*, 68–74.

27. Mackenzie, K.; Bleyl, S.; Georgi, A.; Kopinke, F.-D. *Water Res.* **2012**, *46*, 3817–3826.

28. Tseng, H.-H.; Su, J.-G.; Liang, C. *J. Hazard. Mater.* **2011**, *192*, 500–506.

29. Zhou, Y.; Gao, B.; Zimmerman, A. R.; Chen, H.; Zhang, M.; Cao, X. *Bioresour. Technol.* **2014**, *152*, 538–542.

30. Petala, E.; Dimos, K.; Douvalis, A.; Bakas, T.; Tucek, J.; Zbořil, R.; Karakassides, M. A. *J. Hazard. Mater.* **2013**, *261*, 295–306.

31. Zhan, J.; Sunkara, B.; Zheng, R.; Venkataraman, P.; Owoseni, S.; McPherson, G. L.; John, V. T.; Brown, D.; Culpepper, D. Multifunctional Materials Containing Nanoscale Zerovalent Iron in Carbon Microspheres for the Environmentally Benign Remediation of Chlorinated Hydrocarbons. In *Nanotechnology Applications for Clean Water*, 2nd ed.; Street, A., Sustich, R., Duncan, J., Savage, N., Eds.; William Andrew Publishing: Oxford, 2014; Chapter 26, pp 407−422.

32. Jia, H.; Wang, C. *Chem. Eng. J.* **2012**, *191*, 202–209.

33. Du, Q.; Zhang, S.; Pan, B.; Lv, L.; Zhang, W.; Zhang, Q. *Water Res.* **2013**, *47*, 6064–6074.

34. Fjordbøge, A. S.; Lange, I. V.; Bjerg, P. L.; Binning, P. J.; Riis, C.; Kjeldsen, P. *J. Contam. Hydrol.* **2012**, *140–141*, 67–79.

35. Fjordbøge, A. S.; Riis, C.; Christensen, A. G.; Kjeldsen, P. *J. Contam. Hydrol.* **2012**, *140–141*, 56–66.

36. Jiang, Z.; Lv, L.; Zhang, W.; Du, Q.; Pan, B.; Yang, L.; Zhang, Q. *Water Res.* **2011**, *45*, 2191–2198.

37. Su, Y.-F.; Cheng, Y.-l.; Shih, Y.-H. *J. Environ. Manage.* **2013**, *129*, 361–366.

38. Ling, X.; Li, J.; Zhu, W.; Zhu, Y.; Sun, X.; Shen, J.; Han, W.; Wang, L. *Chemosphere* **2012**, *87*, 655–660.

39. Liu, T.; Yang, X.; Wang, Z.-L.; Yan, X. *Water Res.* **2013**, *47*, 6691–6700.

40. Xu, F.; Deng, S.; Xu, J.; Zhang, W.; Wu, M.; Wang, B.; Huang, J.; Yu, G. *Environ. Sci. Technol.* **2012**, *46*, 4576–4582.

41. Huang, Q.; Liu, W.; Peng, P. A.; Huang, W. *J. Hazard. Mater.* **2013**, *262*, 634–641.

42. Shih, Y.-H.; Chen, M.-Y.; Su, Y.-F. *Appl. Catal., B* **2011**, *105*, 24–29.

43. Zahran, E. M.; Bhattacharyya, D.; Bachas, L. G. *Chemosphere* **2013**, *91*, 165–171.

44. Raizada, P.; Singh, P.; Kumar, A.; Pare, B.; Jonnalagadda, S. B. *Sep. Purif. Technol.* **2014**, *133*, 429–437.

45. Cao, M.; Wang, L.; Wang, L.; Chen, J.; Lu, X. *Chemosphere* **2013**, *90*, 2303–2308.

46. Martins, R. C.; Lopes, D. V.; Quina, M. J.; Quinta-Ferreira, R. M. *Chem. Eng. J.* **2012**, *192*, 219–225.

47. Shen, J.; Ou, C.; Zhou, Z.; Chen, J.; Fang, K.; Sun, X.; Li, J.; Zhou, L.; Wang, L. *J. Hazard. Mater.* **2013**, *260*, 993–1000.

48. Jiang, B.-C.; Lu, Z.-Y.; Liu, F.-Q.; Li, A.-M.; Dai, J.-J.; Xu, L.; Chu, L.-M. *Chem. Eng. J.* **2011**, *174*, 258–265.

49. Devi, L. G.; Rajashekhar, K. E.; Raju, K. S. A.; Kumar, S. G. *J. Mol. Catal.* **2009**, *314*, 88–94.

50. Baric, M.; Majone, M.; Beccari, M.; Papini, M. P. *Chem. Eng. J.* **2012**, *195–196*, 22–30.

51. Calabrò, P. S.; Moraci, N.; Suraci, P. *J. Hazard. Mater.* **2012**, *207–208*, 111–116.

52. Erto, A.; Lancia, A.; Bortone, I.; Di Nardo, A.; Di Natale, M.; Musmarra, D. *J. Environ. Manage.* **2011**, *92*, 23–30.

53. Gibert, O.; Rötting, T.; Cortina, J. L.; de Pablo, J.; Ayora, C.; Carrera, J.; Bolzicco, J. *J. Hazard. Mater.* **2011**, *191*, 287–295.

54. He, F.; Zhao, D.; Paul, C. *Water Res.* **2010**, *44*, 2360–2370.

55. Liendo, M. A.; Navarro Hidalgo, G. E.; Sampaio, C. H.; Heck, N. C. *J. Mater. Res. Technol.* **2012**, *1*, 75–79.

56. Liu, S.-J.; Zhao, Z.-Y.; Li, J.; Wang, J.; Qi, Y. *Water Res.* **2013**, *47*, 5977–5985.

57. Moraci, N.; Calabrò, P. S. *J. Environ. Manage.* **2010**, *91*, 2336–2341.

58. Obiri-Nyarko, F.; Grajales-Mesa, S. J.; Malina, G. *Chemosphere* **2014**, *111*, 243–259.

59. Teerakun, M.; Reungsang, A.; Lin, C.-J.; Liao, C.-H. *J. Environ. Sci.* **2011**, *23*, 560–567.

60. Wang, Q.; Li, Y.; Wang, C.; Wu, Y.; Wang, P. *J. Hazard. Mater.* **2014**, *276*, 415–421.

61. Weber, A.; Ruhl, A. S.; Amos, R. T. *J. Contam. Hydrol.* **2013**, *151*, 68–82.

62. Hoag, G. E.; Collins, J. B.; Holcomb, J. L.; Hoag, J. R.; Nadagouda, M. N.; Varma, R. S. *J. Mater. Chem.* **2009**, *19*, 8671–8677.

63. Markova, Z.; Novak, P.; Kaslik, J.; Plachtova, P.; Brazdova, M.; Jancula, D.; Siskova, K. M.; Machala, L.; Marsalek, B.; Zboril, R.; Varma, R. *ACS Sust. Chem. Eng.* **2014**, *2*, 1674–1680.

64. Smuleac, V.; Varma, R.; Sikdar, S.; Bhattacharyya, D. *J. Memb. Sci.* **2011**, *379*, 131–137.

65. Smuleac, V.; Xiao, L.; Bhattacharyya, D. In *Sustainable Nanotechnology and the Environment: Advances and Achievements*; Shamim, N.; Sharma, V. K. ACS Symposium Series 1124; American Chemical Society: Washington, DC, 2013; pp 41−58.

66. Kuang, Y.; Wang, Q.; Chen, Z.; Megharaj, M.; Naidu, R. *J. Colloid Interface Sci.* **2013**, *410*, 67–73.

67. Weng, X.; Huang, L.; Chen, Z.; Megharaj, M.; Naidu, R. *Ind. Crops Prod.* **2013**, *51*, 342–347.

68. Wang, T.; Lin, J.; Chen, Z.; Megharaj, M.; Naidu, R. *J. Cleaner Prod.* DOI: 10.1016/j.jclepro.2014.07.006.

69. Wang, T.; Jin, X.; Chen, Z.; Megharaj, M.; Naidu, R. *Sci. Tot. Environ.* **2014**, *466–467*, 210–213.

70. Machado, S.; Grosso, J. P.; Nouws, H. P. A.; Albergaria, J. T.; Delerue-Matos, C. *Sci. Tot. Environ.* **2014**, *496*, 233–240.

71. Liu, W.-J.; Qian, T.-T.; Jiang, H. *Chem. Eng. J.* **2014**, *236*, 448–463.

72. Ferrando, R.; Jellinek, J.; Johnston, R. L. *Chem. Rev.* **2008**, *108*, 845–910.

73. Roy, K.; Lahiri, S. *Anal. Chem.* **2008**, *80*, 7504–7507.

74. Doudna, C. M.; Bertino, M. F.; Blum, F. D.; Tokuhiro, A. T.; Lahiri-Dey, D.; Chattopadhyay, S.; Terry, J. *J. Phys. Chem. B* **2003**, *107*, 2966–2970.

75. Suslick, K. S.; Fang, M. M.; Hyeon, T.; Mdleleni, M. M. Applications of Sonochemistry to Materials Synthesis. In *Sonochemistry and Sonoluminescence*; Crum, L., Mason, T., Reisse, J., Suslick, K., Eds.; Springer: Netherlands, 1999; Vol. 524, pp 291−320.

76. Zaranski, Z.; Czujko, T. *J. Alloys Comp.* **2011**, *509* (Supplement 2), S608–S611.

77. Moumeni, H.; Alleg, S.; Greneche, J. M. *J. Alloys Comp.* **2005**, *386*, 12–19.

78. Tang, W. M.; Zheng, Z. X.; Tang, H. J.; Ren, R.; Wu, Y. C. *Intermetallics* **2007**, *15*, 1020–1026.

79. Nayak, S. S.; Wollgarten, M.; Banhart, J.; Pabi, S. K.; Murty, B. S. *Mater. Sci. Eng. A* **2010**, *527*, 2370–2378.

80. Shen, G.; Jiang, D. M.; Lin, F.; Shi, W. Z.; Ma, X. M. *Physica B* **2005**, *367*, 137–141.

81. Liu, W.-J.; Zeng, F.-X.; Jiang, H.; Zhang, X.-S.; Li, W.-W. *Chem. Eng. J.* **2012**, *180*, 9–18.

82. Freitas, J. C. C.; Nunes, E.; Passamani, E. C.; Larica, C.; Kellermann, G.; Craievich, A. F. *Acta Mater.* **2006**, *54*, 5095–5102.

83. Chou, N. H.; Schaak, R. E. *J. Amer. Chem. Soc.* **2007**, *129*, 7339–7345.

84. V. Goia, D.; Matijevic, E. *New J. Chem.* **1998**, *22*, 1203–1215.

85. Huang, S.; Mau, A. W. H. *J. Phys. Chem. B* **2003**, *107*, 8285–8288.

86. Choi, H.; Al-Abed, S. R.; Agarwal, S.; Dionysiou, D. D. *Chem. Mater.* **2008**, *20*, 3649–3655.

87. Li, B.; Wang, J.; Yuan, Y.; Ariga, H.; Takakusagi, S.; Asakura, K. *ACS Catal.* **2011**, *1*, 1521–1528.

88. Tee, Y.-H.; Bachas, L.; Bhattacharyya, D. *J. Phys. Chem. C* **2009**, *113*, 9454–9464.

89. Nadagouda, M. N.; Varma, R. S. *Cryst. Growth Des.* **2007**, *7*, 2582–2587.

90. Liu, X.; Chen, Z.; Chen, Z.; Megharaj, M.; Naidu, R. *Chem. Eng. J.* **2013**, *223*, 764–771.

91. Station, N. A. E. *Remedial Action Report for Nanoscale Particle Treatment of Groundwater at Areas I and J Naval Air Engineering Station Lakehurst*; Lakehurst, NJ, 2006.

92. Gavaskar, A.; Tatar, L.; Condit, W. *NAVFAC Cost and Performance Report. Nanoscale Zero-Valent Iron Technologies For Source Remediation*; NAVFAC, 2005.

93. Henn, K. W.; Henn, W. D. *Utilization of nanoscale zero-valent iron for source remediation - A case study*; Remediation 2006.

94. Agency, U. S. E. P. *Innovative Technology Evaluation Report. Demonstration of in-situ Dehalogenation of DNAPL Through Injection of Emulsified Zero-Valent Iron at Launch Complex 34 in Cape Canaveral Air Force Station, FL*; Cape Canaveral Air Force Station, FL, 2004.

95. Pelina, C.; Mateo, J.; Fogel, S.; Freim, J.; Bickmore, C.; Newman, W.; Crisman, D. *Rapid In-Situ Dechlorination of Solvents by Abiotic and Biotic Mechanisms. Effective Pilot Studies for Combination of Remedial Technologies*; Delta Consultants, Deborah Schnell-Pneumatic Fracturing, Inc., and Clint Bickmore-OnMaterials, LLC, 2005.

96. Scholars, W. W. I. C. F. *The Project on Emerging Nanotechnologies - Inventories Remediation Map*; 2009.
97. Bronstein, K. *Permeable Reactive Barriers for Inorganic and Radionuclide Contamination*; United States Environmental Protection Agency: Washington DC, 2005.

Chapter 2

Evaluation of Hydrothermally Carbonized Hydrochar in Improving Energy Security and Mitigating Greenhouse Gas Emissions

Ganesh K. Parshetti and Rajasekhar Balasubramanian[*]

Department of Civil and Environmental Engineering,
National University of Singapore, EA Engineering Drive 1, Singapore 117576
[*]**E-mail: ceerbala@nus.edu.sg.**

Hydrothermal carbonization (HTC) is a thermochemical process that converts biomass into a densified coal - like material, called HTC-coal or hydrochar by applying high temperature to biomass in a suspension with water under saturated pressure for several hours. The conversion to char via dry pyrolysis is restricted to biomass with dry water content (<10%). However, HTC process opens up the field of potential feedstock to substrates with a high moisture content (>80%) such as municipal biowaste, wet agricultural residues and fecal sludge. Hydrochar as a product is easy to handle with good dewatering properties and when dried, has a high calorific value. It is carbon neutral and is combustible for co-combustion with coal, but the energy and environmental related issues raise questions about its potential for developing countries. Fundamental research was therefore carried out to provide insights into the use of densified hydorchar for improving energy security and mitigating greenhouse gas emissions. Hydrothermally upgraded chars with improved density and friable characteristics were produced from a model feedstock i.e. oil-palm empty fruit bunch (EFB) biomass waste at three temperatures (150, 250, and 350 °C- denoted as H-150, H-250 and H-350). These chars were co-combusted with low rank Indonesian coal and with hydrothermally upgraded coal (HT-coal). The energy output in terms of co-combustion

efficiency and the composition of major gaseous pollutants released from the co-combustion process with specific reference to CO, CO_2, CH_4, NO, and SO_2 were studied in real-time using a thermogravimetric analyzer coupled with a Fourier transform infrared spectrometry. Based on the outcome of this research, recommendations are made regarding the use of EFB hydrochar for improved energy security and mitigation of environmental problems associated with power generation.

Introduction

Oil-palm empty fruit bunch (EFB), the primary solid waste of palm oil mill processing, is abundantly available in Southeast Asia (Malaysia, Indonesia and Thailand). According to Yusoff (*1*), agriculture residues from oil palm industries consist of 13.5% mesocarp fiber, 5.5% palm kernel shell and 22% EFB. Malaysia has approximately 362 palm oil mills, processing about 82 million tons of fresh fruit bunch and producing an estimated 33 million tons of crop residue annually in the form of EFB, fiber and shell (*2*). Lignocellulosic EFB (38.1–59.7 wt.% cellulose, 16.8–22.1 wt.% hemicelluloses, and 10.5–18.1 wt.% lignin) is potentially a low-cost material for production of energy densified carbonaceous products (*3*). Direct co-combustion of EFB with coal is another way to generate heat or energy from this waste biomass (*4, 5*). During the co-firing, high carbon contents of the coal and the highly volatile nature of the biomass can compensate each other and may provide a better temperature/burning profile for the combustion process than individual fuels do (*6*). The temperature/burning profile distinguishes between different coal and hydrochar combustion based on the characteristics of the thermo gravimetric analysis (TGA) and derivative thermogravimetric analysis (DTG) curve such as ignition temperature (T_i), maximum combustion rate temperature (T_{max}), maximum combustion rate (R_{max}), char burn-out temperature (T_f) during their combustion. Both TGA and DTG curves showed improved thermal characteristics (such as ignition temperature (T_i), maximum combustion rate temperature (T_{max}), maximum combustion rate (R_{max}), char burn-out temperature (T_f),) during co-combustion of coal with hydrochar. The temperature/burning profile is very important in ensuring a quality of the product. The cofiring of coal-biomass blends containing up to 20 wt.% biomass in utility pulverized fuel (PF) boilers has been successfully implemented in many countries (*7*). Blends with 50 wt.% and 100 wt.% biomass have also been utilized (*8*). Compared with the blends with 20 wt.% biomass content (*8*), the blends with 50 wt.% biomass showed better performance, with higher combustion efficiency and lower CO_2 emissions. Low-rank coal such as such as lignite and sub-bituminous coal is also frequently carbonized and upgraded by a hydrothermal treatment (HT) prior to its co-combustion with biomass for heat or power generation (*9–12*). Hydrothermal treatment method can lead to a significant reduction of the oxygen functional groups and an increase

in particle size, which could solve the main handling problems associated with low rank coals: high-moisture content and high self-ignition tendency (*9, 11, 12*). In addition, it was found that the absolute heating value of the hydrothermally upgraded coal is comparable to, or even higher than that of the raw coal. The combustion properties of upgraded HTC coal such as ignition temperature (T_i), maximum combustion rate temperature (T_{max}), maximum combustion rate (R_{max}), char burn-out temperature (T_f), and ash yield (*11*) were generally better compared with raw coal. These are reflected in higher T_i, T_{max}, R_{max}, and DTA maximum peaks that result in high calorific value (*11*). Direct cofiring systems are more sensitive to variations in biomass or waste quality, moisture and heterogeneity (*13–15*). Additionally, other problems limit the rate of secondary fuel use in place of the original fossil fuels. For example, ash deposition (fouling and slagging) and corrosion usually increase with the use of biomass replacing coal, which may shorten the lifespan of diverse devices such as boilers (*16, 17*). Direct cofiring systems include next technological solutions such as pretreatment of biomass by hydrothermal carbonization (HTC) (*12, 18–22*). HTC is a pressurized thermal conversion process, conducted at relatively low temperatures (150-350 °C). HTC accelerates biomass coalification by a factor of $10^6–10^9$ within temperatre range from 150-350 °C under rather soft conditions, down to a scale of hours, and also makes it a considerable, technically-attractive alternative for the sequestration of carbon from biomass on large and ultra-large scales (*23, 24*). Coalification, or metamorphosis of biomass refers to gradual changes in the physical and chemical properties of biomass in response to temperature and time. Three major physical factors (1) duration, (2) increasing temperature, and (3) increasing pressure may influence the coalification process. The most widely accepted explanation is that coalification takes place in response to increasing temperature. Moreover, the quality of the HTC char as fuel as compared to the raw material is improved due to its higher calorific value, less moisture and its handling and storage properties (*24*). In addition, inorganic substances are leached into the process water, which reduces the ash content of the product (*25*).

Most of the previous investigations on coal/biomass co-combustion have focused on mass loss rate as a function of various operational parameters such as heating rate and sample size (*4, 5, 26–30*). However, the real time analysis of the production and release of gaseous pollutants during the course of co-combustion of hydrothermally treated coal/biomass has rarely been studied. In order to predict the behavior of hydrothermally prepared char during co-combustion with natural coal and hydrothermally upgraded coal, it is very important to understand its emission characteristics from the environmental point of view. The distinct feature of our study is the combustion behavior and gaseous emissions analysis of blends of hydrothermally treated EFB biomass and coal. Gaseous pollutant that are generally formed during thermal decomposition of organics and bio-polymers such as biomass are carbon dioxide (CO_2), carbon monoxide (CO), methane (CH_4), ethane (C_2H_4), ammonia (NH_3), hydrocyanic acid (HCN), sulfur dioxide (SO_2) and carbonyl sulfide (COS) (*31–33*). Fang et al. (*34*) found that the following gaseous products were emitted from thermal decomposition of different biomass types (merbau, cotton straw, birch)—CO_2, CO, H_2O, CH_4, acetic acid (CH_3COOH) and methanol (CH_3OH). Information on the type, quantity and

time of release of gaseous products is essential to get a complete understanding of the fundamentals and mechanisms involved in the thermal decomposition process and also to formulate effective pollution control strategies. The use of thermogravimetric analysis (TGA) in conjunction with Fourier Transform Infrared Spectrometry (FTIR) is an effective approach to obtain the composition of evolved gases on the basis of their specific absorbance as biomass is thermally decomposed (*7, 32, 33*). This chapter first summarizes the preparation of densified hydrochars and its charactristics followed by the emission behavior of EFB biomass and its hydrochar with coal as well as with hydrothermally treated coal by the TGA-FTIR method. Thus, combustion characteristic factor (*S*) as well as emissions of gaseous pollutants from solid fuels and their blends were presented.

Densified Hydrochar from EFB Biomass and Its Co-Combustion with Coal

EFB was obtained from an oil processing company in Malaysia. EFB is the lignocellulosic material remaining as a by-product of the industrial palm oil process after removal of the nuts. To promote homogeneous mixing of EFB, and to facilitate its effective conversion to hydrochar during HTC treatment, the EFB was processed into fine pieces (~2-6 mm) using a grinder, then air-dried and stored in a sealed container until use. Low rank Indonesian coal was obtained from a coal mining company in Jakarta, Indonesia. Coal was manually chopped into small pieces (~4-5 mm) to promote homogeneous mixing and facilitate their effective up-grading during the HTC treatment.

HTC of EFB was carried out in a 500 mL Parr stirred pressure batch reactor (model 4575) (Figure 1). In a typical run, 25 g of previously dried EFB was dispersed in 250 mL of de-ionized water contained in the reactor. Experiments were conducted at different temperatures (150, 250 and 350 °C) with a constant reaction time of 20 min and under non-stirring conditions. The feedstock concentration and reaction time were chosen based on many previous studies on HTC for the biomass feedstock (*23, 24*). For coal upgrading at 250 °C (20 min), 25 g of coal was dispersed in 250 mL of de-ionized water in the reactor. The reactor was sealed and heated to the desired reaction temperature in an electric furnace. After the desired residence time, the reactor was rapidly cooled to quench the reaction. Residence time is defined as the time the reactor is held and operated at the desired reaction temperature, excluding preheating and cooling time. After the reactor cooled down to the room temperature, it was opened to collect the solid carbonaceous products. The solid product (hydrochar) was recovered by filtration, washed with deionized water and dried in air. The char product was weighed independently and stored in a sealed container until analysis. The hydrochars obtained from EFB biomass processed for 20 min at 150, 250 and 350 °C are denoted as HT-150, HT-250 and HT-350, respectively and the coal obtained after hydrothermal treatment is denoted as HT-coal.
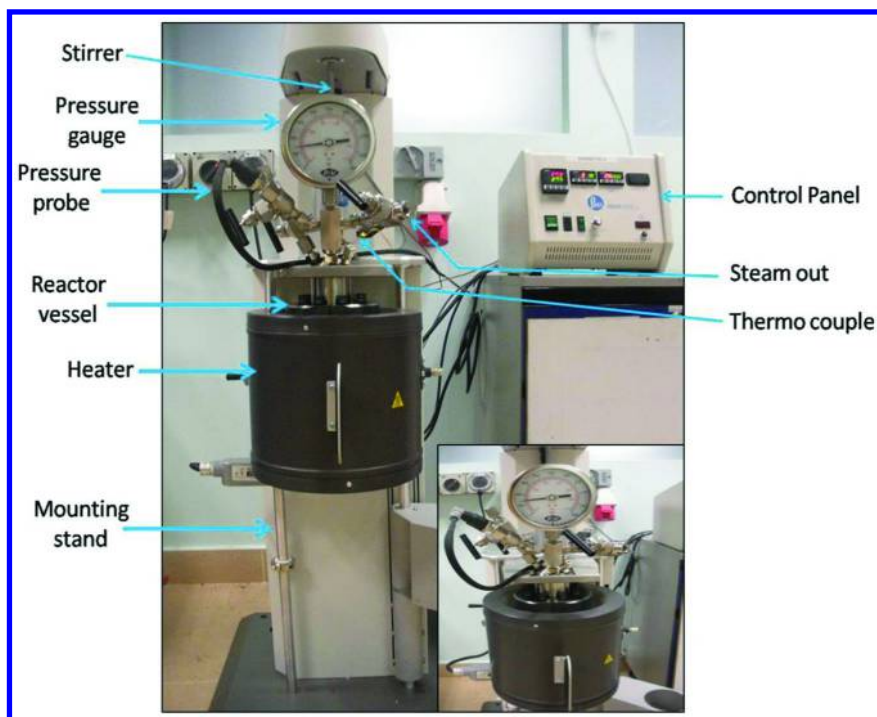
Figure 1. Parr reactor used for hydrothermal carbonization.

The 5E-MAG6600 automatic proximate analyzer was used to determine the weight percentages (wt%) of moisture, volatile matter, fixed carbon and ash in all samples. An elemental analyzer (vario MACRO cube, ELEMENTAR, Germany) was used to carry out ultimate analyses to determine the weight percentages of chemical elements (carbon, hydrogen, nitrogen, oxygen and sulfur) in the samples. In the present study, combustion of all the samples were performed in the furnace of the Perkin Elmer TGA7 system operated at a gas flow (mixture of N_2 (70%) and O_2 (30%)), rate of 100 ml min^{-1} while heating from 25 to 900 °C at a rate of 20 °C min^{-1}. All treated feedstocks/coal samples were ground to micron-sized particles and these particles were placed upon a sieve that passed particles of less than 150 μm (micron). Thus, the particle size of the treated feedstocks/coal was approximately 150 μm for TGA analysis. The weight loss (TG) and the rate of weight loss (DTG) were analyzed to find the key combustion parameters. The ignition temperature and burnout temperatures were determined using the TG-DTG (the first derivative of TG curve) method based on previous publications in the literature (*19*, *20*). In brief, the ignition temperature (T_o) was determined based on the temperature at which the DTG had its peak value and the corresponding slope to the intersection with respect to the TG profile. The burnout temperature (T_f) was detected based on the mass stabilization. The gas products from the combustion of samples in TGA were determined using a coupled, on-line Fourier transform infrared spectrometer (Perkin-Elmer FTIR Spectrum

2000). While other conditions were kept the same as those used in TGA, the sample was controlled at ~20 mg to provide enough gas for analysis. To minimize the secondary reaction, the gaseous products released from thermo-gravimetric balance were swept immediately to a gas cell, followed by detection using the FTIR spectrometer. The transfer line and the head of the TG balance were heated at a constant temperature of 200 °C, to avoid the condensation of volatile decomposition products. The IR was used in a scanning range of 4000–400 cm^{-1}, in terms of wave number. The resolution and sensitivity were set at 4 cm^{-1} and 1, respectively. FTIR spectra of the gaseous products were collected continuously with the baseline corrected.

Hydrochar's Fuel Characteristics

The proximate analysis, ultimate analysis and calorific values of EFB, coal, HT-coal, HT-150, HT-250 and HT-350 are shown in Table 1. As can be seen from the table, the volatile mater in the EFB biomass (82.2% ± 4.3) was almost two times higher than that in coal (56.4% ± 3.4) and HT-coal (48.0% ± 2.9). On the other hand, coal and HT-coal had higher fixed carbon and higher moisture contents in this study. Among the EFB, coal and HT-coal fuels used in this study, coal had the highest ash content (3.2% ± 0.2). The results of ultimate analyses are also given in Table 1. The ultimate analyses revealed the high contents of carbon in both coal and HT-coal (i.e., 45.4 ± 2.7 and 55.2 ± 3.32 wt%, respectively), suggesting a high proportion of organic carbon. Also it can be seen from Table 1, that the coal (1.22% ± 0.07) and HT-coal (1.25% ± 0.07) has higher sulfur content than that of the EFB biomass (0.34% ± 0.01). The higher heating value (HHVs) (35) of HT-coal (22.30 ± 1.35 MJ kg^{-1}) was relatively higher than that of coal (20.71 ± 1.10 MJ kg^{-1}) and EFB biomass (17.93 ± 0.91 MJ kg^{-1}). The higher HHV value o suggests that the hydrothermal treatment resulted in further densification of coal, which can be attributed to a decrease in the ratios of both the O/C (0.51 ± 0.03) and H/C (1.15 ± 0.06) when coal was subjected to the pre-treatment. The characteristics of the hydrochar produced by HTC of EFB were investigated comprehensively to identify the changes of the solid material, especially the carbon component. A higher recovery of hydrochar was observed at lower temperatures, with nearly 76% of the starting dry mass recovered at a reaction temperature of 150 °C, which decreased to approximately 62% at 250 °C and 49% at 350 °C. A sharp decrease in the solid yield with temperature was observed, which can either be due to greater primary decomposition of biomass at high temperatures, or through secondary decomposition of the solid residue, as reported earlier (36). As expected, the mass of volatile carbon in the solid decreased significantly as a result of carbonization, while the fixed carbon percentage increased with increasing operating temperature. Similar observations were reported earlier (37, 38) for municipal waste streams and lignocellulosic biomass. The fixed carbon yield resulting from carbonization was 16.41, 27.41, and 42.41% for H-150, H-250 and H-350, respectively. The carbon content of the hydrochar increased, while the hydrogen and oxygen contents decreased steadily with increasing operating temperature, consistent with the removal of O and H

substances during the HTC process. H/C and O/C atomic ratios, calculated for the initial biomass, and the resulting hydrochars, are displayed using a Van Krevelen diagram, which is useful for representing the conversion of carbohydrate material to carbon-rich material (*39*). This diagram offers a clear insight into the chemical transformations of the carbon rich material, which are demethanation (production of methane), dehydration (production of water) and decarboxylation (production of CO_2), taking place during the process (*39*). The Van Krevelen plot of the EFB biomass and its hydrochars is illustrated in Figure 2. In general, both the H/C and O/C ratios decreased when the temperature was raised. At higher operating temperatures, the dehydration trend became more obvious as compared to the one at the lower operating temperatures. A shift in the O/C ratio suggests that decarboxylation also occurs during the HTC process. Similar results were observed for the hydrothermal carbonization of glucose, cellulose, sucrose, starch and agricultural biomass (*40, 41*).

Table 1. Physical–Chemical Analysis and Calorific Values of the EFB, Coal and HT-Coal. (Source: Parshetti et al., 2013, 2014; Reprinted with permission from Elsevier)

Property	*EFB*	*Co-al*	*HT-Coal*	*HT-1 50*	*HT-2 50*	*HT-3 50*
Elemental analysis (%) (daf[a])						
Carbon	48.30	47.06	55.18	49.58	54.30	66.02
ydrogen	6.66	5.86	5.28	5.91	4.17	4.15
Nitrogen	1.00	1.48	1.73	0.92	1.02	1.12
Sulphur	0.34	1.22	1.25	0.22	0.24	0.28
Oxygen (by difference)	43.70	44.38	36.56	43.37	38.29	28.43
Atomic ratio						
O/C	0.67	0.84	0.49	0.65	0.52	0.32
H/C	1.65	1.55	1.15	1.43	0.92	0.75
Proximate analysis (%)						
Moisture	4.29	10.69	9.08	4.40	5.30	5.21
Volatiles	82.21	52.45	47.08	74.48	63.11	47.52
Ash	3.09	3.22	2.10	4.01	4.16	4.32
Fixed carbon	10.41	33.64	41.74	17.41	27.41	42.41
HHV (MJ kg^{-1})[b]	17.93	20.71	22.30	20.01	22.07	27.20

[a] Dry ash-free   [b] HHV (High Heating Value) = 0.196(FC) + 14.119 (*51*).
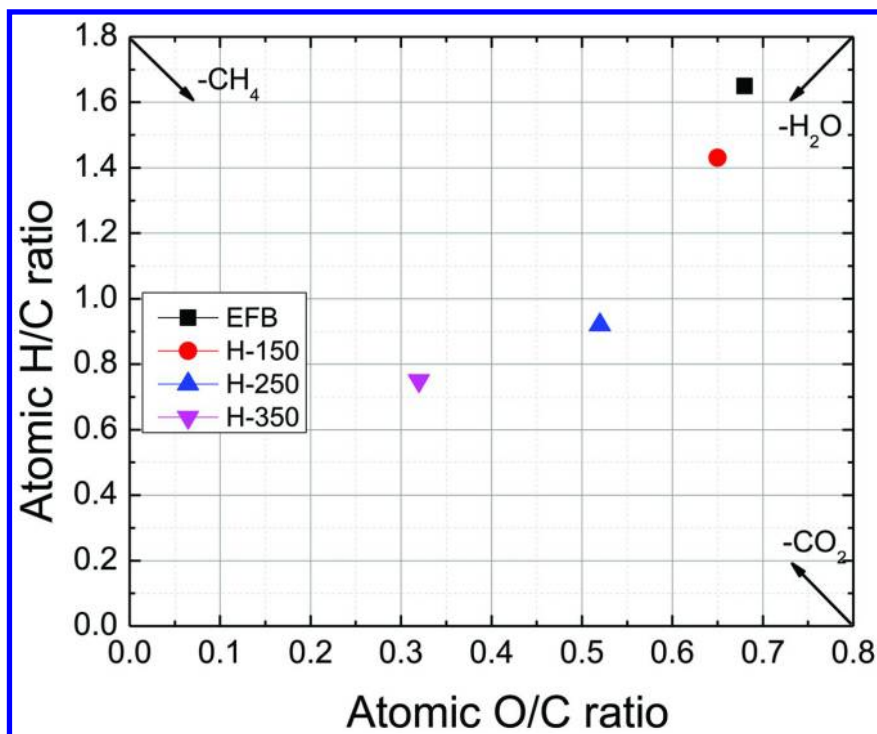
Figure 2. Van Krevelen diagram of the EFB biomass and the carbonized samples (hydrochar) resulting from hydrothermal treatment. Each arrow represents the direction of loss of a particular gas molecule in the course of evolution. (Source: Parshetti et al., 2013; Reprinted with permission from Elsevier.)

Another important characteristic of hydrochars is their high heating value (HHV = $0.196(FC) + 14.119$) (*18*). The calorific value is an indication of the degree of coalification achieved. Higher HTC temperatures promote the dehydration, decarboxylation, and condensation reactions of the coalification process, thereby resulting in energy densification (*38*). The energy densification factors associated with the hydrochars range from 1.02 (H-150) to 1.40 (H-350) and is defined as the ratio of energy content of hydrochar divided by the energy content of feedstock. Energetic retention efficiencies provide a means for comparing the energy remaining within the char and range from 78% (for H-150) to 68% (for H-350) and is defined as the ratio of percent of energy conserved divided by the percentage of mass retained.

Table 2. Combustion Characteristic Factor (S) from the TG/DTG Analysis for Fuels. (Source: Parshetti et al., 2014; Reprinted with permission from Elsevier.)

Combust-properties	$(dm/dt)_{max}$ $(\%min^{-1})$	$(dm/dt)_{mean}$ $(\%min^{-1})$	T_i (°C)[a]	T_f (°C)[b]	$CCF \times 10^{-7}$
EFB	29.12	1.88	220	662	2.40
Coal	24.15	2.14	340	438	1.93
HT-Coal	29.51	2.18	330	430	2.52
EFB (50%) + Coal (50%)	30.90	1.89	328	610	1.83
EFB (50%) + HT-Coal (50%)	38.68	2.18	318	600	2.77
HT-150 (50%) + Coal (50%)	35.07	2.45	345	640	2.47
HT-150 (50%) + HT-Coal (50%)	43.97	2.48	350	660	3.00
HT-250 (50%)+ Coal (50%)	46.32	2.47	360	672	3.02
HT-250 (50%) + HT-Coal (50%)	63.42	2.42	355	667	4.14
HT-350 (50%) + Coal (50%)	30.82	1.87	340	655	1.65
HT-350 (50%) + HT-Coal (50%)	46.12	2.46	365	660	2.98

[a] T_i = Ignition temperature,　[b] T_f = Burnout temperature.

Table 3. Summary of Kinetic Parameters – Activation Energy

Sample	T_i (°C)	T_f (°C)	a ln(AR/beta*E)	(-)b=E/R	Correlation coefficient	Pre-exponential factor (min^{-1}) A	Activation energy (kJ mol^{-1})
EFB	220	662	-3.5278	6653.2	0.956	3908.0175	55.31
Coal	340	438	-2.599	10360	0.99	2786898.2	86.13
HT-Coal	330	430	-0.085	8685	0.99	189185.81	72.20
EFB (50%) + Coal (50%)	328	610	-2.214	10250	0.99	22398.858	85.21
EFB (50%) + HT-Coal (50%)	318	600	-1.615	7628	0.98	30342.761	63.41
HT-150 (50%) + Coal (50%)	345	640	-2.462	10296	0.98	17557.615	85.60
HT-150 (50%) + HT-Coal (50%)	350	660	-0.281	8991.8	0.94	135781.28	74.75
HT-250 (50%) + Coal (50%)	360	672	-3.501	6339	0.95	3824.5978	52.70
HT-250 (50%) + HT-Coal (50%)	355	667	-3.923	6271.2	0.94	2481.095	52.13
HT-350 (50%) + Coal (50%)	340	655	-3.157	6849	0.93	5828.9386	56.94
HT-350 (50%) + HT-Coal (50%)	365	660	-6.003	5037	0.94	248.96149	41.87

Combustion Properties of Hydrochars

To determine the interactive effects of EFB biomass and its hydrochars (H-150, H-250 and H-350) during their co-combustion with coal and HT-coal, a blending ratio of 50% was used. The combustion properties determined from the TG/DTG analysis are presented in Table 2. A parameter called the combustion characteristic factor (CCF) (7) was used as a criterion for fuel combustion performance, and is defined as below:

$$CCF = \frac{\left(\frac{dw}{dt}\right)max \left(\frac{dw}{dt}\right)mean}{T_i{}^2 T_h} \qquad (1)$$

where $(dw/dt)_{max}$ is the rate of weight loss (% min^{-1}); $(dw/dt)_{mean}$ is the average burning velocity (% min^{-1}); T_i is the ignition temperature (K); and T_h is the burnout temperature (K). This factor, which includes the ease of ignition, the firing velocity and the burnout temperature, is a comprehensive combustion parameter. CCF was used to compare the combustion performance of different fuels and their blends, and the CCF values are listed in Table 2. With the exception of coal, EFB (50%)/Coal (50%), HT-350 (50%)/Coal (50%) blends, the values are close to or greater than 2×10^{-7} for all other fuels and blends, indicating their good general combustion performance (7). The CCF values for the hydrochar/HT-coal blends were found to be higher than the values of the hydrochar/coal blends. This observation suggests that the EFB hydrochar has potential to improve the combustion performance of HT-coal while used in the form of pellets after the blending. Addition of hydrothermally carbonized oil palm biomass (EFB) has shown better burning characteristics because of its improved fuel qualities compared to the raw EFB biomass, such as decreased volatile matter/(volatile matter + fixed carbon) ratio and increased carbon content (18). Further, the energy density of EFB hydrochar increased with increasing hydrothermal temperature, with higher heating values being close to those of natural coal. Also, the addition of hydrothermally carbonized oil palm biomass (EFB) lowers the activation energy required during co-combustion with coal (18). Fuels blends with high CCF values, for example, HT-250 (50%) + Coal (50 %) (CCF = 3.02 × 10^{-7}) and HT-250 (50%) + HT-Coal (50 %) (CCF = 4.14 × 10^{-7}), are promising candidates that can be used as solid fuels for energy generation.

Kinetic Analysis

Studies on TGA profiles contribute to enhancing the knowledge of the kinetics of this thermal process and, therefore, to establishing the optimum operational conditions for better utilization of hydrochars. Combustion kinetic parameters were calculated for the temperature ranges as mentioned in Table 3. The mass change vs. temperature can be described as

$$\frac{d\alpha}{dT} = \frac{A}{\beta} e^{-E/RT} (1-\alpha)^n \qquad (2)$$

where n stands for the reaction order and A and E represent the pre-exponential factor and the activation energy of the reaction, respectively and mass change α is defined as,

$$\alpha = \frac{m_0 - m_t}{m_0 - m_f} \qquad (3)$$

where m_0 represents the initial sample mass in an experiment, m_t denotes the current sample mass, and m_f specifies the final sample mass.

Equation 1 can be expressed in an integral form as follows:

$$\int_0^\alpha \frac{d\alpha}{(1-\alpha)^n} = \frac{A}{\beta} \int_{T_0}^T e^{-E/RT} dT \qquad (4)$$

Using the approximation introduced by Coats & Redfern (*18*), equation 4 can be integrated and rearranged into the following logarithmic form.

$$\ln\left[\frac{g(\alpha)}{T^2}\right] = \ln\left[\frac{AR}{\beta E}\left(1 - \frac{2RT}{E}\right)\right] - \frac{E}{RT} \qquad (5)$$

Eq. (4) can be transformed to a linear relation as:

$$y = a + bx \qquad (6)$$

Where a stands for $\ln\left[\frac{AR}{\beta E}\left(1 - \frac{2RT}{E}\right)\right]$, b is $-\frac{E}{R}$ and x is $\frac{1}{T}$. According to Eq. (6), a plot of $\ln[g(\alpha)/T_2]$ against reciprocal of temperature should give a straight line with a slope equal to $-E/R$. $g(\alpha)$ is the integral function of conversion. Apparent activation energy E and the pre-exponential factor A can be calculated by using the slope and intercept obtained from equation 5. Activation energies associated with the combustion of EFB, coal and HT-coal were found to be 55.31, 86.1 and 72.20 kJ mol^{-1}, respectively. Activation energies of the coal blended samples viz EFB (50%)/Coal (50%), HT-150 (50%)/Coal (50%), HT-250 (50%)/Coal (50%) and HT-350 (50%)/Coal (50%) were found to be in the range of 85.21, 85.60, 52.70 and 56.94 kJ mol^{-1} respectively (Table 3).

Activation energies of the hydrothermally upgraded HT-coal blended samples viz EFB (50%)/HT-Coal (50%), HT-150 (50%)/ HT-Coal (50%), HT-250 (50%)/ HT-Coal (50%) and HT-350 (50%)/ HT-Coal (50%) were found to be in the range of 63.41, 74.75, 52.13 and 41.87 kJ mol^{-1} respectively (Table 3). As reported in Table 3, the activation energies of the HT-coal blended samples were lower those of coal blended samples. This trend again shows synergistic interactions between HT-coal and hydrochar components, leading to the decrease of activation energy of combustion. The activation energy of the HT-350 (50%)/ HT-Coal (50%) (41.87 kJ mol^{-1}) blend shows the lowest activation energy. As the activation energy represents the critical energy needed to start combustion (*4*), the coal-hydrochar with the lowest activation energy is recommended.
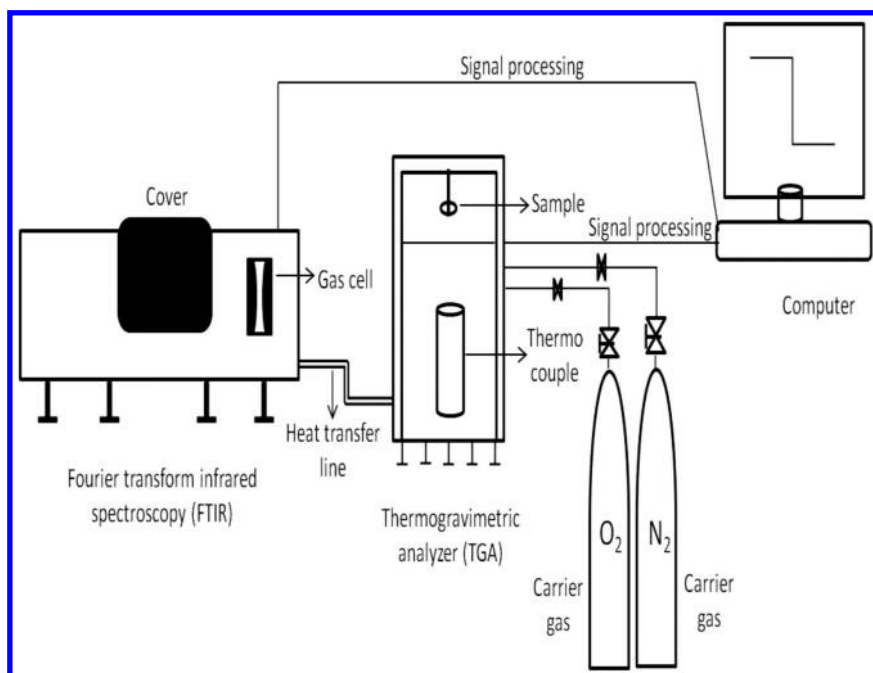
Figure 3. Schematic diagram of the TGA-FTIR system. (Source: Parshetti et al., 2014; Reprinted with permission from Elsevier.)
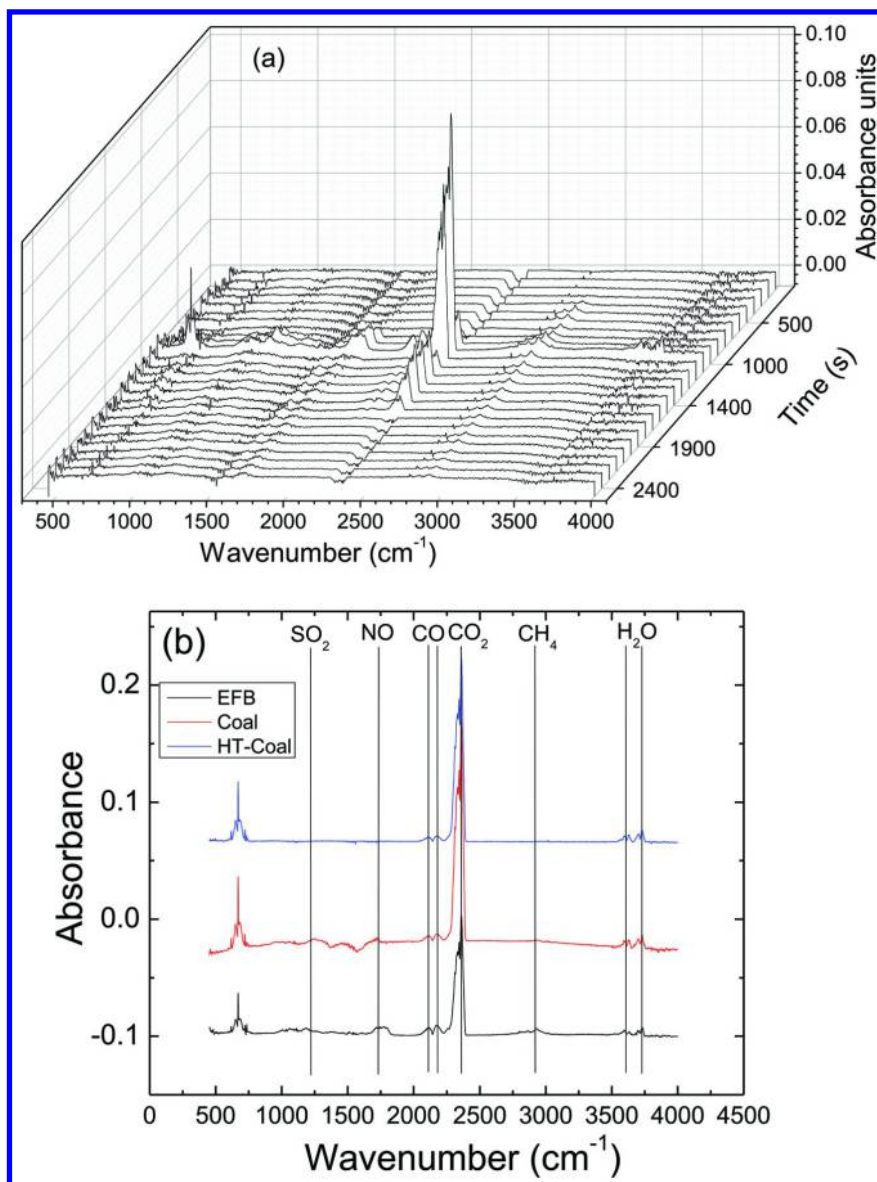
Figure 4. Three-dimensional (3D) FTIR spectral plot of the gases emitted from the combustion of (a) EFB biomass and (b) FTIR spectral plot of the gases produced from the combustion of EFB, coal and HT-coal at a heating rate of 20 °C/min in TGA–FTIR. (Source: Parshetti et al., 2014; Reprinted with permission from Elsevier.)

Table 4. Yields of CO₂, CO, CH₄, NO and SO₂ Species from Combustion of Various Fuels

Property	EFB	Coal	HT-Coal	EFB (50%) + Coal (50%)	EFB (50%) + HT-Coal (50%)	HT-150 (50%) + Coal (50%)	HT-150 (50%) + HT-Coal (50%)	HT-250 (50%) + Coal (50%)	HT-250 (50%) + HT-Coal (50%)	HT-350 (50%) + Coal (50%)	HT-350 (50%) + HT-Coal (50%)
CO_2 integral value	12.101	26.161	7.482	14.015	11.708	6.814	5.532	8.409	2.469	5.689	2.149
CO integral value	1.018	0.981	0.283	0.377	0.292	0.243	0.180	0.300	0.100	0.237	0.058
CH_4 integral value	0.697	0.361	0.102	0.201	0.146	0.054	0.046	0.066	0.025	0.052	0.014
SO_2 integral value	0.070	0.743	0.671	0.178	0.076	0.060	0.069	0.050	0.025	0.026	0.010
NO integral value	0.047	0.371	0.337	0.134	0.025	0.030	0.034	0.037	0.019	0.029	0.011

Analysis of Gaseous Emmision Products

TGA has been demonstrated to be a very valuable technique for studying the combustion of a wide range of solid samples (*7, 33, 42, 43*). When FTIR is used as a complementary technique with TGA, it would provide insightful information on the composition of gaseous products as they evolve from the combustion of solid fuels. We, therefore, used TGA coupled with FTIR in this study to investigate the combustion behavior of all solid fuels and their blends and measure the emission of major gaseous pollutants of environmental concern at a heating rate of 20 °C min^{-1}. Figure 3 shows a schematic diagram of the TGA-FTIR system used in the current study. During the combustion cracking process, the gases released in the TGA were swept immediately to a gas cell, followed by FTIR analysis. A typical three-dimensional plot of the spectra obtained from the gas volatized during the thermal decomposition of EFB biomass in the temperature range of 25–900 °C is shown in Figure 4a; this temperature refers to the operating temperature of the TGA. The volatiles identified with TGA-FTIR analysis in the current study are CH_4 (2978 cm^{-1}), CO (2119 cm^{-1}), CO_2 (2360 & 670 cm^{-1}), NO (1762 cm^{-1}) and SO_2 (1342 cm^{-1}) (as shown in Figure 4b) for individual fuels based on the spectral information available from the literature (*7, 33, 42, 43*). According to the TGA-FTIR study, the evolution of gaseous products increases with the combustion temperature, reaching their maximum values between 220 and 500 °C. Generally, the peak at 3580 cm^{-1} is assigned to the symmetric and asymmetric stretching vibrations of H_2O molecules while those in the range of 3700–3900 cm^{-1} may be associated with rota-vibrational bands of water vapor (*44*). As the combustion temperature increases between 220 and 500 °C, the release of CO_2, CO, CH_4, NO and SO_2 rises significantly (Figure 5-9). The detection of both CO_2 and CO in this temperature range suggests that the decarboxylation (formation of CO & CO_2) reactions are simultaneously favored in this stage of the combustion (*44*). At the higher temperature range from 600 °C to 900 °C, the release of pollutant gases was almost negligible, indicating the completion of combustion (Figure 5-9) (*45, 46*).

CO_2 Emission Patterns

Figure 5 shows the emission of CO_2 from the combustion of EFB, coal and HT-coal and their hydrochar blends at different combustion temperatures. The CO_2 emission profiles for EFB, coal, coal/EFB and coal/hydrochar blends showed two peaks, one in the range of 220 to 420 °C and the other in the range of 420 to 550 °C. However, the first peak reflecting a strong emission of CO_2 was more prominent than the second peak. This observation suggests that the CO_2 emission was relatively higher during the combustion of volatile matters which occurred in the temperature range of 220 to 420 °C. However, the level of CO_2 emission decreased significantly when the combustion temperature increased to the range of 420 to 550 °C at which the char burning appears to have been started. For the HT-coal, HT-coal/EFB and HT-coal/hydrochar blends, the emission profile

of CO_2 had only one peak, suggesting that the major combustion process took place during the initial burning period i.e. 220 to 420 °C. Figure 5 also shows that the CO_2 released had its maximum value for coal based on the absorbance value, which continued to increase beyond the temperature region at which the thermal decomposition occurred (i.e. >550 °C). Possible reasons for the increased emissions of CO_2 include thermal cracking of solid residues left in the fuels, oxidation of the carbonized char, and high temperature thermal decomposition (46–48). The magnitude of the CO_2 emission was generally 10 to 30 times higher than that of other detected gases (CO, CH_4, SO_2 and NO as presented in Figures 6 to 9) in the present study. For the HT-coal and HT-coal/hydrochar blends, the CO_2 emission peak shifted to lower temperatures than what was observed for coal and coal/hydrochar blends. The total CO_2 emission was completely influenced by the contents of fuel in the blends. This was confirmed by the integral areas under the emission curves which are 14.015 for EFB(50%)/Coal(50%), 11.708 for EFB(50%)/HT-Coal(50%), 6.814 for HT-150(50%)/Coal(50%), 5.532 for HT-150(50%)/HT-Coal(50%), 8.409 for HT-250(50%)/Coal(50%), 2.469 for HT-250(50%)/HT-Coal(50%), 5.689 for HT-350(50%)/Coal(50%) and 2.149 for HT-350(50%)/HT-Coal(50%) (Table 4). These results prove that the blending of EFB hydrochar with coal and HT-coal can reduce CO_2 emissions significantly. The hydrothermal treatment changes the properties of hydrochar products like the coalification process. The solid product EFB hydrochar formed from hydrothermal treated biomass is largely formed by recondensation reactions owing to the evolution of H_2O and CO_2 in the dehydration and decarboxylation reactions, which lowers the O/C ratios than the initial biomass product (18). The atomic H/C ratio and the atomic O/C ratio were decreased by increasing the hydrothermal reaction temperature. More of the original feedstock is lost to gaseous (i.e., H_2, CO and CO_2) and liquid by-products. In addition, under hydrothermal treatment temperatures, most of the original carbon stays bound to the final structure. Carbon structures produced by this route are therefore most CO_2-efficient and helps in reduce CO_2 emissions when used in co-combustion processes. Furthermore, the blending of untreated EFB biomass itself with coal and HT-coal could also help in CO_2 reduction, but the emission of other gases should also be considered as discussed in the sections below.

CO Emission Patterns

The CO emission profiles for the fuel samples are shown as a function of combustion temperature in Figure 6. All profiles showed a single peak except that of EFB biomass. The highest CO emission occurred at about 425 °C for the EFB biomass. In addition, a minor secondary peak appeared in the range of 520 to 620 °C. The initial stage of CO release was probably caused by the decarboxylation reaction of alkyl side-chains containing the carbonyl functional groups (-CHO) of lignocellulosic EFB biomass, while the increase of CO at the high temperatures was probably due to secondary reactions (45, 46, 49). For

coal beyond 500 °C, the CO emission increased slowly with temperature rising up to 900 °C as was seen for CO_2. The increase in CO beyond 550 °C might be due to the thermal cracking of evolved tar downstream of the TGA sample holder (*32*). Tar is a mixture of various unknown compounds that are present in TGA-FTIR system as fine aerosol or condensable material (*50*). The CO emission of all fuel blends started around 230 °C and presented differences in the peak position/height due to differences in the relative contents of the main constituents. The EFB/coal and EFB/HT-coal blend decomposed at higher temperatures with a peak around 375 and 350 °C, respectively compared to other blends. Individual CO emission peaks for hydrochar/coal and hydrochar/HT-coal blends were very close to each other compared to EFB/coal and EFB/HT-coal blends. The integral areas under the emission curves are 0.377 for EFB(50%)/Coal(50%), 0.292for EFB(50%)/HT-Coal(50%), 0.243 for HT-150(50%)/Coal(50%), 0.180 for HT-150(50%)/HT-Coal(50%), 0.300 for HT-250(50%)/Coal(50%), 0.100 for HT-250(50%)/HT-Coal(50%), 0.237 for HT-350(50%)/Coal(50%) and 0.058 for HT-350(50%)/HT-Coal(50%) (Table 4). These results reveal that the blending of EFB hydrochar with coal and HT-coal decreases CO emissions considerably.
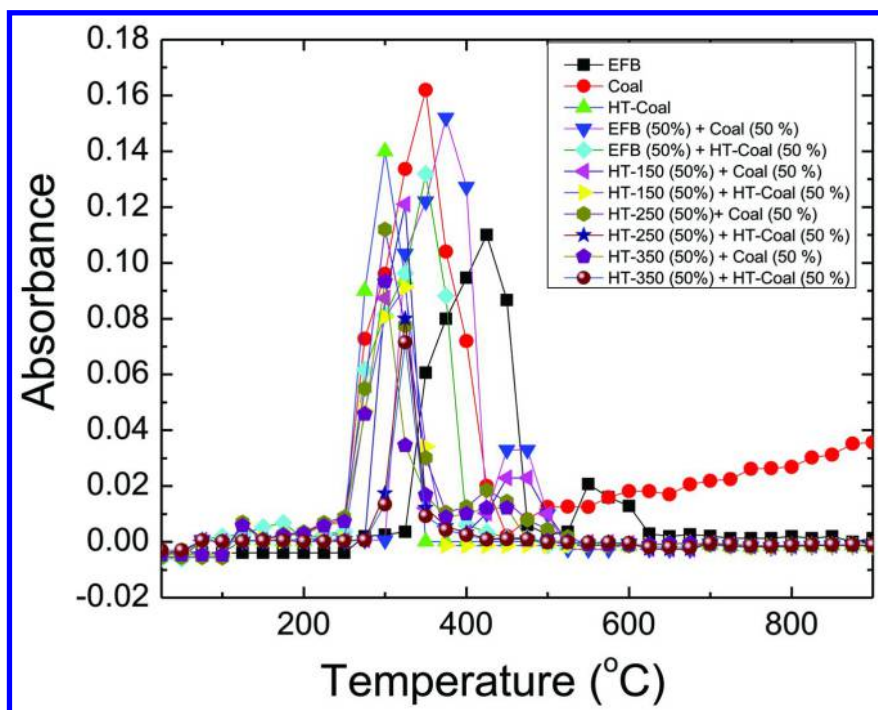
Figure 5. Evolution of CO_2 against the sample bed temperature for the different blends of fuels at a heating rate of 20 °C/min in TGA–FTIR. (Source: Parshetti et al., 2014; Reprinted with permission from Elsevier.)
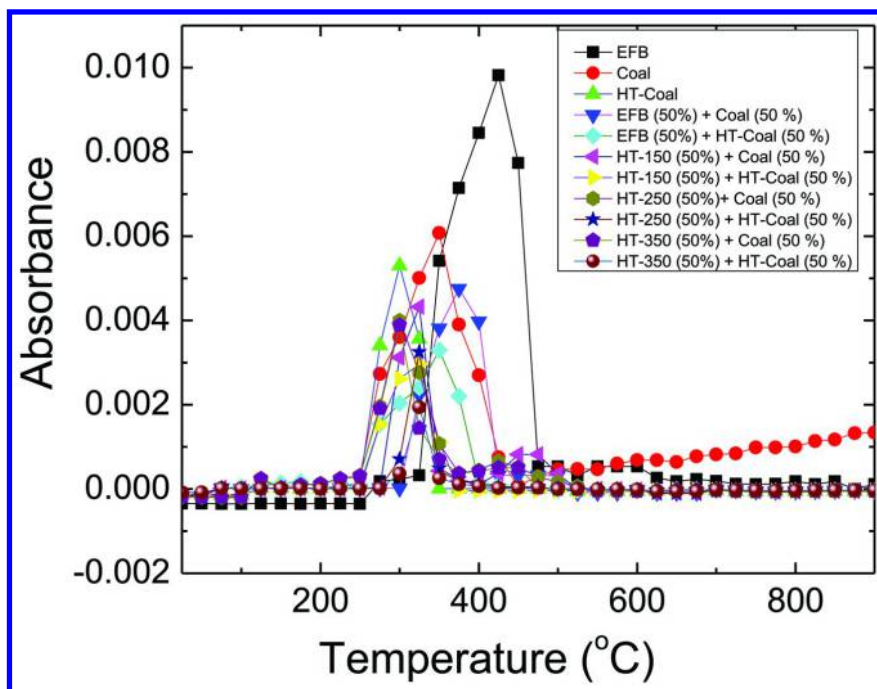
Figure 6. Evolution of CO against the sample bed temperature for the different blends of fuels at a heating rate of 20 °C/min in TGA–FTIR. (Source: Parshetti et al., 2014; Reprinted with permission from Elsevier.)

CH4 Emission Patterns

The CH_4 emission profiles for all the fuel samples and blends are shown as a function of temperature in Figure 7. All profiles show dispersed peaks in the temperature range of 230 to 600 °C when the volatile matter and char were burnt rapidly. The EFB biomass showed two peaks one at 425 and the other at 575 °C, suggesting two burning processes involving volatile materials and fixed carbon. The release of CH_4 in the fixed carbon stage was much lower than that in the volatile material stage. A temperature gap of more than 150 °C was observed for these two stages. The emission of CH_4 at later stage (575 °C) was probably due to the release of methoxyl groups, resulting mainly from lignin decomposition (*46, 49*). Except for the EFB biomass, the CH_4 emission beyond 450 °C was almost negligible with the combustion temperature rising up to 900 °C. There were also few differences in the CH_4 emission profiles for different blends of solid fuels. For EFB(50%)/Coal(50%), and EFB(50%)/HT-Coal(50%), the CH_4 emission peaks were mainly observed at the fixed carbon burning stage between 350 to 380 °C, where as for HT-150(50%)/Coal(50%), HT-150(50%)/HT-Coal(50%), HT-

250(50%)/Coal(50%), HT-250(50%)/HT-Coal(50%), HT-350(50%)/Coal(50%) and HT-350(50%)/HT-Coal(50%) the CH_4 emission peaks were mainly observed at the volatile burning stage between 275 and 340 °C. For the hydrochar blends with coal such as HT-150(50%)/HT-Coal(50%), HT-250(50%)/HT-Coal(50%) and HT-350(50%)/HT-Coal(50%), the peak CH_4 emission level was much lower than other blends. It appeared that the HT-350(50%)/HT-Coal(50%) blend produced the lowest total emission in CH_4. This was confirmed by integrating the area under emission curves for each of the samples. The integral areas under the emission curves are 0.201 for EFB(50%)/Coal(50%), 0.146for EFB(50%)/HT-Coal(50%), 0.054 for HT-150(50%)/Coal(50%), 0.046 for HT-150(50%)/HT-Coal(50%), 0.066 for HT-250(50%)/Coal(50%), 0.025 for HT-250(50%)/HT-Coal(50%), 0.052 for HT-350(50%)/Coal(50%) and 0.014 for HT-350(50%)/HT-Coal(50%) (Table 4).
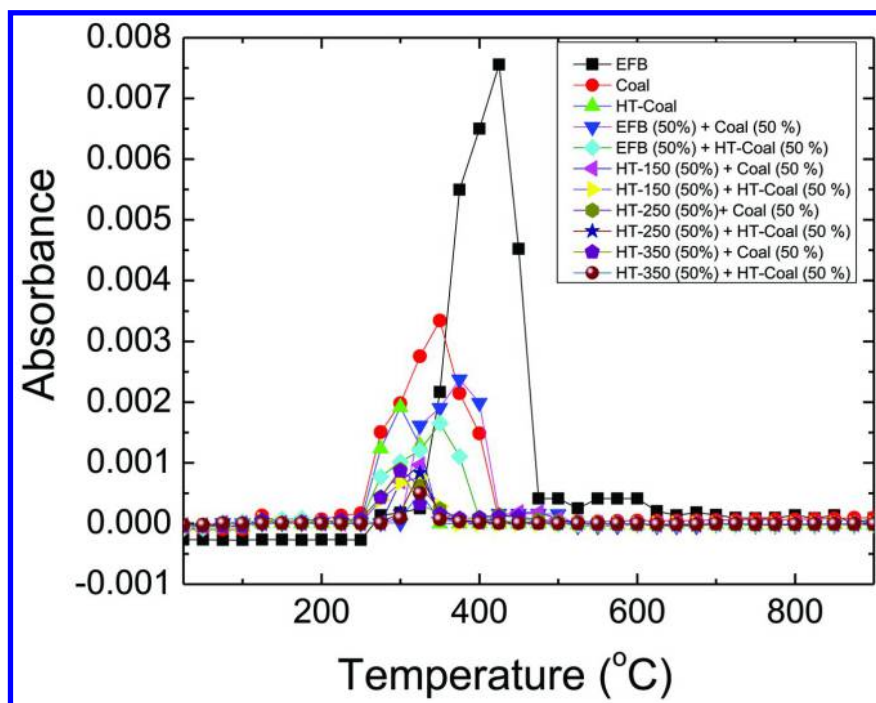
Figure 7. Evolution of CH_4 against the sample bed temperature for the different blends of fuels at a heating rate of 20 °C/min in TGA–FTIR. (Source: Parshetti et al., 2014; Reprinted with permission from Elsevier.)
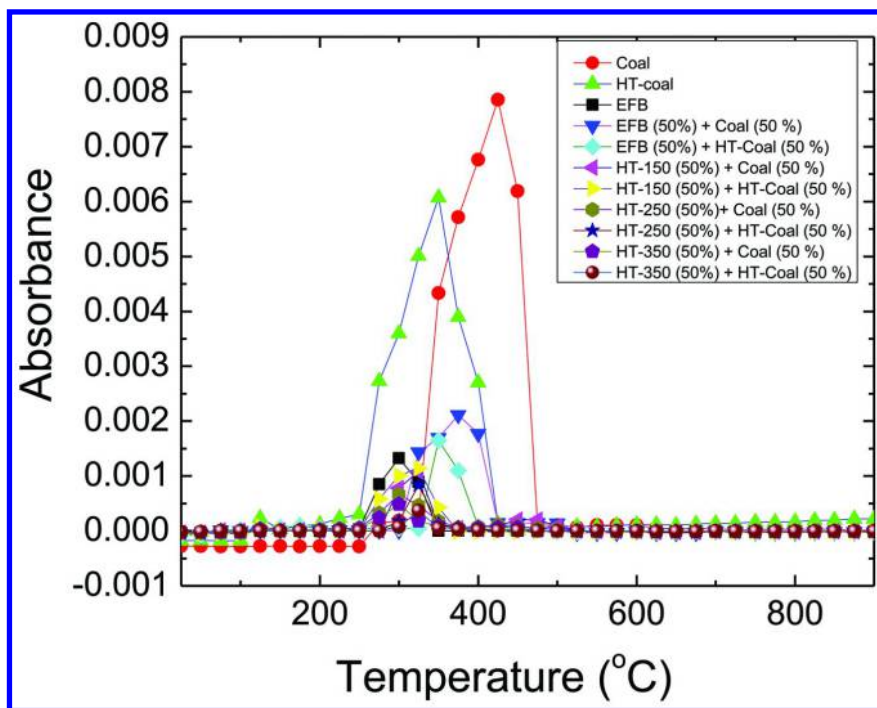
Figure 8. Evolution of SO₂ against the sample bed temperature for the different blends of fuels at a heating rate of 20 °C/min in TGA–FTIR. (Source: Parshetti et al., 2014; Reprinted with permission from Elsevier.)

SO₂ Emission Pattern

Figure 8 shows the existence of a single peak for SO_2 for all fuel samples and blends. The ultimate analysis showed that the amount of S in EFB biomass was less than that in the coal and HT-coal, therefore, the extent of release and the intensity for SO_2 in the coal and HT-coal were much higher than that for EFB. The highest SO_2 emission occurred at about 420 °C and 355 °C for coal and HT-coal, respectively. The SO_2 emission levels in the peak were reduced with addition of the EFB hydrochar in the blends; such reductions are expected because of a lower overall fuel-bound S content and a displacement of sulfur in the fuel blend (*51*). The features of the SO_2 peak were more strongly influenced by the fuel compositions of the blends. Among all blends, the SO_2 emission magnitude was higher for the two blends viz. EFB(50%)/Coal(50%) and EFB(50%)/HT-Coal(50%) and the SO_2 peak also shifted slightly towards the lower temperature with the HT-coal contents. The blend which produced lower SO_2 during combustion was HT-350(50%)/HT-Coal(50%). This was confirmed from the integral areas (Table 4) of the SO_2 emission curves, which are 0.671 for

HT-Coal, 0.178 for EFB(50%)/Coal(50%), 0.076 for EFB(50%)/HT-Coal(50%), 0.060 for HT-150(50%)/Coal(50%), 0.069 for HT-150(50%)/HT-Coal(50%), 0.050 for HT-250(50%)/Coal(50%), 0.025 for HT-250(50%)/HT-Coal(50%), 0.026 for HT-350(50%)/Coal(50%) and 0.010 for HT-350(50%)/HT-Coal(50%).
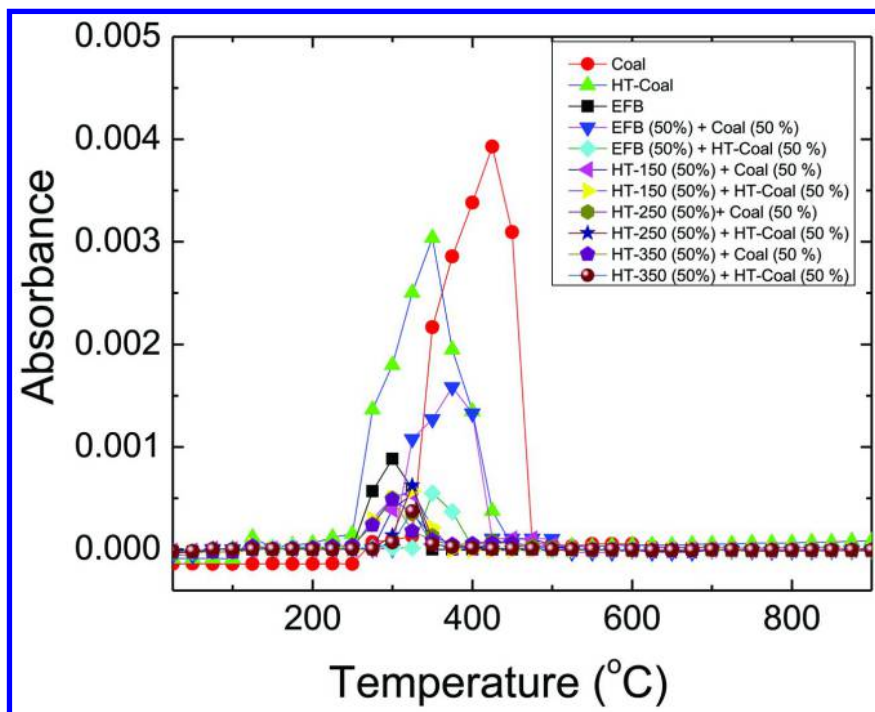
Figure 9. Evolution of NO against the sample bed temperature for the different blends of fuels at a heating rate of 20 °C/min in TGA–FTIR. (Source: Parshetti et al., 2014; Reprinted with permission from Elsevier.)

NO Emission Pattern

Figure 9 showed the NO emission profiles for different fuels. Coal used in the current research has low nitrogen contents. Consequently, the NO emission level was also low and was similar to SO_2 emissions in terms of its magnitude. It can be seen clearly from Figure 9 that all NO emission profiles show a single peak unlike the emission patterns observed for CO_2, CO and CH_4. The NO emission peak appeared at about 426 °C for the coal which showed a maximum emission (Integral area: 0.371). Further, HT-coal (Integral area: 0.337) and EFB(50%)/Coal(50%) blends (Integral area: 0.134) also showed comparatively higher emissions of NO with peaks at 352 and 375 °C, respectively. As reported in the literature (*52, 53*), high-temperature combustion produces more NO, named

"thermal NOx" similar to the process in grate combustion. However, for most of the fuels and blends studied here, a very low amount of NO was released in the high-temperature range. The high volatile contents of biomass derived hydrochar can effectively establish a fuel-rich zone early in the flame that can reduce NO_x emissions. Adding hydrochar can also reduce flame temperatures, leading to lower levels of thermal NO_x (*51*). The degree of the NO peak decreased with the addition of various hydrochar contents in the blends. The solid sample which produced lower NO during combustion and resisted the thermal formation at high temperature is HT-350(50%)/HT-Coal(50%). This is confirmed in the integral areas of the NO emission curves, which are 0.337 for HT-Coal, 0.025 for EFB(50%)/HT-Coal(50%), 0.030 for HT-150(50%)/Coal(50%), 0.034 for HT-150(50%)/HT-Coal(50%), 0.037 for HT-250(50%)/Coal(50%), 0.019 for HT-250(50%)/HT-Coal(50%), 0.029 for HT-350(50%)/Coal(50%) and 0.011 for HT-350(50%)/HT-Coal(50%) (Table 4).

Conclusions and Future Directions

The hydrothermal carbonization of EFB provided densified carbonaceous solid products containing around 50-66% of the carbon originally present in the raw material, depending upon the process temperature used. The composition of the hydrochars suggests that both dehydration and decarboxylation occurred during hydrothermal densification/carbonization. The combustion efficiency and emission characteristics of gaseous pollutants released from the combustion of untreated EFB biomass and its hydrochars with coal and HT-coal were investigated by TGA-FTIR. The combustion of solid carbonaceous fuels in the temperature range of 220 °C to 500 °C led to a maximum release of gaseous pollutants such as CO_2, CO, CH_4, NO and SO_2 for all fuels and their blends investigated in this study. The key combustion parameter, CCF, for most of the fuels and/or their blends was greater than 2, indicating good combustion performance. Also the activation energies of the HT-coal blended samples were lower than that of coal blended samples. Combustion behavior of fuels and their blends show that the burning process was better in blends such as HT-250 (50%)+ Coal (50%) and HT-250 (50%) + HT-Coal (50%) where the rate of weight loss was at its maximum (R_{max}) and the highest CCF value was also achieved, but the emission of gaseous pollutants (CO_2, CO, CH_4, NO and SO_2) was not at its minimum level. On the other hand for blends HT-350 (50%) + Coal (50%) and HT-350 (50%) + HT-Coal (50%) under similar conditions, the lowest amounts of gaseous pollutants (CO_2, CO, CH_4, NO and SO_2) were emitted but R_{max} and CCF decreased. Thus, for the experimental combustion and pollutant emission profiles of hydrochar/coal and hydrochar/HT-coal blend samples, some deviations were observed from the expected trends in terms of their R_{max}, CCF values and emission characteristics. These deviations are indicative of synergistic interactions taking place between the fuels during co-combustion of EFB hydrochars and coal/HT-coal. Overall, the addition of EFB hydrochars to coal and HT-coal resulted in a significant reduction in gaseous pollutant emissions along with good burning performance for some blends; Thus, co-combustion of hydrothermally

upgraded waste biomass with coal or upgraded coal is an attractive option to consider in existing power plants for energy generation because of the major environmental benefits such as reduction in the emission of greenhouse gases (CO_2 and CH_4), acidic gases (SO_2 and NO) and toxic gas (CO).

Although the HTC of EFB biomass is proven to be advantageous to produce energy densified hydrochars and their possible application in emmission control as described above; however there still remain some challenges and questions that should draw scientific attention for future direction in this research: (1) In addition, particulate emissions along with its toxicity studies should also be investigated in order to estimate potential of particulates emissions for health risks, which is currently in progress in our laboratory. (2) Improving HTC of biomass to produce functional carbonaceous hydrochar materials for their possible application in enhancing energy security and mitigating greenhouse gas emissions is an important subject for further investigations. (3) A detailed energetic and economic analysis for the use of hydrochar-coal co-combustion on an industrial scale is required in order to promote it as a possible technology for real applications.

To conclude, co-combustion is a complex process that consists of consecutive heterogeneous and homogeneous reactions. The emissions for each reaction depend on the fuel type, fuel size and properties, on temperature, and on combustion conditions. The study can be available for reference in designing of real-time combustion emission in a commercial boiler or in open stove combustion of HTC char co-combustion with coal and HTC coal. The information presented is useful for the understanding of the hydrothermal treatment of biomass and coal and offers its implications regarding emissions and combustion efficiency for real time applications.

Acknowledgments

References

1. Yusoff, S. *J. Clean. Prod.* **2006**, *14*, 87–93.
2. Goh, C. S.; Tan, K. T.; Lee, K. T.; Bhatia, S. *Bioresour. Technol.* **2010**, *101*, 4834–4841.
3. Abdullah, N.; Gerhauser, H. *Fuel* **2008**, *87*, 2606–2613.
4. Idris, S. S.; Rahman, N. A.; Ismail, K.; Alias, A. B.; Rashid, Z. A.; Aris, M. J. *Bioresour. Technol.* **2010**, *101*, 4584–4592.
5. Idris, S. S.; Rahman, N. A.; Ismail, K. *Bioresour. Technol.* **2012**, *123*, 581–591.
6. De, S.; Assadi, M. *Biomass Bioenergy* **2009**, *33*, 283–293.
7. Wang, C. P.; Wu, Y. J.; Liu, Q.; Yang, H. R.; Wang, F. Y. *Fuel Process. Technol.* **2011**, *92*, 1037–1041.

8. McIlveen-Wright, D. R.; Huang, Y.; Rezvani, S.; Wang, Y. *Fuel* **2007**, *86*, 2032–2042.
9. Katalambula, H.; Gupta, R. *Energy Fuels* **2009**, *23*, 3392–3405.
10. Morimoto, M.; Nakagawa, H.; Miura, K. *Energy Fuels* **2009**, *23*, 4533–4539.
11. Umar, D. F.; Santoso, B.; Usui, H. *Energy Fuels* **2007**, *21*, 3385–3387.
12. Nonaka, M.; Hirajima, T.; Sasaki, K. *Fuel* **2011**, *90*, 2578–2584.
13. Yin, C.; Rosendahl, L. A.; Kaer, S. K. *Prog. Energy Combust. Sci.* **2008**, *34*, 725–754.
14. Xu, X. G.; Li, S. Q.; Li, G. D.; Yao, Q. *Energy Fuels* **2010**, *24*, 241–249.
15. Shao, Y. Y.; Xu, C. B.; Zhu, J.; Preto, F.; Wang, J. S.; Li, H. N.; Badour, C. *Energy Fuels* **2011**, *25*, 2841–2849.
16. Wigley, F.; Williamson, J.; Malmgren, A.; Riley, G. *Fuel Process. Technol.* **2007**, *88*, 1148–1154.
17. Gogebakan, Z.; Gogebakan, Y.; Selcuk, N.; Seliuk, E. *Bioresour. Technol.* **2009**, *100*, 1033–1036.
18. Parshetti, G. K.; Kent Hoekman, S.; Balasubramanian, R. *Bioresour. Technol.* **2013**, *135*, 683–689.
19. Muthuraman, M.; Namioka, T.; Yoshikawa, K. *Appl. Energy* **2010**, *87*, 141–148.
20. Liu, Z. G.; Quek, A.; Hoekman, S. K.; Srinivasan, M. P.; Balasubramanian, R. *Bioresour. Technol.* **2012**, *123*, 646–652.
21. Muthuraman, M.; Namioka, T.; Yoshikawa, K. *Bioresour. Technol.* **2010**, *101*, 2477–2482.
22. Jin, Y.; Lu, L.; Ma, X.; Liu, H.; Chi, Y.; Yoshikawa, K. *Appl. Energy* **2013**, *102*, 563–570.
23. Titirici, M. M.; Thomas, A.; Antonietti, M. *New J. Chem.* **2007**, *31*, 787–789.
24. Titirici, M. M.; White, R. J.; Falco, C.; Sevilla, M. *Energ. Environ. Sci.* **2012**, *5*, 6796–6822.
25. Tremel, A.; Stemann, J.; Herrmann, M.; Erlach, B.; Spliethoff, H. *Fuel* **2012**, *102*, 396–403.
26. Gil, M. V.; Casal, D.; Pevida, C.; Pis, J. J.; Rubiera, F. *Bioresour. Technol.* **2010**, *101*, 5601–5608.
27. McIlveen-Wright, D. R.; Huang, Y.; Rezvani, S.; Mondol, J. D.; Redpath, D.; Anderson, M.; Hewitt, N. J.; Williams, B. C. *Fuel* **2011**, *90*, 11–18.
28. Li, J.; Brzdekiewicz, A.; Yang, W. H.; Blasiak, W. *Appl. Energy* **2012**, *99*, 344–354.
29. Hoffmann, B. S.; Szklo, A.; Schaeffer, R. *Biomass Bioenergy* **2012**, *45*, 295–302.
30. Kubacki, M. L.; Ross, A. B.; Jones, J. M.; Williams, A. *Fuel* **2012**, *101*, 84–89.
31. Lee, S. B.; Fasina, O. *J. Anal. Appl. Pyrol.* **2009**, *86*, 39–43.
32. Di Nola, G.; de Jong, W.; Spliethoff, H. *Fuel Process. Technol.* **2010**, *91*, 103–115.
33. Fasina, O.; Littlefield, B. *Fuel Process. Technol.* **2012**, *102*, 61–66.
34. Fang, M. X.; Shen, D. K.; Li, Y. X.; Yu, C. J.; Luo, Z. Y.; Cen, K. F. *J. Anal. Appl. Pyrol.* **2006**, *77*, 22–27.
35. Demirbas, A. *Prog. Energy Combust. Sci.* **2004**, *30*, 219–230.

36. Xiu, S. N.; Shahbazi, A.; Shirley, V.; Cheng, D. *J. Anal. Appl. Pyrol.* **2010**, *88*, 73–79.
37. Mumme, J.; Eckervogt, L.; Pielert, J.; Diakite, M.; Rupp, F.; Kern, J. *Bioresour. Technol.* **2011**, *102*, 9255–9260.
38. Hoekman, S. K.; Broch, A.; Robbins, C. *Energy Fuels* **2011**, *25*, 1802–1810.
39. Fuertes, A. B.; Arbestain, M. C.; Sevilla, M.; Macia-Agullo, J. A.; Fiol, S.; Lopez, R.; Smernik, R. J.; Aitkenhead, W. P.; Arce, F.; Macias, F. *Aust. J. Soil Res.* **2010**, *48*, 618–626.
40. Sevilla, M.; Fuertes, A. B. *Carbon* **2009**, *47*, 2281–2289.
41. Sevilla, M.; Fuertes, A. B.; Mokaya, R. *Energy Environ. Sci.* **2011**, *4*, 1400–1410.
42. Bassilakis, R.; Carangelo, R. M.; Wojtowicz, M. A. *Fuel* **2001**, *80*, 1765–1786.
43. Shao, J.; Yan, R.; Chen, H.; Wang, B.; Lee, D. H.; Liang, D. T. *Energy Fuels* **2008**, *22*, 38–45.
44. Lopez-Velazquez, M. A.; Santes, V.; Balmaseda, J.; Torres-Garcia, E. *J. Anal. Appl. Pyrol.* **2013**, *99*, 170–177.
45. Cao, J.; Xiao, G.; Xu, X.; Shen, D.; Jin, B. *Fuel Process. Technol.* **2013**, *106*, 41–47.
46. Parshetti, G. K.; Queck, A.; Betha, R.; Balasubramanian, R. *Fuel Process. Technol.* **2014**, *118*, 228–234.
47. Baker, R. R.; Coburn, S.; Liu, C.; Tetteh, J. *J. Anal. Appl. Pyrol.* **2005**, *74*, 171–180.
48. Yang, H. P.; Yan, R.; Chen, H. P.; Lee, D. H.; Zheng, C. G. *Fuel* **2007**, *86*, 1781–1788.
49. Giuntoli, J.; de Jong, W.; Arvelakis, S.; Spliethoff, H.; Verkooijen, A. H. M. *J. Anal. Appl. Pyrol.* **2009**, *85*, 301–312.
50. de Jong, W.; Di Nola, G.; Venneker, B. C. H.; Spliethoff, H.; Wojtowicz, M. A. *Fuel* **2007**, *86*, 2367–2376.
51. Dayton, D. A. *Summary of NO X Emissions Reduction from Biomass Cofiring*, DOE Contract DE - AC36 - 99 - GO10337, NREL/TP - 510 - 32260; National Renewable Energy Laboratory: Golden CO, May, 2002; p 3.
52. Vamvuka, D.; Troulinos, S.; Kastanaki, E *Fuel* **2006**, *85*, 1763–1771.
53. Normann, F.; Andersson, K.; Leckner, B.; Johnsson, F. *Fuel* **2008**, *87*, 3579–3585.

Chapter 3

Synthesis of Fluorogenic Chemosensors for Hg²⁺ Detection Using Naphthalimide Derivatives

Mengshan Lee, Ya-Chi Jang, Walter Den,* and Paiyu Kuo

Department of Environmental Science and Engineering, Tunghai University, Taichuing, Taiwan
***E-mail: wden@thu.edu.tw.**

Mercury ions are considered as severe environmental pollutants as they are widely spread in the atmosphere and surface water from either natural or anthropogenic activities. Current practices in detecting the ions involve sophisticated and costly analytical techniques including atomic absorption spectrometry, atomic emission spectrometry and inductively coupled plasma/mass spectrometry. Fluorogenic chemosensors, on the other hand, offer the unique advantages of high selectivity, high sensitivity, long lifetime and relatively low costs. This study focuses on reviewing current development of fluorogenic chemosensors in mercury ions detection, based on the use of naphthalimide or non-naphthalimide derivatives. The design principles as well as photophysical properties for the fluorogenic chemosensors are discussed. This study concludes with future perspectives of chemosensor design, including employment of C=N isomerization mechanism for fluorescence improvement and utilization of crown ether for improved recognition of mercury ions.

Introduction

Mercury contamination originates from natural and anthropogenic sources including oceanic and volcanic emissions, gold mining activities, industrial activities (e.g. non-ferrous metal manufacturing and cement production) and combustion of fossil fuels (*1*). Adverse health effects, namely cytogenetic

damage, cardiovascular toxicity, digestive, kidney and neurological diseases (2), are usually found when human bodies are chronically exposed to mercury ions (Hg^{2+}), even at a very low concentration, as the ions can easily pass through biological membranes and are bioaccumultable through food chains. Therefore, Hg^{2+} ions especially are considered as hazardous environmental pollutants among other heavy and transition metal ions.

A wide variety of instrumental methods have been developed for the determination of Hg^{2+} in the environment. Sophisticated analytical techniques, including atomic absorption spectrometry, atomic emission spectrometry and inductively coupled plasma/mass spectrometry (3), are commonly applied for Hg^{2+} detection. However, the aforementioned techniques can be time consuming (usually require pretreatment) and at high costs. Therefore, the demand for chemosensors that are selective and sensitive for detection of Hg^{2+} ions is continuously increasing. A great effort has gone to the development of selective chromogenic and fluorogenic chemosensors, as chemosensors can offer the unique advantages of a long lifetime and at relatively low instrumental costs.
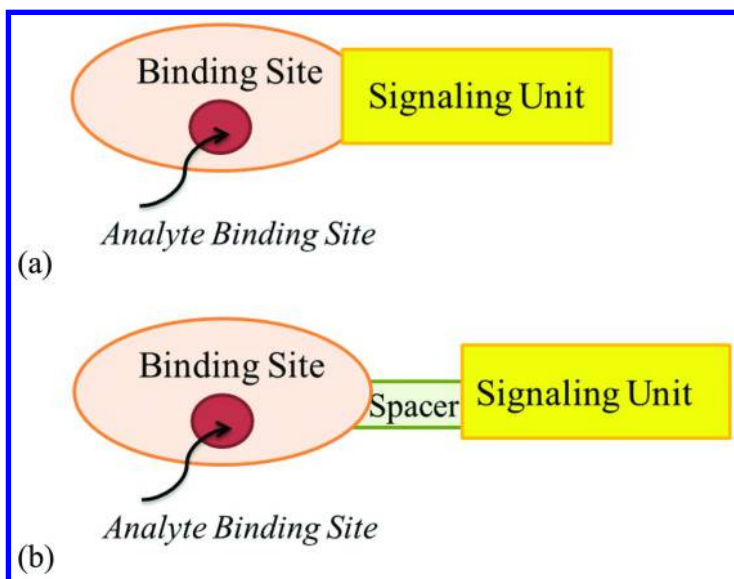
Figure 1. Schematic representation of the design concepts for chemosensors (a) binding site and signaling unit are directly attached (b) binding site and signaling unit are covalently linked with a spacer.

Fluorogenic chemosensors are of particular interest for metal sensing mainly due to its high detection selectivity, sensitivity and simplicity which translates molecular recognition into tangible fluorescence signals (4–6). The chemosensors produce detectable fluorescent signals through changing of their physicochemical properties while interacting with target species (mainly cations) through binding

sites. The binding sites may be directly or integrated through a spacer into the signaling moiety, as shown in Figure 1. For practical applications, photophysical properties such as the capability to absorb and emit at long wavelengths facilitate the use of naked eye detection or the use of inexpensive optical measurements, and these properties are main criteria in fluorescent chemosensors design (*7*, *8*).

A number of approaches regarding the design and synthesis of sensitive and selective fluorogenic chemosensor for Hg^{2+} ions were successfully developed (*9*). Generally, design of the chemosensors are either based on the coordination of Hg^{2+} to S atoms, or to multiple N atoms (*10*). In particular, naphthalimide and rhodamine derivatives, among other chemical probes in practice, are usually chosen as basic molecular probes for the synthesis of fluorescent chemosensors, as they are excellent fluorophores with high stability and quantum yield which contribute to unique photophysical properties (*8*, *11*). While earlier research studies of chemosensors focused on the proof of various synthesis principles, recent ones have become more focused on the investigation of specific sensors for the recognition of a particular ion (in this study, Hg^{2+} ions). Thus, this article aims at summarizing current development of fluorogenic chemosensors in determining Hg^{2+}, starting from reviewing present perspectives on Hg^{2+} sensor designs, followed by discussion on the sensing characteristics of naphthalimide deriva1tives. Future perspectives on the design of chemosensors are also discussed.

Signaling Theory for Fluorescent Chemosensor Design

Signaling theory for fluorescent chemosensors generally is on the basis of changes in a measureable photophysical property in the presence of an analyte in a system. The fluorescent signaling mechanism for chemosensors can be categorized as photoinduced electron transfer (PET), intramolecular charge transfer (ICT), fluorescence resonance energy transfer (FRET) and through-bond energy transfer (TBET) mechanisms; and their schematic representations are summarized in Figure 2.

The PET-type chemosensors, based on changes in quantum yield or fluorescence intensity upon recognition of an analyte, are commonly used in chemosensing applications to date (*12*). A typical PET-based sensing system normally consists of an aromatic fluorophore (electron acceptor), an aliphatic amine (electron donor) and a short methylene chain as a spacer that links the two parts. When the receptor binds with a target species (e.g. Hg^{2+}), the PET process is suppressed and therefore results in fluorescence signals (*13*, *14*). In an ICT-based chemosensor system, the ICT complex is elevated to a higher energy after photoabsorption by charge separation (*15*). The charge separation involves transfer of an electron from a donor to an acceptor, which results in increase in dipole moment. But ICT complex containing only one donor center is highly sensitive that may interfere interpretation of the results (*16*). Moreover, in the case that intramolecular charge transfer occurs with simultaneous twisting of the bonding in the ICT complex, a twisted intramolecular charge transfer (TICT) mechanism is introduced (*17*).
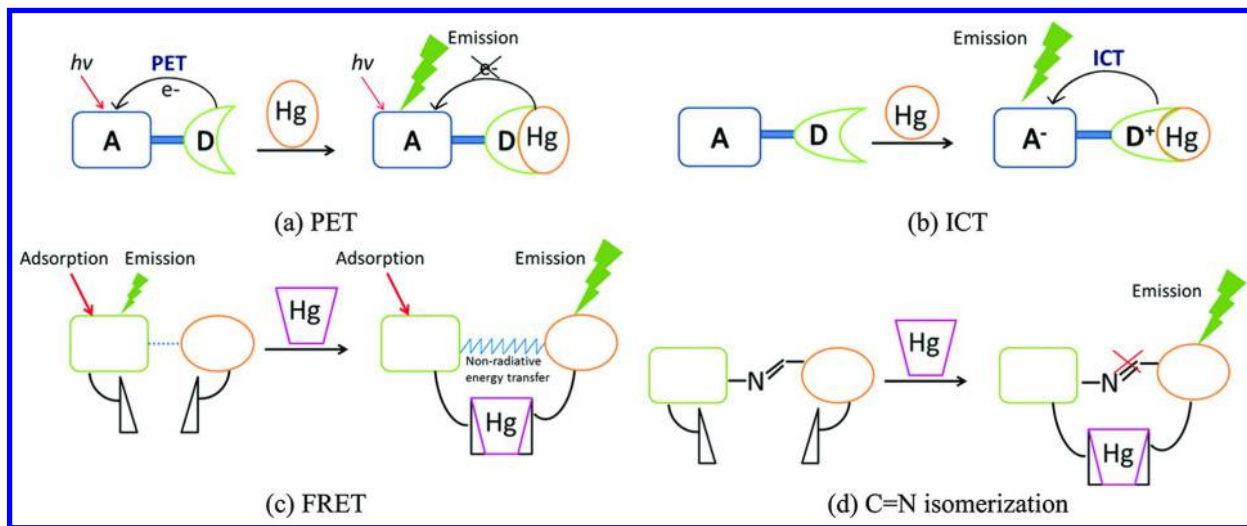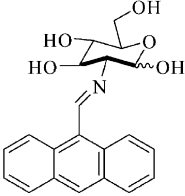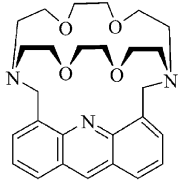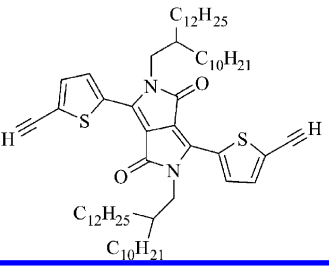
Figure 2. Schematic representation of signaling mechanisms for fluorescent chemosensors (a) PET (b) ICT (c) FRET (d) C=N isomerization.
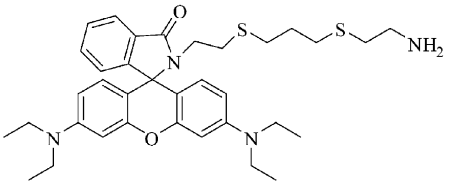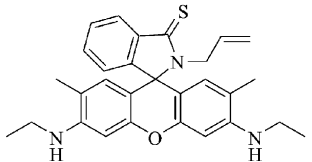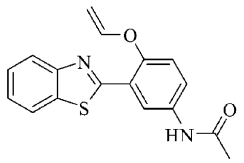
Table 1. Comparison of Fluorogenic Sensing Characteristics for Hg²⁺ (Non-Naphthalimide Derivatives)

Chemosensor probe	Probe structure	Response wavelength	Detection limit	Response time
Anthracenyl–imino– glucosyl(*36*)		410 nm	1.0×10^{-2} nM	N/A
Aridine(*63*)		448 nm	3.0×10^{3} nM	N/A
Diketopyrrolopyrrole(*10*)		603 nm	5.0×10^{2} nM	<5mins

Table 1. (Continued) Comparison of Fluorogenic Sensing Characteristics for Hg²⁺ (Non-Naphthalimide Derivatives)

Chemosensor probe	Probe structure	Response wavelength	Detection limit	Response time
Pentaquinone(*31*)		582 nm	7.0×10^2 nM	N/A
Rhodamine(*26*)		556 nm	1.0×10^{-2} nM	<5 mins

Table 1. (Continued) Comparison of Fluorogenic Sensing Characteristics for Hg²⁺ (Non-Naphthalimide Derivatives)

Chemosensor probe	Probe structure	Response wavelength	Detection limit	Response time
Rhodamine(*11*)		550 nm	5.0×10^{-2} nM	N/A
Rhodamine(*35*)		561 nm	2.75×10^{-1} nM	N/A
Vinyl ether(*33*)		500 nm	1.0×10^{-1} nM	~30 mins

*Lowest detectable concentration reported

FRET mechanism incorporates transfer of excitation energy from a fluorophore at excited electronic state (energy donor) to a fluorophore at ground state (energy acceptor) through a non-conjugated spacer in close proximity, which allows detection of analyte by ratiometric fluorometry (*18*). In the FRET mechanism, sufficiently overlap integral from intersection of the donor fluorescence emission with the acceptor absorbance is required. In contrast to FRET, through-bond energy transfer (TBET) is not limited by the spectral overlap, thus, a large wavelength difference between the two emission peaks could be observed for improved recognition (*19*). TBET is defined as energy transfer through conjugated bonds in which the energy transfer is predominantly via twisted π-electron systems (*20*), therefore, it is expected to exhibit high energy transfer efficiency, fast energy transfer rate and large pseudo-Stoke's shift (*21*).

Additionally, C=N isomerization has been used as a signaling mechanism for fluorescent chemosensors, although it was seldom reported (*22–24*) in the literature. C=N bond is an analog of the C=C bond but differs from an unshared pair of electrons on the nitrogen atom. C=N isomerization is a predominant decay process of excited states in compounds; therefore, those compounds are often nonfluorescent. Formation of covalently bridged C=N structure in the compounds dramatically suppress the C=N isomerization in the excited states, consequently, the compounds show fluorescence. Aside from the covalent bridging of C=N bond, the C=N isomerization may also be inhibited through complexion with the target analyte (*6*).

Current Development of Fluorogenic Chemosensors

Fluorogenic chemosensors for recognition of Hg^{2+} have been extensively explored. Chemical probes that were commonly used for the sensing application include rhodamine, naphthalimide, coumarin, and fluorescein derivatives. Other types of chemical probes were also available yet seldom being reported. Approaches for synthesizing fluorogenic chemosensors for Hg^{2+} recognition are discussed in this section, and the performances for recently developed chemosensors (non-naphthalimide derivatives) are summarized in Table 1.

Rhodamine is considered as an excellent "on-off" type fluorescence probe on the basis of the spirolactam (nonfluorescent) to ring opened amide (fluorescent) equilibrium of rhodamine derivatives (*25*). The rhodamine-based sensor system also possesses excellent features such as large molar extinction coefficient, high fluorescence quantum yield, and long absorption and emission wavelengths (>500 nm) in the visible region (*11*). Rhodamine-appended thiosemicarbazide chemosensors was developed taking the advantages of Hg^{2+}-induced ring-opening reaction from desulfurization of thiosemicarbazide, and therefore emitted strong yellow fluorescence maximizing at 556 nm (*26*). The chemosensors were expected to undergo oxadiazole formation when the thiosemicarbazide moiety was liberated by Hg^{2+}-facilitated ring-opening of the spirocycle grouping. Large fluorescence enhancement can be achieved while rhodamine appended with both thiol and alkyne moieties (*27, 28*). Rhodamine-appended 2-[3-(2-aminoethylsulfanyl)propylsulfanyl]ethanamine chemosensor also showed high sensitivity and selectivity in the detection of Hg^{2+} ions (*11*), as it provided

appropriately located sulfur and nitrogen atoms as the donor atoms that can self-assemble around the Hg^{2+} ions due to the favorable electrostatic interactions (*29*).

Nevertheless, the rhodamine-based chemosensors have limitations of having a very small Stokes shift (around 25 nm), which may lead to self-quenching and fluorescence detection errors due to excitation back-scattering effects (*30*). Pentaquinone derivatives coupling rhodamine moieties was subsequently studied for sensing property improvements (*31*). The pentaquinone-based chemosensor was designed and synthesized to undergo through-bond energy transfer (TBET) theory in the presence of Hg^{2+} ions, leading to fluorescence emission enhancement at 582 nm which could be attributed to the opening of spirolactam ring to an amide form.

Aside from rhodamine derivative-based chemosensors, a variety of chemical probes for Hg^{2+} ion sensing applications are herein discussed. Oligodeoxyribonucleotide (ODN)-based chemosensor that can detect Hg^{2+} ions in aqueous solution with high selectivity was developed, owing to the selectivity of Hg^{2+} ions onto the thymine-thymine base pairs in ODN. In the presence of Hg^{2+}, Hg-mediated base pairs (T-Hg-T) were formed, and enhanced FRET process between the fluorophore (fluorescein) and the quencher (dabcyl) moieties was observed (*32*). Vinyl ether derivative-based chemosensor was developed using a chemical reaction specific to Hg^{2+} species and revealed fluorescence response through the excited state intramolecular proton transfer upon irradiation. The chemosensor was designed based on the metal-promoted hydrolysis of vinyl ether derivatives to generate 2-(benzothiazol-2-yl)phenols, but the reaction was very time consuming (approximately to 30 mins) (*33*). Diketopyrrolopyrrole (DPP), a well-known building block for organic electronic device applications, was used as a fluorophore for both Hg^2 and Cu^{2+} detection. The DPP-based sensor has two reaction sites: an alkyne group for hydration reaction of Hg^{2+}, and a thiophene unit that is highly selective towards Cu^{2+} (*10*). An acridine derivative bearing an immobilized azacrown ligand was introduced as a Hg^{2+} sensor, based on the theory that Hg^{2+} ions tend to form cooperative bindings on the immobilized ligand and the nitrogen atom on acridine. The sensor displayed selective chelation enhanced fluorescence effect due to the interaction between Hg^{2+} and nitrogen on the acridine or inhibition of the PET process from the benzylic nitrogens (*34*).

Although synthesis of chemosensors with high sensitivity and selectivity for Hg^{2+} recognition is well developed, the irreversibility of the sensing reactions still forms a barrier. Therefore, recent efforts have been attended to the investigation on reversible mechanisms for chemosensing. A novel reversible fluorescence turn-on Hg^{2+} chemosensor based on rhodamine composed of a thiol atom and an alkene moiety was explored. The chemosensor demonstrated a large fluorescence enhancement response at 561 nm with high sensitivity (i.e., a detection limit of 27.5 nM), and the binding with Hg^{2+} was reversible with excess addition of EDTA under neutral condition. The reversible sensing mechanism for the chemosensor was drastically distinct that disconnected the binding of Hg^{2+} ion at a thiol atom and alkyne moiety in the rhodamine scaffold (*35*). Another example of using EDTA as a reversing reagent was a gluco-imino-anthracenyl derivative-based chemosensor, in which the EDTA could disable the binding of Hg^{2+} ion in the

complex at imine and aromatic moieties (*36*). The sensor also presented high selectivity in the presence of several biological samples (e.g., blood serum and milk) and ecologically relevant metal ions. In addition, iodide ions (e.g., KI) may be added to the Hg^{2+}-sensor complex to remove the Hg^{2+} ion from the complex; therefore, the chemosensor can be reused for sensing (*37*).

Naphthalimide-Based Fluorogenic Chemosensors
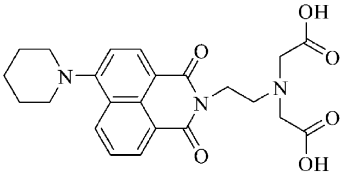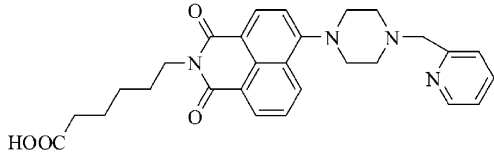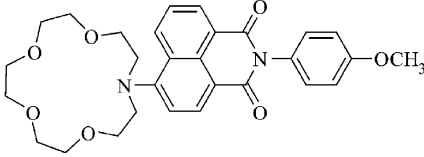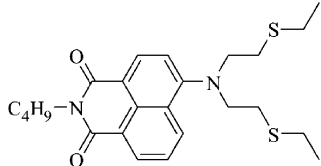
Naphthalimide derivatives are excellent fluorophores with high stability and quantum yield, and have frequently been applied as fluorophores to prepare fluorescent chemosensors for pH, metal cations, and anions in recent years (*38*). Recent development of the naphthalimide derivative-based chemosensors is summarized in Table 2. The photophysical properties of naphthalimide structure are strongly affected by the nature of the substituent (e.g. amino or nitro group) and the substitution pattern employed (e.g. ortho, meta or para substitution), as naphthalimide itself contains a highly versatile building unit that can absorb energy and emit fluorescence at long wavelengths. For example, 1,8-naphthalimides are very sensitive to substitution in its aromatic ring (*39*), nitro functional group attached 1,8-naphthalimide (such as 3- or 4-nitro-1,8-naphthalimide) that is in high energy excited states has a broad absorption band maximized at about 360 nm, whereas amino functional group attached 1,8-naphthalimide (such as 4-amino-1,8-naphthalimide) presents a "push-pull"-based internal charge transfer excited state that contributes to the absorption and emission bands centered at 450 and 550 nm, respectively (*8*). The general design principle for Hg^{2+} chemosensor using 1,8-naphthalimide derivatives is presented in Figure 3. As Hg^{2+} ions tend to have strong quenching effects while binding with the signaling moiety, the 1,8-naphthalimide derivatives reveal fluorescent turn-off response by the formation of imide-Hg^{2+}-imide complex (*40*).
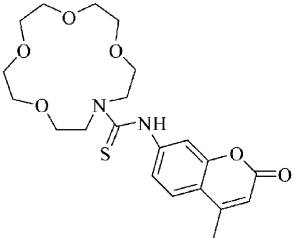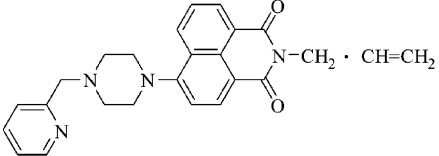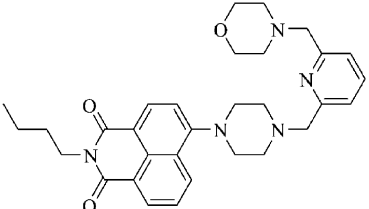
Figure 3. Design principle for Hg^{2+} chemosensor using 1,8-naphthalimide derivatives. (Reproduced with permission from (62). 2013, Elsevier.)

While most of the reported fluorescent chemosensors for recognition of Hg^{2+} were based on fluorescence quenching mechanisms (turn-off), only a few chemosensors were using fluorescence enhancement (FE, turn-on) for recognition of Hg^{2+} in aqueous solution. FE theory was usually preferred in the design of chemosensor as lower detection limit of target species can be potentially achieved. A 1,8-naphthalimides-based fluorescent chemosensor appended with two acetic carboxylic moieties was developed based on the FE theory (*41*). The chemosensor was demonstrated to have high selectivity and sensitivity for recognition of Hg^{2+} ion and exhibited an increase in fluorescent intensity at 562 nm due to the formation of Hg^{2+} inclusion complex.
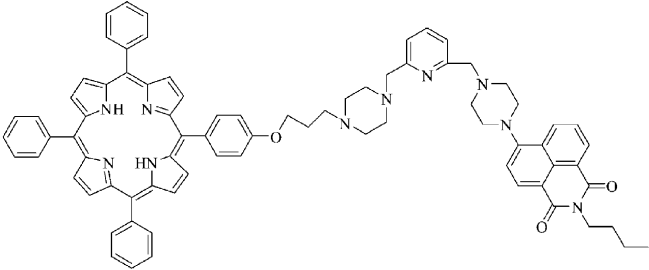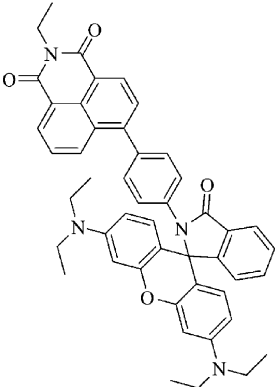
Table 2. Comparison of Fluorogenic Sensing Characteristics for Hg²⁺ (Naphthalimide Derivatives)

Fluorescent probe	Probe structure	Response wavelength	Detection limit	Response time
Acetic carboxylic(*41*)		562 nm	1.0×10^4 nM	N/A
Aliphatic amine(*38*)		529 nm	4.9×10^1 nM	< 1 min
Aza-15-crown-5 ether(*52*)		537 nm	4.0×10^4 nM*	N/A
BTABN(*64*)		530 nm	1.27 nM	<1 min

Table 2. (Continued) Comparison of Fluorogenic Sensing Characteristics for Hg²⁺ (Naphthalimide Derivatives)
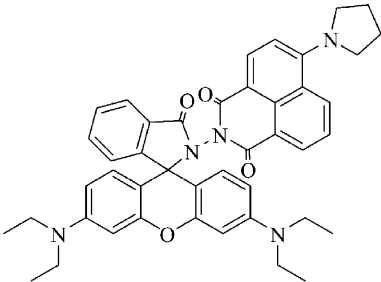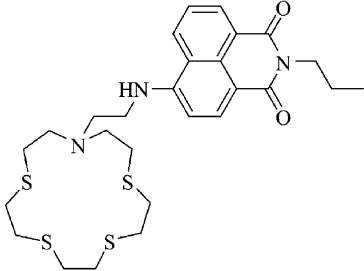
Fluorescent probe	Probe structure	Response wavelength	Detection limit	Response time
Coumarin(*50*)		407 nm	5.0×10^2 nM*	N/A
HEMA(*60*)		520 nm	2.0×10^3 nM	<80 secs
NPM(*59*)		529 nm	6.1×10^1 nM.	N/A

Table 2. (Continued) Comparison of Fluorogenic Sensing Characteristics for Hg^{2+} (Naphthalimide Derivatives)

Fluorescent probe	Probe structure	Response wavelength	Detection limit	Response time
Porphyrin(*55*)		525 nm and 650 nm	2.0×10^1 nM	<2 mins
Rhodamine(*4*)		578 nm	2.0×10^3 nM	N/A

Table 2. (Continued) Comparison of Fluorogenic Sensing Characteristics for Hg²⁺ (Naphthalimide Derivatives)

Fluorescent probe	Probe structure	Response wavelength	Detection limit	Response time
Rhodamine(*42*)		585 nm	3.0×10^1 nM	N/A
Rhodamine(*43*)		585 nm	5.0×10^{-2} nM	N/A

Table 2. (Continued) Comparison of Fluorogenic Sensing Characteristics for Hg²⁺ (Naphthalimide Derivatives)

Fluorescent probe	Probe structure	Response wavelength	Detection limit	Response time
Rhodamine(*44*)		583 nm	1.0×10^{-3} nM	N/A
Thioether-rich crown(*49*)		532 nm	2.5×10^{-1} nM	N/A

*Lowest detectable concentration reported

A naphthalimide-rhodamine-based chemosensor was developed utilizing the TBET theory, as the reaction can result in large Strokes shifts and emission shifts. While naphthalimide moiety was attached with rhodamine through a conjugated spacer (e.g. benzene) in the presence of Hg^{2+} ions, it exhibited TBET along with fluorescence enhancement at 578 nm (orange color) (4). FRET signal mechanism also can be employed for the design of naphthalimide-rhodamine-based chemosensor, in which the fluorescence detection errors due to backscattering effects from the excitation source can be efficiently avoided (30). Therefore, strong red emission (approximately at 585 nm) of rhodamine due to FRET from excitation of the 1,8-naphthalimide could be observed (42–44).

C=N isomerization, on the other hand, can be utilized as a fluorescent enhancement mechanism for Hg^{2+} ion sensing. The fluorescence of Hg^{2+} sensor complex with a covalently bridged C=N structure increases significantly owing to the suppression of C=N isomerization in the excited states (6, 24). This mechanism is relatively new and demonstrates a very significant fluorescence enhancement to metal cations in a simple and effective way. C=N isomerization sensing mechanism was applied to coumarin-based amine chemosensors in detecting Zn^{2+} ions (6) and Cu^{2+} ions (45), as well as to a fluorescein-based imines in detecting Cd^{2+} ions (46). Following the same strategy, a chemosensor was developed using naphthalimide-appended crown ether derivative (dithiodioxomonoaza) for sensing of Hg^{2+} through C=N isomerization with as fast as 18 seconds of response time (47).

Several fluorophore-appended macrocycles such as thia-aza or aza crown ether were shown to respond to Hg^{2+} via photoinduced charge transfer or inhibition of PET (48). An aminonaphthalimide-appended thioether-rich crown fluorescent sensor was a good example exhibiting the turn-on signaling behavior based on the PET mechanism. The sensor exhibited selective fluorescence enhancement effect from inhabitation of PET while forming a Hg^{2+}-containing complex (49). Another example would be a coumarin-based turn-on type chemosensor functionalized through the PET process (50). The sensor consisted of a monoaza-15-crown-5 moiety (an ionophore) connected to a 7-amino-4-methylcoumarin via a thiourea linker (a chromopher). Coordination of Hg^{2+} with the ionophore would cancel the PET process and enhanced the fluorescence intensity, and the interaction of electron transfer from a 15-crown-5 to a chromophore group was confirmed using density functional theory (51). A new 1,8-naphthalimide derivative bearing an aza-15-crown-5 macrocycle was synthesized as a chemosensor for Hg^{2+} using a two-step reaction (52). Upon Hg^{2+} binding, the sensor showed strong fluorescence depletion through ICT mechanism along with a 22 nm blue-shift from an excitation wavelength of 537 nm. However, ICT-type chemosensor probes rely on signal detection of emission spectra shift might cause high degree of overlap while binding target ions (53). FRET-type probes, on the other hand, could theoretically avoid the problem because the emission of the donor at a short wavelength induces emission of the acceptor at a relative longer wavelength (54, 55). Li's group unveiled a naphthalimide-porphyrin fluorogenic chemosensor probe for the detection of Hg^{2+} in aqueous and living cells, based on the FRET mechanism (55). The results showed that fluorescence emissions of two fluorophores were well resolved with a 125 nm difference between the two

maximum emissions. The probe also possessed excellent sensing characteristics of high sensitivity, water solubility, reversibility and fast response time (less than 2 mins).

Naphthalimide derivatives were also commonly applied in organic solutions (i.e. less water soluble), because lipophilic alkyl or phenyl groups were favorably connected to the imide moieties of naphthalimide derivatives (56). One of the best combinations for chemosensor design was the turn-on/aqueous sensors, as chemosensors of this type show improved characteristics, such as the reduced errors during observation and the applicability in the analysis for both aqueous and biological samples (50, 57). Addition of hydrophilic group, such as hexanoic acid group, can make naphthalimide derivatives imide moieties operate in aqueous solution (58). For instance, in the case that Hg^{2+} ions were relatively less detectable in aqueous environment rather than in organic solvent, Li's group used naphthalimide derivative containing a hydrophilic hexanic acid group for the recognition of Hg^{2+} ions in aqueous solution based on PET fluorescence enhancement signaling mechanism (38). The developed fluorescent chemosensor is pH independent in medium condition and has detection limit of 4.93×10^{-8} M with less than 1 minute of response time. An 1,8-naphthalimides-based fluorescent chemosensor appended with two acetic carboxylic moieties was also developed with high water solubility (41).

Recent attention has been paid to the development of multi-function chemosensors, including bifunction detection sensor (i.e. detection of more than one of target species), immobilized sensors, and sensors that can simultaneously detect and remove target species. An aminonaphthalimide-appended thioether-rich crown sensor exhibited bifunctional detection for both Hg^{2+} and Ag^+, based on Hg^{2+}-selective turn-on and Ag^+-selective turn-off signals (49). The similar analogy was applied for an naphthalimide-based bifunctional fluorescent probe containing morpholine moiety that shows highly selective fluorescence turn-on property for Hg^{2+} and turn-off for Cu^{2+} (59). In those studies, the probe complexes showed fluorescence response in the system due to the PET process. Addition of Hg^{2+} into the solution induced a significant enhancement of fluorescence, whereas addition of other species (i.e. Ag^+ and Cu^{2+}) completely quenched the fluorescence emission. For the development of immobilized Hg^{2+} sensors, the naphthalimide derivative with a terminal double bond was prepared and photo-copolymerized with 2-hydroxyethyl methacrylate on a glass surface (60). The resulting sensor underwent FE induced by PET inhibition process in the presence of Hg^{2+}. The immobilized sensor was fully reversible by using HCl solution and remained functional for more than 2 months of continuous use. Zhu's group reported the use of naphthalimide-functionalized magnetic fluorescent nanoparticle to develop a chemosensor capable of simultaneously detecting and removing Hg^{2+} (61, 62). The proposed nanosensors exhibited excellent Hg^{2+} selectivity through the formation of imide-Hg-imide complexes, and the removal of Hg^{2+} was achieved by the aggregation-induced sedimentation strategy (Figure 4).
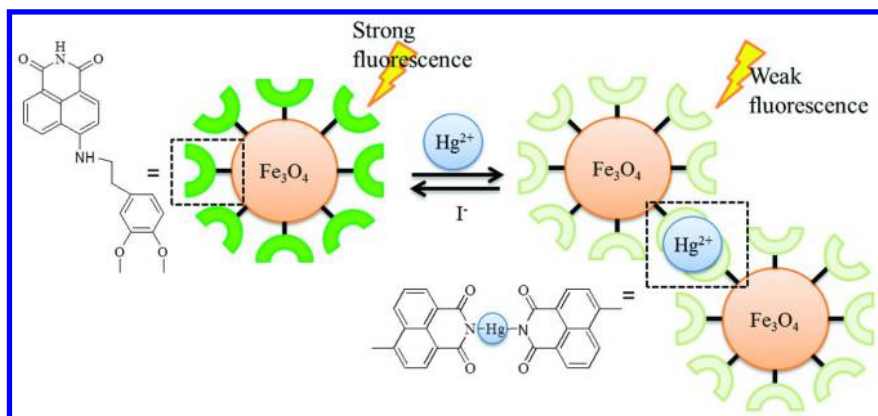
Figure 4. Scheme representation for simultaneous detection and removal of
Hg^{2+}. (Reproduced with permission from (62). 2013, Elsevier.)

Conclusions

This study reviewed the use of naphthalimide derivatives and other popular chemical probes in the field of fluorescent Hg^{2+} sensing. Functionalized naphthalimide sensors certainly have their merits in excellent features of long excitation and emission wavelengths and relatively high quantum efficiency. Moreover, their distinct color or fluorescent changes due to structure substitution make them very promising for ion sensing through fluorescence or naked-eye detection. Future studies for the use of this photophysical rich structure of naphthalimide is encouraged, in which special attention should be paid to its structural modulation of substitution pattern and the nature of substituents during the design process and the experimental procedure.

Despite impressive advances on the current development of fluorogenic chemosensors for Hg^{2+}, there is always a great need for the investigation on new sensors that are capable of recognizing Hg^{2+} ions in the environment with better properties. Continuing efforts can possibly be made in enhancing fluorescence signaling, improving selectivity via avoiding interference from other chemically related metal ions (e.g. Cd^{2+}, Pb^{2+} and Cu^{2+}), improving water solubility, promoting reversibility, and development of multi-function sensors (e.g. detect several toxics simultaneously).

The information discussed in this study, therefore, hopefully can provide insights for future use of the chemosensors and are helpful in improving techniques for direct recognition of Hg^{2+} ions in various applications.

Acknowledgments

References

1. Pirrone, N.; Cinnirella, S.; Finkelman, R. B.; Friedli, H. R.; Leaner, J.; Mason, R.; Mukherjee, A. B.; Stracher, G. B.; Streets, D. G.; Telmer, K. *Atmos. Chem. Phys.* **2010**, *10*, 5951–5964.
2. Passos, C. J.; Mergler, D. *Cad. Saúde Pública* **2008**, *24* (Suppl 4), s503–s520.
3. Selid, P.; Xu, H.; Collins, E. M.; Striped Face-Collins, M.; Zhao, J. X. *Sensors* **2009**, *9*, 5446–5459.
4. Kumar, M.; Kumar, N.; Bhalla, V.; Singh, H.; Sharma, P. R.; Kaur, T. *Org. Lett.* **2011**, *13*, 1422–1425.
5. Wu, J.-S.; Zhou, J.-H.; Wang, P.-F.; Zhang, X.-H.; Wu, S.-K. *Org. Lett.* **2005**, *7*, 2133–2136.
6. Wu, J.-S.; Liu, W.-M.; Zhuang, X.-Q.; Wang, F.; Wang, P.-F.; Tao, S.-L.; Zhang, X.-H.; Wu, S.-K.; Lee, S.-T. *Org. Lett.* **2007**, *9*, 33–36.
7. Plush, S. E.; Gunnlaugsson, T. *Org. Lett.* **2007**, *9*, 1919–1922.
8. Duke, R. M.; Veale, E. B.; Pfeffer, F. M.; Kruger, P. E.; Gunnlaugsson, T. *Chem. Soc. Rev.* **2010**, *39*, 3936–3953.
9. Kim, H. N.; Ren, W. X.; Kim, J. S.; Yoon, J. *Chem. Soc. Rev.* **2012**, *41*, 3210–3244.
10. Kaur, M.; Choi, D. H. *Sens. Actuators, B* **2014**, *190*, 542–548.
11. Wanichacheva, N.; Setthakarn, K.; Prapawattanapol, N.; Hanmeng, O.; Lee, V. S.; Grudpan, K. *J. Lumin.* **2012**, *132*, 35–40.
12. Dos Santos, C. M. G.; Glynn, M.; McCabe, T.; Seixas de Melo, J. S.; Burrows, H. D.; Gunnlaugsson, T. *Supramol. Chem.* **2008**, *20*, 407–418.
13. Zhang, W.; Ma, Z.; Du, L.; Li, M. *Analyst* **2014**, *139*, 2641–2649.
14. Lakowicz, J. R. *Principles of Fluorescence Spectroscopy*; Springer: New York, 2009.
15. Haidekker, M. A.; Theodorakis, E. A. *J. Biol. Eng.* **2010**, *4*, 11.
16. Vachova, L.; Novakova, V.; Kopecky, K.; Miletin, M.; Zimcik, P. *Dalton Trans.* **2012**, *41*, 11651–11656.
17. Pradhan, T.; Gazi, H. A. R.; Biswas, R. *J. Chem. Sci.* **2010**, *122*, 481–487.
18. Culzoni, M. J.; Munoz de la Pena, A.; Machuca, A.; Goicoechea, H. C.; Babiano, R. *Anal. Methods* **2013**, *5*, 30–49.
19. Gong, Y. J.; Zhang, X. B.; Zhang, C. C.; Luo, A. L.; Fu, T.; Tan, W.; Shen, G. L.; Yu, R. Q. *Anal. Chem.* **2012**, *84*, 10777–10784.
20. Bandichhor, R.; Petrescu, A. D.; Vespa, A.; Kier, A. B.; Schroeder, F.; Burgess, K. *J. Am. Chem. Soc.* **2006**, *128*, 10688–10689.
21. Qu, X.; Liu, Q.; Ji, X.; Chen, H.; Zhou, Z.; Shen, Z. *Chem. Commun.* **2012**, *48*, 4600–4602.
22. Johnson, J. E.; Morales, N. M.; Gorczyca, A. M.; Dolliver, D. D.; McAllister, M. A. *J. Org. Chem.* **2001**, *66*, 7979–7985.
23. Wu, J.-S.; Liu, W.-M.; Zhuang, X.-Q.; Wang, F.; Wang, P.-F.; Tao, S.-L.; Zhang, X.-H.; Wu, S.-K.; Lee, S.-T. *Org. Lett.* **2007**, *9*, 33–36.
24. Li, L.; Liu, F.; Li, H.-W. *Spectrochim. Acta, Part A* **2011**, *79*, 1688–1692.
25. Beija, M.; Afonso, C. A. M.; Martinho, J. M. G. *Chem. Soc. Rev.* **2009**, *39*, 2410–2433.
26. Yang, Y.-K.; Yook, K.-J.; Tae, J. *J. Am. Chem. Soc.* **2005**, *127*, 16760.

27. Huang, W.; Zhu, X.; Wua, D.; He, C.; Hu, X.; Duan, C. *Dalton Trans.* **2009**, *47*, 10457–10465.

28. Lin, W.; Cao, X.; Ding, Y.; Yuan, L.; Long, L. *Chem. Commun.* **2010**, *46*, 3529–3531.

29. Wanichacheva, N.; Kamkaew, A.; Watpathomsub, S.; Lee, V. S.; Grudpan, K. *Chem. Lett.* **2010**, *39*, 1099–1250.

30. Tolosa, L.; Nowaczyk, K.; Lakowicz, J. *An Introduction to Laser Spectroscopy*; Kluwer: New York, 2002.

31. Bhalla, V.; Roopa, ; Kumar, M.; Sharma, P. R.; Kaur, T. *Inorg. Chem.* **2012**, *51*, 2150–2156.

32. Ono, A.; Togashi, H. *Angew. Chem., Int. Ed.* **2004**, *43*, 4300–4302.

33. Santra, M.; Roy, B.; Ahn, K. H. *Org. Lett.* **2011**, *13*, 3422–3425.

34. Lee, S. Y.; Kim, H. J.; Wu, J. S.; No, K.; Kim, J. S. *Tetrahedron Lett.* **2008**, *49*, 6141–6144.

35. Lin, W.; Cao, X.; Ding, Y.; Yuan, L.; Yu, Q. *Org. Biomol. Chem.* **2010**, *8*, 3618–3620.

36. Mitra, A.; Mittal, A. K.; Rao, C. P. *Chem. Commun.* **2011**, *47*, 2565–2567.

37. Coronado, E.; Galán-Mascarós, J. R.; Martí-Gastaldo, C.; Palomares, E.; Durrant, J. R.; Vilar, R.; Gratzel, M.; Nazeeruddin, M. K. *J. Am. Chem. Soc.* **2005**, *127*, 12351–12356.

38. Li, C.-Y.; Xu, F.; Li, Y.-F.; Zhou, K.; Zhou, Y. *Anal. Chim. Acta* **2012**, *717*, 122–126.

39. Banerjee, S.; Veale, E. B.; Phelan, C. M.; Murphy, S. A.; Tocci, G. M.; Gillespie, L. J.; Frimannsson, D. O.; Kelly, J. M.; Gunnlaugsson, T. *Chem. Soc. Rev.* **2013**, *42*, 1601–1618.

40. Fang, C.-l.; Zhou, J.; Liu, X.-j.; Cao, Z.-h.; Shangguan, D.-h. *Dalton Trans.* **2011**, *40*, 899–903.

41. Dai, H.; Xu, H. *Bioorg. Med.Chem. Lett.* **2011**, *21*, 5141–5144.

42. Liu, Y.; Lv, X.; Zhao, Y.; Chen, M.; Liu, J.; Wang, P.; Guo, W. *Dyes Pigm.* **2012**, *92*, 909–915.

43. Luxami, V.; Verma, M.; Rani, R.; Paul, K.; Kumar, S. *Org. Biomol. Chem.* **2012**, *10*, 8076–8081.

44. Mahato, P.; Saha, S.; Suresh, E.; Di Liddo, R.; Parnigotto, P. P.; Conconi, M. T.; Kesharwani, M. K.; Ganguly, B.; Das, A. *Inorg. Chem.* **2012**, *51*, 1769–1777.

45. Sheng, J. R.; Feng, F.; Qiang, Y.; Liang, F. G.; Sen, L.; Wei, F.-H. *Anal. Lett.* **2008**, *41*, 2203–2213.

46. Liu, W.; Xu, L.; Sheng, R.; Wang, P.; Li, H.; Wu, S. *Org. Lett.* **2007**, *9*, 3829–3832.

47. Jang, Y.-C.; Lee, M.; Den, W.; Kuo, P. Unpublished work.

48. Descalzo, A. B.; Martínez-Máñez, R.; Radeglia, R.; Rurack, K.; Soto, J. *J. Am. Chem. Soc.* **2003**, *125*, 3418–3419.

49. Chen, T.; Zhu, W.; Xu, Y.; Zhang, S.; Zhang, X.; Qian, X. *Dalton Trans.* **2010**, *39*, 1316–1320.

50. Voutsadaki, S.; Tsikalas, G. K.; Klontzas, E.; Froudakis, G. E.; Katerinopoulos, H. E. *Chem. Commun.* **2010**, *46*, 3292–3297.

51. Kubo, K.; Sakaguchi, S.; Sakurai, T. *Talanta* **1999**, *49*, 735–744.

52. Hou, C.; Urbanec, A. M.; Cao, H. *Tetrahedron Lett.* **2011**, *52*, 4903–4905.
53. Zhang, X.; Xiao, Y.; Qian, X. *Angew. Chem., Int. Ed.* **2008**, *47*, 8025–8029.
54. Coskun, A.; Akkaya, E. U. *J. Am. Chem. Soc.* **2006**, *128*, 14474–14475.
55. Li, C.-Y.; Zhang, X.-B.; Qiao, L.; Zhao, Y.; He, C.-M.; Huan, S.-Y.; Lu, L.-M.; Jian, L.-X.; Shen, G.-L.; Yu, R.-Q. *Anal. Chem.* **2009**, *81*, 9993–10001.
56. Jia, L.; Zhang, Y.; Guo, X.; Qian, X. *Tetrahedron Lett.* **2004**, *45*, 3969–3973.
57. Nolan, E. M.; Lippard, S. J. *Chem. Rev.* **2008**, *108*, 3443–3480.
58. Moro, A. J.; Cywinski, P. J.; Korsten, S.; Mohr, G. J. *Chem. Commun.* **2010**, *46*, 1085–1087.
59. Huang, C.-B.; Li, H.-R.; Luo, Y.; Xu, L. *Dalton Trans.* **2014**, *43*, 8102–8108.
60. Wu, X.-F.; Ma, Q.-J.; Wei, X.-J.; Hou, Y.-M.; Zhu, X. *Sens. Actuators, B* **2013**, *183*, 565–574.
61. Zhao, J.; Zhu, B.; Yu, H.; Yan, L.; Wei, Q.; Du, B. *J. Colloid Interface Sci.* **2013**, *389*, 46–52.
62. Zhu, B.; Zhao, J.; Yu, H.; Yan, L.; Wei, Q.; Du, B. *Opt. Mater.* **2013**, *35*, 2220–2235.
63. Lee, H. N.; Kim, H. N.; Swamy, K. M. K.; Park, M. S.; Kim, J.; Lee, H.; Lee, K.-H.; Park, S.; Yoon, J. *Tetrahedron Lett.* **2008**, *49*, 1261–1265.
64. Zhang, Z.; Chen, Y.; Xu, D.; Yang, L.; Liu, A. *Spectrochim. Acta, Part A* **2013**, *105*, 8–13.

Chapter 4

Visible Light-Activated Photocatalytic Effect of Iron-Containing Silicate Glass - A Review

Y. Takahashi,[1] S. Kubuki,*,[1] and T. Nishida[2]

[1]Department of Chemistry, Graduate School of Science and Engineering, Tokyo Metropolitan University, 1-1 Minami-Osawa, Hachi-oji, Tokyo 192-0397, Japan
[2]Department of Biological and Environmental Chemistry, Faculty of Humanity-Oriented Science and Engineering, Kinki University, 11-6 Kayanomori, Iizuka, Fukuoka 820-8555, Japan
***E-mail: kubuki@tmu.ac.jp.**

In this review, we introduce a relationship between the local structure and visible light activated photocatalytic effect of two types of iron containing silicate glasses, *i.e.*, $15Na_2O \cdot 15CaO \cdot xFe_2O_3 \cdot (70-x)SiO_2$ glass (x = 10-50 in mass %, abbreviated as xNCFS) prepared by melt quenching method and $xFe_2O_3 \cdot (100-x)SiO_2$ glass (x = 10-50 in mass %, abbreviated as xFS) prepared by sol-gel method. They were investigated by applying [57]Fe-Mössbauer spectroscopy (FeMS), X-ray diffractometry (XRD) and ultraviolet-visible light absorption spectroscopy (UV-VIS). In the case of decomposition test using methyleneblue aqueous solution (MB_{aq}) and 50NCFS annealed at 1000 °C for 100 min (50NCFS*a*) without visible light irradiation, peak top of the UV-VIS spectra originally observed at the wavelength of 664 nm was shifted to 615 nm with the decrease in the absorbance (*Abs.*) from 0.866 to 0.495 after 10 days. In contrast, no peaks in the *Abs.* could be observed for the UV-VIS spectra of MB_{aq} decomposed with 50NCFS*a* for one-day under visible light irradiation. First order rate constant (k) of MB_{aq} decomposition using 50NCFS*a* under the visible light was calculated to be 2.87×10^{-2} h^{-1}. [57]Fe-Mössbauer spectrum of 50NCFS*a* consisted of two magnetic sextets due to α-Fe$_2$O$_3$ (isomer shift (δ) : $0.36_{\pm0.01}$ mm s^{-1}, internal magnetic

field (H_{int}) : $51.8_{\pm 0.1}$ T) and $Fe_{1.833}(OH)_{0.5}O_{2.5}$ (δ : $0.34_{\pm 0.10}$ mm s^{-1}, H_{int} : $37.9_{\pm 0.6}$ T). These results indicate that α-Fe_2O_3 precipitated in 50NCFS*a* causes the visible light activated photocatalytic effect. On the other hand, MB$_{aq}$ decomposition test using 50FS annealed at 1000 °C for 3 hour (50FS*a*) resulted in a remarkable decrease in *Abs.* of MB from 1.54 to 0.45 only after 2 h under the visible light, while no significant change in *Abs.* was observed using 10FS*a* and 30FS*a*, respectively of which showed precipitation of fayalite (Fe_2SiO_4) and magnetite (Fe_3O_4). The *k* value of MB$_{aq}$ decomposition using 50FS*a* under the visible light was estimated to be 6.48×10^{-1} h^{-1}, which is much larger than that of 50NCFS*a*. From ^{57}Fe-Mössbauer spectrum of 50FS*a*, only a magnetic sextet due to α-Fe_2O_3 was detected. Tauc's plot obtained from UV-VIS-NIR spectra of 50NCFS*a* and 50FS*a* yielded the band gap energy (E_g) of 2.2 and 2.1 eV, respectively. Because E_g value of α-Fe_2O_3 was estimated to be 2.1 eV, precipitation of α-Fe_2O_3 is essential for the visible light activated photocatalytic effect of 50NCFS*a* and 50FS*a*. It is concluded that iron containing silicate glasses after annealing such as 50NCFS*a* and 50FS*a* exhibit visible light activated photocatalytic effect due to precipitation of α-Fe_2O_3. They can be applicable for environmental purification.

Introduction

Photocatalyst is one of the most effective materials for environmental purification and is extensively investigated for practical application. Anatase type TiO_2 is well known as a photocatalyst which is activated by UV light with the wavelength shorter than 380 nm (*1*). Photocatalysis will become more effective if it exhibits the activity under visible light. A lot of visible light activated photocatalysts are due to anatase type TiO_2 (*2–7*). Visible light activated photocatalysts other than TiO_2 are difficult to use practically, since they might need rare metals such as W, Ga, Au, Ta and Ge (*8–13*). Thus, many kinds of visible light-activated photocatalysts are extensively investigated for environmental purification.

^{57}Fe-Mössbauer spectroscopy is one of the most powerful techniques in order to investigate the local structure of iron in oxide glasses (*14–16*). From the Mössbauer parameters of isomer shift (δ), quadrupole splitting (Δ) and magnetic hyperfine splitting, we can evaluate chemical environment like valence state, coordination number, internal magnetic field and the local distortion around Mössbauer nuclei. Frischat and Tomandl reported that Fe^{II}/Fe^{III} ratio in silicate glass could be estimated by ^{57}Fe-Mössbauer spectroscopy, if the recoil-free fraction of Fe^{III} were equal to that of Fe^{II} (*17*).

As for an investigation concerning environmental purification of oxide glasses, Kubuki *et al.* reported that recycled silicate glass prepared from waste glass bottle showed a decrease in the chemical oxygen demand (COD) from 300 to and 25 mg L^{-1} (*18*, *19*). It is well known that Fe[II] plays an important role in the Fenton method that is effective for water purification (*20*). Fe[II] and Fe[III] are doped together into several photocatalysts in order to enhance the ability of photocatalytic effect (*21*, *22*). These reports suggest that iron-containing silicate glass might be utilized for cleaning waste water or polluted waters as a photocatalyst.

In this review article, we report a relationship between photocatalytic effect and local structure of iron-containing silicate glasses prepared by melt-quenching method and by sol-gel method. The photocatalytic activity and band gap energy were evaluated by using ultraviolet-visible light absorption spectroscopy (UV-VIS), while the structural change caused by annealing of them was characterized by [57]Fe-Mössbauer spectroscopy (FeMS) and X-ray diffractometry (XRD).

Visible Light-Activated Photocatalytic Effect and Structure of Iron-Containing Soda-Lime Silicate Glass Prepared by Melt-Quenching Method

Typical preparing technique of silicate glass is a conventional melt-quenching method at high melting temperatures of 1300-1500 °C. Soda-lime silicate glass is generally prepared with alkaline or alkaline-earth ions such as Na^+ and Ca^{2+} in order to lower the melting temperature. As for environmental purification with soda-lime silicate glass, Kubuki *et al.* revealed that $0.5x(Na_2O \cdot CaO) \cdot (95-x)SiO_2 \cdot 5Fe_2O_3$ glass with '*x*' of 20-40 decomposed organic compounds estimated by chemical oxygen demand (COD), indicating that the iron-containing silicate glass could be utilized for cleaning polluted waters (*23*, *24*). In this section, we report a relationship between local structure and visible light-activated photocatalytic effect of $15Na_2O \cdot 15CaO \cdot xFe_2O_3 \cdot (70-x)SiO_2$ glass (*x* = 10-50 in mass %, abbreviated as *x*NCFS), which was characterized by [57]Fe-Mössbauer spectroscopy (FeMS), X-ray diffractometry (XRD). Soda-lime silicate glass was prepared by conventional melt quenching method at 1400 °C and 1 h (*25*). Glass samples were annealed at 1000 °C for 100 min for evaluating the visible light photocatalytic activity. In order to investigate the photocatalytic activity of these samples, decomposition test of MB was carried out. The schematic drawing and the details of the test were shown in Figure 1. In addition, the spectra of the lamp used in the test are shown in Figure 2.

Mössbauer spectra of *x*NCFS glass before annealing showed one or two doublet(s) due to paramagnetic tetrahedral (T_d) Fe[III] with δ and Δ of 0.23-0.26 mm s^{-1} and 1.01-1.04 mm s^{-1}, respectively, whereas octahedral (O_h) Fe[II] with δ = 1.00-1.03 mm s^{-1} and Δ = 2.03-2.05 mm s^{-1} (*24*). The [57]Fe-Mössbauer spectra of *x*NCFS glass after annealing at 1000 °C for 100 min (*x*NCFS*a*) measured at room temperature are shown in Figure 3 (*25*). A paramagnetic doublet for

Fe^{III}(T_d)O$_4$ with identical δ of 0.25$_{\pm0.01}$ mm s^{-1} and $\varDelta$ of 0.96$_{\pm0.02}$ mm s^{-1} were observed in every case, while linewidth (Γ) decreased from 0.59$_{\pm0.01}$ to 0.59$_{\pm0.01}$, 0.55$_{\pm0.01}$, 0.51$_{\pm0.01}$ and 0.52$_{\pm0.01}$ mm s^{-1} when 'x's were 5, 10, 15, 20, and 25, respectively (Figure 3a – 3e) (25). In addition to the paramagnetic Fe^{III}(T_d)O$_4$, another paramagnetic doublet with δ, $\varDelta$ and Γ of 0.91$_{\pm0.08}$, 2.20$_{\pm0.17}$ and 0.59$_{\pm0.01}$ mm s^{-1} attributed to Fe^{II}(O_h)O$_6$ was detected for xNCFSa with 'x' of 5 and 10 with the absorption area (A) of 13.9 and 4.1 %, respectively (Figure 3a and 3b) (25). Mössbauer spectra of xNCFSa with 'x' being equal to or larger than 30 (Figure 3f – 3j) mainly showed a magnetic sextet with δ and internal magnetic field (H_{int}) of 0.36$_{\pm0.01}$ mm s^{-1} and 51.8$_{\pm0.1}$ T, respectively (25). The value of Γ for the magnetic sextet decreased from 0.53$_{\pm0.01}$ to 0.40$_{\pm0.01}$, 0.38$_{\pm0.01}$, 0.26$_{\pm0.01}$ and 0.26$_{\pm0.01}$ mm s^{-1} and A from 47.2 to 75.9, 93.1, 64.8 and 47.9 % with an increase of 'x' from 30 to 35, 40, 45 and 50, respectively (25). These results indicated that annealing of xNCFS glass with 'x' being equal to or larger than 30 resulted in the precipitation of hematite (α-Fe$_2$O$_3$). As for 45NCFSa and 50NCFSa, another sextets with δ of 0.34$_{\pm0.10}$ mm s^{-1}, H_{int} of 37.9$_{\pm0.6}$ T and Γ of 1.32$_{\pm0.22}$ mm s^{-1} was observed having different 'A's of 19.5 and 39.7 %, respectively (25).
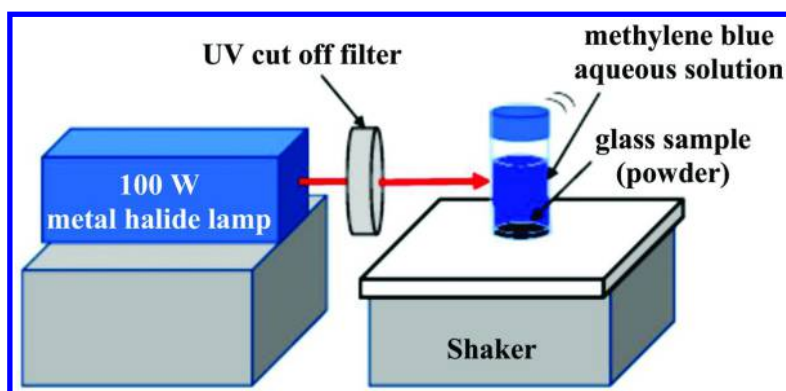
Figure 1. A schematic drawing of experimental set-up of methylene blue decomposition test. 100 W metal halide lamp (Dolan-Jennner Inc., MH-100) with the UV cut-off filter was used as the visible light source. 10 mL of methylene blue aqueous solution and 80 mg of well pulverized glass sample were poured into the 20 ml glass vial. The vial was irradiated with the visible light while shaken. The distance of the light source to vial is 10 cm and the intensity of the light at this point is ca. 6 mW cm^{-2}.
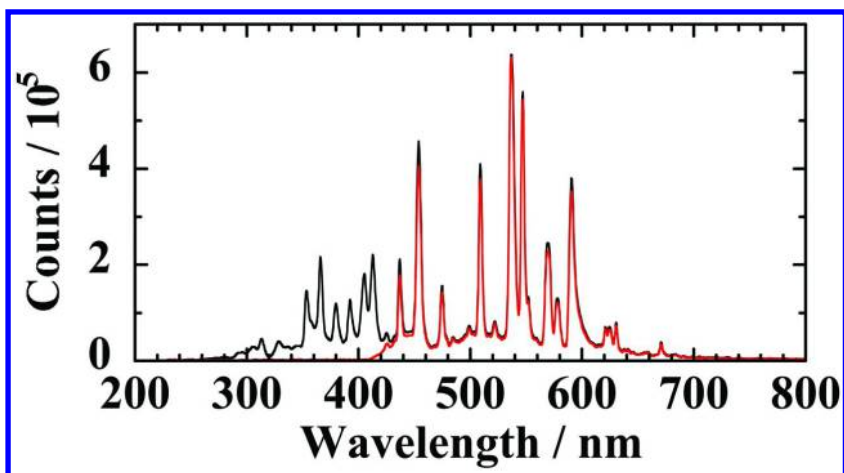
Figure 2. *UV-VIS spectra of the 100 W metal halide lamp (MH-100, Dolan-Jennner Inc.). Red and black lines show the spectra with and without UV cut off filter, respectively.*
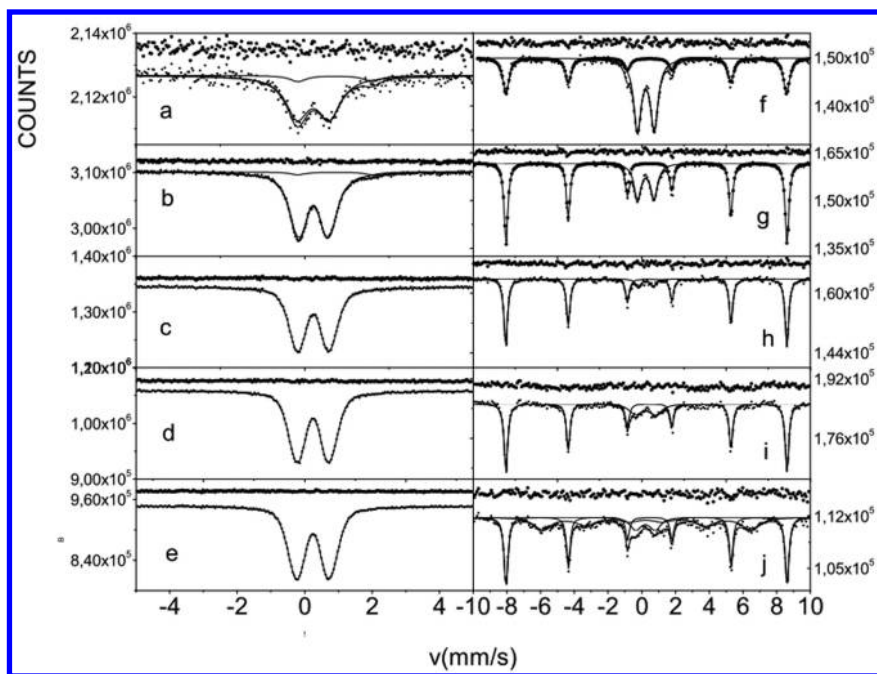
Figure 3. *^{57}Fe-Mössbauer spectra with residuals of 15Na$_2$O•15CaO•xFe$_2$O$_3$•(70–x)SiO$_2$ glass with 'x' of (a) 5, (b) 10, (c) 15, (d) 20, (e) 25, (f) 30, (g) 35, (h) 40, (i) 45 and (j) 50 after annealing at 1000 °C for 100 min. (Reproduced with permission from Ref. (25). 2014, Springer, Inc.)*

XRD patterns of *x*NCFS*a* with '*x*' of 10, 30 and 50 recorded are shown in Figure 4 (*25*). In the case of 10NCFS*a*, some intense peaks could be observed at 2θ of 23.0, 25.2, 28.7 and 29.8 º being attributed to wollastonite (CaSiO$_3$, as illustrated with open triangle in Figure 4a) (*25*). On the other hand, peak intensity of wollastonite decreased and additional intense peaks attributed to hematite (α-Fe$_2$O$_3$, as illustrated with open circle in Figure 4b and 4c), were observed at the 2θ of 33.1, 35.7, and 24.0 º (*25*). In addition, non-stoichiometric iron hydroxyoxide of Fe$_{1.833}$(OH)$_{0.5}$O$_{2.5}$ (solid diamond illustrated in Figure 4b and 4c) was observed at the same 2θ as α-Fe$_2$O$_3$ (*25*). These results show that isothermal annealing at 1000 °C for 100 min of *x*NCFS glass with '*x*' being equal to or larger than 30 resulted in the precipitation of α-Fe$_2$O$_3$, while 45NCFS*a* and 50NCFS*a* the precipitation of Fe$_{1.833}$(OH)$_{0.5}$O$_{2.5}$. ^{57}Fe-Mössbauer spectra and XRD patterns suggest that a broad sextet observed in the ^{57}Fe-Mössbauer spectra of the 45NCFS*a* (Figure 3i) and 50NCFS*a* (Figure 3j) is attributed to Fe$_{1.833}$(OH)$_{0.5}$O$_{2.5}$ having a similar structure as goethite (α-FeOOH) (*26*, *27*). As for the solution of detailed catalytic activity, further studies should be required.
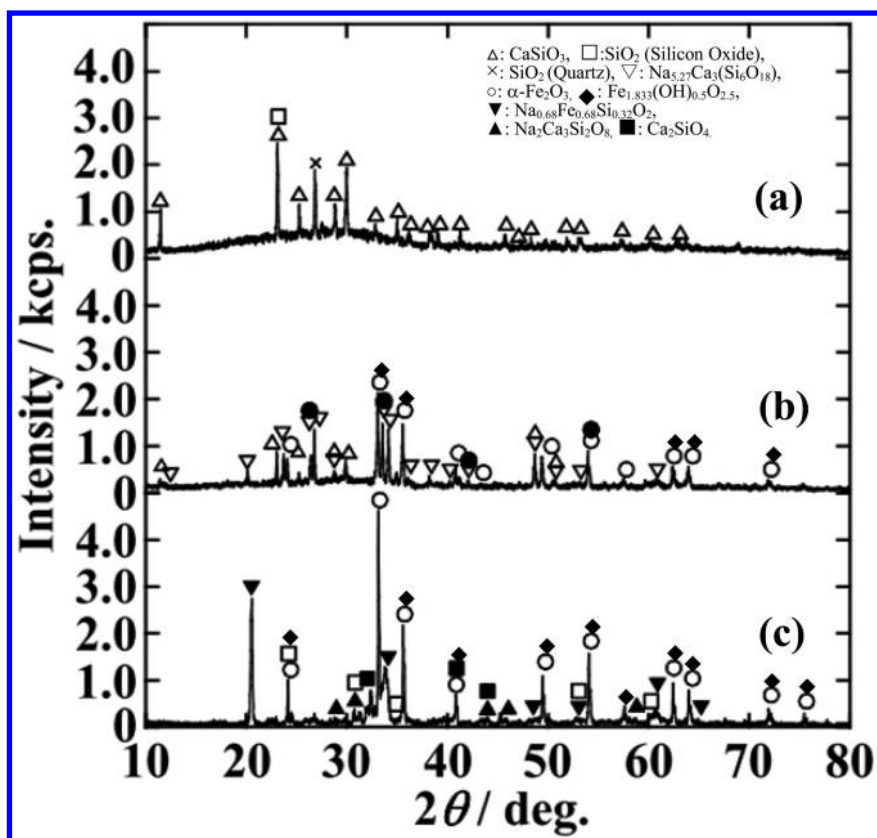
Figure 4. XRD patterns of 15Na$_2$O•15CaO•xFe$_2$O$_3$•(70–x)SiO$_2$ glass with 'x' of (a) 10, (b) 30 and (c) 50 after annealing at 1000 °C for 100 min. (Reproduced with permission from Ref. (25). 2014, Springer, Inc.)
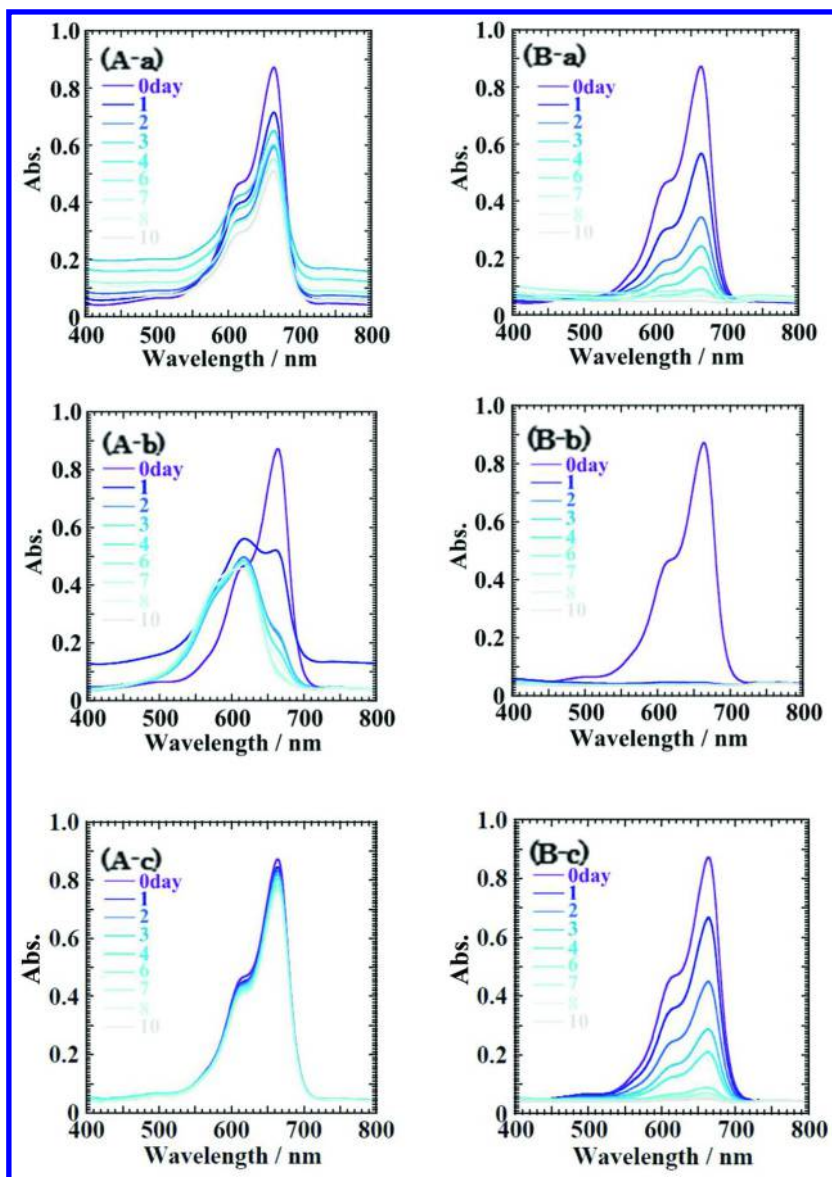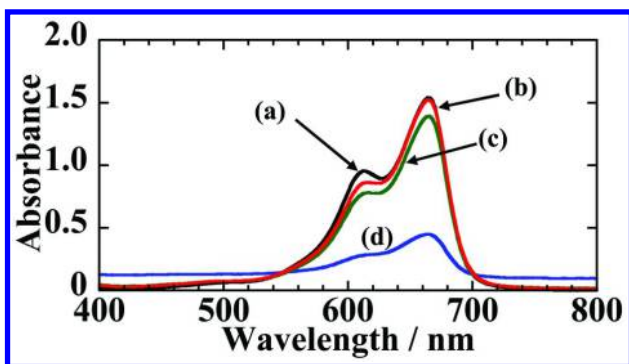
Figure 5. UV-VIS spectra of MB$_{aq}$ before (top) and after (bottom) decomposition test using 15Na$_2$O•15CaO•xFe$_2$O$_3$•(70–x)SiO$_2$ glass with 'x' of (a) 10 and (b) 50 annealing at 1000 °C for 100 min (A) without and (B) with visible light irradiation. Spectra (c) show MB$_{aq}$ after 10-day decomposition test without samples. (Reproduced with permission from Ref. (25). 2014, Springer, Inc.)

UV-VIS spectra of 10 μmol L^{-1} MB$_{aq}$ decomposed with 80 mg of xNCFSa ('x' = 10 and 50) are shown in Figure 5 (25), which was measured before and after 10-day with or without visible light irradiation. After decomposition test under visible-light irradiation without xNCFSa, almost identical UV-VIS spectra were observed (Figure 5A-c) (25). On the other hand, faster decrease in the absorbance (*Abs*.) at 664 nm was observed from 0.872 to 0.665, 0.448, 0.286, 0.208, 0.088, 0.070, 0.058 and 0.050 after decomposition test without xNCFSa under visible light irradiation (Figure 5B-c) (25). These results indicate that MB is decomposed under visible light irradiation. In the case of MB$_{aq}$ decomposition test using 50NCFSa without visible light irradiation, peak top of the UV-VIS spectra originally observed at the wavelength of 664 nm was shifted to 615 nm with a decrease in the *Abs*. from 0.866 to 0.495 after 10-day decomposition (Figure 5A-b) (25). In contrast, no *Abs*. peaks were observed in the UV-VIS spectra of MB$_{aq}$ decomposed with 50NCFSa after one-day under visible light irradiation (Figure 5B-b) (25). These results indicate that MB decomposition rate was remarkably accelerated when α-Fe$_2$O$_3$ and Fe$_{1.833}$(OH)$_{0.5}$O$_{2.5}$ precipitated in 50NCFSa.

Visible Light-Activated Photocatalytic Effect and Structure of Iron-Containing Silicate Glass Prepared by Sol-Gel Method

For comparison, iron-containing silicate glass without sodium and calcium was prepared by sol-gel method, in order to enhance the photocatalytic ability. The preparing method of glass sample is mentioned in our former paper (28). A relationship between the local structure and photocatalytic ability of xFe$_2$O$_3$• (100-x)SiO$_2$ (x = 10-50 in mass %, abbreviated as xFS) was investigated to elucidate the direct influence of iron in silicate glass on the photocatalytic effect. The decomposition test of MB was performed under the same condition as indicated in the previous section except for the initial concentration of MB$_{aq}$.

[57]Fe-Mössbauer spectra of xFS glass with 'x' of 10, 30 and 50 annealing at 1000 °C for 3 h (xFSa) are shown in Figure 6 (28). Mössbauer spectrum of 10FSa (Figure 6a) shows a paramagnetic doublet with δ of 1.16$_{\pm0.01}$ and Δ of 2.83$_{\pm0.02}$ mm s^{-1} (28), indicating precipitation of fayalite (Fe$_2$SiO$_4$) (29). In case of annealed 30FS glass (30FSa), Mössbauer spectrum is composed of a doublet and two sextets due to fayalite (Fe$_2$SiO$_4$, δ: 1.16$_{\pm0.01}$ mm s^{-1}, Δ: 2.86$_{\pm0.02}$ mm s^{-1}, A: 18.0$_{\pm0.5}$ %) and magnetite (Fe$_3$O$_4$, δ: 0.28$_{\pm0.01}$ mm s^{-1}, H_{int}: 48.9$_{\pm0.5}$ T and A: 31.5$_{\pm0.5}$ % for Fe^{III} (T_d) and δ: 0.65$_{\pm0.01}$ mm s^{-1}, H_{int}: 45.3$_{\pm0.5}$ T and A: 45.3$_{\pm0.5}$ % for Fe $^{(II+III)}$(O_h)) (Figure 6b) (28). Furthermore, only a sextet due to hematite (α-Fe$_2$O$_3$) with δ of 0.37$_{\pm0.01}$ mm s^{-1}, and H_{int} of 51.4$_{\pm0.5}$ T was observed in 50FSa glass (Figure 6c) (28).

XRD patterns of xFSa glass with 'x' of 10, 30 and 50 are shown in Figure 7 (28). Sharp intense peaks attributed to fayalite (Fe$_2$SiO$_4$, 2θ: 25.1, 31.6, 35.0, 35.9, 51.4 and 60.8 °), magnetite (Fe$_3$O$_4$, 2θ: 30.1, 31.6, 35.4, 43.0, 57.0 and 62.5

º) and hematite (α-Fe$_2$O$_3$, 2θ : 24.0, 33.1, 35.5, 40.8, 49.4, 54.0, 57.4, 64.3, 63.9, 72.0 and 75.3 º) could be observed for xFSa (28). Considering that no intense peak deriving from silica was observed in the XRD pattern of 50FSa, it seems that hematite phase was dispersed into the amorphous matrix of silicate glass. These results show that the chemical environment of iron in xFSa glass varies with the concentration of Fe$_2$O$_3$ and that the crystalline phase of xFSa can be controlled by the changing the Fe$_2$O$_3$/SiO$_2$ ratio.
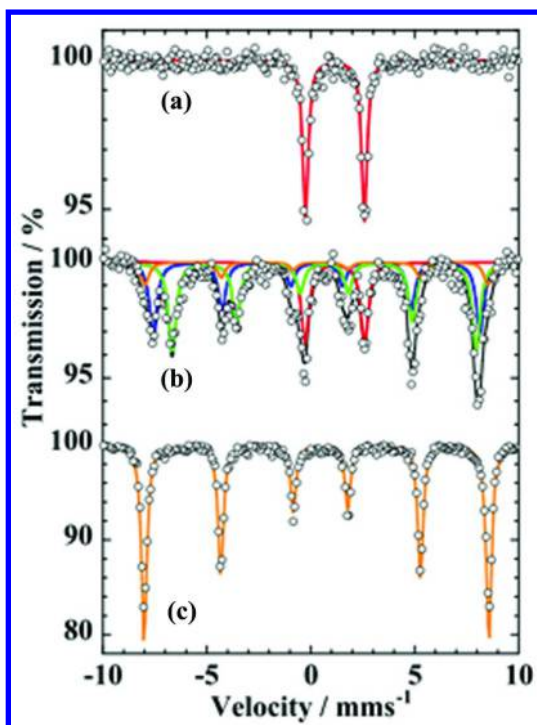
Figure 6. ^{57}Fe-Mössbauer spectra of xFe$_2$O$_3$·(100–x)SiO$_2$ glass with 'x' of (a) 10, (b) 30 and (c) 50 measured after annealing at 1000 °C for 3 h. (Reproduced with permission from Ref. (28). 2014, Springer, Inc.)

UV-VIS spectra of 16.2 μmol L^{-1} MB$_{aq}$ (10 mL) decomposed with 40 mg of xFSa with 'x' of 10, 30 and 50 under visible light irradiation for 2 h are shown in Figure 8 (28). No significant change in UV-VIS spectra was observed after 2h-decomposition test using xFSa with 'x' of 10 and 30 under visible light irradiation (Figure 8b and 8c) (28). In contrast, a remarkable decrease in the

Abs. of MB_{aq} from 1.54 to 0.45 was observed after the 2h-decomposition test using 50FS*a* under visible light irradiation (Figure 8d) (*28*). MB concentration is determined by Lambert-Beer equation, *i.e.*,

$$Abs. = \varepsilon\, C_t\, l \qquad (1),$$

where ε, C_t and l are molar absorption coefficient (= 9.5×10^4 L mol^{-1} cm^{-1} at 664 nm for MB_{aq} (*30*)), MB concentration after *t*-min decomposition and cell length (= 1 cm), respectively. By using *eq.* (1), the concentration of MB was decreased from 16.2 to 4.72 µmol L^{-1} after 2h-decomposition test with 50FS*a* under visible light irradiation.
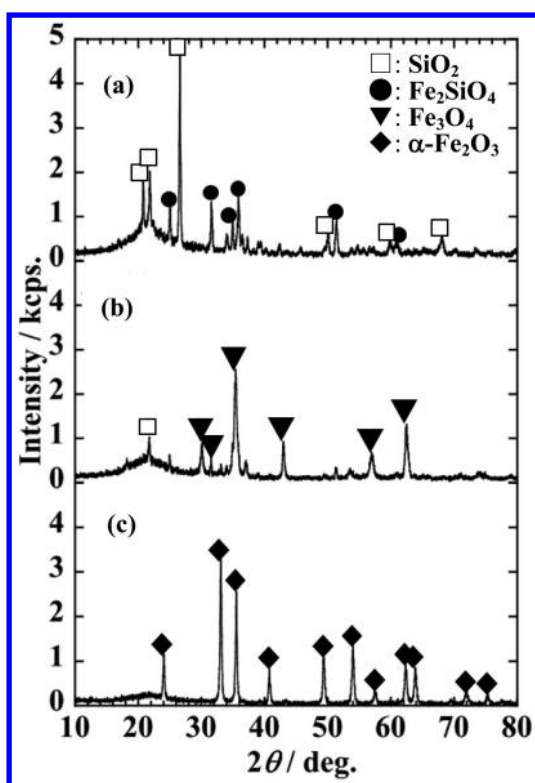
Figure 7. XRD patterns of xFe₂O₃·(100–x)SiO₂ glass with 'x' of (a) 10, (b) 30 and (c) 50 measured after annealing at 1000 °C for 3 h. (Reproduced with permission from Ref. (28). 2014, Springer, Inc.)

Figure 8. UV-VIS spectra of MB$_{aq}$ measured (a) before and after 2 h visible light irradiation of annealed xFe$_2$O$_3$·(100–x)SiO$_2$ glass with 'x' of (b) 10, (c), 30 and (d) 50. (Reproduced with permission from Ref. (28). 2014, Springer, Inc.)

Comparison of the Visible Light-Activated Photocatalytic Effect of Annealed Iron Silicate Glasses

UV-VIS spectra showed a remarkable decrease in the concentration of MB$_{aq}$ in the decomposition tests under visible light irradiation with 50NCFSa prepared by melt-quenching method and with 50FSa by sol-gel method. First order rate constant (k) for the MB decomposition can be estimated by:

$$\ln(C_t/C_0) = -kt \qquad (2),$$

where C_0 is MB concentration before decomposition. The k values of the decomposition tests using xNCFSa and xFSa are summarized in Table 1. For both cases, it is noted that 'k' becomes larger when Fe$_2$O$_3$ content is 50 %. It is suggested that the crystalline phases such as Fe$_{1.833}$(OH)$_{0.5}$O$_{2.5}$ and α-Fe$_2$O$_3$ detected in 50FSa and 50NCFSa by means of FeMS and XRD are related to the photocatalytic effect. Moreover, we can describe that Na$^+$ and Ca^{2+} ions occupying the sites of network modifier in the glass matrix are not essentially related to the photocatalytic effect. Because of the larger 'k' value, it is considered that 50FSa is more suitable for the water purification than 50NCFSa. UV-VIS diffuse reflectance spectra of annealed iron silicate glasses were recorded using UV-VIS-NIR spectrometer equipped with a integrating sphere and the Kubelka-Munk function (31) calculated by using UVProve Ver. 2.43. As a result of Tauc's plot (32, 33), band gap energy (E_g) of 50NCFSa and 50FSa were determined to be 2.23 and 2.11 eV, respectively as shown in Figure 9. Because comparable E_g of 2.14 eV is estimated for reagent α-Fe$_2$O$_3$, it is considered that precipitation of α-Fe$_2$O$_3$ is essential for the photocatalytic effect of 50NCFSa and 50FSa.
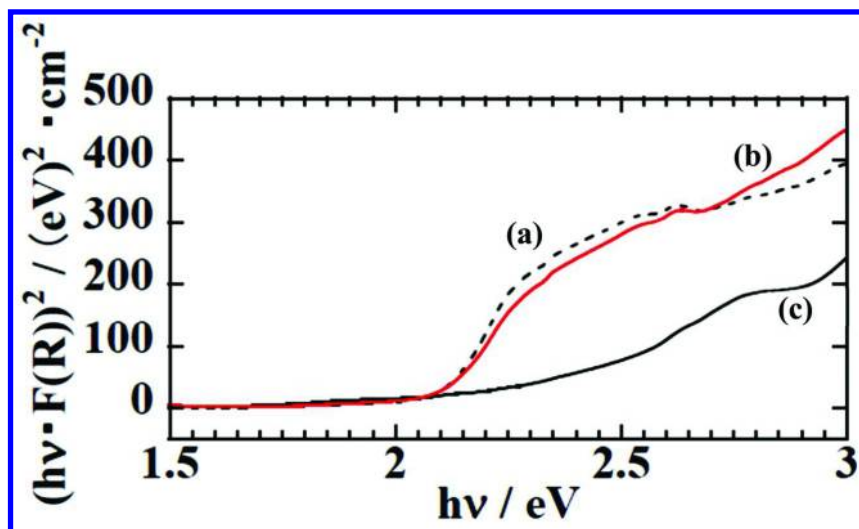
Figure 9. Tauc's plot of (a) reagent α-Fe$_2$O$_3$, (b) 50NCFSa and (c) 50FSa.

Table 1. First Order Rate Constant (k) of MB Decomposition Test Using 15Na$_2$O•15CaO•xFe$_2$O$_3$•(70-x) SiO$_2$ and xFe$_2$O$_3$•(100-x) SiO$_2$ Glasses after Annealing

Sample	k [h^{-1}] (under the light)	k [h^{-1}] (in the dark)
15Na$_2$O•15CaO•10Fe$_2$O$_3$•60SiO$_2$	0	$(1.00\pm0.12)\times10^{-3}$
15Na$_2$O•15CaO•30Fe$_2$O$_3$•40SiO$_2$	0	$(1.37\pm0.09)\times10^{-3}$
15Na$_2$O•15CaO•50Fe$_2$O$_3$•20SiO$_2$	$(2.87\pm0.10)\times10^{-2}$	$(6.61\pm0.60)\times10^{-3}$
90SiO$_2$•10Fe$_2$O$_3$	$(1.31\pm0.006)\times10^{-2}$	0
70SiO$_2$•30Fe$_2$O$_3$	$(5.62\pm0.008)\times10^{-2}$	$(5.22\pm0.002)\times10^{-2}$
50SiO$_2$•50Fe$_2$O$_3$	$(6.48\pm0.007)\times10^{-1}$	$(5.62\pm0.007)\times10^{-1}$

Conclusion

A relationship between the local structure and visible light activated catalytic effect were investigated in annealed 15Na$_2$O•15CaO•xFe$_2$O$_3$•(70-x)SiO$_2$ glass (xNCFSa) and xFe$_2$O$_3$• (100-x)SiO$_2$ glass (xFSa) by using FeMS, XRD and UV-VIS. As a result, following results could be obtained;

1) ^{57}Fe-Mössbauer spectra and XRD patterns of xNCFS with 'x' of larger than 30 mass % measured after isothermal annealing at 1000 °C for 100 min resulted in the precipitation of hematite (α-Fe$_2$O$_3$) and non-stoichiometric iron hydroxyoxide (Fe$_{1.833}$(OH)$_{0.5}$O$_{2.5}$), in addition to the paramagnetic tetrahedral Fe^{III} component. Amount of the precipitated hematite monotonously increased with the Fe$_2$O$_3$ content from 5 to 40 % before the precipitation of iron hydroxyoxide started. UV-VIS spectra showed a remarkable decrease in the concentration of MB in the decomposing test with annealed 50NCFS glass under visible light irradiation.

2) In case of iron-containing Na$^+$ and Ca^{2+} free silicate glass, xFS glasses with 'x' of 10, 30 and 50 after isothermal annealing at 1000 °C for 3 h resulted in the precipitation of Fe$_2$SiO$_4$, Fe$_3$O$_4$ and α-Fe$_2$O$_3$, respectively. Decomposition test using MB$_{aq}$ and annealed 50FS glass showed the largest first order rate constant (k) of 6.48×10^{-1} h^{-1} under visible light irradiation.

3) The band gap energy (E_g) obtained from Tauc's plot of 50NCFS and 50FS glasses after annealing are estimated to be 2.2 and 2.1 eV, respectively. A comparable E_g of 2.1 eV was obtained for α-Fe$_2$O$_3$, indicating that the precipitation of α-Fe$_2$O$_3$ caused by annealing of 50NCFS and 50FS glasses is essential for the visible light activated photocatalytic effect.

It is concluded that iron-containing silicate glass can be utilized for environmental purification as a photocatalyst activated by visible light.

References

1. Fujishima, A.; Honda, K. *Nature* **1972**, *238*, 37–38.
2. Premkumar, J. *Chem. Mater.* **2004**, *16* (21), 3980–3981.
3. Yu, H.; Irie, H.; Shimodaira, Y.; Hosogi, Y.; Kuroda, Y.; Miyauchi, M.; Hashimoto, K. *J. Phys. Chem. C* **2010**, *114* (39), 16481–16487.
4. Liao, G.; Chen, S.; Quan, X.; Chen, H.; Zhang, Y. *Environ. Sci. Technol.* **2010**, *44* (9), 3481–3485.
5. Tanaka, A.; Sakaguchi, S.; Hashimoto, K.; Kominami, H. *ACS Catal.* **2013**, *3* (1), 79–85.
6. Ali, R.; Abu Bakar, W. A. W.; Teck, L. K. *Mod. Appl. Sci.* **2010**, *4* (1), 59–67.
7. Chen, X.; Burda, C. *J. Am. Chem. Soc.* **2008**, *130* (15), 5018–5019.
8. Pincella, F.; Isozaki, K.; Miki, K. *Light: Sci. Appl.* **2014**, e133doi:10.1038/lsa.2014.14.
9. Kato, H.; Asakura, K.; Kudo, A. *J. Am. Chem. Soc.* **2003**, *125* (10), 3082–3089.
10. Kato, H.; Kudo, A. *J. Phys. Chem.* **2001**, *105* (19), 4285–4292.
11. Maeda, K.; Teramura, K.; Lu, D.; Takata, T.; Saito, N.; Inoue, Y.; Domen, K. *Nature* **2006**, *440*, 22.

12. Ma, S. S. K.; Maeda, K.; Abe, R.; Domen, K. *Energy Environ. Sci.* **2012**, *5*, 8390–8397.

13. Mueller, N. C.; Nowack, B. *Environ. Sci. Technol.* **2008**, *42*, 4447–4453.

14. Nishida, T. *J. Non-Cryst. Solid* **1994**, *117* (2), 257–268.

15. Homonnay, Z.; Music, S.; Nishida, T.; Kopelev, N. S.; Vertes, A. Mössbauer effect in inorganic glasses. In *Mössbauer Spectroscopy of Sophisticated Oxides*; Vertes, A., Homonnay, Z., Eds.; Akademiai Kiado: Hungary, 1997; Chapter 2, pp 27−87.

16. Kubuki, S.; Nishida, T. Water purification and characterization of recycled iron-silicate glass. In *Mössbauer Spectroscopy Applications in Chemistry, Biology, and Nanotechnology*; Sharma, V. K., Klingelhofer, G., Nishida, T., Eds.; John Wiley Sons: New York, 2013; Chapter 31, pp 595−607.

17. Frischat, G. H.; Tomandl, G. *Glastech. Ber.* **1969**, *42*, 182.

18. Kubuki, S.; Kawakami, N.; Matsumura, H.; Fujisato, T.; Nishida, T.; Fukagawa, M. *J. Technol. Edu.* **2004**, *11* (2), 77–82.

19. Tamaki, J.; Kubuki, S.; Nishida, T. *Bull. Fac. Hum.* **2006**, 7–12 URL: http://id.ndl.go.jp/bib/8595851.

20. Moura, M. C. C.; Araujo, M. H.; Costa, R. C. C.; Fabris, J. D.; Ardisson, J. D.; Macedo, W. A. A.; Lago, R. M. *Chemosphere* **2005**, *60*, 1118–1123.

21. Lezner, M.; Grabowska, E.; Zaleska, A. *Physicochem. Probl. Miner. Process.* **2012**, *48* (1), 193–200.

22. Carneiro, J. O.; Teixeira, V.; Portinha, A.; Magalhães, A.; Coutinho, P.; Tavares, C. J.; Newton, R. *Mat. Sci. Eng., B* **2007**, *138* (2), 144–150.

23. Kubuki, S.; Iwanuma, J.; Akiyama, K.; Homonnay, Z.; Kuzmann, E.; Nishida, T. *Am. Inst. Phys. Conf. Proc. Ser.* **2012**, *1489*, 41–46.

24. Kubuki, S.; Iwanuma, J.; Akiyama, K.; Homonnay, Z.; Kuzmann, E.; Nishida, T. *Hyperfine. Interact.* **2013**, *218*, 41–45.

25. Kubuki, S.; Iwanuma, J.; Takahashi, Y.; Akiyama, K.; Homonnay, Z.; Sinkó, K.; Kuzmann, E.; Nishida, T. *J. Radioanal. Nucl. Chem.* **2014**, *301*, 1–7.

26. Kalmykova, Y.; Knutsson, J.; Strömvall, A. M.; Hargelius, K. *Proc. 9th Highway Urban Environ. Symp.* **2009**, 307–318.

27. Ahmed, N.; Maitra, S.; Dutta, B. K.; Ahmed, F. *J. Environ. Sci.* **2009**, *21*, 1735–1740.

28. Takahashi, Y.; Kubuki, S.; Akiyama, K.; Sinkó, K.; Kuzmann, E.; Homonnay, Z.; Ristić, M.; Nishida, T. *Hyperfine Interact.* **2014**, *226* (1-3), 747–753.

29. Šepelák, V.; Bégin-Colin, S.; Caër, G. L. *Dalton Trans.* **2012**, *41*, 11927–11948.

30. Bergmann, K.; O'Konski, C. T. *J. Phys. Chem.* **1963**, *67*, 2169–2177.

31. Kubelka, M.; Munk, F. *Z. Tech. Phys.* **1931**, *12*, 593–601.

32. Tauc, T.; Grigorovici, R.; Vancu, A. *Phys. Status Solidi* **1966**, *15*, 627.

33. Davis, E. A.; Mott, N. F. *Philos. Mag.* **1970**, *22*, 903.

Chapter 5

Thickness Dependent Photocatalytic Performance of Nanocrystalline TiO$_2$ Thin Films

Chung-Yi Wu,[1] Yu-Shiu Lo,[1,2] and Chien-Hou Wua[*,1]

[1]Department of Biomedical Engineering and Environmental Sciences, National Tsing Hua University, Hsinchu 30013, Taiwan
[2]Center for Measurement Standards, Industrial Technology Research Institute, Hsinchu 30071, Taiwan
[*]E-mail: chwu@mx.nthu.edu.tw.

TiO$_2$ nanocrystalline thin films were prepared with spin coating by using sols deriving from titanium tetraisopropoxide (TTIP). The thin films were formed on soda lime glass and characterized by scanning electron microscopy, X-ray diffraction, X-ray photoelectron spectroscopy, ellipsometry, and photoluminescence spectroscopy. The photocatalytic activity of the thin films was tested by the degradation of acid yellow 17 under UV irradiation. The results indicated that the photocatalytic activity was strongly correlated with the number of coatings and followed Langmuir-type kinetics. For thin films prepared by 0.1 M TTIP, the maximum specific photocatalytic activity occurred at 5 coatings with thickness of 93 ± 1 nm. A model was proposed to rationalize the dependence of the film thickness on the photocatalytic activity, which predicted the existence of an optimum film thickness.

Introduction

TiO$_2$ has emerged as one of the most fascinating materials in the environmental and energy fields (*1–7*). In recent years, TiO$_2$ has shown great potential as a promising photocatalyst in the treatment of water pollutants (*8, 9*). The use of TiO$_2$ powders has the advantage of high surface area; however, a major disadvantage is the need of an additional and expensive post-treatment to separate and recycle TiO$_2$ from the treated water. This can be overcome by immobilizing TiO$_2$ as films on a solid substrate. Table 1 lists a variety of methods used to prepare TiO$_2$ thin films (*10–46*). Among these techniques, sol–gel is considered one of the most promising techniques for preparing nanosized TiO$_2$ thin films with high photocatalytic activities owing to its low cost, relative simplicity, and easier control of the composition of the deposited films (*47*).

The photocatalytic performance of films is deeply influenced by several factors such as crystal size, surface area, crystal structure, surface defect state, and film thickness (*13, 48, 49*). These factors are very sensitive to preparation methods and deposition conditions (*50*). Although the photocatalytic reaction is fundamentally a surface reaction, a film thickness dependence of photocatalysis has been observed in several different materials including not only TiO$_2$ but also ZnO, indium tin oxide, hematite, etc (*31, 49, 51–59*). In most cases, the photocatalytic activity was strongly related to the film thickness. Sheng et al. reported that the built-in potential V_d in Schottky barriers prevents the recombination of charge carriers formed by light excitation and assists the holes in moving toward the film surface to become active in photocatalysis, as shown in Figure 1 (*51*). The activity of the TiO$_2$ multilayer thin films showed a rapid attenuation as the thickness was decreased to the depletion layer width X_d. Figure 2 shows the change of acetic acid concentraiton after a 15 hr photocatalytic reaction on TiO$_2$ films of different thickness. The steplike dependence of thin film thickness was ascribed to the characteristic thickness t_{ch}, varying slightly around 150-250 nm, which presumably corresponds to the depletion layer width X_d. The combination of electrochemical and photocatalytic technologies offers the opportunity to promote the separation between the electron-hole photogenerated and to prevent their recombination (*4*). Several TiO$_2$ thin film electrodes have been fabricated and the photoelectrocatalytic oxidation process examined (*39, 60, 61*). As shown in Figure 3, application of an anodic bias of +0.3V caused the electrons in TiO$_2$ film to migrate to an external circuit, thereby suppressing electron-hole recombination and allowing the holes to accumulate at the film surface as trapped holes to form reactive oxygen species such as •OH$_{surface}$ radicals (*60*). The incident light may produce maximum number of electron–hole pairs for an optimum thickness. With further increase in the thickness, though the generation rate remains constant, the migration length of the carriers to the surface of the catalyst increases where the carriers experience higher recombination rates, resulting in a decrease in the photocatalytic activity (*49*).

Table 1. Methods for the Preparation of TiO² Thin Films

Method	Morphology	Application	Target compound for photocatalysis	Reference
Chemical				
Sol-gel	Nanoparticles	Photocatalysis	Phenol Stearic acid Methylene blue Acid yellow 17 Methylene blue	Sonawane and Dongare, 2006 (*10*) Simonsen et al., 2009 (*10*) Yao et al., 2011 (*12*) Wu et al., 2013 (*13*) Fateh et al., 2013 (*14*)
Spray-pyrolysis	Nanoparticles	Self-cleaning glass Photocatalysis	azo pyridone dye	Weng et al., 2005 (*15*) Dostanic et al., 2012 (*16*)
Chemical vapor deposition (CVD)	Nanoparticles	Photocatalysis Dye sensitization solar cell	Methyl orange Methylene blue Resazurin ink	Chang et al., 2009 (*17*) Wu et al., 2011 (*18*) Sathasivam et al., 2014 (*19*) Chen et al., 2010 (*20*)
Electrophoretic deposition	Nanoparticles	Photocatalysis Dye sensitization solar cell Dye sensitization solar cell	Orange-II	Peralta-Hernandez et al., 2007 (*21*) Wu et al., 2011 (*22*) Liou et al., 2011 (*23*)
Hydrothermal	Nanotubes Nanoparticles Nanotubes	Self-cleaning glass Photocatalysis	Malachite green Acetaldehyde	Miyauchi and Tokudome, 2007 (*24*) Sayýlkan et al., 2008 (*25*) Vijayan et al., 2010 (*26*)
Anodic oxidation	Nanotubes Nanocolumns Nanotubes	Photocatalysis Hydrogen sensing Photoelectrochemical	Acid orange 7, methylene blue Water	Macak et al., 2007 (*27*) Shimizu et al., 2007 (*28*) Allam et al., 2010 (*29*)

87

Table 1. (Continued). Methods for the Preparation of TiO² Thin Films

Method	Morphology	Application	Target compound for photocatalysis	Reference
Physical				
Doctor blade	According to preformed nanoparticles	Photocatalysis	Methyl orange Succinonitrile	Andronic and Duta, 2008 (*30*) Carbonell et al., 2008 (*31*)
Screen-printing	According to preformed nanoparticles	Photocatalysis Dye sensitization solar cell	Methyl orange	Tsoukleris et al., 2007 (*32*) Fan et al., 2010 (*33*)
Magnetron sputtering	Nanoparticles	Photocatalysis	2-propanol Methylene blue Methylene blue Rhodamine 6G	Kitano et al., 2006 (*34*) Chen et al., 2012 (*35*) Kuo et al., 2012 (*36*) Barrocas et al., 2013 (*37*)
Pulsed laser deposition	Nanoparticles	Photocatalysis	Oleic acid Chlortetracycline Methyl orange	Remsa et al., 2012 (*38*) Daghrir et al., 2012 (*39*) Luttrell et al., 2014 (*40*)
Electron-beam evaporation	Nanoparticles	Photocatalysis	Reactive yellow 2 Methylene blue	Habibi and Talebian, 2007 (*41*) Hsu et al., 2007 (*42*)
Glancing angle deposition	Nanoparticles Nanocolumns	Dye sensitization solar cell Antireflective coatings		Yang et al., 2009 (*43*) Gonzalez-Garcia et al., 2012 (*44*)
Plasma spray	Nanoparticles	Photocatalysis	Benzene Methylene blue	Chen et al., 2006 (*45*) Miyata et al., 2006 (*46*)
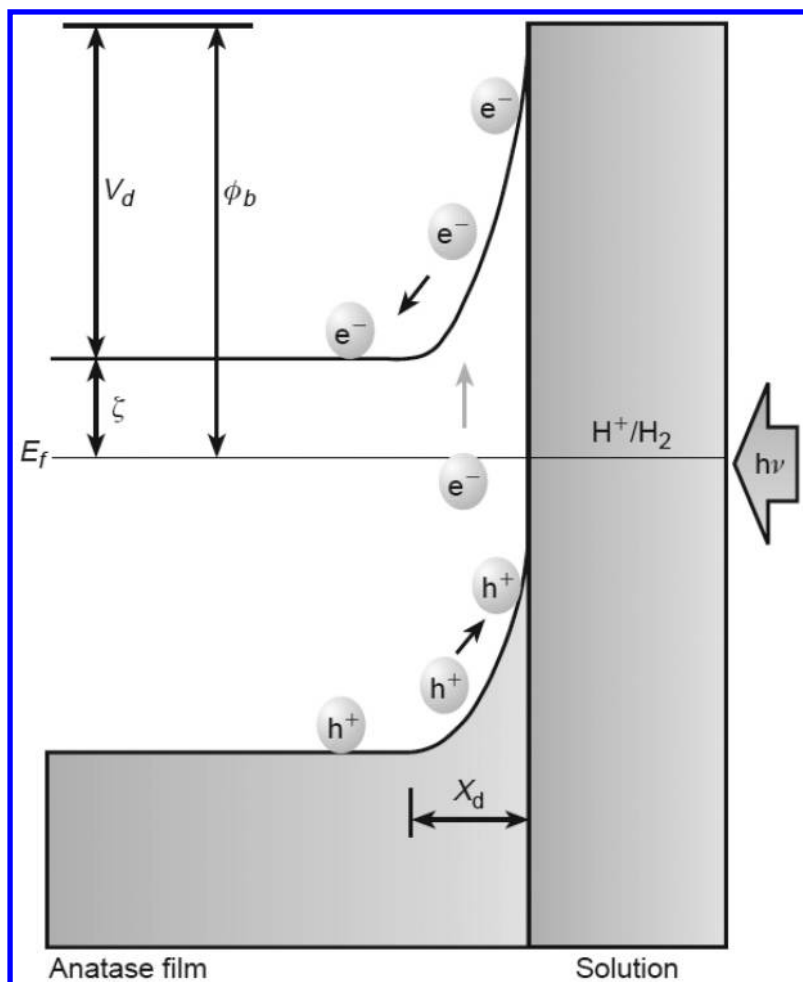
Figure 1. Schottky barrier formed in solid-liquid interface. (Reproduced with permission from (51). Copyright 2014, Springer.)

The light penetration depth was also proposed as a major reason for the thickness dependence of activity. Figure 4 shows the process for the preparation of thin film of TiO_2 nanoparticles with photonic sponge architecture using a blend of latex spheres of different sizes and proportions as templates, and placing photoactive Degussa P25 titania nanoparticles (*31*). The photocatalytic performance for the TiO_2 films having photonic sponge architecture was inversely proportional to the thickness. The ZnO nanoplatelets showed a similar trend (*58*). This may be explained by the higher surface-to-volume ratio of the nanoplatelets. On the other hand, with the increase of catalyst film thickness, both external and internal mass transfer may play significant roles in overall photocatalytic processes (*62*). Figure 5(a) shows that benzoic acid concentration in the bulk solution was decreased due to the rate of adsorption increased with the increasing

flow rate. It indicates that the external mass-transfer resistence can be reduced to a negligible value by increasing the circulating flow rate. In order to determine the effective diffusivity (D_e), dynamic physical adsorption experiments over a thicker catalyst layer were performed for three different initial concentrations of benzoic acid. The result is shown in Figure 5(b), and a good agreement with the experimental data was obtained when D_e was assumed in the model to be 1.0×10^{-10} m²/s. It indicates that internal mass transfer is an intrinsic property of the catalyst film and determined by the nature of the catalyst and the coating techniques used only.
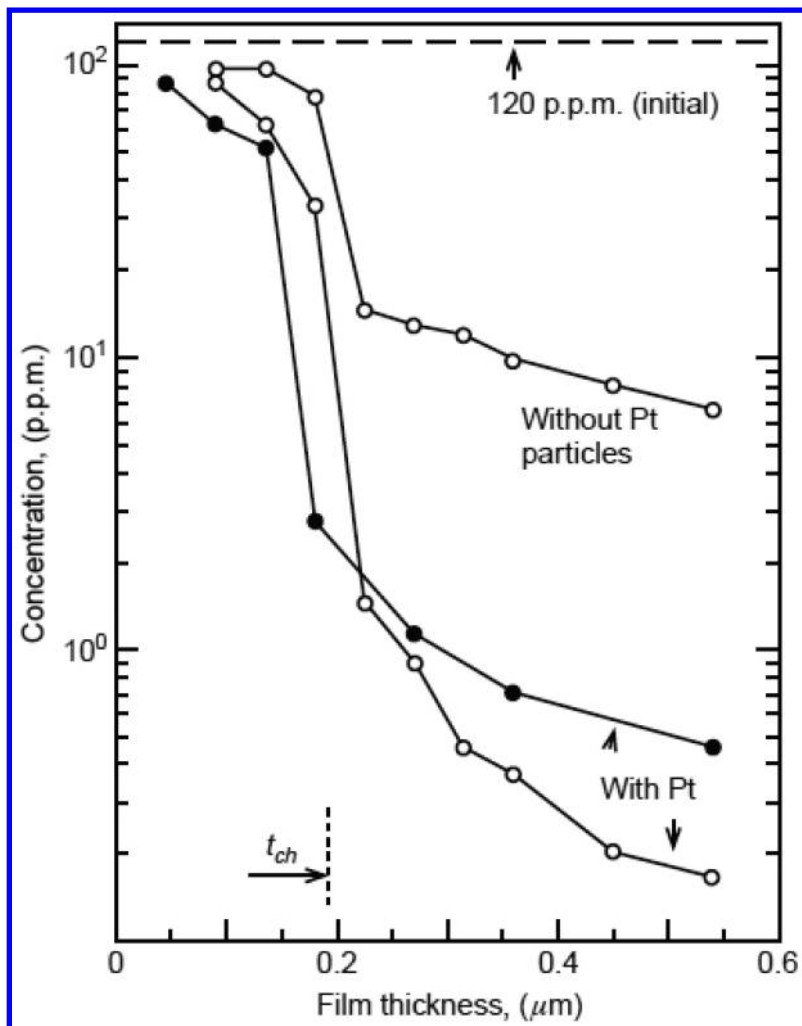
Figure 2. Thickness dependence of activity for TiO₂ films deposited at temperatures of 200 °C (○) and 250 °C (●) (tested after 15 h UV-irradiation). (Reproduced with permission from (51). Copyright 2014, Springer.)
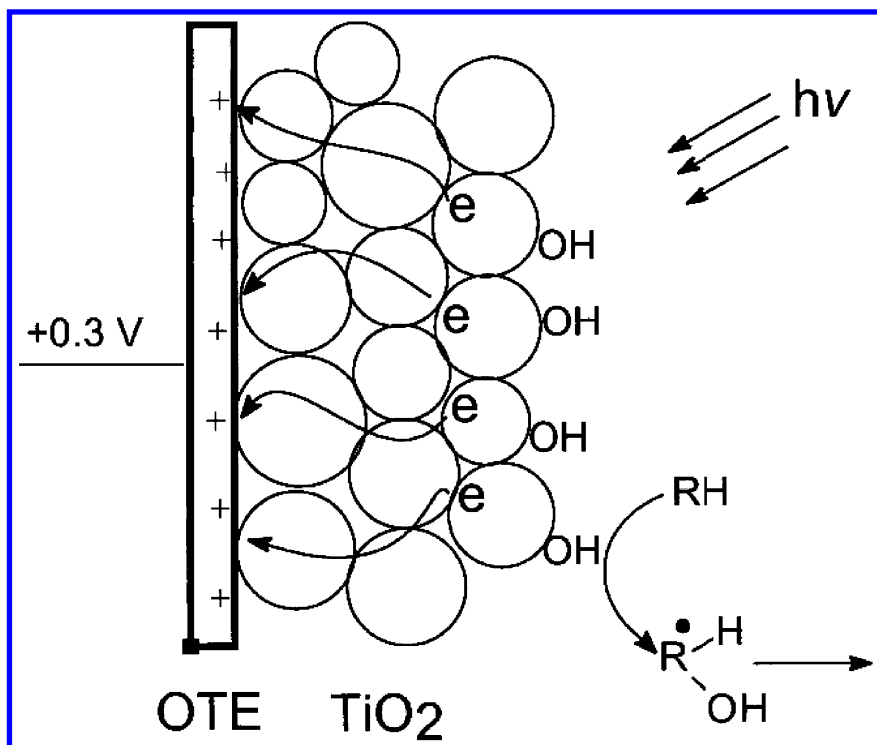
Figure 3. Schematic of photo-induced formation mechanism of electron-hole pair on a TiO₂/OTE thin film electrode with the presence of organic pollutant (RH). (Reproduced with permission from (60). Copyright 2014, Elsevier.)
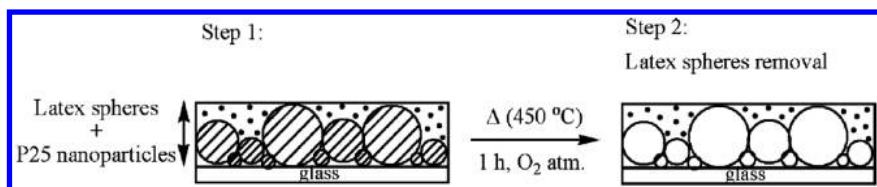
Figure 4. Process for the preparation of thin film of TiO₂ nanoparticles with photonic sponge architecture. (Reproduced with permission from (31). Copyright 2014, Royal Society of Chemistry.)

(a)

(b)

$D_e = 1.0 \times 10^{-10} \, m^2/s$
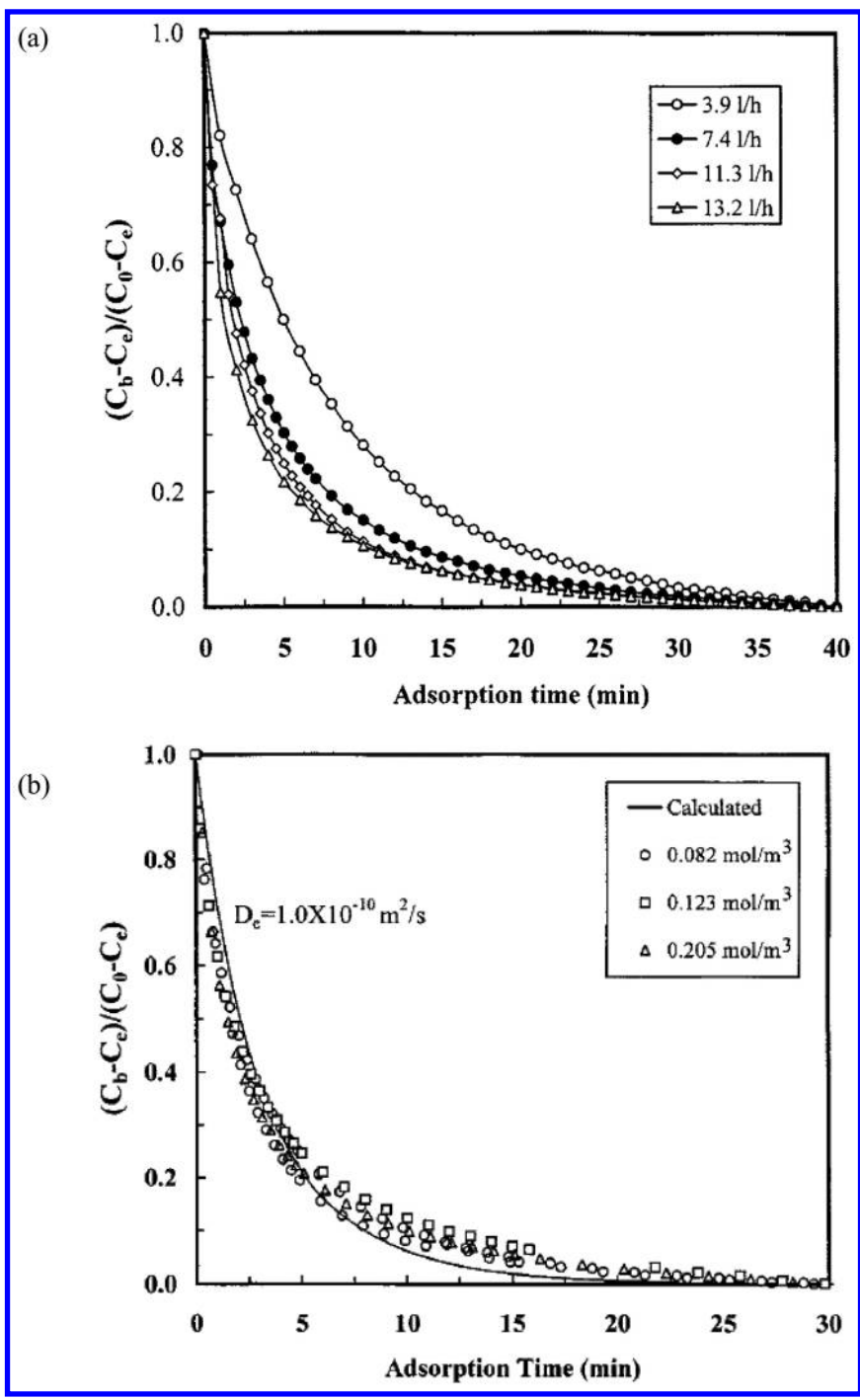
Figure 5. (a) Influence of circulating flow rate on the physical adsorption rate.
Experimental conditions: m (catalyst mass) = 8.1×10⁻⁵ kg; v (liquid volume)
= 3.5×10⁻⁵ m³; A (surface area of catalyst film) = 4.17×10⁻³ m²; T = 300 K.
(b) Determination of effective diffusivity of benzoic acid in TiO₂ catalyst film.
Experimental conditions: m = 5.51×10⁻⁵ kg; v = 3.2×10⁻⁵ m³; K (adsorption
rate constant) = 0.2 s⁻¹; ε (porosity of the catalyst layer) = 0.34; ρₚ (density of
catalyst particle) = 3800 kg/m³; H (thickness of the catalyst film) = 5.27×10⁻⁶
m; Re (Reynolds number) = 141; T = 300 K. (Reproduced with permission from
(62). Copyright 2014, John Wiley and Sons.)
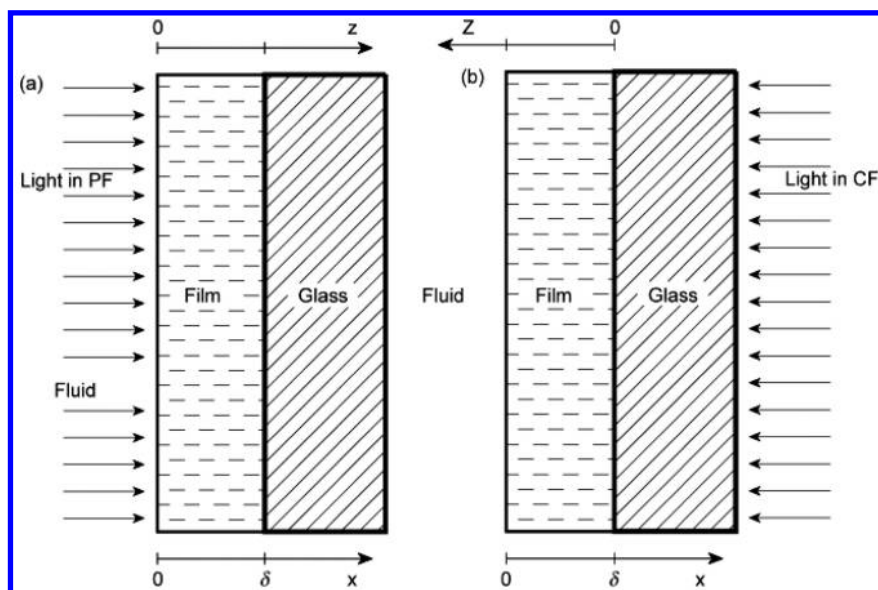
Figure 6. Schematic representation of the photocatalytic reactors under two
different illumination directions: (a) parallel flow (PF); (b) counter flow (CF).
(Reproduced with permission from (63). Copyright 2014, Elsevier.)

The design of the reactors with photocatalyst films should also be taken into account for the thickness dependence of photocatalytic activity (*63*). Referring to the scheme in Figure 6, the light enters the film alternatively from the fluid–film interface or from the glass–film interface. In the first case, the photons travel in parallel flow (PF) with respect to the diffusive transport of the reactants and in the second case in counter flow (CF). The direction that the film is illuminated (PF or CF) can greatly affect the obtainable rate of removal of organic pollutants. As shown in Figure 7, the rate of degradation monotonically increases with the thickness of the film towards an asymptotic value in PF, whereas in CF the rate of degradation reaches a maximum at an optimal value of the optical thickness.

The results can be explained by considering the two effects of an increase of film thickness on the mass of photocatalyst and on the transport of the organic pollutants and of the photons. An increase of film thickness provides more reaction sites for photocatalysis; nevertheless, it hinders the transport of pllutants and photons inside the photocatalytic film.
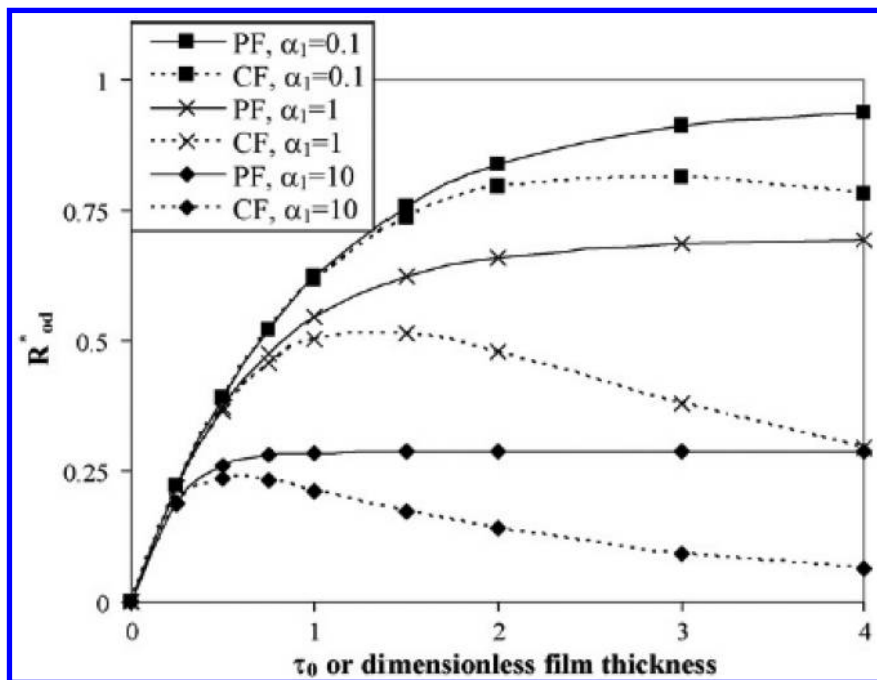
Figure 7. Dimensionless observed rate of degradation vs. the dimensionless thickness τ_0 of the film for a range of values of a dimensionless parameter α_1. α_1 is an intervening parameter which equals to $kI_0/(k_aD_e)$ where k is the rate constant for a organic pollutant, I_0 is the intensity of the radiant energy that enters the film, ka is the absorption coefficient of the radiation, and D_e is the effective diffusivity. (Reproduced with permission from (63). Copyright 2014, Elsevier.)

From this introduction, it is apparent that the film thickness plays an important role in the photocatalytic activity. This chapter summarizes the preparation methods for TiO_2 thin films and the effects of film thickness on the photocatalytic performance. TiO_2 nanocrystalline thin films prepared by sol–gel spin coating are used as examples with good mechanical and photocatalytical stabilities. The surface morphology, crystal structure, chemical composition, and thickness of as-deposited thin films are studied. The correlation between thickness and photocatalytic activity of TiO_2 thin films has been described and compared.
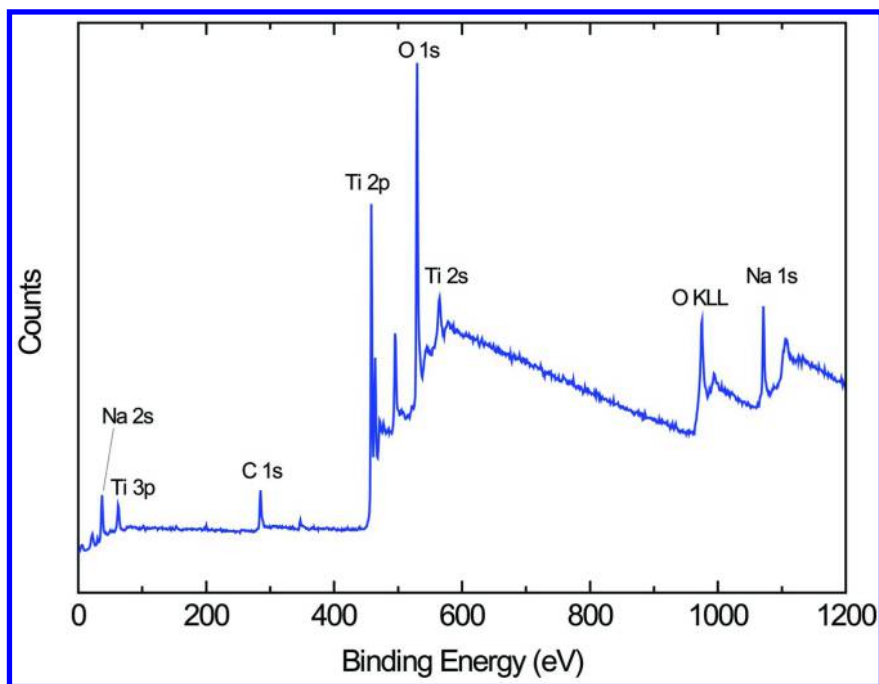
Figure 8. XPS survey spectrum of TiO₂ thin film prepared by 0.3 M TTIP as precursor and calcined at 450 °C for 3 h. (Reproduced with permission from (13). Copyright 2014, Elsevier.)

Results and Discussion

Thin Film Characterization

TiO$_2$ thin films were prepared from TTIP as the precursor under pH of 3.5 ± 0.5 by sol–gel spin coating on glass substrates and with calcination temperature of 450 °C for 3 h. The thin films exhibited superior homogeneous aggregation on the substrate, good optical transparency, superhydrophilicity, and reliable thickness. Figure 8 shows a typical XPS spectrum for the surface of TiO$_2$ thin film deposited on glass. It can be seen that the film deposited on glass contains Ti, O, C, and Na. The atomic percentages of Ti, O, C, and Na on the surface of the film were 21.4, 53.3, 18.0, and 7.3%, respectively. As a rechecking for the stoichiometric formation of TiO$_2$, the O/Ti ratio was determined to be 2.5, which exhibits excess oxygen content related to hydroxyl groups and film density (*64*). The element C could come from the residual carbon from precursor solution and the hydrocarbon from pumping oil. The element Na could be attributed to the diffusion of sodium ions from the glass substrate (*65*). A number of studies have shown that the

diffusion of sodium ions into the TiO_2 film during the calcination step would significantly deteriorate the photocatalytic activity because of the formation of surface and bulk recombination centers (*66–68*). High concentration sodium could even prevent formation of the photoactive anatase phase. Compared with previous observations, the small content of Na in the film has little effect on the chemical state of Ti and crystalline structure of TiO_2. This could be attributed to the low calcination temperature and the pre-treatment cleaning of the glass substrate to retard the diffusion of sodium ions. Figure 9 shows the high resolution XPS spectrum of the O 1s core level. The peak deconvolution indicated that the peaks at 530.0 and 531.5 eV could correspond to Ti–O in TiO_2 and the hydroxyl group, respectively. The spectrum is in good agreement with the standard spectrum of TiO_2 and demonstrates that TiO_2 has been successfully deposited on glass substrate by sol–gel spin coating (*69, 70*).
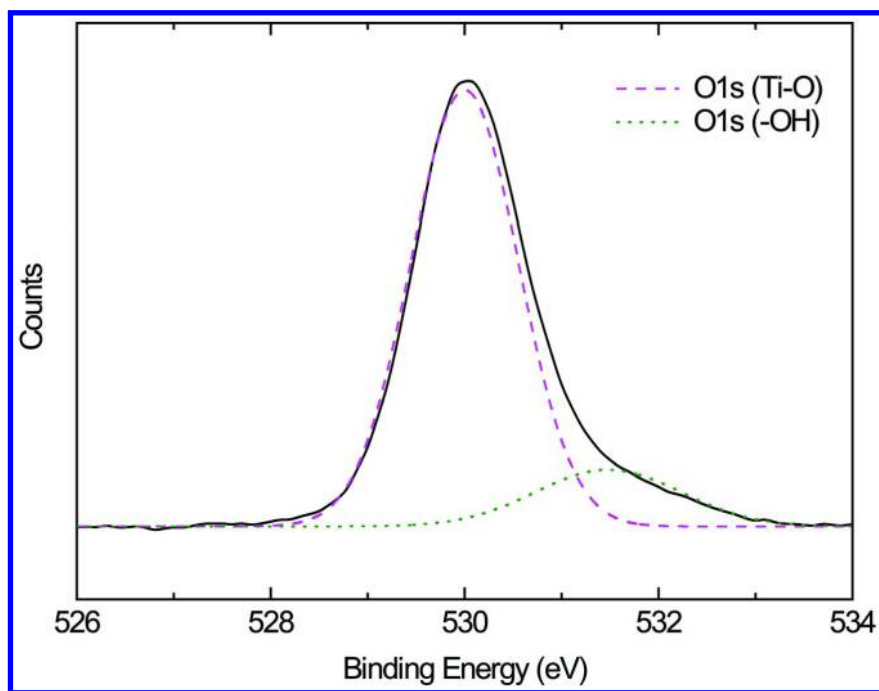
Figure 9. High resolution XPS spectrum of the O 1s region for the TiO₂ thin film prepared by 0.3 M TTIP as precursor and calcined at 450 °C for 3 h. (Reproduced with permission from (13). Copyright 2014, Elsevier.)

Photoluminescence (PL) emission analysis has been used to investigate the transfer behavior of the photogenerated electron–hole pairs in the photocatalysts (*71, 72*). The photoluminescence (PL) spectra of the thin films were excited at a wavelength of 285 nm at room temperature and the PL spectra were analyzed in the range of 300–550 nm for TiO_2 thin film, Na-free TiO_2 film, and commercial P25. As shown in Figure 10, PL spectra with similar shapes were obtained and the PL intensity decreased with decreasing the content of Na in the film. This indicates that the presence of Na may form extra recombination centers and enhance the recombination rates. In this study, the small content of Na in the film could be considered as a background effect in the recombination of electron–hole pairs (*57, 72, 73*).
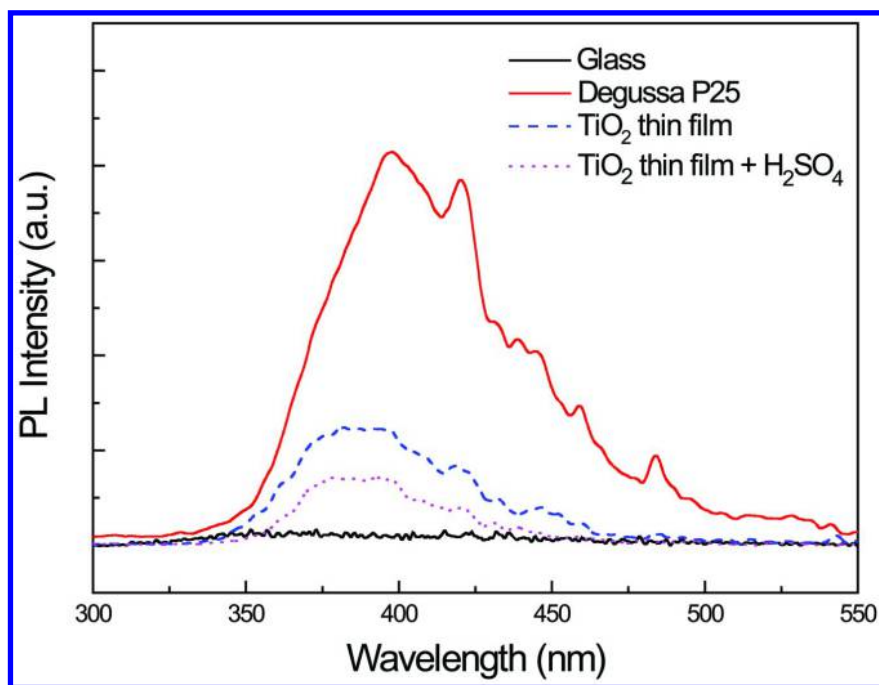
Figure 10. Photoluminescence spectra of Degussa P25 dispersed on the glass, TiO2 thin film, Na-free TiO2 film by 1M sulfuric acid treatment, and bare glass. Experimental condition: Both excitation and emission slits were set at 4nm. The scan speed was 400 nm/min. Spectra were accumulated for 5 scans. The thicknesses of TiO_2 thin film and Na-free TiO2 film were the same as 150 nm. The PL intensity of Degussa P25 is much greater than those of TiO2 thin films because of the amount of P25, not the effect of Na. (Unpublished results.)

SEM has been demonstrated to be a very versatile and powerful tool for surface imaging at the submicrometer level and the revelation of the surface characteristics of the films. Figure 11 shows FE-SEM images of TiO_2 thin films

prepared with different concentrations of TTIP and calcined at 450 °C for 3 h. It was observed that the particle size and average roughness of the films decreased with increasing TTIP concentration. A similar trend was observed for the preparation of TiO_2 nanoparticles (74, 75). This would be due to the different formation rate of TiO_2 nanoparticles by hydrolysis of TTIP.
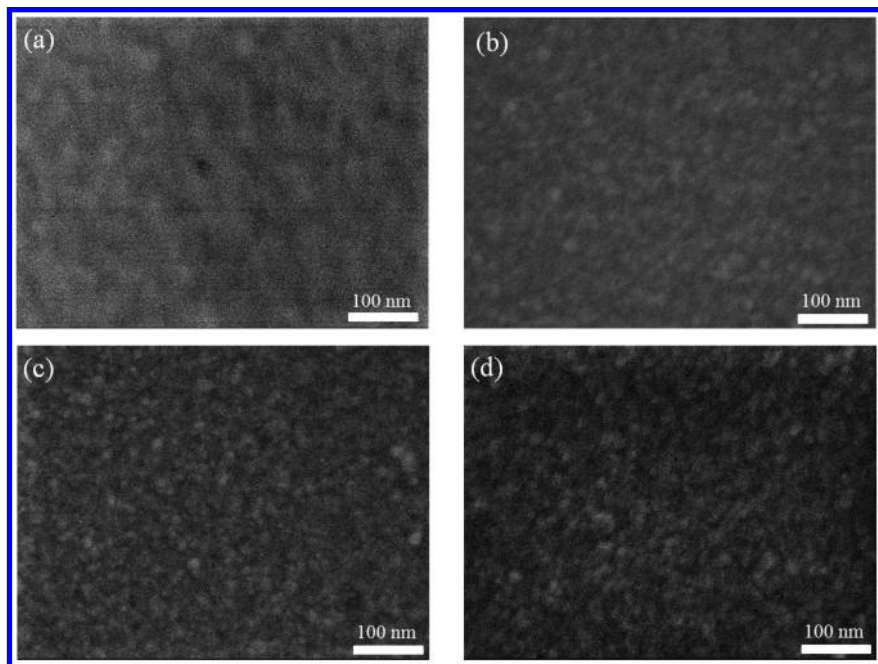
Figure 11. FE-SEM images of TiO₂ thin films prepared with different concentrations of TTIP as precursor and calcined at 450 °C for 3 h: (a) 0.1M, (b) 0.2M, (c) 0.3M, and (d) 0.4M. (Unpublished results.)

Figure 12 shows the XRD patterns of TiO_2 thin films deposited on glass plate and calcined at 250, 350, 450, and 550 °C. The XRD patterns show peaks attributed to (101), (004), (200), (105), and (211) reflections of the anatase. With increased calcination temperature, all the peaks became sharper and narrower, indicating promotion of the crystallinity degree of the sample. The calcination temperature could accelerate the phase transition of titania from amorphous to anatase phase and no rutile phase was observed for temperatures up to 550 °C. As shown in Figure 12, the film calcinated above 450 °C has good crystallinity and all XRD peaks are attributed to anatase. The average particle size estimated from the Scherrer equation was 16.3 nm from the film calcined at 250 °C and they increased to 20.4, 21.4, and 27.1 nm at 350, 450, and 550 °C, respectively. After calcination at 450 °C for 3h, the film shows a contact angle less than 1°. The superhydrophilicity behavior could be attributed to the clean surface, surface porosity, and the increased amount of surface hydroxyl groups (76–78).
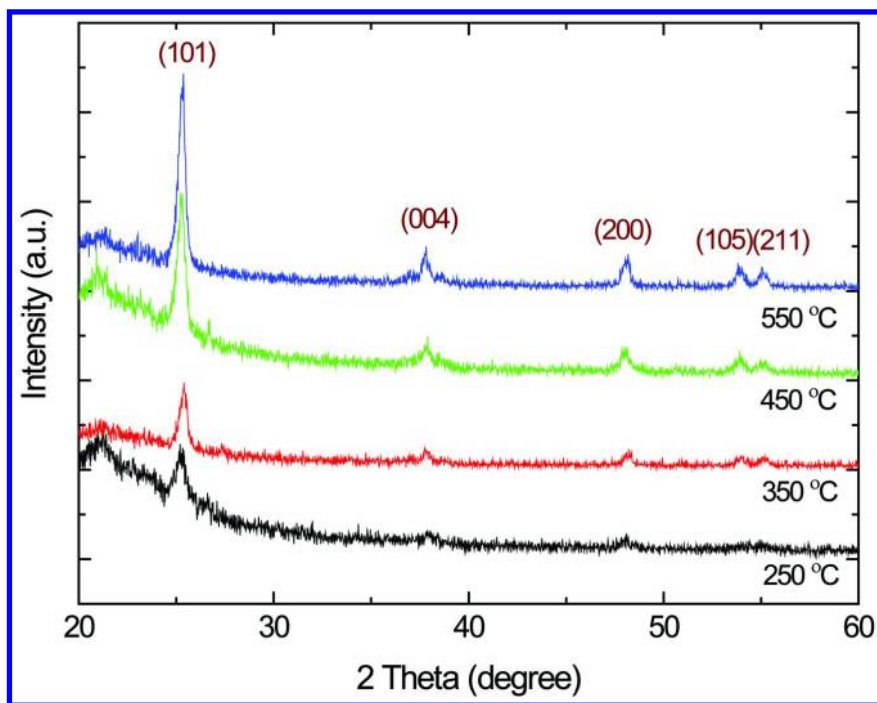
Figure 12. XRD patterns of TiO₂ thin films prepared with 0.3M TTIP as precursor and calcined at different temperatures for 3 h. (Reproduced with permission from (13). Copyright 2014, Elsevier.)

Figure 13 shows a linear relationship between thickness of TiO_2 thin films and number of coating cycles with different TTIP concentrations. It can be seen that under a constant TTIP concentration, the thickness was proportional to the number of coating cycles. The growth rate of film thickness per coating cycle increased gradually with increasing TTIP concentration. This indicates that the sol–gel spin coating for the preparation of the films was a very reliable method. The increasing film thicknesses per coating cycle were estimated to be about 14, 24, 48, and 53 nm with precursor concentration of 0.1, 0.2, 0.3, and 0.4 M, respectively. Since the first coating was formed on the glass substrate, the increasing film thickness per coating cycle was smaller than the first coating (*52, 53*).

Photocatalytic Activity

The photocatalytic activity of TiO_2 thin films was evaluated by the degradation of acid yellow 17 in aqueous solutions. The intensity band corresponding to acid yellow 17 at 400 nm decreases with the extension of the exposure time, and disappears almost completely after 11 h. Figure 14 illustrates the effect of film thickness on the photodegradation of acid yellow 17. In Figure 14, the dye concentration kept constant before and after containing TiO_2 thin films for 2 h

in the dark, so the dye has weak adsorption on the TiO_2 thin films under the conditions of the experiments. The photocatalytic degradation rate followed zero-order kinetic with respect to the acid yellow 17 concentration and the photocatalytic activity of the film increased with the number of coating cycles. The results are in general agreement that at high concentrations of the organic substrate or at relatively low concentrations of the catalyst, the reaction rate should remain constant and thus zero order kinetics (*79, 80*). The maximum specific photocatalytic activity occurred at 5 coatings with thickness of 93 ± 1 nm. With the increase of film thickness, the internal mass transfer and light penetration depth may play dominant roles by limiting utilization of the active sites for photocatalytic activity. The photocatalytic degradation of Rhodamine B shows a similar trend. Figure 15 shows the photocatalytic degradation of Rhodamine B for different thicknesses of indium tin oxide (ITO). The incident light may produce maximum number of electron–hole pairs for an optimum thickness. With further increase in the thickness, though the generation rate remains constant, the migration length of the carriers to the surface of the catalyst increases where the carriers experience higher recombination rates, resulting in a decrease in the photocatalytic activity.
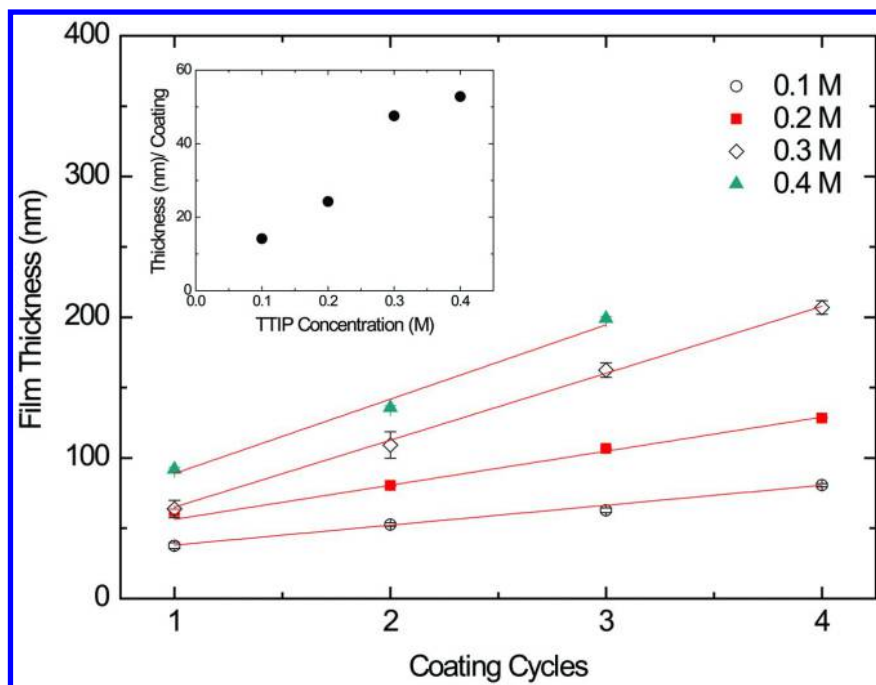
Figure 13. Effect of number of coatings on the film thickness as a function of TTIP concentration. TiO_2 thin films were prepared with TTIP as precursor and calcined at 450 °C for 3 h. Inset: growth rate of film thickness per coating cycle with TTIP concentration. Error bars represent standard deviations of three replicate experiments. (Reproduced with permission from (13). Copyright 2014, Elsevier.)
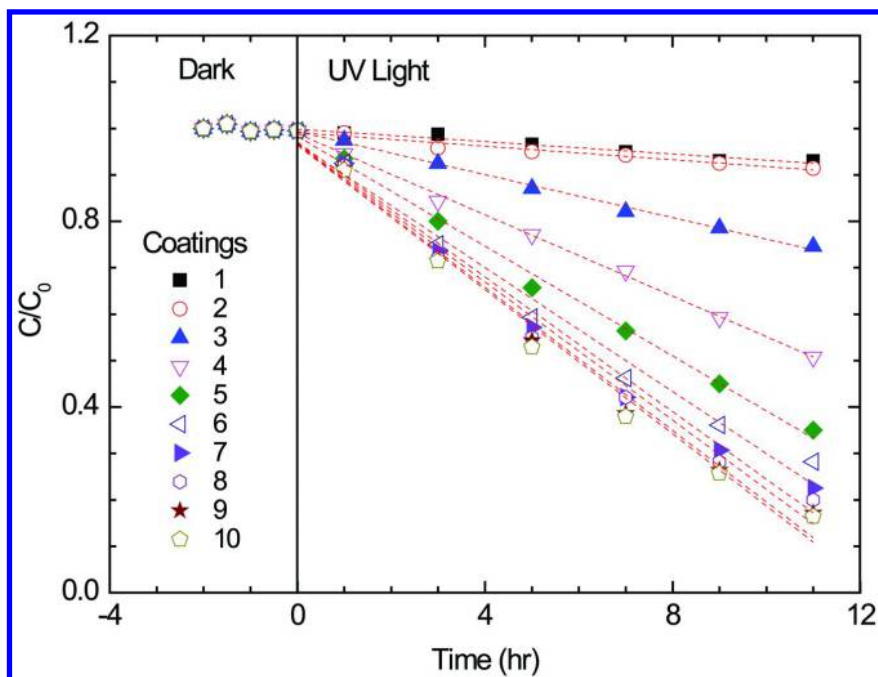
Figure 14. Effect of film thickness of TiO₂ on the photodegradation of acid yellow 17 as a function of irradiation time. TiO₂ thin films were prepared with 0.1 M TTIP as precursor and calcined at 450 °C for 3 h. Irradiation intensity was 10 W at 254 nm. The film area was 1.5 cm × 1.5 cm. The concentration of acid yellow 17 was 10 ppm with maximum absorption at 400 nm. (Reproduced with permission from (13). Copyright 2014, Elsevier.)

Figure 16 shows the variation in degradation rate constant of acid yellow 17 against TiO₂ amount which is linearly proportional to the number of coating cycles. The degradation rate constant was kept low and independent on the TiO₂ amount when the film thickness was less than 53 nm (or 2 coatings). When the thickness was more than 53 nm, the rate constant was found to increase with increasing the number of coating cycles and then approaching a limiting value, which was typical Langmuir-type kinetics. As expected, a linear expression can be conveniently obtained by plotting effective concentration of TiO₂ divided from rate constant (*[TiO₂]ₑff/k*) against effective concentration of TiO₂ (*[TiO₂]ₑff*). The effective concentration of TiO₂ is determined by the deduction of the first two coatings from the total amount of TiO₂. A plot of *[TiO₂]ₑff/k* against *[TiO₂]ₑff* gives the values of slope (*1/kₚ*) and intercept (*1/(kₚK)*) as shown in the inset of Figure 16. From the intercept and slope of this curve, values of *kₚ* and *K* were found to be 1.9 µM/h and 106 L/g, respectively. Similar values were obtained directly from the nonlinear regression. The trend may mainly result from the increase in amount of TiO₂ participating in the photocatalytic reaction and the limiting value may be

attributed to a constant number of surface active sites in a restricted area (*81, 82*). Although the TiO$_2$ thin films show lower photocatalytic activity than mesoporous TiO$_2$-anatase thin films reported in previous studied (*47*), the amount of TiO$_2$ is extremely small in the studied system (0.014 g/L for the 5 coating film).
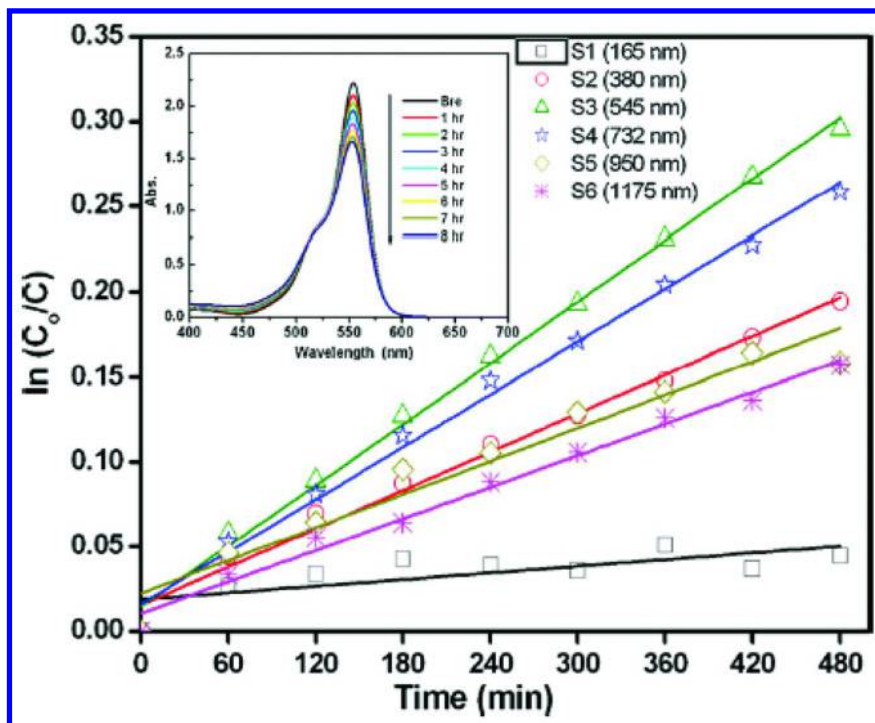
Figure 15. Photocatalytic degradation of Rhodamine B for different thicknesses of ITO thin films. The inset shows the absorption spectra of S3 sample for different time intervals. (Reproduced with permission from (49). Copyright 2014, Elsevier.)

Generally speaking, the photocatalytic activity is proportional to the film thickness. However, when the film thickness increases beyond the light penetration depth, then those organic molecules located in the non-irradiated part of the layer do not undergo degradation, as shown in Figure 17. The photocatalytic performance for the TiO$_2$ films could be inversely proportional to the thickness. On the basis of the results of this study and the literature (*31, 49, 51, 55–58*), the photocatalytic process for degradation of acid yellow 17 on TiO$_2$ thin films is depicted in Figure 18. The photocatalytic process can be divided into two classes. Class 1 is characterized by a low constant activity when the film thickness is less than the depletion layer width, i.e. 53 nm in the studied system. Typically, the photo-excited valence-band holes at the surface initiate the degradation process and the conduction-band electrons into inner layers are necessary to prevent recombination. When the thickness is less than the depletion

layer width, the electron transfer to the insulating support is not possible, so the recombination of charge carriers is inevitable. When the film thickness is larger than the depletion layer width, a considerable higher activity is dominated as class 2. The degradation rate constant increases with increasing the number of coating cycles, which can be attributable to the increase of the amount of TiO$_2$ providing more reaction sites for photocatalysis. With further increase in the thickness, the light penetration depth, the mass transfer of acid yellow 17 into the film to reach the active adsorption sites, and the migration length of the carriers to the surface of the catalyst are considered as major factors for the decrease of photocatalytic activity. Table 2 summarizes several major factors which could greatly influence the photocatalytic activity (*13, 31, 49, 51, 55, 62, 83*). The obtained results indicate that an optimum film thickness may usually exist for the photocatalytic activity of TiO$_2$ thin films. It should be noticed that the amounts of hydroxyl surface groups could be another important factor in the photocatalytic activity (*14, 66, 84–87*). Therefore, further studies regarding the amounts of hydroxyl groups on the surface of TiO$_2$ are desirable to achieve a more thorough understanding of the effect of film thickness on the photocatalytic activity of TiO$_2$ thin films.
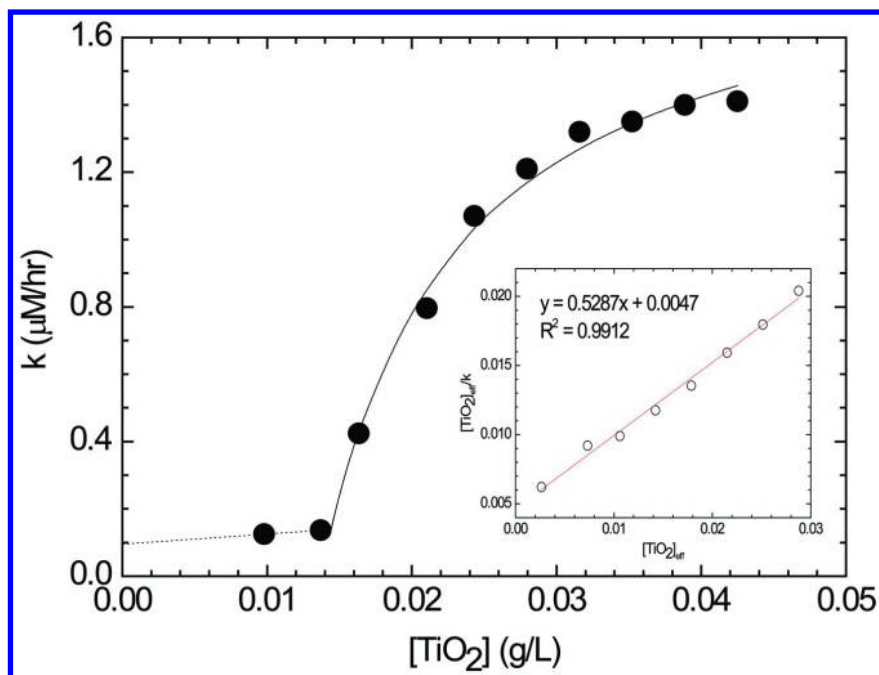
Figure 16. Effect of TiO$_2$ concentration on the pseudo-zero photodegradation rate constant (k). The inset shows a plot of [TiO$_2$]$_{eff}$/k against [TiO$_2$]$_{eff}$ where [TiO$_2$]$_{eff}$ is the effective concentration of TiO$_2$ determined by the difference of the total amount of TiO$_2$ and the first two coatings. (Reproduced with permission from (13). Copyright 2014, Elsevier.)

Table 2. Effect of Film Thickness on the Photocatalytic Activity

Factor	Description	Optimum thickness	Photocatalyst	Preparation method	Target compound	Reference
Schottky barrier	Prevention of electron-hole recombination	>200 nm	TiO$_2$ (100% Anatase)	Magnetron sputtering	Acetic acid	Sheng et al., 1997 (*51*)
Electron-hole recombination	Capture of photogenerated negative charges by Ag centers	Two layers	0.25% Ag:TiO$_2$	Sol–gel spin coating	Rhodamine B	Malagutti et al., 2009 (*55*)
Mass transfer	Organic pollutant mobility in bulk solution and catalyst thin film	5000 nm	TiO$_2$ (80% Anatase, 20% Rutile)	Dip coating	Benzoic acid	Chen et al., 2000 (*62*)
Migration length	Carries transfer to catalyst surface	545 nm	Indium tin oxide (ITO)	Magnetron sputtering	Rhodamine B	Kumar et al., 2011 (*49*)
Light penetration	Photo-energy utilization	3000 nm	TiO$_2$ photonic sponge (80% Anatase, 20% Rutile)	Doctor blade	Succinonitrile	Carbonell et al., 2008 (*31*)
Mass transfer, migration length, and light penetration	The correlation between film thickness and photocatalytic activity	93 nm	TiO$_2$ (100% Anatase)	Solï¿½gel spin coating	Acid yellow 17	Wu et al., 2013 (*13*)
Surface active sites and crystal structure	Reaction temperature to determine the thickness and morphology	1300 nm	Bismuth oxybromide (BiOBr)	Solvothermal synthesis	Methyl orange	Liu et al., 2014 (*83*)
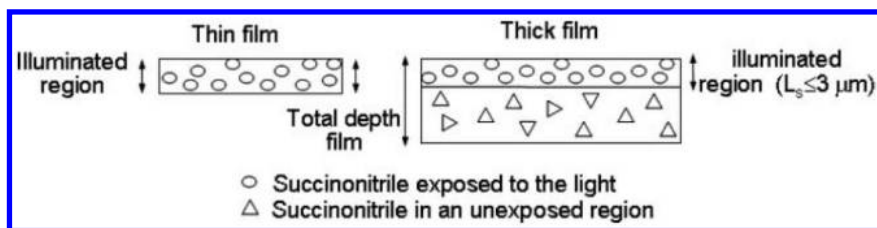
Figure 17. Scheme of the cross sections of thin and thick films illustrating the inefficient irradiation when the film thickness is larger than the light penetration depth. (Reproduced with permission from (31). Copyright 2014, Royal Society of Chemistry.)
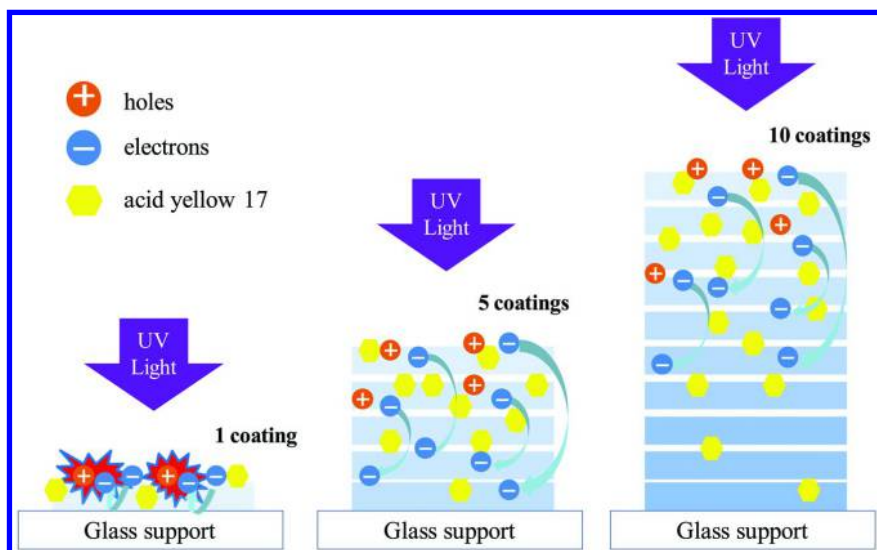
Figure 18. Pictorial representation of cross sections of thin films with different coatings illustrating the effect of film thickness on the photocatalytic activity. The recombination of electron hole pairs is illustrated in one coating system. The UV–vis light penetration depth and the mass transfer of acid yellow 17 into the film to reach the active adsorption sites are shown in 10 coating system. (Reproduced with permission from (13). Copyright 2014, Elsevier.)

Conclusions

Various methods for the preparation of TiO$_2$ thin films have been briefly reviewed. The films prepared by sol–gel spin coating exhibit superior homogeneous aggregation on the substrate, good optical transparency, superhydrophilicity, reliable thickness, and high photocatalytic activity, and are

suitable for the study of the correlation between thickness and photocatalytic activity. This chapter summarizes the effects of film thickness on the photocatalytic performance and provides relevant information for further processing highly effective TiO₂ thin films and for their potential use in environmental remediation applications.

Acknowledgments

References

1. Fujishima, A.; Zhang, X.; Tryk, D. A. *Surf. Sci. Rep.* **2008**, *63*, 515–582.
2. Nakata, K.; Fujishima, A. *J. Photochem. Photobiol., C* **2012**, *13*, 169–189.
3. Park, H.; Park, Y.; Kim, W.; Choi, W. *J. Photochem. Photobiol., C* **2013**, *15*, 1–20.
4. Daghrir, R.; Drogui, P.; Robert, D. *Ind. Eng. Chem. Res.* **2013**, *52*, 3581–3599.
5. Kumar, S. G.; Devi, L. G. *J. Phys. Chem. A* **2011**, *115*, 13211–13241.
6. Chen, C.; Ma, W.; Zhao, J. *Chem. Soc. Rev.* **2010**, *39*, 4206–4219.
7. Pelaez, M.; Nolan, N. T.; Pillai, S. C.; Seery, M. K.; Falaras, P.; Kontos, A. G.; Dunlop, P. S. M.; Hamilton, J. W. J.; Byrne, J. A.; O'Shea, K.; Entezari, M. H.; Dionysiou, D. D. *Appl. Catal., B* **2012**, *125*, 331–349.
8. Chong, M. N.; Jin, B.; Chow, C. W. K.; Saint, C. *Water Res.* **2010**, *44*, 2997–3027.
9. Lee, S. Y.; Park, S. J. *J. Ind. Eng. Chem.* **2013**, *19*, 1761–1769.
10. Sonawane, R. S.; Dongare, M. K. *J. Mol. Catal. A: Chem.* **2006**, *243*, 68–76.
11. Simonsen, M. E.; Li, Z.; Sogaard, E. G. *Appl. Surf. Sci.* **2009**, *255*, 8054–8062.
12. Yao, J.; Bai, Y.; Chen, N.; Takahashi, M.; Yoko, T. *J. Am. Ceram. Soc.* **2011**, *94*, 1191–1197.
13. Wu, C. Y.; Lee, Y. L.; Lo, Y. S.; Lin, C. J.; Wu, C. H. *Appl. Surf. Sci.* **2013**, *280*, 737–744.
14. Fateh, R.; Dillert, R.; Bahnemann, D. *Langmuir* **2013**, *29*, 3730–3739.
15. Weng, W.; Ma, M.; Du, P.; Zhao, G.; Shen, G.; Wang, J.; Han, G. *Surf. Coat. Technol.* **2005**, *198*, 340–344.
16. Dostanic, J.; Grbic, B.; Radic, N.; Stefanov, P.; Saponjic, Z.; Buha, J.; Mijin, D. *Chem. Eng. J.* **2012**, *180*, 57–65.
17. Chang, J. H.; Ellis, A. V.; Hsieh, Y. H.; Tung, C. H.; Shen, S. Y. *Sci. Total Environ.* **2009**, *407*, 5914–5920.
18. Wu, C. Y.; Chiang, B. S.; Chang, S.; Liu, D. S. *Appl. Surf. Sci.* **2011**, *257*, 1893–1897.

19. Sathasivam, S.; Kafizas, A.; Ponja, S.; Chadwick, N.; Bhachu, D. S.; Bawaked, S. M.; Obaid, A. Y.; Al-Thabaiti, S.; Basahel, S. N.; Carmalt, C. J.; Parkin, I. P. *Chem. Vap. Deposition* **2014**, *20*, 69–79.
20. Chen, Y. J.; Lo, Y. S.; Huang, C. H.; Cai, Y. C.; Hsu, M. C. *Mater. Chem. Phys.* **2010**, *120*, 181–186.
21. Peralta-Hernandez, J. M.; Manriquez, J.; Meas-Vong, Y.; Rodriguez, F. J.; Chapman, T. W.; Maldonado, M. I.; Godinez, L. A. *J. Hazard. Mater.* **2007**, *147*, 588–593.
22. Wu, M. S.; Tsai, C. H.; Jow, J. J.; Wei, T. C. *Electrochim. Acta* **2011**, *56*, 8906–8911.
23. Liou, Y. J.; Hsiao, P. T.; Chen, L. C.; Chu, Y. Y.; Teng, H. *J. Phys. Chem. C* **2011**, *115*, 25580–25589.
24. Miyauchi, M.; Tokudome, H. *J. Mater. Chem.* **2007**, *17*, 2095–2100.
25. Sayikan, F.; Asilturk, M.; Tatar, P.; Kiraz, N.; Sener, S.; Arpac, E.; Sayikan, H. *Mater. Res. Bull.* **2008**, *43*, 127–134.
26. Vijayan, B.; Dimitrijevic, N. M.; Rajh, T.; Gray, K. *J. Phys. Chem. C* **2010**, *114*, 12994–13002.
27. Macak, J. M.; Zlamal, M.; Krysa, J.; Schmuki, P. *Small* **2007**, *3*, 300–304.
28. Shimizu, Y.; Hyodo, T.; Egashira, M. *Sens. Actuators, B* **2007**, *121*, 219–230.
29. Allam, N. K.; El-Sayed, M. A. *J. Phys. Chem. C* **2010**, *114*, 12024–12029.
30. Andronic, L.; Duta, A. *Mater. Chem. Phys.* **2008**, *112*, 1078–1082.
31. Carbonell, E.; Ramiro-Manzano, F.; Rodriguez, I.; Corma, A.; Meseguer, F.; Garcia, H. *Photochem. Photobiol. Sci.* **2008**, *7*, 931–935.
32. Tsoukleris, D. S.; Kontos, A. I.; Aloupogiannis, P.; Falaras, P. *Catal. Today* **2007**, *124*, 110–117.
33. Fan, K.; Liu, M.; Peng, T.; Ma, L.; Dai, K. *Renew. Energy* **2010**, *35*, 555–561.
34. Kitano, M.; Funatsu, K.; Matsuoka, M.; Ueshima, M.; Anpo, M. *J. Phys. Chem. B* **2006**, *110*, 25266–25272.
35. Chen, D. Y.; Tsao, C. C.; Hsu, C. Y. *Curr. Appl. Phys.* **2012**, *12*, 179–183.
36. Kuo, C. G.; Hsu, C. Y.; Wang, S. S.; Wen, D. C. *Appl. Surf. Sci.* **2012**, *258*, 6952–6957.
37. Barrocas, B.; Monteiro, O. C.; Melo Jorge, M. E.; Serio, S. *Appl. Surf. Sci.* **2013**, *264*, 111–116.
38. Remsa, J.; Miksovsky, J.; Jelinek, M. *Appl. Surf. Sci.* **2012**, *258*, 9333–9336.
39. Daghrir, R.; Drogui, P.; Ka, I.; El Khakani, M. A. *J. Hazard. Mater.* **2012**, *199–200*, 15–24.
40. Luttrell, T.; Halpegamage, S.; Sutter, E.; Batzill, M. *Thin Solid Films* **2014**, *564*, 146–155.
41. Habibi, M. H.; Talebian, N. *Dyes Pigm.* **2007**, *73*, 186–194.
42. Hsu, S. W.; Yang, T. S.; Chen, T. K.; Wong, M. S. *Thin Solid Films* **2007**, *515*, 3521–3526.
43. Yang, H. Y.; Lee, M. F.; Huang, C. H.; Lo, Y. S.; Chen, Y. J.; Wong, M. S. *Thin Solid Films* **2009**, *518*, 1590–1594.
44. Gonzalez-Garcia, L.; Parra-Barranco, J.; Sanchez-Valencia, J. R.; Barranco, A.; Borras, A.; Gonzalez-Elipe, A. R.; Garcia-Gutierrez, M. C.; Hernandez, J. J.; Rueda, D. R.; Ezquerra, T. A. *Nanotechnology* **2012**, *23*, 205701–205710.

45. Chen, H.; Lee, S. W.; Kim, T. H.; Hur, B. Y. *J. Eur. Ceram. Soc.* **2006**, *26*, 2231–2239.
46. Miyata, T.; Tsukada, S.; Minami, T. *Thin Solid Films* **2006**, *496*, 136–140.
47. Arconada, N.; Duran, A.; Suarez, S.; Portela, R.; Coronado, J. M.; Sanchez, B.; Castro, Y. *Appl. Catal., B* **2009**, *86*, 1–7.
48. Akpan, U. G.; Hameed, B. H. *J. Hazard. Mater.* **2009**, *170*, 520–529.
49. Kumar, K. J.; Raju, N. R. C.; Subrahmanyam, A. *Appl. Surf. Sci.* **2011**, *257*, 3075–3080.
50. Smirnov, M.; Baban, C.; Rusu, G. I. *Appl. Surf. Sci.* **2010**, *256*, 2405–2408.
51. Sheng, J.; Karasawa, J.; Fukami, T. *J. Mater. Sci. Lett.* **1997**, *16*, 1709–1711.
52. Yu, J.; Zhao, X.; Zhao, Q. *J. Mater. Sci. Lett.* **2000**, *19*, 1015–1017.
53. Balasubramanian, G.; Dionysiou, D. D.; Suidan, M. T.; Baudin, I.; Laine, J. M. *Appl. Catal., B* **2004**, *47*, 73–84.
54. Addamo, M.; Augugliaro, V.; Di Paola, A.; Garcia-Lopez, E.; Loddo, V.; Marci, G.; Palmisano, L. *Thin Solid Films* **2008**, *516*, 3802–3807.
55. Malagutti, A. R.; Mourao, H. A. J. L.; Garbin, J. R.; Ribeiro, C. *Appl. Catal., B* **2009**, *90*, 205–212.
56. Ismail, A. A.; Bahnemann, D. W.; Rathousky, J.; Yarovyi, V.; Wark, M. *J. Mater. Chem.* **2011**, *21*, 7802–7810.
57. Akhavan, O. *Appl. Surf. Sci.* **2010**, *257*, 1724–1728.
58. Ye, C.; Bando, Y.; Shen, G.; Golberg, D. *J. Phys. Chem. B* **2006**, *110*, 15146–15151.
59. Chen, Y. H.; Tu, K. J. *Int. J. Photoenergy* **2012**, *2012*, 980595.
60. Hidaka, H.; Ajisaka, K.; Horikoshi, S.; Oyama, T.; Takeuchi, K.; Zhao, J.; Serpone, N. *J. Photochem. Photobiol., A* **2001**, *138*, 185–192.
61. Berger, T.; Monllor-Satoca, D.; Jankulovska, M.; Lana-Villarreal, T.; Gomez, R. *ChemPhysChem* **2012**, *13*, 2824–2875.
62. Chen, D.; Li, F.; Ray, A. K. *AIChE J.* **2000**, *46*, 1034–1045.
63. Camera-Roda, G.; Santarelli, F. *Catal. Today* **2007**, *129*, 161–168.
64. Wang, Z.; Helmersson, U.; Kall, P. O. *Thin Solid Films* **2002**, *405*, 50–54.
65. Yuksel, B.; Sam, E. D.; Aktas, O. C.; Urgen, M.; Cakir, A. F. *Appl. Surf. Sci.* **2009**, *255*, 4001–4004.
66. Yu, J. C.; Yu, J.; Zhao, J. *Appl. Catal., B* **2002**, *36*, 31–43.
67. Nam, H. J.; Amemiya, T.; Murabayashi, M.; Itoh, K. *J. Phys. Chem. B* **2004**, *108*, 8254–8259.
68. Yu, H.; Yu, J.; Cheng, B. *Catal. Commun.* **2006**, *7*, 1000–1004.
69. Yu, J.; Yu, J. C.; Ho, W.; Jiang, Z. *New J. Chem.* **2002**, *26*, 607–613.
70. Wang, D.; Xiao, L.; Luo, Q.; Li, X.; An, J.; Duan, Y. *J. Hazard. Mater.* **2011**, *192*, 150–159.
71. Huang, X. X.; Zhang, W. G. *Appl. Surf. Sci.* **2008**, *254*, 3403–3407.
72. Akhavan, O.; Ghaderi, E. *Surf. Coat. Technol.* **2010**, *204*, 3676–3683.
73. Zhang, X.; Lei, L. *Appl. Surf. Sci.* **2008**, *254*, 2406–2412.
74. Chae, S. Y.; Park, M. K.; Lee, S. K.; Kim, T. Y.; Kim, S. K.; Lee, W. I. *Chem. Mater.* **2003**, *15*, 3326–3331.
75. Mahshid, S.; Askari, M.; Ghamsari, M. S.; Afshar, N.; Lahuti, S. *J. Alloys Compd.* **2009**, *478*, 586–589.

76. Ashkarran, A. A.; Mohammadizadeh, M. R. *Mater. Res. Bull.* **2008**, *43*, 522–530.
77. Akhavan, O.; Mehrabian, M.; Mirabbaszadeh, K.; Azimirad, R. *J. Phys. D: Appl. Phys.* **2009**, *42*, 225305.
78. Nam, S. H.; Cho, S. J.; Jung, C. K.; Boo, J. H.; Sicha, J.; Herman, D.; Musil, J.; Vlcek, J. *Thin Solid Films* **2011**, *519*, 6944–6950.
79. Krysa, J.; Waldner, G.; Mestankova, H.; Jirkovsky, J.; Grabner, G. *Appl. Catal., B* **2006**, *64*, 290–301.
80. Wang, D. M.; Lin, H. Y.; Shah, S. I.; Ni, C. Y.; Huang, C. P. *Sep. Purif. Technol.* **2009**, *67*, 127–134.
81. Chen, D.; Ray, A. K. *Water Res.* **1998**, *32*, 3223–3234.
82. Daneshvar, N.; Rabbani, M.; Modirshahla, N.; Behnajady, M. A. *J. Photochem. Photobiol., A* **2004**, *168*, 39–45.
83. Liu, Z.; Wu, B.; Niu, J.; Huang, X.; Zhu, Y. *Appl. Surf. Sci.* **2014**, *288*, 369–372.
84. Pan, L.; Zou, J. J.; Zhang, X.; Wang, L. *J. Am. Chem. Soc.* **2011**, *133*, 10000–10002.
85. Jassby, D.; Budarz, J. F.; Wiesner, M. *Environ. Sci. Technol.* **2012**, *46*, 6934–6941.
86. Wang, J.; Liu, X.; Li, R.; Qiao, P.; Xiao, L.; Fan, J. *Catal. Commun.* **2012**, *19*, 96–99.
87. Wang, J.; Liu, Z.; Cai, R. *Environ. Sci. Technol.* **2008**, *42*, 5759–5764.

Chapter 6

Preparation of ZnO Photocatalyst by Plasma-Enhanced Vapor Deposition and Their Photocatalytic Activity

Jian-Tang Chen, Mengshan Lee, and Walter Den*

Department of Environmental Science and Engineering, Tunghai University No. 1727, Sec. 4, Taiwan Boulevard, Taichung 407, Taiwan *E-mail: wden@thu.edu.tw.

This study aims to fabricate ZnO photocatalyst on anodic aluminum oxide (AAO) membranes using radio frequency plasma enhanced chemical vapor deposition (RF-PECVD), and to investigate the influence of catalyst morphology on its photocatalytic performance. ZnO particles were found to be evenly deposited at the edges around pores and formed rod-like or ring-like shaped catalyst arrays under specific conditions. Isopropyl alcohol was used as a target pollutant for evaluation of photocatalytic performance of ZnO catalyst under UV light of 365 nm. Substantial degradation of IPA (approximately 90 to 95%) was achieved in a batch system, and the rate of degradation followed zero order reaction kinetics. It was also evident that the degradation efficiency was positively correlated to the catalyst morphology, as nanorod shaped catalysts tended to have relatively higher activate surface area than ring-like or thin film shaped catalysts.

Introduction

Heterogeneous photocatalysis has been considered as a cost-effective and emerging solution to many environmental pollution problems. Therefore, over the last decades, great efforts have been put to the development of novel photocatalysts for environmental applications. Titanium dioxide (TiO_2) and zinc oxide (ZnO) are important photocatalysts with superior activity that utilize photons as excitation sources for the mineralization of contaminants (*1*, *2*). Zinc oxide, a semiconductor-based photocatalyst, has received considerable attention owing to its photocatalytic activity (wide direct bandgap between 3.2 to 3.4 eV) and favorable characteristics of availability, stability and low cost (*3*, *4*). These characteristics have made ZnO a promising photocatalyst with the activity comparable to TiO_2 (*5*). Moreover, ZnO has been reported to be more efficient at photodegradation of contaminants than TiO_2 under certain conditions (*6*, *7*).

As the performance of a photocatalyst is strongly affected by its material properties, efforts have recently been made to the improvement of crystallinity and morphology of the photocatalysts. The recent trend in the study of photocatalysis of ZnO is predominantly based on nanostructured catalysts (*8*). Different nanostructures of ZnO, such as nanoparticles, nanorods, nanobelts, nanorings, and nanowires, have been successfully synthesized under explicit growth conditions (*9*, *10*). Various preparation techniques, namely hydrothermal process (*10*), electrochemical and sol-gel deposition (*7*, *11*), sputtering(*12*), chemical vapor deposition (*13*, *14*), have been attempted to synthesis high quality and nano-crystalline ZnO photocatalysts onto types of supporters. Plasma enhanced chemical vapor deposition (PECVD), on the other hand, is a powerful and flexible technique for deposition of thin layers, nanocomposites or nanostructures (*15–18*). PECVD stands as a viable means to deposit ZnO at low temperatures using stable precursors, such as diethyl zinc (DEZn) (*19*) and zinc (II) acetylacetonate (Zn(acac)$_2$) (*20*). The use of metal organic chemicals as precursors also leads to preparation of high purity ZnO catalysts (*21*).

This study attempts to use a microporous anodic alumina oxide (AAO) membrane as a supporter to fabricate arrays of rod-like-shaped ZnO catalysts via radio frequency plasma-enhanced chemical vapor deposition (RF-PECVD) using DEZn as precursor. This study also aims to investigate the effects of operational parameters of carrier gas flowrates on the formation of ZnO arrays and their associated photocatalytic performances in the degradation of gaseous IPA under ultraviolet (UV) irradiations.

Experimental Methods

Deposition Experiments

ZnO arrays were prepared using the plasma-enhanced chemical vapor deposition technique, which was conducted in a low-pressure RF-PECVD chamber with an operating frequency at 13.56 MHz. The plasma output power was controlled at 150W, and the chamber pressure was operated at 1.5 torr (0.2 kPa). Schematic presentation of the experimental set-up is shown in Figure 1.
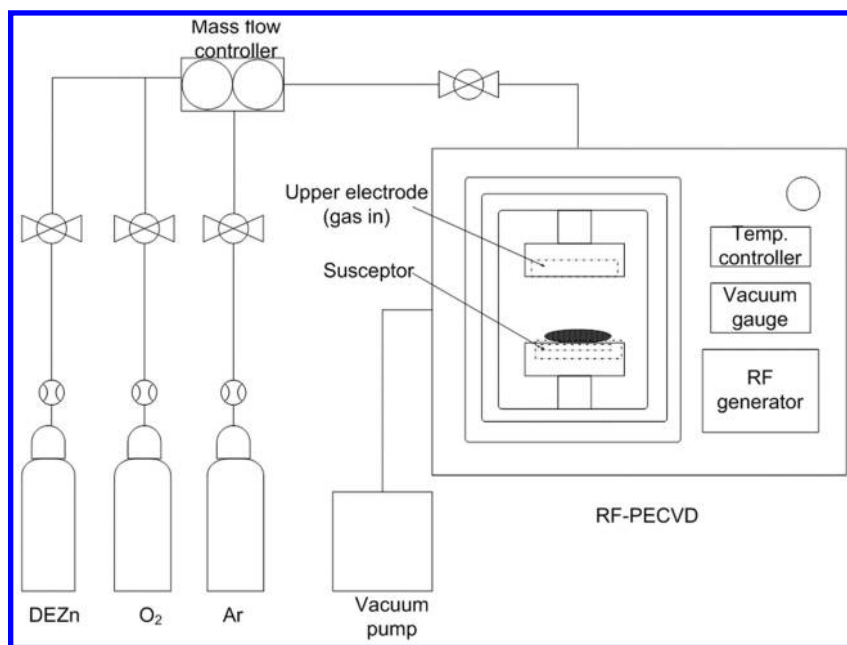
Figure 1. Schematics of the experimental apparatus and set-up.

Diethyl zinc (DEZn) was used as the source precursor through solvent purging, and the transferred was heat-wrapped at 80°C to minimize condensation in the tubings and fittings. The wide spread use of DEZn is primarily due to its high vapor pressure at room temperature and high pyrolytic decomposition temperature, which allows its use over a wide temperature range (*19*). Mixture of oxygen (O_2) and argon (Ar) were used as the carrier gas and plasma gas, respectively, for the preparation of ZnO catalyst arrays. The flow rates of Ar, O_2 and DEZn were controlled at a range of 50-300, 50-150 and 50-600 mL/min, respectively, using three independent mass flow controllers.

47-mm anodic aluminum oxide (AAO) membranes (Anodisc, Whatman) with average pore size of 100 nm were used as supporter templates on which the deposition occurred. The membrane was fixed on a 100-mm glass substrate, placed on the lower electrode in the CVD chamber, and was heated up to 300°C. The finished samples were either calcinated or used as is.

Characterization

The growth characteristics of ZnO arrays on AAO membranes were observed by field-emission scanning electron microscopy (FE-SEM) (JEOL JSM-6700F, Japan). And, the amount of ZnO (in weight) deposited onto the AAO membrane was determined by flame atomic absorption spectrometry (FAAS) after wet acid digestion treatment with nitric acid (1M) at 50°C for 24 hours (*22*).

Photocatalysis Experiments

The photocatalytic activity of the prepared ZnO arrays was evaluated by degradation of gaseous-phase isopropanol (IPA) in a batch reactor under UV light of 365nm. The light intensity of UV was 0.6 mW/cm². Before exposing to UV, an idling time in dark was allowed for the gaseous phase IPA concentration to reach equilibrium. The time-dependent IPA concentration was sampled with a 1-mL gas-tight syringe and analyzed by a gas chromatography (GC-3900, Varian) equipped with a flame ionization detector and a capillary analytical column. The influence of ZnO catalyst weight and morphology on the degradation of IPA was investigated in this study.

Results and Discussion

Deposition of ZnO Catalyst Arrays

ZnO photocatalyst arrays were successfully prepared using AAO-template-assisted growth mechanism. Field-emission scanning electron microscopy (FE-SEM) studies on the prepared catalysts revealed that the rod-like material consisted mainly of ZnO nanostructures, as shown in Figure 2. The images ~~revealed~~ indicated that the rod-like ZnO catalysts had diameters between 50 to 100 nm. Increase in Ar flow rates was demonstrated to have positive impacts on the deposition of ZnO catalysts. As the deposition process began, vaporous ZnO species were subsequently transported and condensed onto the surface of the membranes. The deposition started at the edge of the porous openings, and then branched out across all the edges with a thin deposition, which resulted in a ring-like ZnO arrays as shown in Figure 2(b). Figure 2(c) and 2(d) depicted that further growth of ZnO would gradually cover the porous openings to become a bundle of rod-shaped materials, as the growth occurred from the edge of the openings and extended upwards and outwards. In the case that the deposition continued, it was expected that the excess growth of ZnO would eventually turn into a solid film on top of the membranes.

Figure 3 depicts a schematic diagram illustrating the growth of ZnO on AAO membranes. The growth mechanism for ZnO is mainly controlled by the anisotropic surface energy in ZnO, which depends on the crystal faces of wurtzite ZnO (*21*). It was proposed that a textured material (in this study was the porous AAO membrane) could provide a surface containing seeds with *c*-axis-preferred orientation and had relatively high surface energy for catalyst deposition and nanorods formation (*23*, *24*). Therefore, in the initial stage of deposition, as evidenced in Figure 2, ZnO particles was deposited at the edge of the porous openings, instead of inside the pores. This could be partly explained by the fact that the relatively high depth-width ratio (approximately 1000:1) of pores on the AAO membrane limited the vaporous ZnO species to be diffused and deposited into the pores. In addition, when high-speed laminar gas flows existed in the growth condition, turbulent flows were induced between the nanostructures of AAO membranes, which resulted in adsorption of reactant gases only on tips

(*21*). Continuous deposition of vaporous ZnO species onto the membrane surface contributed to the nucleation of nanorods. Nucleation of nanorods that grow aligned along a particular direction then could be attributed to the atomic steps at substrate surface (*25, 26*). When the species continued to build up in both vertical and lateral directions, a solid film consisting of enlarged and elongated ZnO nanorods was formed. Figure 2(b) and 2(d) confirmed that the growth path of ZnO catalysts was initiated from ring arrays to aggregated rods, and, further deposition of the catalyst species on top of the rods resulted in enlarged and elongated nanorods structures.
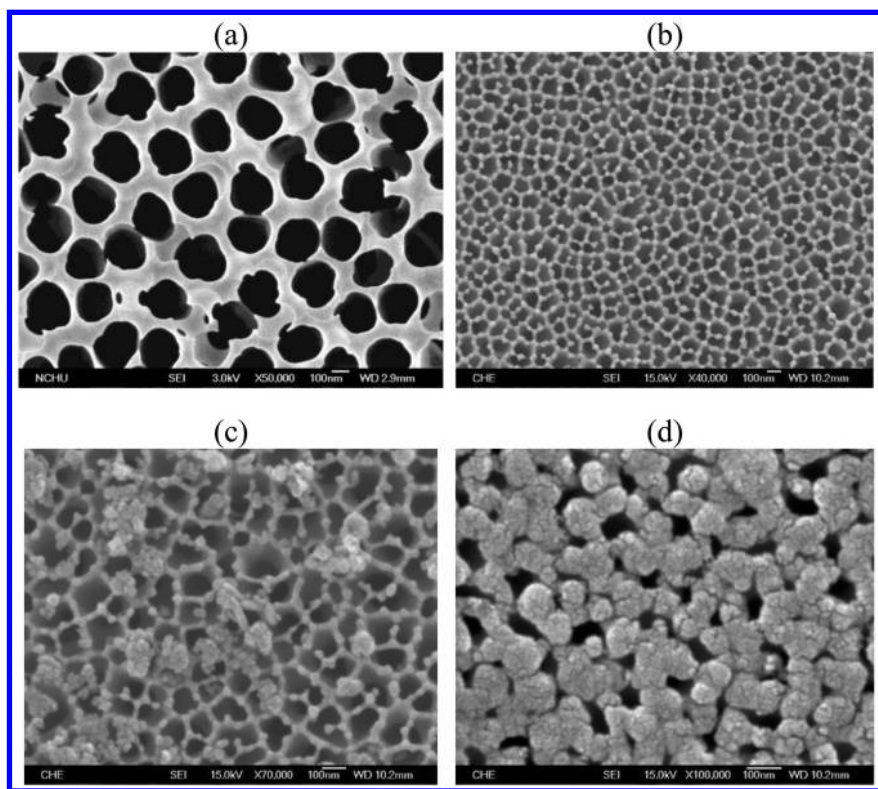
Figure 2. Growth of ZnO on AAO membranes: (a) bare membrane; (b) ring-like catalyst arrays (Ar=50 ml/min); (c) excess deposition of rod-like catalysts over ring-like arrays (Ar=150 ml/min); (d) aggregation of rod-like catalysts (Ar=300 ml/min) (all were controlled at O₂=50 ml/min and DEZn=400 ml/min).
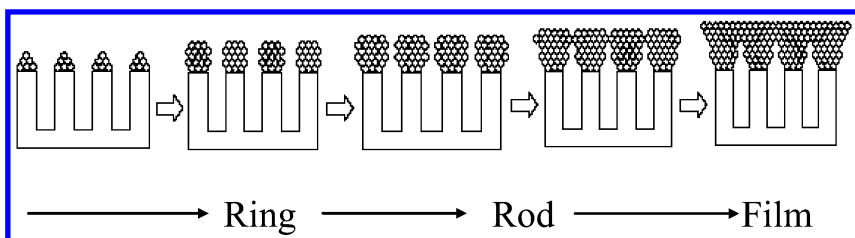
Figure 3. Schematic view of the proposed growth mechanism in cross-sections (left to right: particles are deposited at edges to form ring-like and rod-like structures, and then gradually aggregated to become a film consisting of elongated and enlarged rod bundles).

The influence of carrier gas flowrates on the deposition of ZnO catalysts was also investigated. Variation in growth weight of ZnO versus O_2 and Ar flowrates is shown in Figure 4. At controlled Ar flowrates, increase in O_2 flowrates did not affect the deposition amount of ZnO catalyst. However, increase in Ar flowrates contributed to a slight growing trend in the catalyst deposition. Moreover, while the Ar flowrate was at lower levels, the deposition of catalysts tended to be in rod-like or ring-like shapes, but when the flowrate was at higher levels, aggregation of rod-like shaped catalysts was observed. This result also confirmed the findings that the deposition weight was proportional to the carrier gas flowrate of Ar. Higher Ar carrier flowrates normally led to production of finer catalyst droplets (27), thus, enhanced the delivery rates of precursors to form thicker catalysts (28).
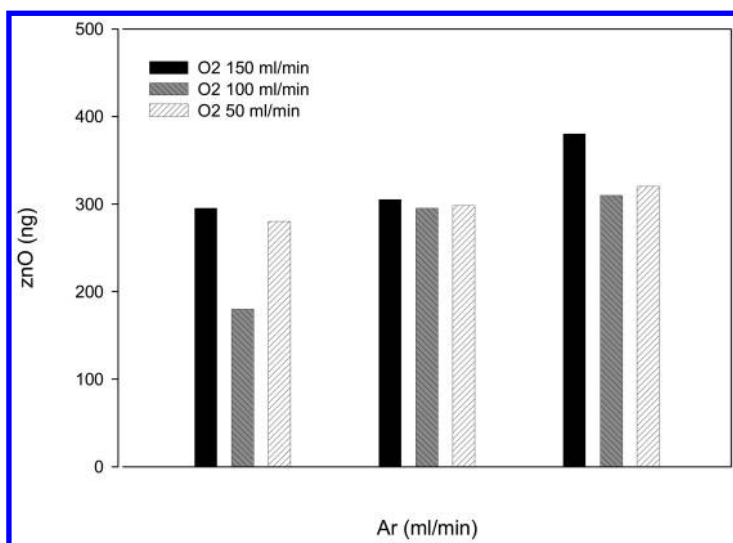
Figure 4. Correlation between carrier gas flowrates (oxygen) and plasma gas flowrates (argon) onto weight of catalyst deposits.

Photocatalysis Tests

The photocatalytic performance of the prepared ZnO catalyst arrays was investigated by a batch photocatalysis test under explosion of UV light. The photocatalysis tests were conducted using IPA as the target contaminant with an initial concentration in the vicinity of 80 ppmv. The influence of ZnO catalyst weight and morphology on the degradation of IPA was investigated.

With respect to the photocatalysis tests of IPA, in the absence of ZnO catalyst, nearly no IPA degradation was observed under direct UV irradiation. On the other hand, in the present of ZnO catalyst, significant IPA reduction occurred once UV the lamp was activated. Figure 5 reveals the linear decay of IPA via photodegradation using rod-like shaped ZnO catalyst. Linear decays were also observed for ring-like shaped and film catalysts. While most of the photocatalytic reactions were typically analyzed in terms of pseudo-first-order and first-order, this study showed zero-order reactions. As the total amount of ZnO catalyst containing in the reactor was significantly lower than that of IPA, the catalysts were easily saturated with the reactants, in which caused slow reaction rates. Moreover, IPA was reported as a potential hole scavenger that prevented the formation of hydroxyl radicals for further degradation of itself or other coexisting contaminants (*29*), which led to inhibition of the photocatalytic reaction. Therefore, the photocatalytic decomposition of IPA using ZnO catalysts was observed by zero-order kinetics.
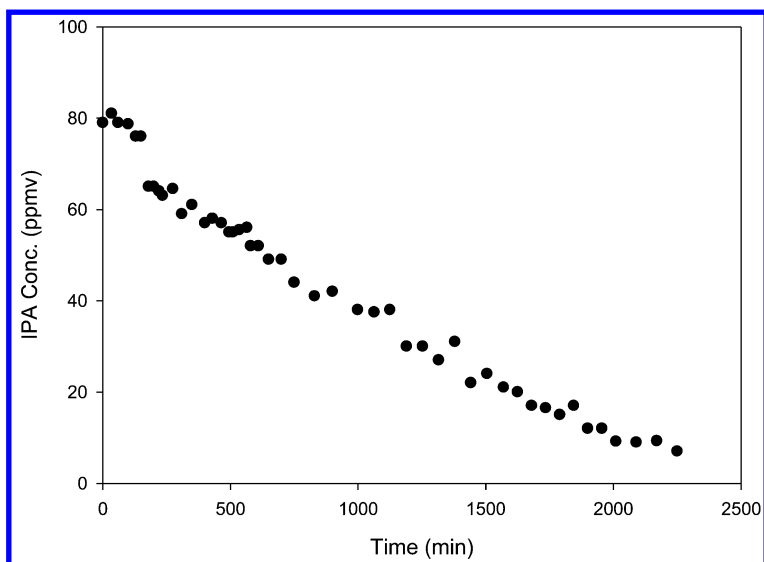
Figure 5. Photodegradability of IPA using rod-like shaped catalyst arrays (391 ng) under UV irradiation (IPA initial concentration=80 ppmv).

The effect of photocatalyst weight on the photodegradation of IPA was studied at 184 ng, 319 ng and 391 ng, while all the prepared catalysts were in rod-like structures. As shown in Table 1, a slight increase in the rate of degradation was observed with an increase in the catalyst weight. Further increase in catalyst

weight might result in decrease in the degradation rate. Excess deposition of ZnO catalysts on the AAO surface would turn its morphology into less favorable film structures, while rods and rings shapes were more favorable structures owing to their relatively higher reactive surface area for formation of hydroxyl radicals. Similar result was also found in the studies of decolorization of azo dye acid red 14 (*30*), direct yellow 12 (*29*), and Ponceau S (*31*). Increase in catalyst weight (either in terms of suspension concentration or thin film coating on a reactor) may affect the light penetration depth and charge diffusion length, which consequently decrease the rates of degradation reaction. In this study, as the catalyst morphology changed along with the changes in catalyst weights, the results of weight effects on their photocatalytic activity might vary from one catalyst morphology to another.

Table 1. Correlation of ZnO Deposition to Reaction Kinetics (Zero-Order)

ZnO deposition		*Rate constant, k*	R^2
Catalyst weight	391 ng	3.30×10^{-2}	0.972
	319 ng	3.03×10^{-2}	0.977
	184 ng	2.62×10^{-2}	0.975
Morphology	Film (521 ng)	8.70×10^{-3}	0.983
	Ring (102 ng)	9.50×10^{-3}	0.967
	Rods (378 ng)	3.70×10^{-2}	0.978

In the study of influence of catalyst morphology on the photodegradation of IPA, three types of ZnO nanostructures, including film, rod-like and ring-like shapes, were applied for the comparative study. It was obvious that the rod-like-shaped catalyst (378 ng) demonstrated the highest degradation rate, followed by ring-like-shaped (102 ng) and film-shaped catalysts (521 ng), as shown in Table 1. This could be mainly due to its relatively high reactive surface area and sufficient amount of reactants for rod-like-shaped catalyst, as the nanorods were found to be formed on top of the ring-shape arrays (see Figure 2(c)). Ring-like catalyst arrays, on the contrary, showed well-distributed deposition but only in a very small amount (Figure 2(b)), which led to decrease in reactive surface area, thus, decreased the activity of the catalysts. Dense deposition of catalyst in a film structure also contributed to decrease in reactive surface area for degradation activities. Similar results were found in literatures that textured surface and complex morphology of ZnO catalyst posted higher catalytic efficiency than as-formed ZnO composite (*19*, *32–34*).

To conclude, the results from photocatalysis tests confirmed that the photocatalyst activities for the ZnO arrays prepared in this study showed dependence on catalyst morphology and active surface area. As a nanostructured catalyst has very different physical and chemical properties from bulk materials, its catalytic activity could be enhanced from increased surface area as well as change of surface properties (*35*).

Conclusions

Fabrication of ZnO catalyst arrays on microporous AAO membranes via RF-PECVD process using DEZn as the precursor was investigated in this study. Owning to the surface energy of ZnO, its growth appeared to start from the edges of the pore openings by atomic steps, and then gradually expanded outwards and upwards, in which formed catalyst arrays in rod-like and ring-like shapes. In the study of photocatalysis tests using IPA as target pollutant under UV irradiations (365 nm), it was found that the degradation rates followed zero-order kinetics, and the rates were highly dependent on catalyst morphology. Specifically, rod-like shaped ZnO catalysts had the highest photocatalytic performance among the catalysts in other shape forms, which could be attributed to its relatively high reactive surface area.

Acknowledgments

References

1. Barnes, R.; Molina, R.; Xu, J.; Dobson, P.; Thompson, I. *J. Nanopart. Res.* **2013**, *15*, 1–11.
2. Hameed, A.; Aslam, M.; I.M.I., I.; Chandrasekaran, S.; Kadi, M. W.; Gondal, M. A. *Appl. Catal., B* **2014**, *160-161*, 227–239.
3. Velmurugan, R.; Swaminathan, M. *Sol. Energy Mater. Sol. Cells* **2011**, *95*, 942–950.
4. Muthirulan, P.; Meenakshisundararam, M.; Kannan, N. *J. Adv. Res.* **2013**, *4*, 479–484.
5. Krishnakumar, B.; Swaminathan, M. *Spectrochim. Acta, Part A* **2011**, *81*, 739–744.
6. Shakthivel, S.; Neppolian, B.; Shankar, M. V.; Arabindo, B.; Palanichamy, M.; Murugesan, V. *Sol. Energy Mater. Sol. Cells* **2003**, *77*, 65–82.
7. Hayata, K.; Gondal, M. A.; Khaled, M. M.; Ahmed, S.; Shemsi, A. M. *Appl. Catal., A* **2011**, *393*, 122–129.
8. Baruah, S.; Rafique, R. F.; Dutta, J. *Nano* **2008**, *3*, 399–407.
9. Wang, Z. L. *J. Phys.: Condens. Matter* **2004**, *16*, R828–R858.
10. Baruah, S.; Dutta, J. *Sci. Technol. Adv. Mater.* **2009**, *10*, 013001.
11. Spanhel, L. *J. Sol-Gel Sci. Technol.* **2006**, *39*, 7–24.
12. Minami, T.; Miyata, T.; Ohtani, Y. *Phys. Status Solidi A* **2007**, *204*, 3145–3151.
13. Gulino, A.; Castelli, F.; Dapporto, P.; Rossi, P.; Fragalà, I. *Chem. Mater.* **2000**, *12*, 548–554.
14. Haga, K.; Suzuki, T.; Kashiwaba, Y.; Watanabe, H.; Zhang, B. P.; Segawa, Y. *Thin Solid Films* **2003**, *433*, 131–134.

15. Kitova, S.; Kalaglarski, I.; Stoimenov, R.; Kazakov, R. *Bulg. J. Phys.* **2013**, *40*, 361–366.
16. Ito, Y.; Sakai, O.; Tachibana, K. *Thin Solid Films* **2010**, *518*, 3513–3516.
17. Panigrahi, J.; Behera, D.; Mohanty, I.; Subudhi, U.; Nayak, B. B.; Acharya, B. S. *Appl. Surf. Sci.* **2011**, *258*, 304–311.
18. Johnson, K. W.; Guruvenketa, S.; Sailera, R. A.; Ahrenkielc, S. P.; Schulz, D. L. *Thin Solid Films* **2013**, *548*, 210–219.
19. Shishodia, P. K.; Kim, H. J.; Wakahara, A.; Yoshida, A.; Shishodia, G.; Mehra, R. M. *J. Non-Cryst. Solids* **2006**, *352*, 2343–2346.
20. Minchev, M.; Kitova, S.; Danev, G. *J. Optoelectron. Adv. Mater.* **2010**, *11*, 1312–1315.
21. Yi, G.-C.; Wang, C.; W., P. *Semicond. Sci. Technol.* **2005**, *20*, S22.
22. Balcerzak, M. *Anal. Sci.* **2002**, *18*, 737–750.
23. Park, S. H.; Han, S. W. *J. Nanosci. Nanotechnol.* **2007**, *7*, 1–4.
24. Solis-Pomar, F.; Martinez, E.; Melendrez, M. F.; Perez-Tijerina, E. *Nanoscale Res. Lett.* **2011**, *6*, 524.
25. Munuera, C.; Zúñiga-Pérez, J.; Rommeluere, J. F.; Sallet, V.; Triboulet, R.; Soria, F.; Muñoz-Sanjosé, V.; Ocal, C. *J. Cryst. Growth* **2004**, *264*, 70–78.
26. Perillat-Merceroz, G.; Jouneau, P. H.; Feuillet1, G.; Thierry, R.; Rosina, M.; Ferret, P. *J. Phys.: Conf. Ser.* **2010**, *209*, 012034.
27. Lee, C. J.; Lyu, S. C.; Kim, H.-W.; Park, C.-Y.; Yang, C.-W. *Chem. Phys. Lett.* **2002**, *359*, 109–114.
28. Bekermann, D.; Gasparotto, A.; Barreca, D.; Bovo, L.; Devi, A.; Fischer, R. A.; Lebedev, O. I.; Maccato, C.; Tondello, E.; Van Tendeloo, G. *Cryst. Growth Des.* **2010**, *10*, 2011–2018.
29. Rao, A. N.; Sivasankar, B.; Sadasivam, V. *J. Mol. Catal. A: Chem.* **2009**, *306*, 77–81.
30. Daneshvar, N.; Salari, D.; Khataee, A. R. *J. Photochem. Photobiol., A* **2004**, *162*, 317–322.
31. Muslim, M.; Habib, M. A.; Mahmood, A. J.; Islam, T. S. A.; Ismail, M. I. *Int. Nano Lett.* **2012**, *2*, 30.
32. Liang, Y. Q.; Gao, Z. H.; Cui, Z. D.; Zhu, S. L.; Li, Z. Y.; Yang, X. J. *Curr. Nanosci.* **2014**, *10*, 389–393.
33. Wang, Y.; Li, X.; Lu, G.; Chen, G.; Chen, Y. *Mater. Lett.* **2008**, *62*, 2359–2362.
34. Chen, S.; Gasteiger, H. A.; Hayakama, K.; Tada, T.; Yang, S. H. *J. Electrochem. Soc.* **2010**, *157*, A82–A97.
35. Hariharan, C. *Appl. Catal., A* **2006**, *304*, 55–61.

Chapter 7

Is Surface Doping or Bulk Doping More Beneficial to the Photocatalytic Activity of TiO$_2$

Sue-min Chang*

Institute of Environmental Engineering, National Chiao Tung University, 1001 University Road, Hsinchu, 30010, Taiwan
***E-mail: chang@mail.nctu.edu.tw.**

Doping has been demonstrated to inhibit charge recombination and improve photocatalytic activity of photocatalysts. Conventional doping incorporates hetero-ions into the bulk lattice. In the presence of the defects, few charge carriers are trapped to suppress band-to-band recombination. Because most of trapped carriers annihilate with the counterparts, a low doping level is required, and the optimal doping concentration decreases with increasing particle size. Surface doping, on the other hand, only introduces dopants into the surface lattice. Surface-doped ions create an internal electric field to drive charge carriers to quickly drift to the surface. In addition, they trap the carriers and mediate charge transfer to the chemisorbed species. Compared to bulk doping, surface doping not only inhibits both bulk and surface recombination but also improves interfacial charge transfer, thus is more effective to improve photocatalytic activity.

I. Introduction

Titanium dioxide (TiO$_2$)-based photocatalysis is one of the promising green technologies for both environmental protection and energy conversion. When TiO$_2$ absorb the photons which have the energy equal to or higher than the bandgap, electron transition from the valence band to the conduction band generates electron-hole pairs. The charge carriers with suitable redox potential are able to reduce and oxidize the adsorbed species, and this behavior has

been applied to decompose organic pollutants, recover heavy-metals, produce hydrogen from water, and reduce CO_2 to generate hydrocarbons (*1–4*). The number of charge carriers determines photocatalytic activity. Figure 1 illustrates the fate of charge carriers in the photocatalysis. Effective charge carriers need to successfully diffuse from the bulk to the surface, and subsequently transfer to the adsorbed species to induce surface reactions. However, recombination generally consumes numerous carriers, thus causing low photocatalytic activity. Charge recombination is controlled by the microstructures and chemical compositions of photocatalysts. To maintain a high level of charge carriers for efficient photocatalysis, many efforts have been devoted to modify the microstructures of photocatalysts with selected hetero-elements (*5, 6*).

Doping is the common strategy used to improve the photocatalytic activity. Through introducing impurities into the TiO_2 matrix, lattice defects are created and the corresponding energy states result in the band structure. When charge carriers diffuse by the imperfection sites, few of them are trapped by the defects and separated from the TiO_2 matrix. Charge trapping either reduces the carrier density in the TiO_2 matrix or leads to the diffusion-time difference between the carriers, thus inhibiting charge recombination (*5, 7*). Conventional doping incorporates hetero-ions substitutionally or interstitially into the bulk lattice by sol-gel, hydrothermal, co-precipitation, vapor deposition, or sputtering methods (*8–12*). Many cations and anions (C, N, B, and F) have been incorporated into the TiO_2 matrix to enhance photocatalytic activity (*13–19*). Due to the presence of impurity states in the band structure, doping also narrows the bandgap of TiO_2 materials and enables the photocatalysts to be visible-light-driven (*20, 21*). Although the advantages of doping on photocatalytic activity have been extensively demonstrated, many studies still found the adverse effect (*22, 23*). The controversy mainly arises from varies conditions, including the types of dopants, doping levels, and the sizes of TiO_2 particles, in different systems.

In addition to bulk doping, an alternative doping strategy, namely surface doping, was developed recently. Instead of dispersing dopants throughout the entire matrix, surface doping introduces hetero-ions only into the surface lattice (*16*). The surface-doped ions play the key role in the kinetics of interfacial charge transfer. They are able to interact with both charge carriers and reactants to mediate charge transfer. The alternative pathways provided by surface-doped ions for the charge transfer not only inhibit surface recombination but also promote charge transfer efficiency. Improved photocatalytic activity by surface doping has been demonstrated (*6, 16, 24, 25*). To design advanced photocatalysts for efficient reactions, the relative influences of different doping modes on the photocatalytic activity raises great interests.

In this article, the doping effects on the photocatalytic performance are re-examined according to the types and concentrations of dopants. Moreover, the contributions of bulk and surface doping to the photocatalytic activity are comprehensively reviewed, and their roles in the photocatalytic behavior are discussed. An optimal doping mode is suggested in the end of this article based on the capability in inhibition of recombination and promotion of interfacial charge transfer. Surface doping exhibits superiority in both aspects, thus is more beneficial than bulk doping to improve photocatalytic activity.
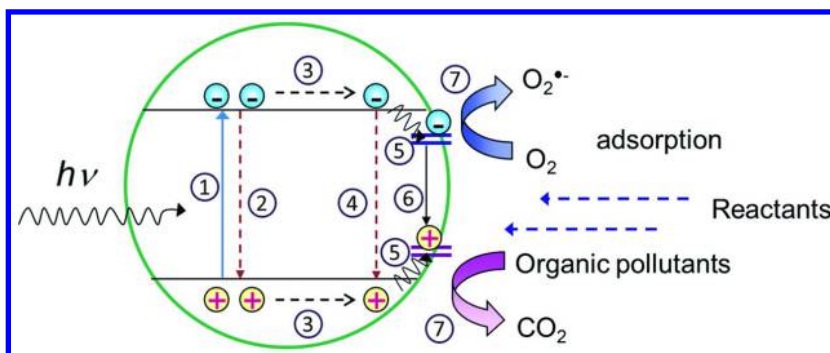
Figure 1. The fate of charge carriers in the photocatalysis. 1. Charge generation, 2. Band-to-band recombination taking place immediately after charge generation, 3. Charge migration from the bulk to the sirface, 4. Recombination when the carriers migrate to the surface, 5. Charge trapping by surface defects, 6. Mediated recombination, 7. Interfacial charge transfer to the adsorbed species.

II. The Effects of Dopants on the Photocatalytic Activity

From energy point of view, electrons automatically transfer from a high energy state to a low energy state. Such relaxation leads electrons and holes to be trapped by the states with the potential lower than the conduction band and higher than the valence band, and followed by recombination with their counterparts. The kinetics of relaxation and recombination correlates to the energy difference between the bands and the localized states. Therefore, the potential of doping states in the doped TiO_2 photocatalysts determines the photocatalytic activity. Figure 2 shows the interactions of bulk-doped ions with charge carriers. Due to the interaction with the orbitals of the Ti^{4+} and O^{2-} ions, the doped ions with different electronic configurations position differently in the band structure. Through investigating the roles of 21 types of dopants in the photocatalytic activity of quantum sized TiO_2 colloids, Choi et al. (5) found that doping with Fe^{3+}, Mo^{5+}, Ru^{3+}, Os^{3+}, Re^{5+}, V^{4+}, and Rh^{3+} ions enhanced the activity, whereas the Co^{3+} and Al^{3+} ions decreased the activity. The ions with the energy states in the bands or close to the bands are beneficial to the activity because they shallowly trap charge carriers to inhibit band-to-band recombination and then again release the carriers by thermal excitation. On the other hand, the ions, which only can trap one type of charge carriers, are detrimental to the activity because they quickly mediate the trapped carriers to recombine with the counterparts. The ions with closed-shell electronic configurations are unfavorable to charge trapping, thus are ineffective to the activity. Chang and Liu (26) reported that doping TiO_2 particles with $Fe^{2+/3+}$, $Cu^{+/2+}$ and $V^{3+/4+}$ ions improved the photocatalytic activity, whereas $Mn^{3+/4+}$, Ce^{2+}, and W^{6+} ions caused negative effects. Their findings agree with the

deduction given by Choi et al. (*5*) that the ions with the energy states in the bands or close to the bands contribute to high photocatalytic activity. Moreover, they indicated that suitable dopants have d-d transitions in the irradiation spectrum or multiple unoccupied/occupied states in the band gap. In contrast, unsuitable dopants introduce both occupied and unoccupied states in the mid-band-gap region. Such dopants simultaneously trap both electrons and holes and then promptly mediate recombination through intra-atomic relaxation, thus are highly capable of consuming charge carriers to cause low photocatalytic activity. Although improved photocatalytic activity by doping has been demonstrated, Nagaventi et al. (*22*) found that, irrespective of types of dopants, doped TiO_2 photocatalysts exhibited lower activity than un-doped powders. According to the decreased intensity in the photoluminescence, they considered that the substituted ions in the bulk lattice act as recombination centers, and inhibited photocatalytic activity is the only consequence of doping.

The discrepancy in the doping effects mainly arises from different doping levels. Dopants improve photocatalytic activity only when their concentration is low. In fact, de-trapping of deeply trapped carriers is inefficient, and most of the carries recombine with the counterparts at the trapping sites. Due to a high density of charge carriers in the bands causes significant band-to-band recombination, slight sacrifice of charge carriers retards the recombination and allows more carriers to successfully reach the surface for surface reactions. The optimal doping concentration is generally in the range of 0.05-1.0 at.% (*27*). When the concentration is higher than the optimal value, tunneling recombination between the close trapping sites together with tremendous mediated recombination in turn reduce the photocatalytic activity (*5*). The optimal concentration is particle-size dependent. Zhang et al. (*7*) reported that the optimal Fe^{3+} loading was 0.2 at.% for the TiO_2 particles with 6 nm, and it decreased to 0.05 at.% when the size increased to 11 nm. A model calculation developed by Bohl et al. (*27*) showed an inverse linearity between the optimal doping concentration and the particle size. Charge carriers in large particles need to diffuse a long distance to the surface, thus having a higher probability to meet dopants and be trapped. To reduce the trapping-mediated recombination, a low doping level is required for a large particle.

Regardless of doping, substantial amounts of intrinsic defects, including Ti^{3+} ions and oxygen vacancies, are introduced into the TiO_2 lattice as they are prepared (*28*). These intrinsic defects behave like dopants and also can reduce charge recombination to enhance photocatalytic activity (*1*). When charge carriers successfully escape from bulk recombination and reach the surface, interfacial transfer to the adsorbed species becomes the determining step and the influence of surface doping on the photocatalytic activity turns more dominate. It is reported that surface recombination is responsible for the low photocatalytic activity of TiO_2 particles when their size is smaller than 11-15 nm (*7, 26*). In the presence of dopants within the lattice of the TiO_2 nanocrystals enhanced the photocatalytic activity and the role of the dopants in the improved activity is mainly to prevent charge recombination at the surface (*7*). These findings seem to point out that the hetero-ions staying within the surface lattice are more influential than staying homogeneously in the bulk lattice in promoting photocatalytic activity.
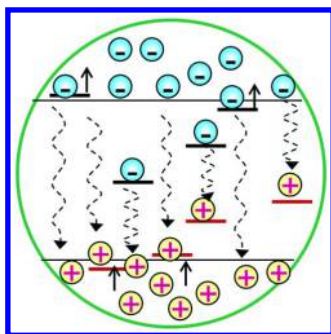
Figure 2. The inteactions of bulk-doped ions with charge carriers. Curved and straight lines represent electronic relaxation and thermal induced excitation, respectively. After charge tapping, further relaxation leads the trapped carriers to annihilate with their counterparts. The shallowly trapped carriers could de-trap to escape from recombination through thermal excitation.

III. Photocatalytic Activity of Surface-Doped TiO₂ Photocatalysts

While the photocatalytic behavior of bulk-doped photocatalysts has been extensively studied, the effects of surface doping on the photocatalytic activity just raise attention. It is generally takes two steps to dope impurities into the surface lattice. The first step involves the preparation of un-doped TiO_2 powders/films, and then the un-doped samples are coated with a doped film or impregnating into the solution containing dopants (*6, 16, 24, 29*). To incorporate Co^{3+} ions into the surface lattice of a TiO_2 film, Zhao et al. (*24*) conducted the Co^{3+} ions to the TiO_2 surface by an impregnation method, and then calcined the sample to trigger the adsorbed Co^{3+} ions to diffuse into the surface lattice (< 100 nm). The surface-doped film exhibited 1.5-times higher photocatalytic activity than the un-doped sample for decoloration of acid naphthol red in the solution. Reduced intensity in the photoluminescence of the surface-doped film indicates that the Co^{3+} ions inhibited charge recombination. Li et al. (*29*) doped S ions into the 50-nm surface layer of a TiO_2 film through the similar processes, and found that the surface-S-doped film exhibited 2.2-times higher activity than the un-doped film. Chang and Liu (*6, 16*) directly loaded a doped thin film onto as-prepared TiO_2 powders using a sol-gel method, and then crystallized the composite by calcination. The metal ions, including $Fe^{2+/3+}$, $Cu^{+/2+}$ and $V^{3+/4+}$ ions, were demonstrated to successfully improve the photocatalytic activity at least by two times.

Based on the different reactivity of the precursors in a non-hydrolytic sol-gel reaction, Chang and Doong (*3*) specifically incorporated Zr^{4+} ions into several surface atomic layers of TiO_2 nanocrystals in one step. Because Ti-precursors underwent faster cross condensation than the Zr-precursors, TiO_2 cores were generated in advance, followed by the growth of Zr-doped-TiO_2 layers on the surface. The photocatalytic activity of the TiO_2 nanocrystals was

remarkably improved by 10 times in the presence of the surface-doped Zr^{4+} ions. Tri-octyl-phosphine oxide (TOPO), which was used as the capping agent in the non-hydrolytic sol-gel process, chemically bonded to the nanocrystals. In the following study, Chang et al. (*30*) calcined the TOPO-capped nanocrystals in the ambient air to burn out the organic moiety of the TOPO and incorporated the P ions into the surface lattice. After calcination at 550°C, the P-doped TiO_2 particles were less photocatalytic active than the pure TiO_2 powders, while the P-Zr-co-doped TiO_2 sample exhibited higher activity. The detrimental effect of the doped P^{5+} ions is due to their unoccupied levels, which position close to the valence band, are highly capable of mediating charge recombination (*31*, *32*). The doped Zr^{4+} ions introduced unoccupied states in the conduction band. In the presence of the co-dopant, charge carriers can be trapped at different sites to reduce recombination, thus improving the photocatalytic activity. When calcination temperature increased to 950°C, thermal energy was high enough to fuse the nanocrystals and drove the P^{5+} and Zr^{4+} ions to segregate from the boundary to the surface of the fused crystals. Due to a slight solubility of Zr^{4+} ions in the TiO_2 matrix, few amounts of the doped Zr^{4+} ions were remained in the bulk lattice of the fused crystals. The P-doped TiO_2 powders exhibited the highest activity, followed by the P-Zr-co-doped TiO_2 and the pure TiO_2 powders in order. Polyphosphate species, oxygen vacancies, and dehydroxylated surface contribute to the high activity of the P-doped TiO_2 sample. On the other hand, the Zr^{4+} ions left in the bulk lattice result in the reduced activity of the P-Zr-co-doped TiO_2 sample.

IV. The Roles of Surface-Doped Ions in the Photocatalytic Activity

The hetero-ions doped in the surface lattice play multiple roles in the photocatalytic activity. Figure 3 illustrates the roles of surface-doped ions in the photocatalysis. Surface doped ions introduce surface states into the doped photocatalysts which lead to a potential difference relative to the bands. The internal electric field propels charge carries to migrate quickly from the bulk to the surface. The promoted migration kinetics reduces bulk recombination. Similar behavior was found in the doped and un-doped TiO_2 composites. Liu et al. (*33*, *34*) reported that the internal electric field between the un-doped and the doped TiO_2 colloids effectively separated charge carriers to inhibit recombination. As the result, the un-evenly doped composite performed higher photocatalytic activity than the evenly doped and un-doped particles. When tremendous amounts of charge carriers reach the surface, charge trapping by the surface-doped ions suppresses the charge recombination. Through determination of surface-trapped holes by EPR, Chang's group reported that the quantity of the trapped carriers was greatly preserved in the presence of $V^{3+/4+/5+}$, Zr^{4+}, and P^{5+} ions within the surface lattice (*16*, *30*, *31*). Surface-doped ions with appropriate electronic states in the band structure can stabilize carriers before they participate in surface reactions. From a model simulation for the kinetics of charge relaxation in the surface-Ru-doped TiO_2 rods, Inerbaev et al. (*35*) revealed that the electron

relaxation from the conduction band to the Ru states is faster than the hole relaxation to the same site. The different relaxation rates retard the Ru-mediated recombination and improve the photocatalytic activity. In addition, $Fe^{2+/3+}$, $V^{3+/4+}$, Cu^+, Sn^{2+} and W^{6+} ions, which introduce energy states close to or in the bands, multiple occupied/un-occupied states in the band gap, or d-d transition in the irradiation spectra, also have been demonstrated to mediate recombination slowly (*6, 36*). Unlike the trapped carriers within the bulk lattice, the trapped carriers by the surface-doped ions still have chance to transfer to the adsorbed species through bonding or tunneling. Moreover, surface doping creates acidic sites and oxygen vacancies which allow chemisorption of reactants to facilitate the charge transfer (*37–40*). The mediated transfer via the surface-doped ions provides alternative pathways to conduct the carriers into the surface reactions, thus greatly improving the charge utilization as well as photocatalytic activity.

Depending on the types and concentrations of the dopants in the surface lattice, mediated recombination in some cases competes with interfacial transfer to reduce photocatalytic activity. The detrimental effects of $Mn^{3+/4+}$ ions on the photocatalytic activity of surface-doped TiO_2 particles have been demonstrated (*6*). The doped $Mn^{3+/4+}$ ions are able to trap both electrons and holes to induce annihilation through intra-atomic relaxation. The relaxation is too fast to allow the trapped carriers to undergo interfacial transfer, thus consuming a lot of the carriers to cause the low activity. An appropriate amount of dopants is also essential for improved activity. Over doping promotes tunneling-induced recombination, and inhibit photocatalytic activity as the consequence. The optimal surface Fe/Ti ratio of 0.67 was reported for the highest photocatalytic activity of Fe-surface-doped TiO_2 particles (*6*). Because surface-doped ions involve in the interfacial charge transfer, the optimal doping level for surface-doped photocatalysts is much higher than that (0.05-1.0 at.%) for bulk-doped ones.
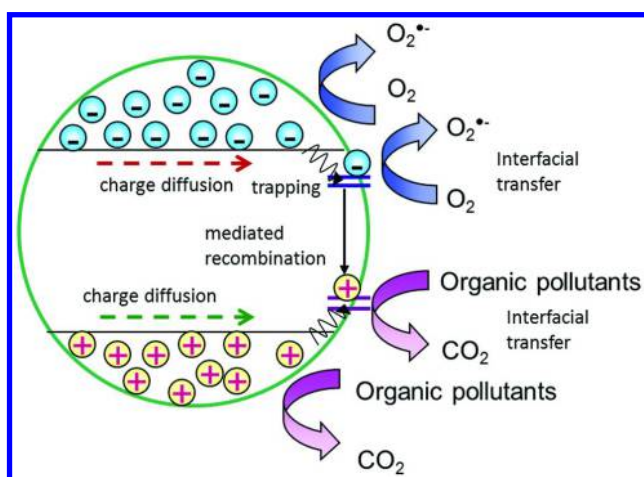
Figure 3. The roles of surface-doped ions in the photocatalysis. Surface-doped ions drive charge carriers to migrate to the surface, and trap the carriers to mediate interfacial charge transfer. Mediated recombination after trapping competes with interfacial charge transfer to determine the photocatalytic activity.

Adequate surface acidity also plays a crucial role in photocatalytic performance. Although surface acidity facilitates the charge transfer from the doped ions to the chemisorbed reactants, over strong acidity in turn causes an adverse effect. The doped Ce^{2+} and W^{6+} ions, which have high coordination numbers and electronegativity, were found to reduce the photocatalytic performance of the surface-doped powders (*6*). The two types of ions tightly bonded the O_2^- species to confine the electrons between them and the O_2 molecules when the O_2 molecules received the elelctrons from the TiO_2 surface. The charge confinement at the surface greatly limits the following charge transfer, and is the cause of deactivation.
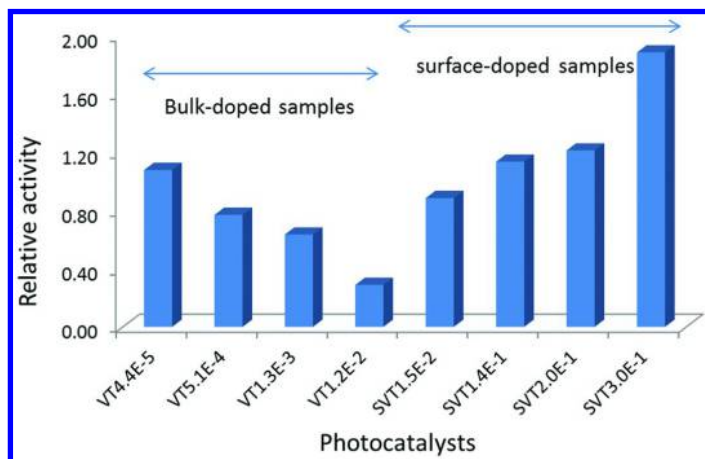
Figure 4. The relative photocatalytic activity of the TiO₂ powders in the presence of V ions within the bulk or surface lattice. The relative activity is defined as the ratio between the activity of the doped sample and that of the un-doped sample. The VT and SVT represent the bulk- and surface-doped samples, respectively, and the numbers behind the VT and SVT indicate the bulk and surface V/Ti ratios, respectively.

V. Comparisons on the Photocatalytic Activity of Surface- And Bulk-Doped TiO₂ Photocatalysts

Chang and Liu selected V ions as the dopant to systematically examine the influence of surface- and bulk-doping on the photocatalytic activity of TiO_2 powders (*16*). Figure 4 shows the effects of surface- and bulk-doped V ions on the enhancement and reduction of the photocatalytic activity. The bulk-doped V ions slightly enhanced the photocatalytic activity at a V/Ti ratio of 4.4×10^{-5}, and the activity dropped dramatically with the increasing concentration. In contrast, the surface-doped V ions significantly improved the activity by 2 times when the surface V/Ti ratio rose to 3.0×10^{-1}. Ould-Chikh et al. (*25*) reported that though both bulk- and surface-doped Cr^{3+} ions caused the deactivation of TiO_2 particles under UV irradiation, bulk-doping reduced the activity to a higher

extent than surface-doping did. On the other hand, the Cr^{3+} ions in both the doping modes enhanced the photocatalytic activity in the visible-light region, and surface-doping was more effective than bulk-doping to improve the activity. An EPR measurement clearly indicated that a higher quantity of surface-trapped holes was preserved in the surface-doped samples, whereas charge carriers were severely exhausted in the bulk-doped powders because most of trapped carriers were unable to escape from the trapping sites and eventually underwent annihilation within the bulk lattice. Li et al. (*29*) measured the photoluminescence of S-surface-doped and bulk-doped TiO_2 films and found that surface-doping resulted in a lower intensity than bulk doping did. This phenomenon reveals that surface doping suppresses band-to-band recombination as the result of fast charge migration triggered by an internal electric field. Compared to bulk doping, surface doping inhibits charge recombination and promotes interfacial charge transfer, thus is more effective to improve photocatalytic activity.

VI. Conclusion

Surface doping is more beneficial than bulk doping to improve photocatalytic activity because it preserves a higher degree of charge carriers and promotes charge utilization. By building an internal electric field, surface-doped ions drive charge carriers to quickly drift to the surface and prevent bulk recombination. In addition, they trap the carriers and mediate charge transfer to the chemisorbed species. The alternative pathways provided by the doped ions greatly inhibit surface recombination and facilitate the interfacial charge transfer, thus allowing more carriers to participate in the surface reactions. In contrast, bulk doping mediates recombination severely to cause low photocatalytic activity except when trace amounts of dopants are present. The types of dopants, doing levels, and doping thicknesses determine the photocatalytic activity of surface-doped photocatalysts. Studies with respect to the influence of these factors on the photocatalytic behavior are still few, and need more efforts to clarify their relationships insightfully.

Acknowledgments

References

1. Liu, L. J.; Zhao, H. L.; Andino, J. M.; Li, Y. *ACS Catal.* **2012**, *2* (8), 1817–1828.
2. Ni, M.; Leung, M. K. H.; Leung, D. Y. C.; Sumathy, K. *Renewable Sustainable Energy Rev.* **2007**, *11* (3), 401–425.
3. Chang, S. M.; Doong, R. A. *J. Phys. Chem. B* **2006**, *110* (42), 20808–20814.
4. Chen, H.; Shao, Y.; Xu, Z. Y.; Wan, H. Q.; Wan, Y. Q.; Zheng, S. R.; Zhu, D. Q. *Appl. Catal., B.* **2011**, *105* (3-4), 255–262.

5. Choi, W. Y.; Termin, A.; Hoffmann, M. R. *J. Phys. Chem.* **1994**, *98* (51), 13669–13679.

6. Chang, S. M.; Liu, W. S. *Appl. Catal., B* **2014**, *156*, 466–475.

7. Zhang, Z. B.; Wang, C. C.; Zakaria, R.; Ying, J. Y. *J. Phys. Chem. B* **1998**, *102* (52), 10871–10878.

8. Xu, A. W.; Gao, Y.; Liu, H. Q. *J. Catal.* **2002**, *207* (2), 151–157.

9. Zhu, J. F.; Deng, Z. G.; Chen, F.; Zhang, J. L.; Chen, H. J.; Anpo, M.; Huang, J. Z.; Zhang, L. Z. *Appl. Catal., B* **2006**, *62* (3-4), 329–335.

10. Parida, K. M.; Naik, B. *J. Colloid Interface Sci.* **2009**, *333* (1), 269–276.

11. Matsuoka, M.; Kitano, M.; Takeuchi, M.; Tsujimaru, K.; Anpo, M.; Thomas, J. M. *Catal. Today* **2007**, *122* (1-2), 51–61.

12. Dunnill, C. W. H.; Aiken, Z. A.; Pratten, J.; Wilson, M.; Morgan, D. J.; Parkin, I. P. *J. Photochem. Photobiol., A* **2009**, *207* (2-3), 244–253.

13. Adan, C.; Bahamonde, A.; Fernandez-Garcia, M.; Martinez-Arias, A. *Appl. Catal., B* **2007**, *72* (1-2), 11–17.

14. Colon, G.; Maicu, M.; Hidalgo, M. C.; Navio, J. A. *Appl. Catal., B* **2006**, *67* (1-2), 41–51.

15. Lukac, J.; Klementova, M.; Bezdicka, P.; Bakardjieva, S.; Subrt, J.; Szatmary, L.; Bastl, Z.; Jirkovsky, J. *Appl. Catal., B* **2007**, *74* (1-2), 83–91.

16. Chang, S. M.; Liu, W. S. *Appl. Catal., B* **2011**, *101* (3-4), 333–342.

17. Wang, H.; Lewis, J. P. *J. Phys.: Condens. Mater.* **2006**, *18* (2), 421–434.

18. Deng, L. X.; Chen, Y. L.; Yao, M. Y.; Wang, S. R.; Zhu, B. L.; Huang, W. P.; Zhang, S. M. *J. Sol-Gel Sci. Technol.* **2010**, *53* (3), 535–541.

19. Yu, J. C.; Yu, J. G.; Ho, W. K.; Jiang, Z. T.; Zhang, L. Z. *Chem. Mater.* **2002**, *14* (9), 3808–3816.

20. Chen, X. B.; Burda, C. *J. Am. Chem. Soc.* **2008**, *130* (15), 5018–5019.

21. Sathish, M.; Viswanathan, B.; Viswanath, R. P.; Gopinath, C. S. *Chem. Mater.* **2005**, *17* (25), 6349–6353.

22. Nagaveni, K.; Hegde, M. S.; Madras, G. *J. Phys. Chem. B* **2004**, *108* (52), 20204–20212.

23. Irie, H.; Watanabe, Y.; Hashimoto, K. *J. Phys. Chem. B* **2003**, *107* (23), 5483–5486.

24. Zhao, N.; Yao, Y.; Feng, J. J.; Yao, M. M.; Li, F. *Water Air Soil Pollut.* **2012**, *223* (9), 5855–5864.

25. Ould-Chikh, S.; Proux, O.; Afanasiev, P.; Khrouz, L.; Hedhili, M. N.; Anjum, D. H.; Harb, M.; Geantet, C.; Basset, J. M.; Puzenat, E. *ChemSusChem* **2014**, *7* (5), 1361–1371.

26. Baiju, K. V.; Shukla, S.; Sandhya, K. S.; James, J.; Warrier, K. G. K. *J. Phys. Chem. C* **2007**, *111* (21), 7612–7622.

27. Bloh, J. Z.; Dillert, R.; Bahnemann, D. W. *J. Phys. Chem. C* **2012**, *116* (48), 25558–25562.

28. Santara, B.; Giri, P. K.; Imakita, K.; Fujii, M. *Nanoscale* **2013**, *5* (12), 5476–5488.

29. Li, F.; Zhao, N.; Guan, L. X.; Feng, J. J.; Yao, M. M. *Water Air Soil Pollut.* **2013**, *224* (5).

30. Chang, S. M.; Hou, C. Y.; Lo, P. H.; Chang, C. T. *Appl. Catal., B* **2009**, *90* (1-2), 233–241.

31. Chang, S. M.; Lo, P. H.; Chang, C. T. *Appl. Catal., B* **2009**, *91* (3-4), 619–627.
32. Yang, K. S.; Dai, Y.; Huang, B. B. *J. Phys. Chem. C* **2007**, *111* (51), 18985–18994.
33. Liu, S.; Chen, Y. S. *Catal. Commun.* **2009**, *10* (6), 894–899.
34. Liu, S.; Xie, T. H.; Chen, Z.; Wu, J. T. *Appl. Surf. Sci.* **2009**, *255* (20), 8587–8592.
35. Inerbaev, T. M.; Hoefelmeyer, J. D.; Kilin, D. S. *J. Phys. Chem. C* **2013**, *117* (19), 9673–9692.
36. Oropeza, F. E.; Mei, B.; Sinev, I.; Becerikli, A. E.; Muhler, M.; Strunk, J. *Appl. Catal., B* **2013**, *140*, 51–59.
37. Schaub, R.; Thostrup, P.; Lopez, N.; Laegsgaard, E.; Stensgaard, I.; Norskov, J. K.; Besenbacher, F. *Phys. Rev. Lett.* **2001**, *87* (26), 266104.
38. Linsebigler, A. L.; Lu, G. Q.; Yates, J. T. *Chem. Rev.* **1995**, *95* (3), 735–758.
39. Liu, L. J.; Li, Y. *Aerosol Air Qual. Res.* **2014**, *14* (2), 453–469.
40. Thompson, T. L.; Yates, J. T. *Top. Catal.* **2005**, *35* (3-4), 197–210.

Chapter 8

Fabrication of Titanium Dioxide Nanotube Array as a Photocathode for Hydrogen Evolution

Huang-ru Liao and Ruey-an Doong[*]

Department of Biomedical Engineering and Environmental Sciences, National Tsing Hua University, Hsinchu, 30013, Taiwan
[*]E-mail: radoong@mx.nthu.edu.tw.

In this study, we present an effective method to fabricate TiO_2-based photocathode for hydrogen production. The Pt/TiO_2 composites were synthesized by using TiO_2 nanotube arrays (TNTAs) as a support. The TNTAs were electrochemically fabricated using 20×18 mm^2 titanium foils as the anode. Pt ions were loaded onto the TNTAs to form Pt/TiO_2 nanocomposites for the enhancement of photoelectron-chemical performance of water splitting. The highly oriented and ordered TNTAs at about 100 nm in diameter and 17 μm in length was obtained after 8 h of anodization. The TEM images showed that Pt nanoparticles were well-dispersed on the surface of TNTAs with diameters of 1.5-5 nm. In addition, TiO_2 and Pt/TiO_2 nanotube arrays were used for photoelectrochemical water splitting in 0.5 M Na_2SO_4 electrolyte under UV light irradiation at 10 mW/cm^2. The photocurrent density at a overpotential of -0.65 V vs. Ag/AgCl (-0.1 V vs. RHE) by Pt/TiO_2 composite was higher than the pure TiO_2 nanotube arrays electrode. In addition, the overpotential of TNTAs in the presence of UV light was 0.1 V lower but and the hydrogen production was 1.3 times higher than that in dark. The hydrogen generation by TNTAs and Pt/TNTAs at -0.85V vs. Ag/AgCl under UV light irradiation was 1.9 and 15.5 times higher than that in dark.

Results obtained in this study clearly show that the Pt/TNTA photocathode with optimal operational conditions could lead to the enhanced photoelectrochemical performance for H_2 gas generation from water.

Introduction

Photoelectrohcemical splitting of water to produce hydrogen and oxygen in the presence of semiconductors and UV light has been developed for more than 40 years. Since then, many semiconductor materials have been investigated for hydrogen generation under different environmental conditions and semiconductors. Several studies have depicted that the use of semiconductor materials such as Si (*1–6*), Cu_2O (*7*), $CaFe_2O_4$ (*8*), $CuIn_xGa_ySe_2$(CIGS) (*9*) and GaP (*10*) have been demonstrated to have a good photocatalytic activity toward water splitting. However, most of these materials have the problems of photo-corrosion, poor stability, shorter absorption wavelength, high cost, and need of external bias. Among the semiconductors used, titanium dioxide (TiO_2) is one of the attractive semiconductor materials because of its cost, good stability, non-toxic, and suitable band gap of 3.0-3.2 eV.

Polymorphic TiO_2 including anatase, rutile, and brookite phases are among the most interesting nanostructures for a wide variety of applications in energy and environmental fields including pigments, photocatalysts, catalyst supports, sensors, and dye-sensitized solar cells because of their unique photo-induced electron transfer efficiency, high chemical stability, nontoxicity, and electrical conductivity. More recently, the fabrication of one-dimensional TiO_2 nanotube structures for a wide variety of applications has received much attention. The unique properties of TiO_2 nanotube array (TNTA) with large surface area and tunable morphology has been used as the active materials for dye sensitized solar cells (*11*), antibacterial agents (*12*), hydrogen sensing (*13*), photocatalyst (*14–16*), and photoelectrochemical water photolysis (*17, 18*). In addition, the fabrication of TNTAs using electrochemical processes have been demonstrated to be an effective photoelectrode for photoelectrochemical water splitting with markedly improved efficiency (*19*). The nanotube structure creates a higher surface area compared with other materials, leading to the increase in efficient absorption by scattering the path length of incident photons (*20*). In addition, the nanotubural morphology is associated with a decrease in bulk recombination. Due to the thin walls and small diameters of TNTAs, mobile charge carriers are generated in close proximity to the surface where electrons or holes can be captured within surface bonds (*21*). However, electron-hole recombination also increases with the increase in length of TiO_2 nanotubes (*22*). Therefore, the optimization of TNTAs is required to obtain the better absorption efficiency and good electrochemical performance on water splitting.

Although the TiO_2 has good photocatalytic activity toward water splitting, the production rate of H_2 is usually low. The transition metal modified TiO_2 nanotube arrays have been demonstrated to significantly enhance photoelectrochemical

activity of hydrogen generation (*19, 23*). Usually metals with Fermi level lower than that of TiO_2 can rapidly transfer photoexcited electrons from TiO_2 to metal particles, and, therefore, reduce the possibility of electron-hole recombination and lead to efficient charge separation (*23*). Ye et al. (*24*) have used hydrothermal method to prepared Pd/TNTAs for water splitting, and found that the photoelectric conversion efficiency was nearly 100% at 330 nm. The evolution rate of H_2 gas also increased to 492 μmol h^{-1} cm^{-2}. In addition to Pd, platinum metal (Pt) is an active catalyst material for hydrogen generation. The deposition of Pt nanoparticles on TiO_2 surface could lead to the efficient reaction with proton to provide hydrogen evolution and enhance photoelectrochemical performance on water splitting. However, the electrochemical performance of Pt/TNTAs as the photocathode remains unclear and the production of H_2 gas from water splitting by Pt/TNTAs has received less attention.

In this study, the pure TNTAs as well as Pt-modified (Pt/TNTAs) were fabricated to serve as the photocathodes for photochemical hydrogen evolution from water. TNTAs were fabricated by using anodiztion method and the Pt ions were added to reductively formation of Pt/TNTAs nnocomposition. The morphology and crystllinitiy of Pt/TNTAs were characterized by scanning/transmission electron microscopy and X-ray diffractometry, respectively. In addition, the photoelectrochemical performance of TNTAs and Pt/TNTAs for H_2 production from water splitting were examined.

Materials and Methods

Chemicals

Ammonium floride (NH_4F, 99.9 %), ethylene glycol ($C_2H_6O_2$, > 99 %), 2-propanol (C_3H_8O, 99.9 %), and anhydrous methanol were purchased from J. T. Becker. Dihydrogen hexachloroplatinate (IV) hexahydrate ($H_2PtCl_6 \cdot 6H_2O$, 99.95 %), titanium foil (0.25 mm, 99.5%), and platium wire (0.25 mm, 99.9%) were obtained from Alfa Aesar. Sodium borohydride ($NaBH_4$, > 98 %) was purchased from Fluka. All other chemicals were of analytical grade and were used without further purification. In addition, all the solutions were prepared by deionized distilled water (Millipore,18.3 mΩ cm) unless otherwise mentioned.

Fabrication of TiO_2 Nanotube Arrays by Anodic Oxidation

Titanium foils were subjected to potentiostatic anodization in a two-electrode electrochemical cell with a Ti foils and platinum wire as the anode and cathode, respectively. The Ti foils were cut into pieces at 20×18 mm² before anodization, and then the Ti foils were washed with ethanol, isopropanol and methanol sonically sequentially for 15 min to remove impurities on the surface of Ti foils. After rising with deionized distilled water and drying in air, the Ti foils were immersed in ethylene glycol electrolytes containing 0.26 wt% NH_4F and 3 % deionized distilled water and started to anodic oxidation at 55 V for 2, 8, 14 16, and 20 h. After

anodization, the Ti foils were soaked in anhydrous methanol by ultrasonic for 10 min to remove nanofibrous debris on the surface of Ti foils and then further calcined at different temperatures (400, 500, 600, 700, and 800 °C) in air for 4 h.

Fabrication of Pt/TNTAs

The Pt/TNTAs nanocomposites were fabricated using photoelectrochemical reduction method. The TNTAs was first immersed in 27 mL of solution consisting of 0.5 mL of 1000 mg/L Pt standard solution, 1.5 mL of ethanol (99.8 %) and 25 mL of deionized distilled water. After puring with nitrogen gas for 30 min, The mixture was illuminated by 8×8 W UV light at 365 nm for 1 h in N_2, and then was dried in oven at 100 °C

Characterization of TNTAs and Pt/TNTAs

The crystalline structure of TNTAs and Pt/TNTAs were obtained using an X-ray diffractometer (XRD, Bruker NEW D8 ADVANCE, Germany) with Ni-filtered Cu Kα radiation ($\lambda = 1.5406$ Å) and operated at an accelerating voltage and an emission current of 40 kV and 40 mA, respectively. The X-ray diffraction patterns were acquired over the 2θ range from 20° to 90° at a sampling width of 0.05°. The average crystallite size was estimated by the Scherrer equation, d = $0.89\lambda/(B_{cos}\theta_B)$, where d is the average crystallite size; B is the full-width at half maximum (FWHM) of the peak; λ is the wavelength of Cu Kα irradiation source; and θ_B is a Bragg's angle of $2\theta/2$.

The morphology and particle size of the Pt/TNTAs were examined by transmission electron microscope (TEM, JEOL 2010) operating at 200 kV. The Pt/TNTAs were suspended in ethanol before the immersion of a holey carbon support film on a copper grid. The surface morphology of the TNTAs was examined by field-emission scanning electron microscope (FE-SEM, JEOL, JSM-6330F). The vapor evaporative deposition of a thin Au coating film was provided by anodic deposition onto the surface to improve surface charge dissipation and optical resolution. In addition, the optical property of TNTAs and Pt/TNTAs were measured by a Hitachi U-3010 UV–Vis spectrophotometer using a 1-cm path length quartz cuvette over the wavelength range from 200 to 700 nm.

Photoelectrochemical Test

The photoelectrochemical measurements were performed in a three-electrode cell in the presence of 0.5 M Na_2SO_4 as the electrolytes. Platinum foil and Ag/AgCl were used as the counter and reference electrodes, respectively. The electrolyte was first purged with argon for 30 min to remove O_2 in solutions prior to the experiment. A 400 W Hg lamp with the light intensity of 10 mW/cm^2 was used as the light source. The potential of the work electrode is linearly swept at a rate of 10 mV/s from -0.8 to 1 V vs. Ag/AgCl.

Results and Discussion

Characterization of TNTAs

The morphology of TNTAs changes during the anodization processes. Therefore, the morphology including length and wall thickness of TNTAs were identified with SEM. Figure 1 shows the cross-sectional and top view SEM images of TNTAs at various anodization times ranging from 2 to 14 h. The TNTAs were grown at 55V in ethylene glycol containing 0.26 wt% NH_4F. It is clear that the length as well as wall thickness of TNTAs increased with the increase in anodization time from 2 to 14 h. During the electrochemical anodization process, the electrical field would induce the chemical dissolution of Ti foils, and the presence of fluoride ions in NH_4F would dominate the etching reaction of Ti, while the major oxidation power were generated from the electrochemical dissociation of water to convert the dissolved Ti into TiO_2. Therefore, TNTAs were formed as a result of etching of Ti foils at the electrolyte/oxide interface and oxidation of Ti at the oxide/Ti interface. As shown in Figure 1, the tubular surfaces of TNTAs were clearly observed at various anodization times, and the inner diameters were in the range 80-100 nm.
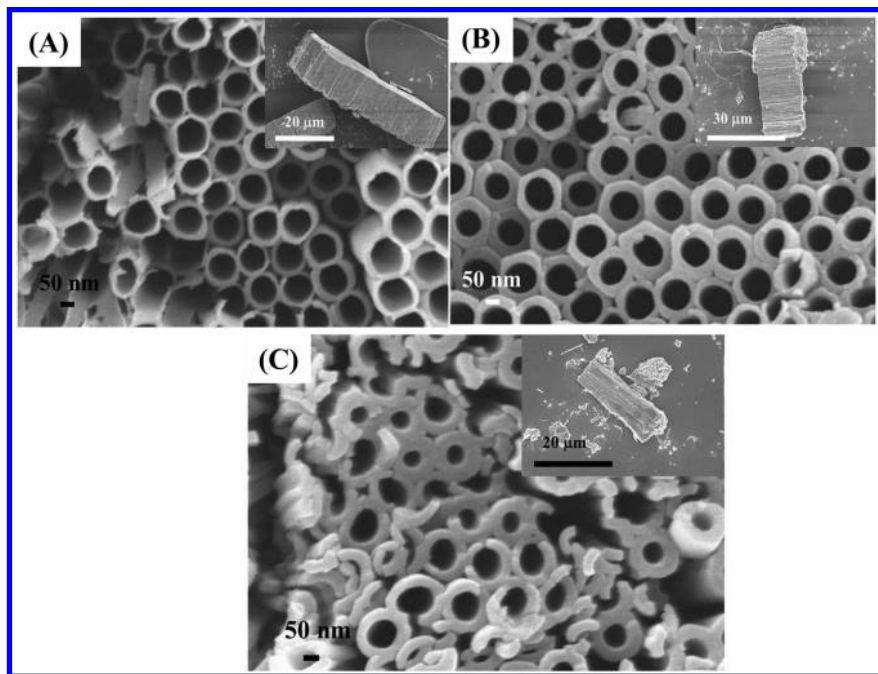
Figure 1. The SEM images of TNTAs surface at different anodization times of (A) 2 h, (B) 8 h, (C) 14 h. The inset image is cross-sectional image of TNTAs.
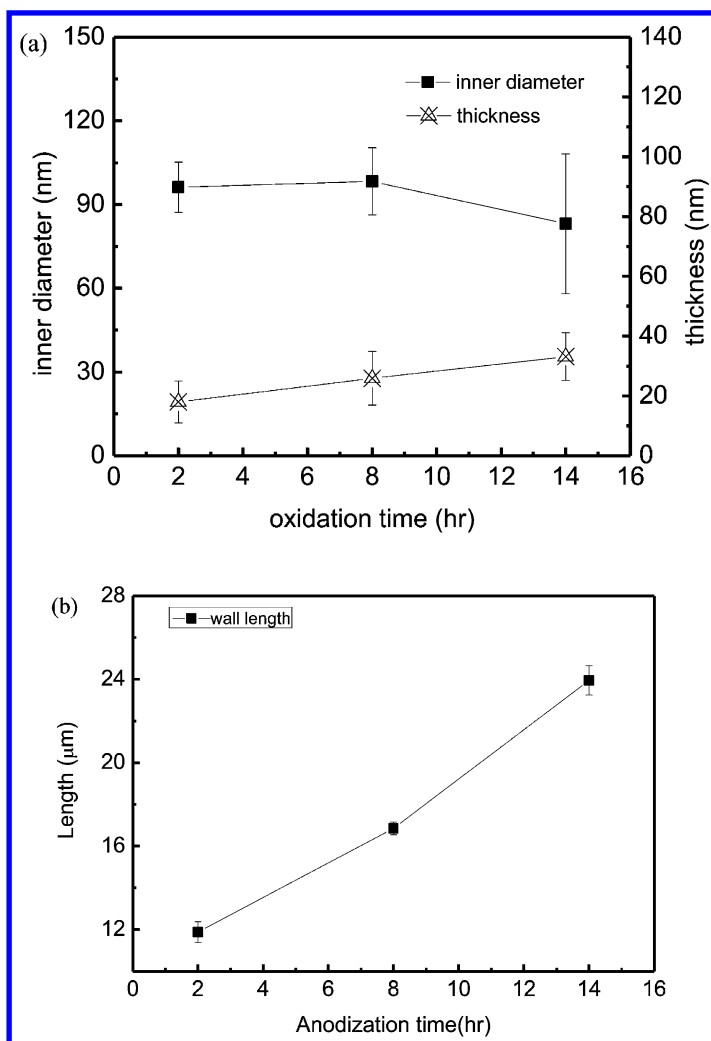
Figure 2. (a) The inner diameter and wall thickness and (b) length of TNTAs as a function of anodization time ranging from 2 to 14 h.

Figure 2 shows the diameter and length of TNTAs as a function of anodization time to clarify the relationship between TNTA morphology and anodization time. It is clear that the inner diameter of TNTAs was 96 ± 9 and 98 ± 12 nm at 2 and 8 h, respectively, showing that anodization time has less influence on the change in diameter of TNTAs when the anodization time is short (< 8 h). However, the increase in anodization time to 14 h slightly decreased the diameter of TNTAs to 83 ± 25 nm, presumably due to the increase in wall thickness at long anodization time. As shown in Figure 2a, the wall thickness of TNTAs increased slightly from 17 ± 7 nm at 2 h to 33 ± 8 nm at 14 h, indicating that the increase in anodization time could effectively increase the wall thickness of TNTAs. In addition, the

increase in anodization time also increases the length of TNTAs. Figure 2(b) shows the length of TNTAs as a function of anodization time. The length of TNTAs increased significantly from 11.9 μm at 2 h to 23.9 μm at 14 h. These results clearly show that the morphology of TNTAs is significantly influenced by the anodization time. The cross-sectional image of TNTAs shown in Figure 1c was smooth, suggesting that the mobility of the fluoride ions was suppressed in the viscous ethylene glycol electrolytes. Since the anodization time of 8 h can produce good morphology of TNTAs with stable inner diameters and lengths, 8 h was used for further experiments to produce TNTAs.

Figure 3 shows The XRD patterns of the TNTAs prepared at various calcinations temperatures ranging from 400 to 800 °C. At low calcinations temperatures of 400-600 °C, several strong diffraction peaks at $2\theta = 25.3°$, 37.8°, 48.0°, 53.9°, 55.1°, and 62.7°, which can be indexed as the (101), (004), (200), (105), (211), (204) reflection of anatase TiO_2 (JPCDS 21-1272), were clearly observed. After calcination at high than 700 °C, the diffraction peak of rutile phase at 27.3° 2θ was observed (JPCDS 01-089-0552), indicating the phase transformation of TiO_2 from anatase to rutile at 700 °C. On the basis of the Scherrer's equation of (101) reflection of anatase TiO_2 crystals, the average grain sizes of anatase TiO_2 phase were 23.1, 24.3, 28.5, 49.4, and 39.8 nm at 400, 500, 600, 700, and 800 °C,respectively. The grain size of anatase TiO_2 increased initially with the increase in temperature from 400 to 700 °C. However, the grain size of TiO_2 decreased at 800 °C, presumably due to the collapse of the tubular structures of TNTAs to form dense rutile phase.
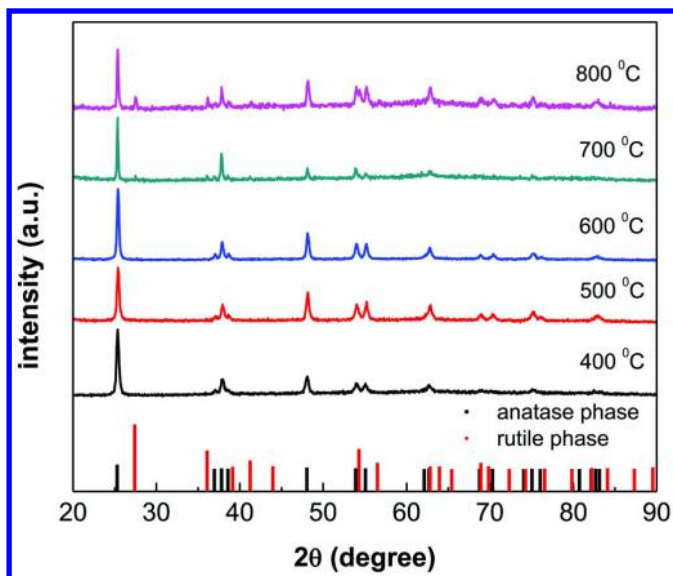
Figure 3. X-ray diffraction patterns of TNTAs calcined in air at various temperatures ranging from 400 to 800 °C.

Table 1. The Morphology, Crystallinity, Specific Surface Area, and Band Gap of TNTAs at Different Calcination Temperatures

anneal temperature (°C)	morphology	crystal phase	S_{BET} (m^2/g)	band gap (eV)
400	nanotube	anatase	31.4	3.10
600	nanotube	anatase	24.8	3.16
700	Nanotube/particle	anatase/rutile	13.2	3.32
800	microparticle	anatase/rutile	7.0	3.26
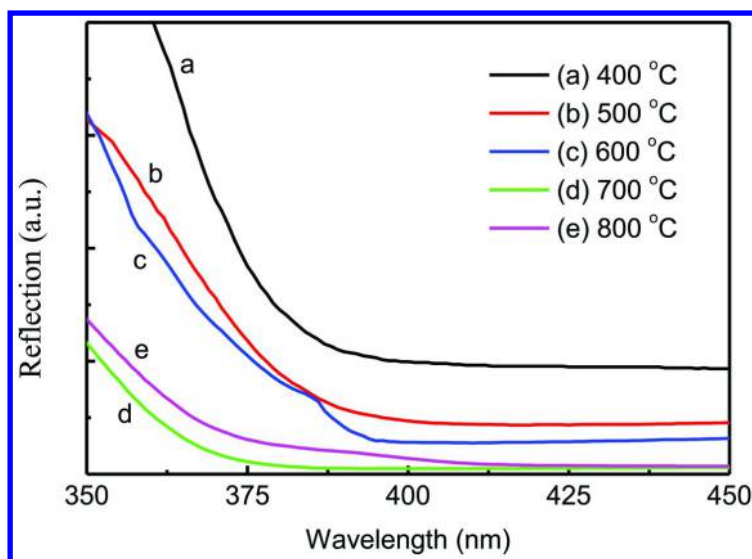
Figure 4. The optical property of TNTAs at different calcination temperatures ranging from 400 to 800 °C.

The optical property of TNTAs at various calcination temperatures was further examined. As shown in Figure 4, an absorption edge of calcined TNTAs was observed when the wavelength was less than 400 nm. The absorption edge of calcined TNTAs decreased from 400 nm at 400 °C to 355 nm at 700 °C, clearly indicating a blue-shift in absorption wavelength when the calcination temperature of TNTAs increased from 400 to 700 ºC. However, the absorption wavelength red-shfted to around 380 nm as the calcination temperature increased to 800 °C. It is noteworthy that the increase in calcination temperature would

increase the ratio of rutile TiO_2, and the bangap of TNTAs at high temperature should be decreased. In this study, however, the bangap of TNTAs increased as the temperature increased. Table 1 shows the morphology and microstructures of TNTAs at selected calcination temperatures. It is clear that the bandgaps of TNTAs were 3.10, 3.16 and 3.32 eV when the calcination temperatures were 400, 600, and 700 °C, respectively, an then slightly decreased to 3.26 eV at 800 °C. The major crystalline phase of TNTAs was anatase at temperature lower than 600 °C, and then transformed to the mixture of anatase/rutile at 700-800 °C. These results clearly indicate that the large bangap of TNTAs at 400-700 °C is mainly attributed to the production of oxygen vacancy in TNTAs. The diffusion rate of oxygen molecules in TNTA increased when the calcination temperature increased from 400 to 700 °C, resuling in the increase in oxygen vancancy to produce a blue-shift in wavelength adsorption. However, the ratio of rutile TiO_2 increased as the temperature increased from 700 to 800 °C, and subsequently descreased the band gap of TNTAs. It is also noted that the specific surface areas fo TNTAs decrased from 31.4 to 7.0 m²/g when the temperature increased from 400 to 800 °C. Therefore, the calcinations temperature of 400 °C was selected for further experiments.

Photoelectrochemical Performance of Calcined TNTAs

The photoelectrochemical measurements were carried out by using various anodization temperatures of TNTAs as the photoelectrodes. Figure 5 shows the photoelectrochemical response of the TNTAs electrodes as a function of calcination temperature. In addition, the LSVs were recorded under UV light irradiation at 10 mW/cm². The photocurrent density decreased with the increase in calcination temperature and the current density of TNTAs decreased from -1.12 V mA/cm² (at 0 V vs. RHE) at 400 °C to only -3×10^{-4} mA/cm² at 800 °C, presumably due to the disruption of the tubular structure and the formation of rutile phase at high calcination temperature. The photoconversion efficiency, η, can be calculated using the following equation (*24*):

$$\eta = \frac{-j_p(E_{app} - E_{H_2}^0)}{I_0} \tag{1}$$

Where j_p is the current density (mA/cm²), E_{app} is the applied potential, E^0_{H2} is the standard potential of hydrogen electrode (0 V vs. RHE), and I_0 is the intensity of incident light (power density). The photoconversion efficiency shown in Figure 6 indicates that the highest efficiency of 3.4 % was obtained when TNTAs was calcined at 400 °C. From the SEM images and XRD patterns, it can be concluded that the anatase phase structure could enhance the photocatalytic properties due to the fact that redox potential of valence band of anatase phase TiO_2 was more negative than that of rutile phase. In addition, the high aspect ratio of TNTAs at low calcination temperature could increase the specific surface area (Table 1) to enhance the hydrogen generation rate, resulting in the increase in the overall photoelectrochemical response of TNTAs.
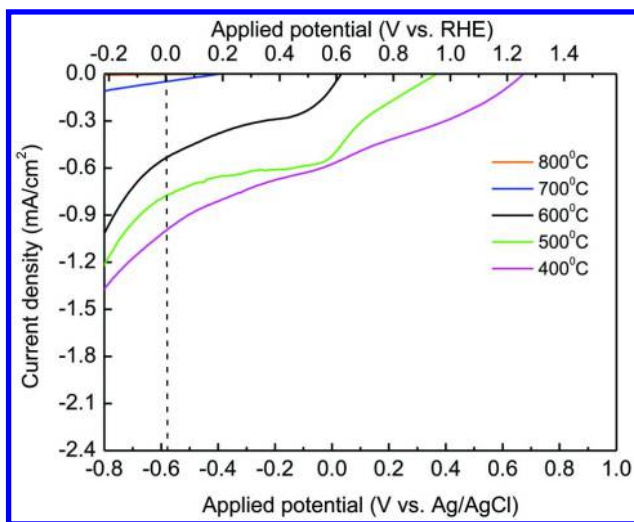
Figure 5. Linear sweeps voltammogram of TNTAs calcined in air at various temperatures ranging from 400 to 800 °C.
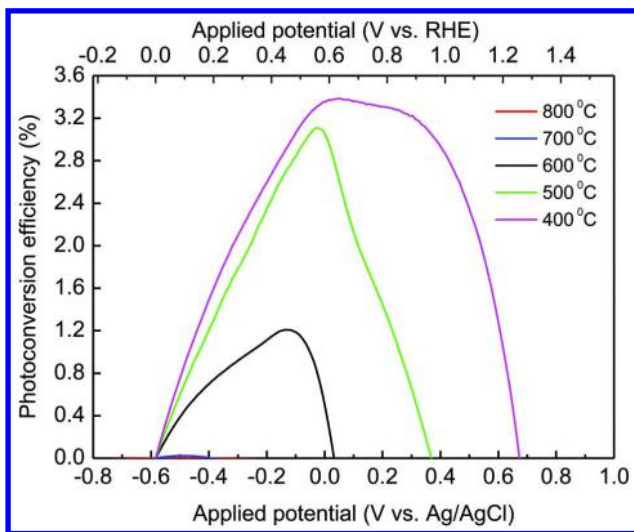
Figure 6. Comparison of photoconversion efficiencies of calcined TNTAs in the presence of 400 W light. The TNTAs were calcined in air at various temperatures ranging from 400 to 800 ℃.

Characterization and Electrochemical Performance of Pt/TNTAs

Although the TNTAs prepared at 8 h of anodization time and then calcined at 400 °C can produce hydrogen gas from water splitting, the production rate is not high. To enhance the hydrogen evolution from water by TNTAs, 0.09 wt% Pt were deposited onto surface of TiO_2 nanotube arrays structures and then used for water splitting. Figure 7 shows the TEM images of Pt/TNTAs in the presence of 0.09 wt% Pt. The TNTAs calcined at 400 ºC showed the clear tubular structures, which is in good agreement with the results obtained from SEM image. In addition, some Pt nanoparticles were deposited onto the TNTA surface. The particle sizes were in the range 1.5 - 5 nm with the mean diameter of 2.9 nm, clearly indicating that the Pt nanoparticles were successfullt well dispersed onto the TNTA surface.
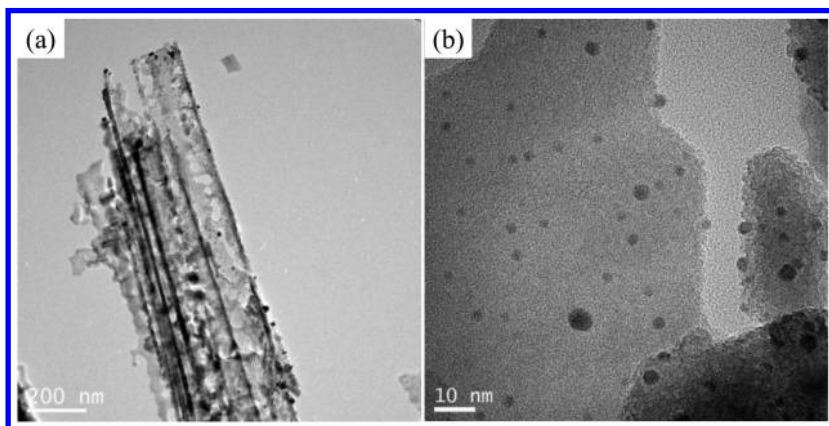
Figure 7. The (a) TEM image of Pt-TNTAs and (b) Pt nanoparticles onto TNTA surface.

Figure 8 shows the linear sweeps voltammograms and photoconversion efficiencies of Pt/TNTAs calcined in air at 400 °C. The photoconversion efficiency of TNTAs enhanced significantly after the deposition of Pt nanoparticles, and the photocurrent increased from -1 mA/cm^2 for pure TNTAs electrode to -2.86 mA/cm^2 for Pt/TNTAs at 0 V vs. RHE, which corresponds to a 2.9-time increase in production rate. In addition, the photoconversion efficiencies (η) increased from 3.39 % to 7.20 % when Pt nanoparticles was deposited. This enhanced photoconversion efficiency is mainly attributed by the effective charge separation. Compared with the pure TiO_2 electrodes, the extra-bias required for the maximized photoconversion efficiency shifts slightly to the cathodic direction. This shift represents the modification of Pt/TNTA surface by the Pt nanoparticles as well as the change in photoelectrochemical performance of the Pt-TiO_2 composite electrodes. Therefore, the Pt/TiO_2 materials can serve as a efficient photocathode for photoelectrochemical performance, and the photoconversion efficiency for Pt/TNTAs nanocomposites is 3.2 times higher than that of the pure TNTAs.
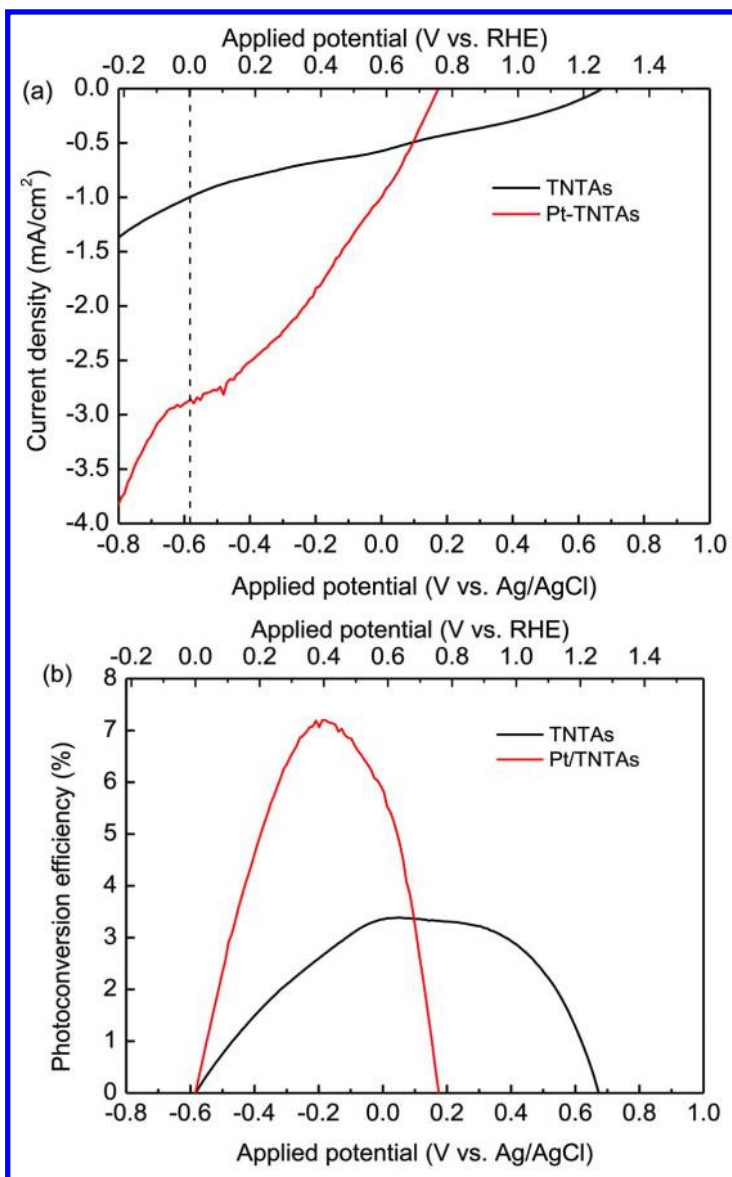
Figure 8. (a) Linear sweeps voltammogram and (b) photoconversion efficiency of TNTAs and Pt/TNTA.

Figure 9 compares the evolved amounts of H_2 gas produced from the water splitting by pure TNTAs and Pt/TNTAs as a function of applied potential under the irradiation of 400 W Hg light. In the dark reaction, the hydrogen gas evolved from water splitting by Pt, pure TNTAs and Pt/TNTs was observed only when the overpotential was higher than -0.75 V vs. Ag/AgCl (-0.2 V vs. RHE). However,

the evolution rate for H_2 production was low and only 0.092, 0.514, and 0.76 µmol cm^{-2} hr^{-1} for Pt, pure TNTAs and Pt/TNTs, respectively, were obtained. It is noteworthy that the produced amounts of H_2 gas by TNTA-based nanomaterials was 5.6-8.3 times higher than that of pure Pt, which is mainly attributed to the fact that TNTA-based nanomaterials has high exposure area than that of Pt wire, resulting in the production of more reactive sites for H_2 production at the same applied voltage.
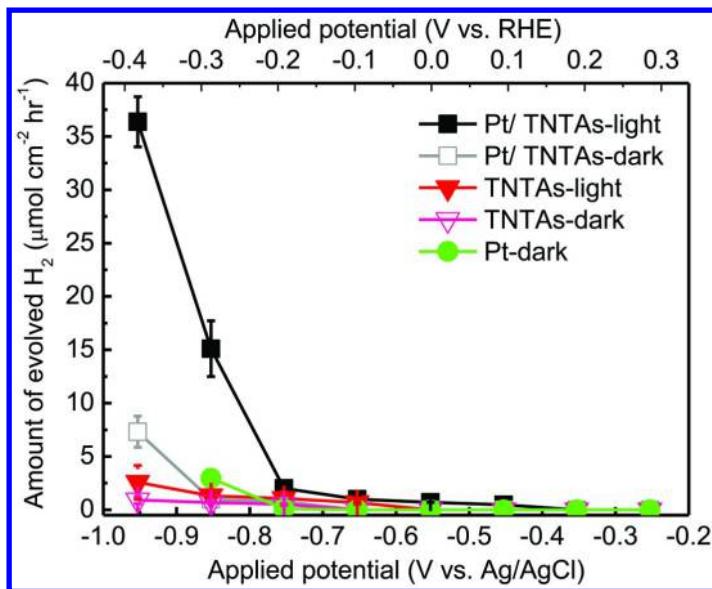
Figure 9. The produced H_2 gas as the function of applied potential by different TNTA-based nanomaterials.

The evolution of hydrogen gas from water splitting by TNTA-based nanomaterials was significantly enhanced in the presence of UV light. As shown in Figure 9, the overpotential for H_2 generation by Pt/TNTAs was -0.45 V vs. Ag/AgCl (+0.1 V vs. RHE), which is 0.2V lower than that by TNTA, showing that addition of Pt is conducive to the reduction of water. It is noteworthy that the produce H_2 gas was 1.308 and 15.105 µmol cm^{-2} hr^{-1} for TNTAs and Pt/TNTAs, repsecptively, at -0.85 V, which were 1.9 and 15.5 times higher than those in dark reaction, clearly indicating that high applied volatge can enhance the production of H_2 gas from water in the presence of TNTA-based nanomaterials. In addition, a 1.4-time higher in H_2 gas productionby Pt/TNTAs was observed when compared with that of TNTAs in the presecne of UV light and at -0.85V, showing that Pt/TNTA is a promising nanomaterials for evolution of hydrogen gas from water.

Conclusions

In this study, the TNTAs and Pt/ TNTAs composites were synthesized using Ti foils as the substrate in the presence of 0.26 wt% NH_4F. The TNTAs were electrochemically fabricated using 20×18 mm² titanium and Pt foils as the anode and cathode, respectively. In addition, Pt ions were loaded onto the TiO_2 nanotube arrays to from Pt/TNTAs composites for enhanced photoelectrochemical performance. The physicochemical properties of TNTAs and Pt/TNTAs including morphology, crystallinity, and surface areas were determined. In addition, effect of operational parameters including anodic time and anneal temperature on the photoelectrochemical reaction were examined and optimized. The TiO_2 nanotubes have about 96 nm in diameter, 18 nm in thickness, and 11.9 μm in length after 2 h of anodization. In addition, TNTAs and Pt/TNTAs were used as a photocathode for photoelectrochemical hydrogen generation. Under illumination of 10 mW/ cm² in 0.5 M Na_2SO_4 solution, the photocurrent current density was -2.86 mA/ cm² at 0 V (vs. RHE) by Pt/TNTs, which was higher than that of pure TiO_2 nanotube arrays). The photoconversion efficiency was found to be 7.20 % and 3.39% for Pt/TNTAs and TNTAs, respectively. Results obtained in this study show that Pt/TNTAs could also be an effective photocathode with optimal operational conditions for photoelectrochemical hydrogen evolution.

Acknowledgments

References

1. Sun, K.; Madsen, K.; Andersen, P.; Bao, W. N.; Sun, Z. L.; Wang, D. L. *Nanotechnology* **2012**, *23*, 194013.
2. Seger, B.; Pedersen, T.; Laursen, A. B.; Vesborg, P. C. K.; Hansen, O.; Chorkendorff, I. *J. Am. Chem. Soc.* **2013**, *135*, 1057–1064.
3. Seger, B.; Laursen, A. B.; Vesborg, P. C. K.; Pedersen, T.; Hansen, O.; Dahl, S.; Chorkendorff, I. *Angew. Chem., Int. Ed.* **2012**, *51*, 9128–9131.
4. Boettcher, S. W.; Warren, E. L.; Putnam, M. C.; Santori, E. A.; Turner-Evans, D.; Kelzenberg, M. D.; Walter, M. G.; McKone, J. R.; Brunschwig, B. S.; Atwater, H. A.; Lewis, N. S. *J. Am. Chem. Soc.* **2011**, *133*, 1216–1219.
5. Hou, Y. D.; Abrams, B. L.; Vesborg, P. C. K.; Bjorketun, M. E.; Herbst, K.; Bech, L.; Setti, A. M.; Damsgaard, C. D.; Pedersen, T.; Hansen, O.; Rossmeisl, J.; Dahl, S.; Norskov, J. K.; Chorkendorff, I. *Nat. Mater.* **2011**, *10*, 434–438.
6. Lombardi, I.; Marchionna, S.; Zangari, G.; Pizzini, S. *Langmuir* **2007**, *23*, 12413–12420.
7. Paracchino, A.; Laporte, V.; Sivula, K.; Gratzel, M.; Thimsen, E. *Nat. Mater.* **2011**, *10*, 456–461.
8. Ida, S.; Yamada, K.; Matsunaga, T.; Hagiwara, H.; Matsumoto, Y.; Ishihara, T. *J. Am. Chem. Soc.* **2010**, *132*, 17343–17345.

9. Price, M. J.; Maldonado, S. *J. Phys. Chem. C* **2009**, *113*, 11988–11994.

10. Yokoyama, D.; Minegishi, T.; Maeda, K.; Katayama, M.; Kubota, J.; Yamada, A.; Konagai, M.; Domen, K. *Electrochem. Commun.* **2010**, *12*, 851–853.

11. Paulose, M.; Mor, G. K.; Varghese, O. K.; Shankar, K.; Grimes, C. A. *J. Photochem. Photobiol., A* **2006**, *178*, 8–15.

12. Zhao, W.; Wang, Z. Y.; Shen, X. Y.; Li, J. L.; Xu, C. B.; Gan, Z. X. *Int. J. Hydrogen Energy* **2012**, *37*, 908–915.

13. Varghese, O. K.; Gong, D. W.; Paulose, M.; Ong, K. G.; Dickey, E. C.; Grimes, C. A. *Adv. Mater.* **2003**, *15*, 624–627.

14. Macak, J. M.; Tsuchiya, H.; Schmuki, P. *Angew. Chem., Int. Ed.* **2005**, *44*, 2100–2102.

15. Feng, X. J.; Sloppy, J. D.; LaTemp, T. J.; Paulose, M.; Komarneni, S.; Bao, N. Z.; Grimes, C. A. *J. Mater. Chem.* **2011**, *21*, 13429–13433.

16. Paulose, M.; Prakasam, H. E.; Varghese, O. K.; Peng, L.; Popat, K. C.; Mor, G. K.; Desai, T. A.; Grimes, C. A. *J. Phys. Chem. C* **2007**, *111*, 14992–14997.

17. Liu, Z.; Zhang, X.; Nishimoto, S.; Jin, M.; Tryk, D. A.; Murakami, T.; Fujishima, A. *J. Phys. Chem. C* **2008**, *112*, 253–259.

18. Gong, J.; Lai, Y.; Lin, C. *Electrochim. Acta* **2010**, *55*, 4776–4782.

19. An, W. J.; Wang, W. N.; Ramalingam, B.; Mukherjee, S.; Daubayev, B.; Gangopadhyay, S.; Biswas, P. *Langmuir* **2012**, *28*, 7528–7534.

20. Shankar, K.; Mor, G. K.; Prakasam, H. E.; Yoriya, S.; Paulose, M.; Varghese, O. K.; Grimes, C. A. *Nanotechnology* **2007**, *18*, 065707.

21. Lubberhuizen, W. H.; Vanmaekelbergh, D.; Van Faassen, E. *J. Porous Mater.* **2000**, *7*, 147–152.

22. Grimes, C. A. *J. Mater. Chem.* **2007**, *17*, 1451–1457.

23. Zhang, Z. H.; Zhang, L. B.; Hedhili, M. N.; Zhang, H. N.; Wang, P. *Nano Lett.* **2013**, *13*, 14–20.

24. Ye, M.; Gong, J.; Lai, Y.; Lin, C.; Lin, Z. *J. Am. Chem. Soc.* **2012**, *134*, 15720–15723.

Chapter 9

Efficient Electricity Generation and Degradation of Organic Pollutants in Wastewater Using Ag-BiOI Photoactivated Fuel Cell

Chun He,[1,3] Yibing Gong,[1] Shuzhen Li,[1] Lingling Hu,[1] Yichang Yang,[1] Lianpeng Sun,[1,3] and Dong Shu[*,2]

**[1]School of Environmental Science and Engineering, Sun Yat-sen University, Guangzhou, 510275, China
[2]Key Lab of Technology on Electrochemical Energy Storage and Power Generation in Guangdong Universities, School of Chemistry and Environment, South China Normal University, Guangzhou, 510006, China
[3]Guangdong Provincial Key Laboratory of Environmental Pollution Control and Remediation Technology, Guangzhou, 510275, China
[*]E-mail: dshu@scnu.edu.cn.**

A visible-light-driven photo fuel cell (PFC) system, consisting of a Ag-BiOI/ITO photoanode and a Pt photocathode, was used to generate electricity by using wastewater organic compounds as electrolyte and fuel. The prepared BiOI and Ag-BiOI/ITO photoanodes were characterized by X-ray diffraction (XRD), scanning electronic microscope (SEM), transmission electron microscopy (TEM), X-ray photoelectron spectroscopy (XPS), and UV-Vis diffuse reflectance spectroscopy (DRS) to examine the surface structure, chemical composition, and the properties of light absorption. The photoactivity of Ag-BiOI/ITO photoanodes was evaluated in the term of the electricity generation efficiency and degradation efficiency for recalcitrant organic pollutants. Compared with a BiOI/ITO photoanode, it was found that the efficiency of electricity generation using the Ag-BiOI/ITO photoanode was significantly higher in PFC system under visible light. Similarly, the photocatalytic degradation efficiency of wastewater organic pollutants using Ag-BiOI/ITO photoanode was significantly higher than that

of BiOI/ITO. The enhancement in the electricity generation efficiency and degradation efficiency for wastewater organic pollutants is attributed to the action of these dopants Ag on BiOI surface, which play a key role by driving the electrons to the cathode via an external circuit.

1. Introduction

In the past decade, the interest of recovering energy released from degradation of organic pollutants during waste treatment has been received much attention because of the depletion of fossil fuels and increase of environmental problems (*1–3*). Since the first report of solar-driven photoelectrochemical (PEC) energy conversion in 1972 (*4*), the photoelectrochemical cell has been extensively studied. Alternative, photoactivated fuel cell (PFC) is an ideal clean energy device for solving the problems about the depletion of fossil fuels and increasing industrial wastewater, which consumes "fuel" (i.e. organic pollutants) via the photoelectrochemical oxidation to generate electricity. In a typical PFC process, an amount of photoelectrons are excited from the valence band of the photocatalysts to the conduction band, generating holes-electrons pairs (*5–7*). The photogenerated electrons can be transferred spontaneously to a cathode through an external circuit due to the existing potential bias between the photoanode and cathode and thus generate electricity, whereas the positive holes are powerful oxidants for degrading the organic pollutants to provide the source of electricity. TiO_2, as one of the prominent semiconductor photocatalysts, was extensively investigated for serving as a PFC photoanode electrode (*8–15*). However, owing to its lager bandgap (3.2 eV) that only excited by UV irradiation ($\lambda < 380$ nm) has limited its application in contaminants removal processes (*16, 17*). Thus, exploring the high efficiency photocatalysts with narrow band gap which function in the visible light region has attracted a remarkable attention.

The recent promising results have been achieved using bismuth iodide (BiOI) with the narrow bandgap in the application of the photocatalytic degradation for organic compounds due to their unique optical properties (*18–25*). A high photocatalytic activity in the degradation of methyl orange under visible light irradiation was obtained over BiOI microspheres (*24*). Zhang and co-workers reported that BiOCl exhibited better performance than TiO_2 on photocatalytic degradation of methyl orange under visible light irradiation (*25*). Also, BiOI has been reported to exhibit excellent photoelectrochemical property as solar cells (*26–29*). Thus, BiOI could be served as a promising photoanode candidate in PFC to generate electricity under visible light.

Especially, in a single crystal semiconductor-based photoactivated fuel cell, the problem of charge recombination can be overcome, since the photogenerated electrons can be transferred to a cathode through an external circuit due to the

existing potential bias between the photoanode and cathode (*6*, *7*). Actually, pioneer studies demonstrated that the semiconductor films immobilized on conductive substrate provide also alternative way of manipulating photocatalytic reaction in the presence of very lower potential bias (*30*, *31*). However, it should be noted that the photogenerated electrons and holes in the excited states a can easily recombine to dissipate the input energy as heat, if the photogenerated electrons negative charges are not effectively separated and further transferred out of semiconductor films (*31*, *32*). Thus, the impedance of electron mass transfer between the semiconductor film and its supporting media is also a critical factor in PFC system. Originally, to facilitate the separation of photoinduced carrier in the semiconductor, one approach was to deposit BiOI with noble metal such as platinum and silver (*33*, *34*). The deposited metal on the surface of BiOI anode not only can increase the lifetime of holes and suppress the electron–hole recombination, but also can facilitate the transfer of the accumulated photogenerated electrons from metal particles to another compartment of cell, which is beneficial to the generated electricity efficiency. Thus, it is interesting to investigate the photoactivated fuel cell performance of Ag-BiOI/ITO photoanodes in the PFC system. It is expected that BiOI/ITO photoanode deposited with excellent conductivity metallic Ag is beneficial to maximizing the efficiency of electricity generation in BiOI-based PFC system.

In this study, the synthesized Ag-BiOI/ITO films were used as photoanodes to construct a PFC working device under visible light. The photoactivity of BiOI-based photoanodes was evaluated in the term of the electricity generation efficiency and degradation efficiency in BiOI-based PFC device using bisphenol A (BPA) as the model fuel, since BPA is an synthetic chemical produced worldwide in the millions of tons each year and is used to manufacture polycarbonate and epoxy resins (*35*), which are used in baby bottles, as protective coatings on food containers, and for composites and sealants in dentistry. Moreover, the mechanism of the charge transfer between the interfaces of Ag/BiOI in the process of PFC working device was also investigated.

2. Materials and Methods

2.1. Materials

$Bi(NO_3)_3 \cdot 5H_2O$, KI, $AgNO_3$, *p*-nitrophenol (*p*-NP), with analytical grade were purchased from Tianjing Fuchen Chemical Reagent Co. Ltd., China. Ethylene glycol, isopropanol, ethanol, formic acid were purchased from Guangdong Fenchuan Chemical Co. Ltd., China. Acid Orange II (AOII) was purchased from Aldrich. Bisphenol A (BPA) with analytical grade were purchased from Aladdin Chemistry co. Ltd., China The chemicals with analytical grade were obtained as reagents and used without further purification. Indium tin oxide (ITO)-coated conductive glass with a resistance of 20 Ω/square was obtained from Nanya Technol. Co., Shenzhen, China. Deionized water was used throughout this study.

2.2. Preparation of BiOI Particles

BiOI particles were synthesized by a solvothermal process similar to the literature except for the different stoichiometric ratio of reagents (20). 0.05 mol of Bi(NO₃)₃ · 5H₂O was added into a 300 ml of ethylene glycol solution containing dissolved KI with the equivalent molar ratio. The mixture was stirred at room temperature for 1 h until the solution presented the homogeneous phase and then transferred into the 100 mL Teflon-lined stainless steel autoclave and kept at 160 °C for 12 h. Subsequently, the autoclave was cooled to room temperature gradually. Finally, the precipitate was centrifuged, filtered through a 0.22 μm Millipore membrane, then washed with deionized water and ethanol for three times until there were no other possible impurities in the product. The resulting product was dried in a vacuum oven at 70 °C for 6 h.

2.3. Preparation of BiOI/ITO Electrode

The BiOI/ITO electrode was prepared according to the following dip-coating procedure given in the literature (36). Briefly, 0.2 g BiOI powder was added to 50 ml of distilled water. The mixture was sonicated for 30 min to break up loosely attached aggregates and then was vigorously agitated to form a fine suspension solution. Then, the BiOI suspension was loaded on an ITO glass plate (4 cm ×4 cm) by a dip-casting method, dried for 20 min on a hot plate at 100 °C, resulting in BiOI electrodes.

2.4. Preparation of Ag-BiOI/ITO Electrodes

Ag-BiOI/ITO was prepared by the method of photoreduction deposition. The glass plate with BiOI/ITO film was immersed in 40 ml of 10 mM L^{-1}AgNO₃ aqueous solution containing 10 mmol l^{-1} HCOOH as a hole scavenger. Then the system was illuminated with a 150 W high-pressure mercury lamp for certain time to conduct the photoreduction reaction, in which Ag^+ was reduced to Ag and uniformly deposited on the surface of BiOI particles. Finally, BiOI film deposited with Ag was dried on a hot plate at 100 °C for 20 min, resulting in an Ag-BiOI/ITO electrode. A series of Ag-BiOI/ITO films was prepared by changing the photoreduction reaction time. An EDS analysis was carried out to further determine the amount of Ag deposition in BiOI/ITO films. The results indicated that the amount of Ag in these four Ag-BiOI/ITO films prepared by the photoreaction were of 0.53%, 1.32%, 2.51%, 5.46% (Wt. Ag/Wt. BiOI), corresponding to the samples prepared by photoreduction reaction of 1 min, 5 min, 10 min, 20 min, 30 min, respectively.

2.5. Characterization

X-ray diffraction (XRD) was conducted using a diffractometer (Bruker AXS, Germany) with radiation of Cu target (K_α, λ = 1.54059 Å). The morphology of the samples were analyzed with JSM-6330F field scanning electron microscopy (SEM, JEOL, Japan) using an acceleration voltage of 20 kV and transmission

electron microscope (TEM, JEM-2010HR). Spectrophotometer (Shimadzu UV-PC3101PC) with an integrating sphere (Specular Reflectance ATT.5DEG) was used to record their diffuse reflectance spectra (DRS), in which a baseline was corrected by using a calibrated sample of barium sulfate. The current-voltage (*J-V*) characteristics of BiOI/ITO and Ag-BiOI/ITO electrodes were used to investigate the electricity generation performance in the PFC system. The photoelectrochemical measurements of BiOI/ITO and Ag-BiOI/ITO electrodes in PFC system were performed using an IM6ex electrochemical workstation (Zahner, Germany) and Autolab (Netherlands) in a rectangular-shaped quartz reactor with 5 cm × 1.0 cm × 5.0 cm (length × width × height) using a three electrode system. This assembly was composed of a Ag-BiOI/ITO electrode as the working electrodes, a Pt wire as the counter electrode with an area of 4 cm × 4 cm, and a saturated calomel electrode (SCE) as the reference electrode. A 150 W Xe lamp (Shanghai Lansheng Co. Ltd., China) with UV cutoff filter (providing visible light with λ > 400 nm) was used as the visible light source. The intensities of visible light were measured as 22 mW cm^{-2} on the irradiated surface of the reactor.

2.6. PFC Setup

PFC experiment was conducted in a two-compartment (anodic and cathodic) reactor. The photo-anodic compartment of PFC reactor consists of A 150 W middle-pressure Xenon arc lamp with a filter to remove λ < 400 nm wavelength, a double-welled quartz glass cooling tube with a 5.0 mm-thick cooling water, a batch quartz glass reactor (5.5 cm× 1.5 cm× 9.0 cm) open to air and a Ag-BiOI/ITO electrode. The cooling tube in which Xenon lamp was suspended was placed in front of the rectangular quartz reactor. The Ag-BiOI/ITO electrode was immersed in the reactor, located 2.0 cm in front of the UV lamp. The cathode room is a similar apparatus but a Pt electrode as a counter one. The two compartments were connected via a salt bridge.

2.7. Experimental Procedures

In a typical batch experiment, 20 mL of 20 mg L^{-1} BPA solutions as the simulated wastewater were used as the fuel during investigation the performance of electricity generation in PFC system. 0.05 mol L^{-1} Na$_2$SO$_4$ was added into the solution as the supporting electrolyte. Prior to irradiation, the solution in the cell was stirred in the dark for 20 min to establish the adsorption−desorption equilibrium. During the reaction, the sample were taken using a syringe at a given time intervals.

2.8. Analysis

The concentration of BPA and *p*-NP was determined by high performance liquid chromatography (HPLC, Shimadzu Essentia LC-15C) consisting of a reverse-phase column (Agilent TC-C18, 5 μm 250 × 4.6 mm) and a UV detector (SPD-15C). For *p*-NP, a mobile phase containing methanol and water at 70:30

(v/v) was used with a flow rate of 0.8 mL min⁻¹. A detection wavelength of 326 nm for *p*-NP was applied and the retention time of *p*-NP peak under these conditions was recorded at 5.26 min. For BPA, A mobile phase containing methanol and water at 85: 15 (v/v) was used with a flow rate of 0.8 mL min⁻¹. A detection wavelength of 280 nm for BPA was applied and the retention time of BPA peak under these conditions was recorded at 5.127 min. The concentration of AOII solution was analyzed by UV-vis spectroscopy (UV-2501PC, Shimadzu) at a maximum wavelength of 484 nm.

The degradation efficiency for organic pollutants was calculated as follows:

$$\text{Degradation efficiency (\%)} = \frac{(C_0 - C_t)}{C_0} \times 100 \tag{1}$$

where C_0 is the initial organic pollutant concentration in the solution (mg L⁻¹), and C_t is organic pollutant concentration at reaction time t in the solution (mg L⁻¹).

3. Results and Discussion

3.1. Characterization of Ag-BiOI film

The prepared BiOI and Ag-BiOI films were first examined by XRD shown in Fig. 1a. The crystalline diffraction peaks at 23.7º, 29.4, 31.7º, 32.8, 45.4 and 46.7º were identified as the (101), (102), (110), (111), (200) and (104) planes of tetragonal phase of BiOI, in a well accordance with the values in the database of BiOI (JCPDS Card No. 10-0445). In the meantime, the crystalline diffraction peak of Ag at around $2\theta = 38$ ° can only be found in Ag-BiOI/ITO film. The EDS spectrum for Ag-BiOI indicated the existence of element Bi, I, O, Ag, confirming that Ag was deposited on BiOI (Figure 1b).

The prepared BiOI/ITO and Ag-BiOI/ITO films were examined by SEM and their images were presented in Figure 2. It can be seen clearly that both BiOI/ITO and Ag-BiOI/ITO films had a porous surface and were composed of well-defined microspheres (Figure 2a-b). The higher-magnification SEM images revealed that BiOI microspheres were composed of nanoplates (inset in Figure 2a), and the morphology of Ag-BiOI (Figure 2c-f) is similar to that of BiOI. In addition, it was noted that the surface of Ag-BiOI microspheres seemed less porous with the increased deposited Ag amount, due to the deposited Ag filled on the surface of BiOI microspheres. The thickness of prepared films was estimated to be 4-5 μm from SEM image.

The HRTEM images indicates that some small nanoparticles were observed in the nanoplates of Ag-BiOI (Figure 3a), and the lattice spacing of the small nanoparticle is 0.236 nm for Ag (111) plane (Figure 3b). TEM analysis clearly further demonstrated that Ag nanoparticle was deposited on the surface of BiOI.
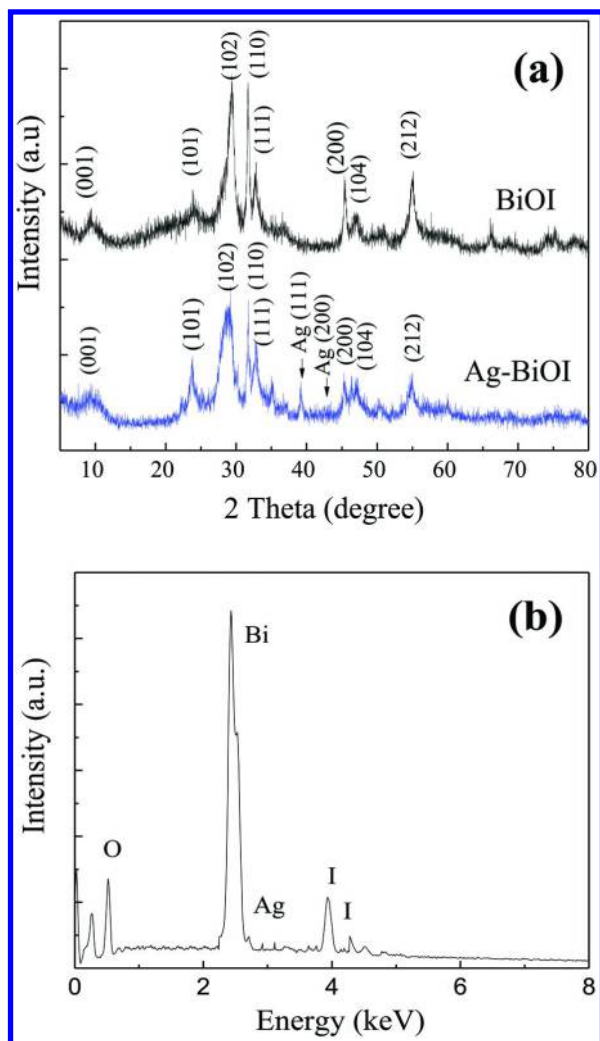
Figure 1. (a) XRD patterns of BiOI and Ag-BiOI from film, and (b) EDS spectrum for 5.46%Ag-BiOI.

To investigate the optical properties, the as-prepared samples were analyzed by UV–Vis absorption spectra in the wavelength range of 200–800 nm, and the absorption spectra of BiOI and Ag-BiOI were shown in Figure 4. It can be seen that Ag-BiOI had better optical absorption generally in the visible light range, which increased with the increase of Ag amount significantly. Moreover, a new significant absorption peak occurred in the region of 500–650 nm, which was attributed to the deposited Ag on the surface of BiOI. The results demonstrated that Ag-BiOI nanocomposites had a significant enhanced absorption in the visible region between 600 and 800 nm due to Ag deposition.
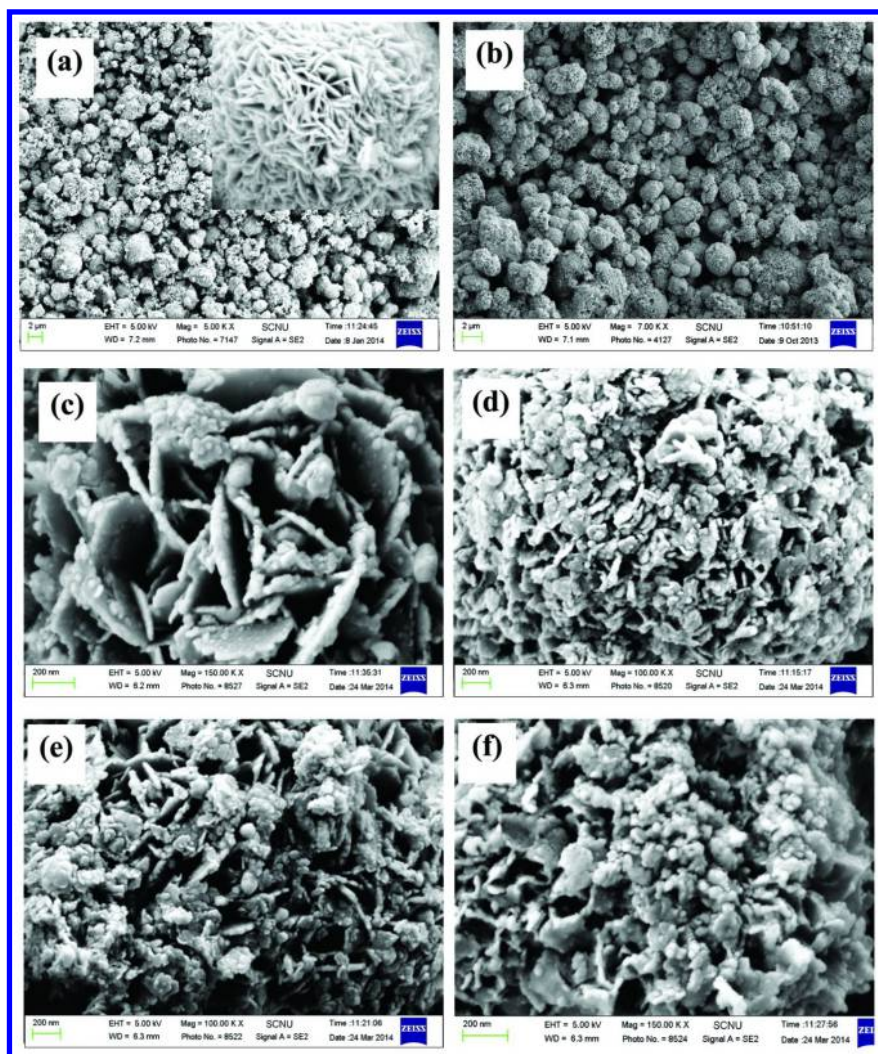
Figure 2. SEM images of (a) BiOI, (b-c) 0.53%Ag-BiOI, (d) 1.32%Ag-BiOI, (e) 2.51%Ag-BiOI, (f) 5.46%Ag-BiOI.

3.2. Performance of Electricity Generation Using BiOI and Ag-BiOI in PFC

Under visible light irradiation, the photocalyst in PFC system was excited to generate electron-hole pairs, the photogenerated electrons spontaneously transfer to counter cathode through an external circuit in the existence of the potential difference, and electricity was generated. The performance of electricity

generation using BiOI and Ag-BiOI electrodes in PFC system was evaluated by the current-voltage $(J\text{-}V)$ and current-power $(J\text{-}JV)$ characteristics in 20 mg L^{-1} BPA aqueous solution under visible light. The power (P) of electricity generation using BiOI-based electrodes in PFC systems can be expressed as follows:

$$P = J \cdot V \qquad (2)$$

where J, V, and P is current density (μA cm^{-2}), voltage (V), and power (μW cm^{-2}), respectively.
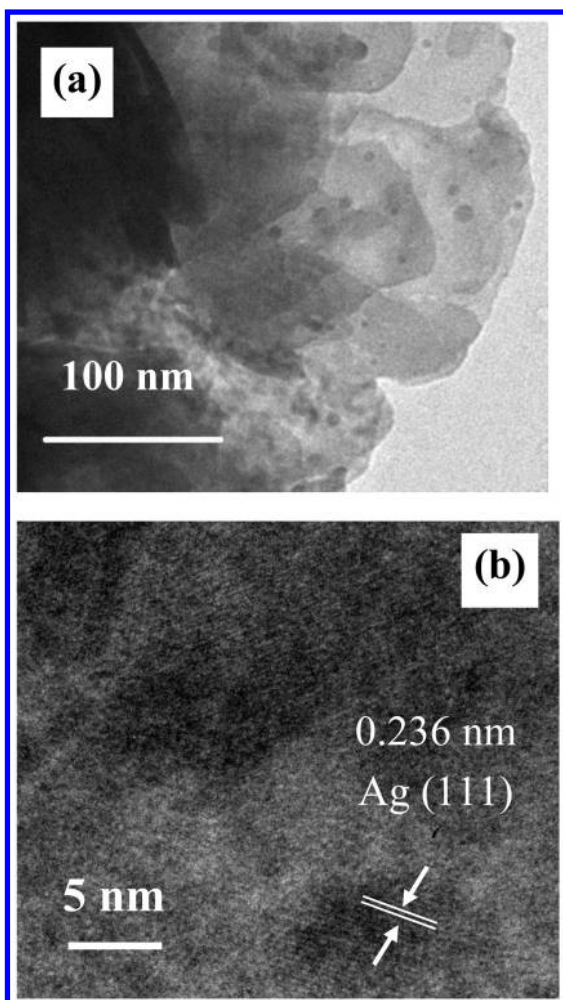
Figure 3. (a) TEM image and (b) HRTEM image of 0.53%Ag-BiOI.

Figure 5a presented the current-voltage (*J-V*) plot for Ag-BiOI/ITO electrodes in PFC system. Firstly, it was found that the deposited Ag amount of on Ag-BiOI/ITO affected the open-circuit voltage (V_{oc}). There was an enhancement in the open-circuit voltage (V_{oc}) for Ag-BiOI/ITO compared with BiOI/ITO, and the Ag-BiOI/ITO with the deposited Ag amount of 2.51% exhibited the maximum V_{oc} with the value of 0.689 V vs. SCE in PFC. Generally, the magnitude of V_{oc} represents the energy difference between the Fermi level of semiconductor film and the reduction potential of the redox couple in the solution. In dark, the Fermi level of a semiconductor film equilibrates with the redox couple in solution; upon illumination of the film with bandgap excitation, the photogenerated electrons accumulate in the film, leading to a shifting of Fermi level to more negative potential. As a result, any accumulation of electrons in the film will present a greater shift in V_{oc}. In our experiments, an increase in V_{oc} is observed with Ag nanoparticle deposition increases up to wt. 2.51% (Ag/BiOI), then, V_{oc} decreases. The increase is consistent with the fact that Ag nanoparticles is highly electronegative as the Fermi level can be shifted to negative potentials with chemical modification or charging effect (*36*), while the decrease can be attributed to the absorption or/and block of incident light by Ag nanoparticles on the surface of the film. The highest V_{oc} possibly represents a balance result of above two effects. Secondly, it was found that the photocurrent of Ag-BiOI/ITO electrodes is also dependent on the deposited Ag amount. Under visible light, the anodic photocurrent of the Ag-BiOI/ITO electrode was greater than that of BiOI/ITO electrode.
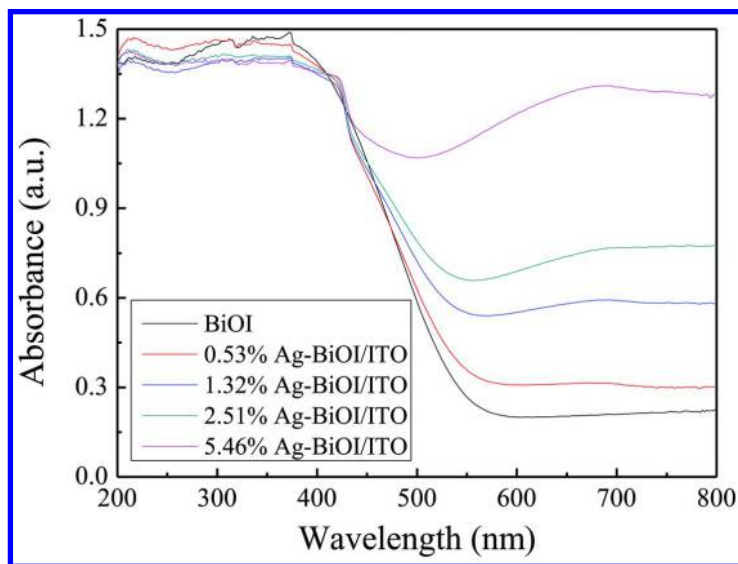
Figure 4. Change of diffuse reflectance spectra of BiOI films with different amount of Ag deposition.
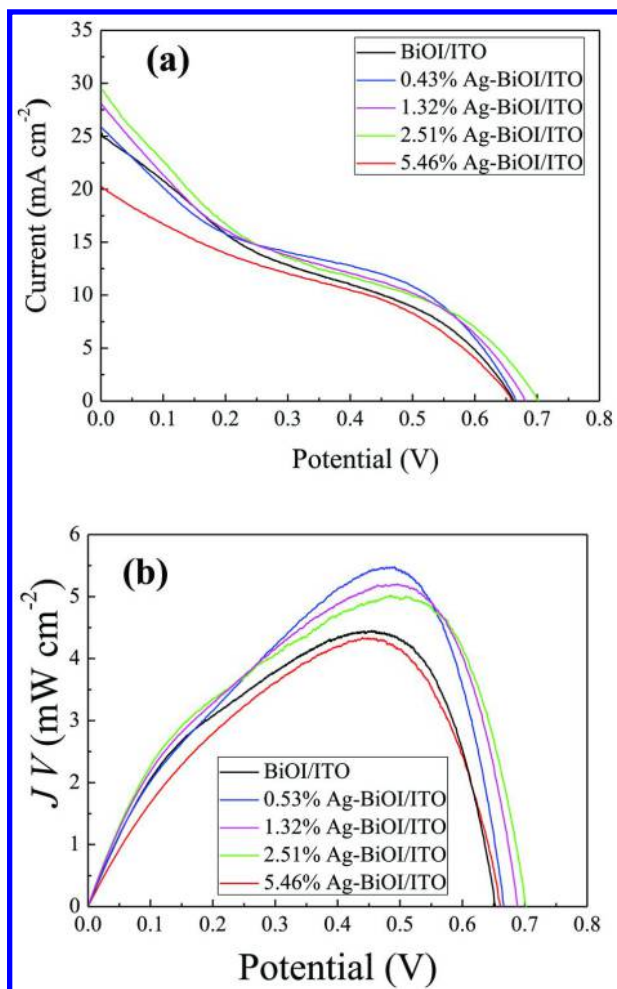
Figure 5. (a) Current-voltage (J-V) plots and (b) power-voltage (JV-V) plots for Ag-BiOI/ITO in PFC system under visible light. Conditions: 20 mg L⁻¹ BPA concentration, 0.05 mol L⁻¹ Na₂SO₄.

Similarly, an increase in the anodic photocurrent of Ag-BiOI/ITO electrode is observed when Ag nanoparticle deposition increases up to 2.51%. The relative higher values of J_{sc} and power density on Ag-BiOI/ITO than that of BiOI/ITO might result from a better electron transfer rate between the solid–liquid interfaces, so that the photogenerated electrons were more easily transferred out of the BiOI to form a greater current in the external circuit.

Figure 5b showed the power-voltage (JV-V) plot for Ag-BiOI/ITO electrodes in PFC system. It was observed that the power density of Ag-BiOI/ITO electrodes with Ag deposition amount increases up to wt. 2.51% is higher than that of

BiOI/ITO electrode in the range of 0-0.689 V. The maximum values of *JV* for BiOI/ITO, 0.53%Ag-BiOI/ITO, 1.32%Ag-BiOI/ITO and 2.51%Ag-BiOI/ITO were 4.402, 5.480, 5.203, and 5.025 µA cm^{-2}, respectively, which were higher than that of BiOI/ITO (20.24 µA cm^{-2}). The greater generated electricity of Ag-BiOI/ITO indicates that: (i) The deposited Ag on the surface of BiOI film not only can suppress the electron–hole recombination and increase the lifetime of electrons and holes; (ii) Ag in Ag-BiOI/ITO electrode can improve the film conductivity so that the remained electrons more easily transfer out of the film to form additional current in the external circuit.
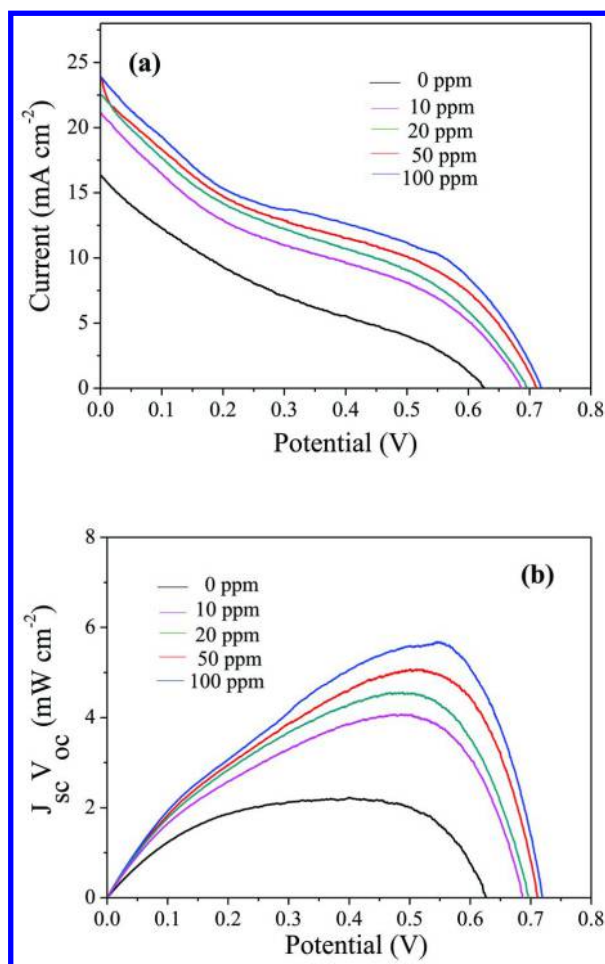
Figure 6. (a) Current-voltage (J-V) plot and (b) current-power (J-JV) plot for 0.53%Ag-BiOI/ITO electrodes with different BPA concentration (containing 0.05 mol L^{-1} Na$_2$SO$_4$) in PFC system under visible light irradiation.

3.3. Effect of Fuel on Efficiency of Electricity Generation

The effect of BPA concentration on the short-circuit density (J_{sc}) and power density (JV) for Ag-BiOI/ITO is shown in Figure 6. It can be seen that J_{sc} increased with the increase in BPA concentration. The J_{sc} for 0.53%Ag-BiOI/ITO in the presence of 100 ppm BPA is 23.86 µA cm^{-2}, which is1.5 times than that in the absence of BPA. Similarly, the power density also increased with the increase in BPA concentration. The maximum power density of 0.53%Ag-BiOI/ITO at 100 ppm BPA was 5.7 µW cm^{-2}, which is 2.6 times higher than that in the absence of BPA. Apparently, this increased short-circuit density and power density is due to the effective hole scavenging in the presence of the sacrificial organic substance (BPA) that results in the liberation of more free electrons, leading to the enhancement in the electricity generation.

3.4. Fill Factor of Ag-BiOI/ITO in PFC System

The open-circuit voltage (Voc), short-circuit current density (J_{sc}) and fill factors (ff) using Ag-BiOI/ITO electrodes in the PFC system were listed in Table 1. The fill factor is calculated according to eq 4 (37):

$$ff = \frac{JV\,\mathrm{max}}{JscVoc} \qquad (3)$$

Table 1. Current-Voltage Characteristics of Ag-BiOI/ITO in PFC under Visible Light

Anodes	Fuel	C_{BPA} (ppm)	Jsc (µA cm^{-2})	Voc (V)	JV_{max} (µW cm^{-2})	ff
BiOI/ITO	BPA	20	25.35	0.663	4.402	0.261
0.53%Ag-BiOI/ITO	BPA	20	25.80	0.667	5.480	0.318
1.32% Ag-BiOI/ITO	BPA	20	28.07	0.681	5.203	0.272
2.51% Ag-BiOI/ITO	BPA	20	28.71	0.689	5.025	0.254
5.46% Ag-BiOI/ITO	BPA	20	20.21	0.661	4.329	0.324

where JV_{max} is the maximum power density (µW cm^{-2}) of Ag-BiOI/ITO anode in PFC obtained from the J-JV plots. The fill factor indicated the deviation of the actual maximum power density produced in PFC system from the value of $J_{sc}\,V_{oc}$ (µW cm^{-2}), i.e. the product of the highest possible values of photocurrent density and photovoltage. Therefore, the fill factor may indicate the performance of electricity generation in a PFC system, that is, the higher the fill factor is, the

higher the efficiency of electricity generation in PFC system is (*31*). The values of *ff* for BiOI/ITO, 0.53%Ag-BiOI/ITO, 1.32%Ag-BiOI/ITO, and 2.51%Ag-BiOI/ITO in PFC system were 0.261, 0.318, 0.272, and 0.254, respectively. The results indicated that 0.53%Ag-BiOI/ITO electrodes are the effective anodes to generate electricity in PFC.

3.5. Degradation of Organic Pollutants for Ag-BiOI/ITO in PFC

The degradation efficiency for BPA using Ag-BiOI/ITO with different deposited Ag amount in PFC system was evaluated by studying the degradation of BPA in aqueous solution with an initial concentration of 20 mg L^{-1} BPA and under visible light illumination. All tests lasted for 120 min and the experimental results are shown in Figure 7. It can be seen that the degradation efficiency of BPA for Ag-BiOI/ITO electrode in PFC is apparent higher than that for BiOI/ITO electrode, respectively. For example, the degradation efficiency of BPA for BiOI/ITO in PFC is 72%, while the degradation efficiency of BPA for 0.53%Ag-BiOI/ITO electrodes in PFC is 87%. Moreover, the degradation efficiency increased with increasing amount of deposited Ag from 0.0 to 2.51%. The enhanced degradation efficiency for Ag-BiOI/ITO is attributed to the action of Ag deposits on BiOI surface, which play a key role by attracting conduction band photoelectrons.
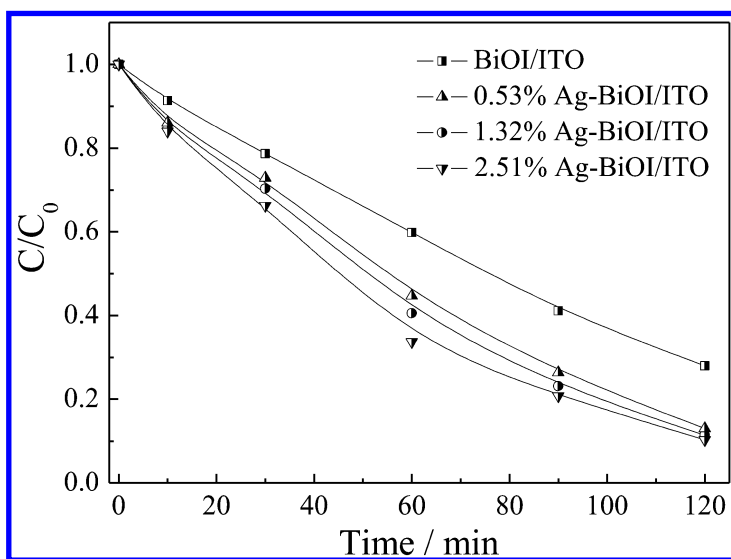
Figure 7. Degradation efficiency of BPA using Ag-BiOI/ITO anodes in PFC. Conditions: 20 mg L^{-1} BPA concentration, 0.05 mol L^{-1} Na_2SO_4.

Conclusion

A visible-light-driven photo fuel cell (PFC) device, consisting of a Ag-BiOI/ITO photoanode and a Pt photocathode, was used to generate electricity by using organic compounds. The photoactivity of Ag-BiOI/ITO photoanode was evaluated in the term of electricity generation efficiency and degradation efficiency for organic pollutants. The Ag-BiOI/ITO photoanode demonstrated a better efficiency of electricity generation and degradation for organic pollutants in PFC system under visible light. The enhancement in the efficiency of electricity generation and degradation for organic pollutants denotes that deposited Ag can not only trap the photogenerated electrons but also improve the film conductivity so that the remained electrons more easily transfer out of the film to form additional current in the external circuit. Therefore, Ag-BiOI/ITO electrode have better performance of electricity and photocatalytic activities in a BiOI/MWCNT reaction system as a result of the effective separation of photogenerated electron-hole pairs in the presence of deposited Ag.

Acknowledgments

References

1. Lewis, N. S. *Science* **2007**, *315*, 798–801.
2. Cook, T. R.; Dogutan, D. K.; Reece, S. Y.; Surendranath, Y.; Teets, T. S.; Nocera, D. G. *Chem. Rev.* **2010**, *110*, 6474–6502.
3. Zhu, J.; Yu, Z.; Burkhard, G. F.; Hsu, C. M.; Connor, S. T.; Xu, Y.; Wang, Q.; McGehee, M.; Fan, S.; Cui, Y. *Nano Lett.* **2008**, *9*, 279–282.
4. Sunada, K.; Kikuchi, Y.; Hashimoto, K.; Fujishima, A. *Environ. Sci. Technol.* **1998**, *32*, 726–728.
5. Li, K.; Xu, Y.; He, Y.; Yang, C.; Wang, Y.; Jia, J. *Environ. Sci. Technol.* **2013**, *47*, 3490–3497.
6. Ueno, H.; Nemoto, J.; Ohnuki, K.; Horikawa, M.; Hoshino, M.; Kaneko, M. *J. Appl. Electrochem.* **2009**, *39*, 1897–1905.
7. Daskalaki, V. M.; Kondarides, D. I. *Catal. Today* **2009**, *144*, 75–80.
8. Lianos, P. *J. Hazard. Mater.* **2011**, *185*, 575–590.
9. Kaneko, M.; Nemoto, J.; Ueno, H.; Gokan, N.; Ohnuki, K.; Horikawa, M.; Saito, R.; Shibata, Y. *Electrochem. Commun.* **2006**, *8*, 336–340.
10. Antoniadou, M.; Lianos, P. *Appl. Catal., B* **2010**, *99*, 307–313.

11. Antoniadou, M.; Lianos, P. *Photochem. Photobiol. Sci.* **2011**, *431*, 431–435.
12. Liu, Y. B.; Li, J. H.; Zhou, B. X.; Chen, H. C.; Wang, Z. S.; Cai, W. M. *Chem. Commun.* **2011**, *47*, 10314–10316.
13. Chen, X.; Liu, L.; Yu, P. Y.; Mao, S. S. *Science* **2011**, *331*, 746–750.
14. Tada, H.; Jin, Q. L.; Nishijima, H.; Yamamoto, H.; Fujishima, M.; Okuoka, S. I.; Hattori, T.; Sumida, Y.; Kobayashi, H. *Angew. Chem., Int. Ed.* **2011**, *50*, 3501–3505.
15. Livraghi, S.; Paganini, M. C.; Giamello, E.; Selloni, A.; Valentin, C. D.; Pacchioni, G. *J. Am. Chem. Soc.* **2006**, *128*, 15666–15671.
16. Osterloh, F. E. *Chem. Mater.* **2008**, *20*, 35–54.
17. Antoniadou, M.; Lianos, P. *Photochem. Photobiol. Sci.* **2011**, *431*, 431–435.
18. Su, M.; He, C.; Zhu, L.; Sun, Z.; Shan, C.; Zhang, Q.; Shu, D.; Qiu, R.; Xiong, Y. *J. Hazard. Mater.* **2012**, *229*, 72–82.
19. Ren, K. X.; Zhang, K.; Liu, J.; Luo, L. D.; Huang, Y. B.; Yu, X. B. *Cryst. Eng. Comm.* **2012**, *14*, 4384–4390.
20. Xiao, X.; Zhang, W. D. *J. Mater. Chem.* **2010**, *20*, 5866–5870.
21. Li, Y. Y.; Wang, J. S.; Yao, H. C.; Dang, L. Y.; Li, Z. G. *J. Mol. Catal. A: Chem.* **2011**, *334*, 116–122.
22. Zhang, X.; Ai, Z. H.; Jia, F. L.; Zhang, L. Z. *J. Phys. Chem. C* **2008**, *112*, 747–753.
23. Yu, J. C.; Yu, J. G.; Ho, W. K.; Jiang, Z. T.; Zhang, L. Z. *Chem. Mater.* **2002**, *14*, 3808–3816.
24. Ge, S.; Zhao, K.; Zhang, L. Z. *J. Nanopart. Res.* **2012**, *14*, 1015.
25. Liu, H.; Cao, W. R.; Su, Y.; Wang, Y.; Wang, X. H. *Appl. Catal. B: Environ.* **2012**, *111– 112*, 271–279.
26. Poznyak, S. K.; Kulak, A. I. *Electrochim. Acta* **1990**, *35*, 1941–1947.
27. Wang, K. W.; Jia, F. L.; Zhang, L. Z. *Mater. Lett.* **2013**, *92*, 354–357.
28. Zhao, K.; Zhang, X.; Zhang, L. Z. *Electrochem. Commun.* **2009**, *11*, 612–615.
29. Wang, K. W.; Jia, F. L.; Zheng, Z.; Zhang, L. Z. *Electrochem. Commun.* **2010**, *12*, 1764–1767.
30. Kim, D. H.; Anderson, M. A. *Environ. Sci. Technol.* **1994**, *28*, 479.
31. He, C.; Li, X. Z.; Graham, N.; Wang, Y. *Appl. Catal. A* **2006**, *305*, 54–63.
32. Chen, X. B.; Shen, S. H.; Guo, L. J.; Mao, S. S. *Chem. Rev.* **2010**, *110*, 6503–6570.
33. Yu, C. L.; Yu, J. C.; Fan, C. F.; Wen, H. R.; Hu, S. J. *Mater. Sci. Eng., B* **2010**, *166*, 213–219.
34. Yang, L. B.; Jiang, X.; Ruan, W. D.; Yang, J. G.; Zhao, B.; Xu, W. Q.; Lombardi, J. R. *J. Phys. Chem. C* **2009**, *113*, 16226–16231.
35. Sajiki, J.; Yonekubo, J. *Chemosphere* **2003**, *51*, 55–62.
36. He, C.; Shu, D.; Su, M.; Xia, D.; Abou Asi, M.; Lin, L.; Xiong, Y. *Desalination* **2010**, *253*, 88–93.
37. Xia, J. X.; Yin, S.; Li, H. M.; Xu, H.; Xu, L.; Zhang, Q. *Colloids Surf., A* **2011**, *387*, 23–28.

Chapter 10

Iron-Enriched Mineral Oxides: A Class of Sustainable Oxygenation Catalysts for Water Decontamination

Yue Li[1] and Weile Yan[*],[1]

[1]Department of Civil and Environmental Engineering, Texas Tech University, Lubbock, Texas 79409, U.S.A.
[*]E-mail: weile.yan@ttu.edu.

Iron-based catalysts have attracted much interest in recent years owing to its benign nature, abundant presence in the natural environment, and strong catalytic activity for oxygenation reactions. Compared to pure iron oxides, the reactivity of iron species attached to a separate mineral phase has received limited attention, although surfaces arising from the incorporation of aqueous iron on mineral phases such as alumina and silica can have a significance presence in the natural and engineered aquatic systems. Initial and ongoing studies by the authors suggest that the properties of the surface-residing iron species, including the surface density, state of dispersion, and coordination environment have considerable impacts on the ability of these iron-enriched mineral oxides in catalyzing the oxidation of aquatic contaminants in the presence of H_2O_2. These properties are strongly influenced by the properties of the mineral oxides, the aqueous chemistry, and the nature of iron precursors. While initial results suggest potential application of iron-enriched mineral phases as a class of benign catalysts for water purification or decontamination, challenges remain to quantitatively assess their surface characteristics in order to predict reactivity of solids formed under diverse aqueous conditions.

Introduction

Environmental Chemistry of Fe(II) and Fe(III) at Solid−Water Interfaces

The interactions between iron and natural minerals have been under intense studies in recent decades. The attention is not only because of the abundance and participation of iron in a variety of geochemical transformations but also the strong anthropogenic input in redistributing iron species in the natural environment. Iron is the fourth most abundant element in the Earth's crust, and ranks the second in the metal abundances (*1, 2*). Human activities, such as mining of iron-containing mineral ores and extraction of groundwater, along with natural processes such as mineral weathering have brought about a net accumulation of iron in the Earth's surface environment (*3, 4*). Iron-bearing minerals play significant roles in metal adsorption/precipitation, redox transformation of nutrients and trace elements, and microbiological metabolic cycles. In these processes, iron is mainly present in the divalent (Fe(II) or ferrous iron) or trivalent (Fe(III) or ferric iron) state, and toggling between the two major oxidation states of iron is a vital mechanism nature adopts to drive energy exchange within the vast ecological system. A unique attribute of iron that profoundly influences its environmental chemistry is the dramatically different solubility of Fe(II) and Fe(III) compounds. Both aqueous Fe(II) and Fe(III) ions are subject to hydrolysis when there is a significant presence of OH$^-$ ions in water. Hydrolysis occurs to a greater extent with an increasing pH (Equations 1a & b) (*5, 6*). Ferrous ions are fairly soluble around neutral pH values. They are mainly in a hexa-aquo form as $Fe(H_2O)_6{}^{2+}$ in acidic water and become hydroxide-complexed when pH is above 3 (*7*). Fe(III), on the other hand, exists as $Fe(H_2O)_6{}^{3+}$ in strictly acidic environment containing noncomplexing counterions only. Hydrolyzed Fe(III) becomes the dominant form when pH increases above 3. All the hydrolysis products of Fe(III) have low solubility, and they undergo oxolation and olation to form poly-nuclear iron complexes that eventually precipitate out as ferric (oxyhydr)oxides (*8*). Fe(II) may also co-precipitate with Fe(III) to form mixed Fe(II)-Fe(III) oxides at pH greater than 3 (*9*).

$$Fe(H_2O)_6{}^{2+} + H_2O \leftrightarrow Fe(H_2O)_5OH^+ + H_3O^+ \qquad \text{(1a)}$$

$$Fe(H_2O)_6{}^{2+} + 2H_2O \leftrightarrow Fe(H_2O)_4(OH)_2 + 2H_3O^+ \qquad \text{(1b)}$$

$$Fe^{3+} \leftrightarrow FeOH^{2+} \leftrightarrow Fe(OH)_2^+ \leftrightarrow Fe_2(OH)_2^{4+} \leftrightarrow$$

$$other\ polynuclear\ species \leftrightarrow Fe_2O_3 \cdot nH_2O(s) \qquad \text{(2)}$$
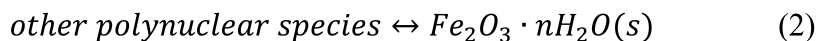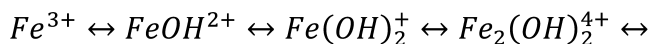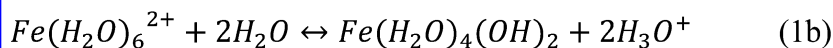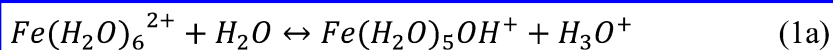
Redox conditions in the environment and solubility of the two iron species dictate an elevated presence of dissolved iron, predominantly as Fe(II), in groundwater. As groundwater moves closer to the soil surface, an increasing

level of dissolved oxygen drives the oxidation of Fe(II) to Fe(III). Precipitation of Fe(III) (oxyhydr)oxide begins with nucleation of polymeric Fe(III) clusters in the homogeneous solution phase or heterogeneously through assembling nuclei on the surface of a substrate (*10–12*). Homogeneous nucleation generally entails a higher activation energy barrier than heterogeneous nucleation, which partly explains the observed relative slow kinetics of Fe(II) oxidation in the absence of solid surfaces (*13*). In natural waters, surfaces of common mineral oxides such as silica and aluminosilicates are efficient at catalyzing the oxidation of Fe(II) to Fe(III) by dissolved oxygen at circumneutral pH. It is thought that oxidation is preceded by an adsorption step where the hydroxyl groups on the mineral surfaces act as ligands to bind with Fe(II) and facilitate its conversion to the ferric state (*14*). Depending on the surface energies of the substrates vs. the surface anchored iron species, more iron from the solution phase may precipitate on the substrate (nucleation) or on the existing nuclei to form bigger particles (growth) (*15*). The outcome of the two competing processes is delicately balanced by the nature of the substrate and dissolved iron as well as the ionic strength and composition of the solution. For instance, through *in-situ* measurements of ferric hydroxide nucleation and growth on quartz, muscovite, and corundum, Hu *et al.* concluded that nucleation is more favored on corundum than on the other two mineral substrates owing to a combination of a high substrate-water interfacial energy, low precipitate-substrate interfacial energy, and good lattice compatibility between the corundum and the ferric hydroxide phases (*12*).

In accordance with the discussion above, it is reasonable to expect that, in situations where there is a large presence of solid-water interface relative to the aqueous phase (*e.g.,* near the oxic/anoxic transition zones of subsurface soils), iron oxidation and precipitation on solids would dominate over homogeneous nucleation, thereby accounting for the ubiquitous occurrence of iron-impregnated mineral particles in the surface or shallow underground environment. A vast body of literature exists on the adsorptive properties of single-phase iron (oxyhyr)oxide particles (*e.g.*, poorly crystalline ferrihydrite, goethite, hematite, and magnetite) (*16–20*). They are shown to play a major role in controlling the mobility of trace elements in the environment by virtue of their high surface areas and adsorption capacities (*4, 21*). In comparison, the chemistry and environmental behavior of interfacial iron species (*i.e.,* iron residing on the surface of a dissimilar mineral phase) have not been systematically investigated. Based on the studies of iron oxides, it is anticipated that the incorporation of iron on background mineral phases would result in higher surface areas and adsorption capacities relative to the unamended substrates. However, the redox lability of the interfacial iron species relative to single-phase iron oxides is harder to predict, as it is often observed in heterogeneous catalysis that the interactions between substrates and the surficial redox-active metal species can significantly alter the catalytic activity of the metal catalysts. Indeed, various forms of synthetic iron catalysts have been applied in many environmental applications, and studies of these materials can provide a relevant context for us to probe into the reactivity of iron residing on common mineral interface found in environmental systems.

Iron-Based Catalysts for Environmental Decontamination

The use of dissolved iron and other transition metal ions as homogeneous catalysts in advanced oxidation of recalcitrant organic pollutants have been well documented (*22–25*). The processes typically involve the generation of radicals, particularly the strong, nonselective hydroxyl radicals, with the addition of oxidants such as ozone and hydrogen peroxide at an ambient temperature or with the use of air (i.e., oxygen) at elevated temperatures. With hydrogen peroxide as a radical precursor, cyclic reactions between Fe(II) and Fe(III) take place in the solution phase (Scheme 1), constituting the classic Fenton reaction and one of the most important abiotic pathways for water decontamination. The hydroxyl radicals may attack organic compounds by hydrogen-abstraction, addition to carbon double bonds, or addition to aromatic rings (*26*). The latter two processes form organic radicals, which in the presence of molecular oxygen may lead to peroxyl radicals (R-OO·) or superoxide ($O_2^{·-}$), propagating more complete oxidative transformation (*7*).

$$H_2O_2 \quad Fe(II) \quad HO^- + HO·$$
$$HO_2· \quad Fe(III) \quad H_2O_2$$
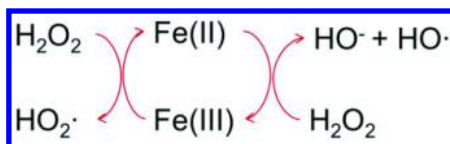
Scheme 1. Chemistry of Classic Fenton Process

The optimal pH of the classic Fenton reaction is in the range of pH 2-4 due to a compromise between an increasing reactivity with hydrolyzed Fe(II) and a lower solubility of Fe(III) as pH rises (*7*). As such, Fenton reaction requires acidification of influent and neutralization of treated water in addition to sludge disposal and catalyst recycling operations.

Considerable efforts have been made to immobilize iron on solid supports such as silica, alumina, and aluminosilicate (*e.g.*, zeolites) to enable reactions at solid/gas or solid/liquid interfaces. Solid catalysts are inherently more desirable due to the high costs associated with catalyst synthesis, separation and recycling in the homogeneous systems. Compared to bulk iron oxide particles, supported iron has been shown to be highly active in selective partial oxidation (*e.g.*, the highly sought-after methane to methanol conversion) (*27, 28*) and in Fenton-like oxidation of organic contaminants (*29–32*), indicating a very strong synergy between iron and the underlying supports. The mechanism of this enhancement effect is subject to ongoing investigations; however, drawing on the knowledge of other analogous heterogeneous catalytic systems, the authors hypothesize that the reactivity of interfacial iron species may be affected by one or a combination of the following effects:

Effect on Physical Dispersion of Iron Species

Depending on the nature of the substrates and the solution conditions, iron may exist as isolated adsorbates, molecular clusters (e.g., as polynuclear complexes), or discrete iron oxide precipitates. It has been demonstrated that alumina and zeolite favor surface adsorption over the formation of bulk iron oxide precipitates, thereby increasing the active sites available for reactions (*27, 33*). Such phenomena can be explained through classical nucleation theories based on interfacial energies and electrostatic interactions (*15*), although the observations may also reflect a contribution from the acid-base chemistry and electronic properties of the substrate surface (as discussed below).

Effect on Surface Acid-Base Characteristics

The availability and strength of surface acid sites are salient properties controlling catalyst activity and selectivity (*34*). Pure silica tetrahedra have no acidity on the surface. Isomorphical substitution of Si(IV) by Al(III) creates negative charges, which are compensated by positive ions such as H^+, giving rise to Brønsted acidity (*35*). Additionally, Al(III) and Fe(III) are strong Lewis acids. The strong electron negativity of the trivalent metals is able to induce Brønsted acidity on the neighboring OH groups (*36, 37*). In the case of non-selective oxygenation reactions by supported iron catalysts, it is perceived that Brønsted and Lewis acid sites may promote the reduction of Fe(III) to Fe(II), a rate-limiting step in Fenton chemistry, and the catalytic decomposition of H_2O_2 to reactive oxygen species (ROS) (*33*).

Effect on Electronic Structures of Metals

On hydrous oxide surfaces, coordination of metal ions with the surface $\equiv$OH groups may alter the electron density at the metal center and affect charge transfer rates. This effect has been described by Wehrli *et al.* when studying oxidation of transition metals (*e.g.*, Fe(II), V(IV)) on hydrous mineral surfaces (*14, 38*).

There has been long-running debates concerning the nature of the oxidants produced by surface-catalyzed H_2O_2 decomposition. Both free radicals (*e.g.*, hydroxyl and superoxide radicals) and ferryl species (-Fe^{IV}=O) are considered to be the probable oxygenation agents (*39–44*). The actual contribution of each is strongly affected by the coordination environment of iron and the reaction conditions (*40*). Experimentally, the generation of hydroxyl radicals may be detected through the use of selective probe compounds such as formic acid or benzoic acid (*45, 46*), or via electron spin resonance spectroscopy or fluorescence techniques (*47, 48*).
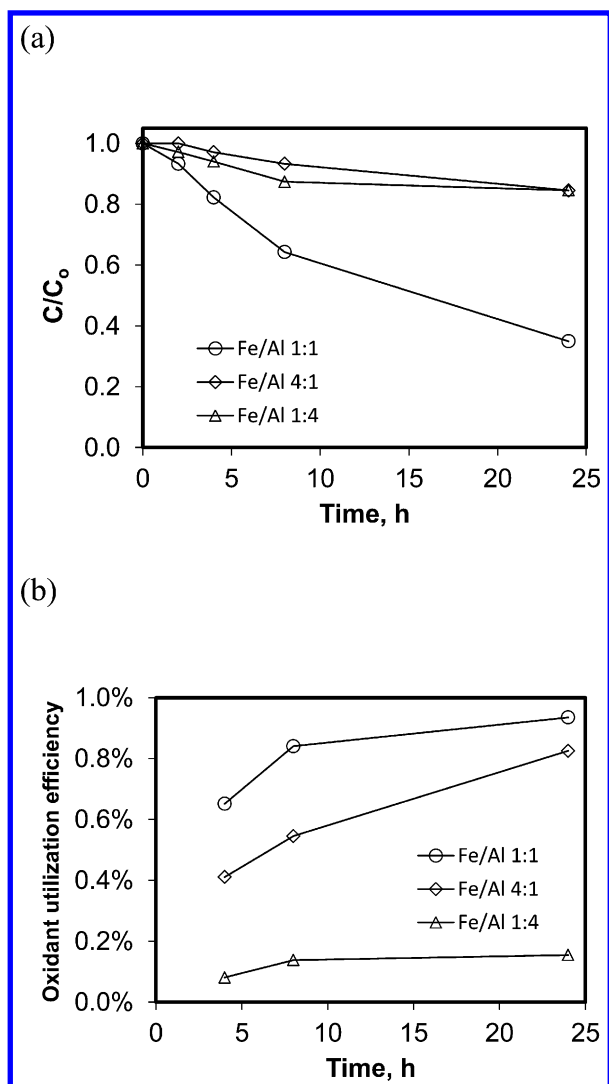
Figure 1. (a) Phenol oxidation catalyzed by Fe/Al xerogels of varying composition, and (b) oxidant consumption efficiency determined by the ratio of phenol oxidized over H_2O_2 consumed (both in mM). Xerogel loading was 4 g/L. Initial concentrations of phenol and H_2O_2 were 0.17 mM and 17 mM, respectively. Solids were annealed at 800 °C.

A challenge often encountered in studies of heterogeneous catalytic reactions is our limited ability in characterizing the structure of redox-active species on the surfaces and quantifying total surface reactive sites. In the absence of accurate descriptors of surface properties, studies have to resort to qualitative or empirical

parameters, which renders it difficult to predict the reactivity of surfaces in complex aquatic systems. Kwan & Voelker proposed that the production rate of HO· is proportional to the product of surface area and H_2O_2 concentration in a solution multiplied by a coordinating factor unique to certain iron-containing minerals (*49*). Their model fits reasonably well with the experimentally observed formic acid degradation but over-predicts OH· generation in other cases. In general, the yield of oxidants and the product distribution are sensitive to solution pH (*50*, *51*), suggesting the complex interplay between surface iron species and those solubilized by intermediate products (e.g. small organic acids). Elucidating the roles of different forms of iron species would require carefully designed experiments and complementary investigations of the aqueous and surface chemistry.

In the following section, the authors intend to briefly discuss two studies they have undertaken to understand the reactivity of Fe(III)-enriched minerals. The objective is to identify surface characteristics that have important bearings on iron catalytic activity. Such knowledge is preliminary at this time and it mainly serves to highlight a need for more diverse and complementary approaches to investigate the surfaces in order to acquire a deep understanding about the role of interfacial iron species in catalyzing the transformation of aqueous contaminants and the potential of harnessing their reactivity in water purification and decontaminantion applications.
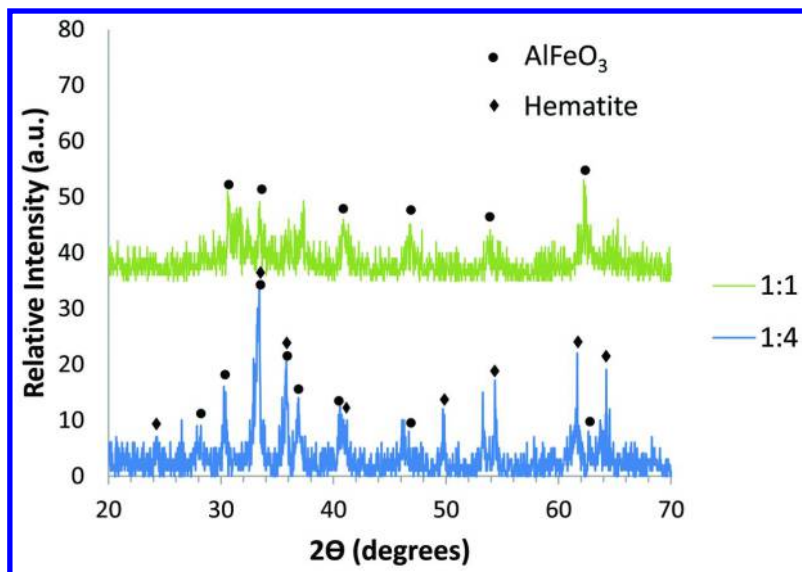
Figure 2. Powder X-ray diffraction patterns for the Al/Fe xerogels annealed at 800°C for 6 hours.
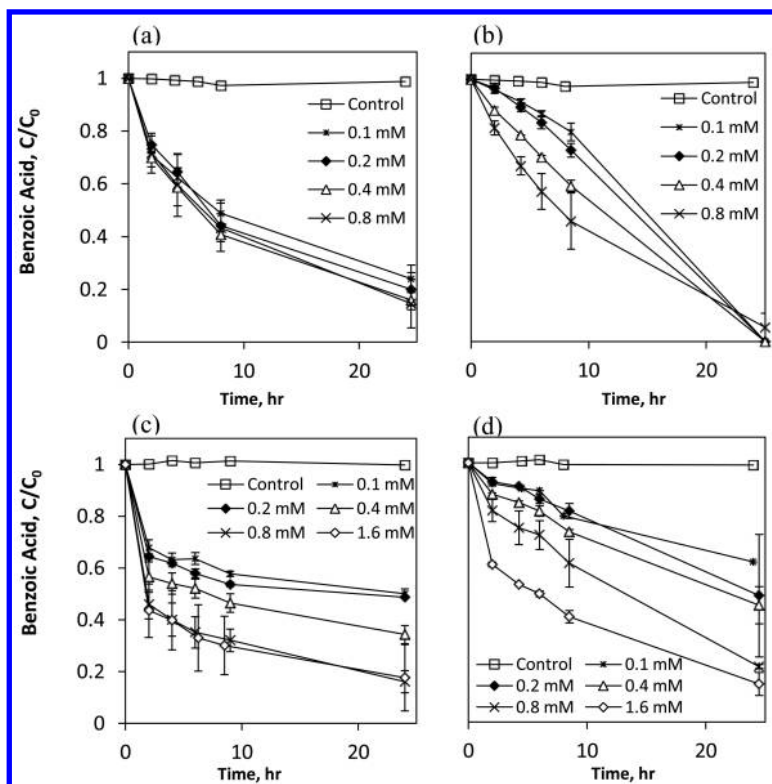
Figure 3. Transformation of benzoic acid catalyzed by Fe(III)-impregnated alumina nanoparticles ((a) & (c)) and Fe(III)-impregnated silica nanoparticles ((b) & (d)). Mineral solids in (a) & (b) were prepared by immersing pristine silica or alumina nanoparticles in Fe(II) solutions for 24 h, while those in (c) and (d) were equilibrated in Fe(III) solutions. Values shown in the legends are the initial concentrations of the iron solutions. The initial concentrations of benzoic acid and H_2O_2 were 0.078 and 11 mM, respectively. Solids were dosed at 1.5 g/L.

Case Study I: Fe(III)/Al(III) Xerogels for Catalytic Oxidation of Phenol

Colloidal particles with high surface areas and low densities can be prepared through sol-gel-derived synthesis methods, among which the well-established epoxide-driven poly-condensation of metal precursors is a facile approach to prepare single phase or binary mixtures of a wide variety of transition metal oxides (*52, 53*). Compared to conventional methods of catalyst preparation such as wet impregnation processes, sol-gel methods afford more control over the morphology and composition of particles while maximizing the interaction volume between two metal precursors (as in binary systems). In this study, aluminum nitrate and ferric chloride at an appropriate molar ratio (Fe/Al ratio of

1:4, 1:1, and 4:1) were dissolved in isopropanol. A precise quantity of propylene oxide was added to the metal solution as a proton scavenger to trigger controlled hydrolysis and polymerization of the metal salts. The resultant suspension was air-dried for 24 hours and annealed in a furnace at up to 800 °C for 6 h to form Fe/Al xerogels. The catalytic activity of these xerogels was evaluated through phenol oxidation in the presence of H_2O_2. Control experiments suggest negligible adsorption of phenol to the solid phase. As shown in Figure 1, the ratio of Fe(III)/Al(III) precursors has a marked effect on the activity of xerogel to catalyze the oxidation of phenol. The most reactive xerogel was made from equivalent molar concentrations of Fe(III) and Al(III) (Fe:Al = 1:1) (Figure 1a). The same solid is also the most oxidant-efficient catalyst as it generates the greatest amount of reactive oxygen species (ROS) per mole of H_2O_2 consumed (Figure 1b). Notably, X-ray diffraction analysis shows the 1:1 Fe/Al xerogel has a diffraction pattern corresponding to aluminum iron oxide ($AlFeO_3$, PDF# 30-24), whereas further increasing the Fe/Al ratio led to the formation of hematite in addition to $AlFeO_3$ (Figure 2). The observation of optimal reaction rate and H_2O_2 utilization efficiency for particles with an intermediate iron content implies that the structural organization of Fe(III) in the xerogel has a significant impact on the particles' redox activity. Fe(III) dispersed in a Al-Fe mixed oxide is more active than a separate phase of iron oxide formed at a higher Al/Fe ratio. The latter is known to elicit rapid unproductive H_2O_2 disproportionation instead of taking up a Fenton-like pathway to generate reactive oxidants (*22, 27, 30*).

Case Study II: Oxidation Activity of Fe(III)-Impregnated Silica and Alumina in Simulated Natural Waters

This study is part of an on-going effort to understand the effects of solution chemistry on the surface properties and reactivity of the resultant iron-impregnated mineral oxides. Commercial silica and alumina aerogels were used as proxies of the colloid-sized silica and alumina particles present in the aquatic environment. The impregnation of iron follows simple aqueous adsorption procedures, where pristine aerogels (at 0.6 g/L) were immersed in solutions amended with 5 – 10 mM NaCl as background electrolytes and dissolved iron (as Fe(II) or Fe(III)) at a concentration ranging from 0.1 to 1.6 mM for 24 h. The Fe(II) and Fe(III) stock solutions were prepared from $FeSO_4 \cdot 7H_2O$ and $FeCl_3 \cdot 6H_2O$, respectively. As the adsorption experiments were performed in equilibrium with the atmospheric environment, the surface-adsorbed Fe(II) should be readily converted to Fe(III) within the immersion period, hence the notation of Fe(II) or Fe(III) in Figure 3 and 4 are strictly referring to the valance state of iron in the starting solutions. Since groundwater carries a significant source of dissolved iron (as Fe(II) predominantly), this surface impregnation process bears significant relevance to an ubiquitous phenomenon of accumulation of iron onto mineral colloids as water flows from a reducing environment to the surface atmospheric environment. The catalytic activity of the Fe(III)-amended minerals was investigated using benzoate as a target compound and H_2O_2 as the source of oxidants. Parallel experiments in the absence of H_2O_2 were carried out to assess the potential adsorption of

benzoate to alumina (*54, 55*) and to a less extent silica (*56*). Figure 3 shows the decreases in benzoate concentrations in the presence of various mineral solids. All mineral particles, including those exposed to low concentrations of dissolved iron, acquire a significant level of catalytic activity with the incorporation of iron on the surface. Correcting the substrate adsorption effect allows us to determine the rates of benzoate oxidation as a function of Fe surface density (Figure 4, for solids immersed in Fe(II) solutions only). An important feature shown in this figure is that the curves corresponding to different mineral substrates largely fall on the same line when reactivity was plotted as a function of iron surface density. Moreover, the reactivity of each type of solid reaches a plateau as the Fe density rises beyond ~ 3 Fe atoms/nm^2, implying a surface saturation effect typical of heterogeneous catalysts. While the amount of data precludes us from making strong inference here, it is evident that there is a strong correlation between the reactivity of these mineral colloids and the quantity of surface-residing iron species. Furthermore, the saturation of catalytic oxidation activity at high Fe loadings points out that the availability and the nature of background mineral particles, such as silica and alumina, likely exert a greater influence on the redox activity in the aquatic systems than previously recognized.
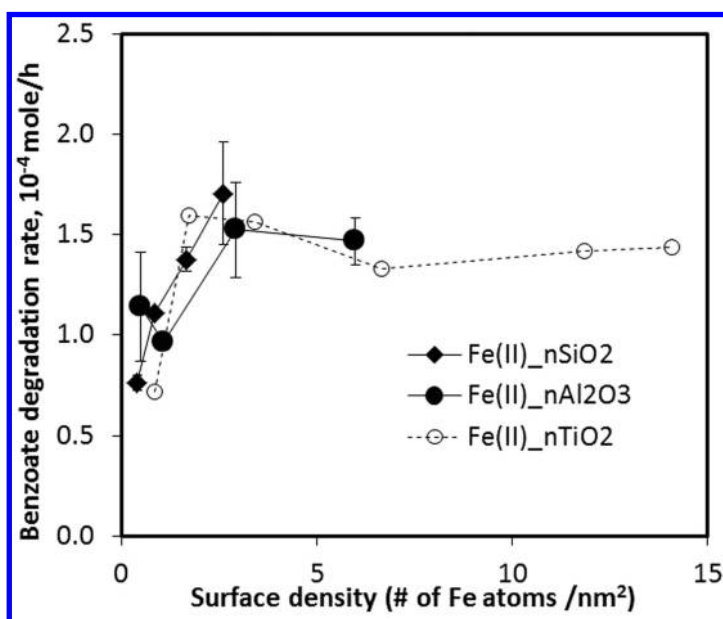
Figure 4. Oxidative transformation rate of benzoate as a function of Fe surface density. Solids were prepared by immersing in Fe(II) solutions for 24 h.

Acknowledgments

The authors would like to thank Drs. Louisa Hope-weeks and Fernando Hung for their help in preparing and characterizing the Al/Fe xerogel materials.

References

1.   Taylor, K. G.; Konhauser, K. O. *Elements* **2011**, *7* (2), 83–88.
2.   Cornell, R. M.; Schwertmann, U. Introduction to the iron oxides. In *The iron oxides: structure, properties, reactions, occurrences and uses*, 2nd ed.; John Wiley & Sons: Weinheim, Germany, 2006; pp 1−5.
3.   Muller, D. B.; Wang, T.; Duval, B.; Graedel, T. E. *Proc. Natl. Acad. Sci. U.S.A.* **2006**, *103* (44), 16111–16116.
4.   Hassellov, M.; von der Kammer, F. *Elements* **2008**, *4* (6), 401–406.
5.   Wells, C.; Salam, M. *Nature* **1965**, *205*, 690–692.
6.   Wells, C.; Salam, M. *J. Chem. Soc. A* **1968**, 24–29.
7.   Pignatello, J. J.; Oliveros, E.; MacKay, A. *Crit. Rev. Environ. Sci. Technol.* **2006**, *36* (1), 1–84.
8.   Henry, M.; Jolivet, J. P.; Livage, J. *Chemistry, Spectroscopy and Applications of Sol-Gel Glasses*; Springer: New York, 1992; Vol. 77, pp 153−206.
9.   Larese-Casanova, P.; Kappler, A. *Geochim. Cosmochim. Acta* **2012**, *91* (0), 171–186.
10. Roelands, C. M.; ter Horst, J. H.; Kramer, H. J.; Jansens, P. J. *Cryst. Growth Des.* **2006**, *6* (6), 1380–1392.
11. Wolthoorn, A.; Temminghoff, E. J. M.; Weng, L. P. *Appl. Geochem.* **2004**, *19* (4), 611–622.
12. Hu, Y.; Neil, C.; Lee, B.; Jun, Y.-S. *Environ. Sci. Technol.* **2013**, *47* (16), 9198–9206.
13. Sung, W.; Morgan, J. J. *Environ. Sci. Technol.* **1980**, *14* (5), 561–568.
14. Wehrli, B.; Sulzberger, B.; Stumm, W. *Chem. Geol.* **1989**, *78* (3-4), 167–179.
15. Jun, Y.-S.; Lee, B.; Waychunas, G. A. *Environ. Sci. Technol.* **2010**, *44* (21), 8182–8189.
16. Davis, J. A.; Leckie, J. O. *Environ. Sci. Technol.* **1978**, *12* (12), 1309–1315.
17. Benjamin, M. M. *Environ. Sci. Technol.* **1983**, *17* (11), 686–692.
18. Ali, M. A.; Dzombak, D. A. *Geochim. Cosmochim. Acta* **1996**, *60* (2), 291–304.
19. Buerge-Weirich, D.; Behra, P.; Sigg, L. *Aquat. Geochem.* **2003**, *9* (2), 65–85.
20. Coughlin, B. R.; Stone, A. T. *Environ. Sci. Technol.* **1995**, *29* (9), 2445–2455.
21. Hochella, M. F., Jr.; Lower, S. K.; Maurice, P. A.; Penn, R. L.; Sahai, N.; Sparks, D. L.; Twining, B. S. *Science* **2008**, *319* (5870), 1631–1635.
22. Pignatello, J. J. *Environ. Sci. Technol.* **1992**, *26* (5), 944–951.
23. Wang, J. L.; Xu, L. J. *Crit. Rev. Environ. Sci. Technol.* **2012**, *42* (3), 251–325.
24. Sun, C.; Chen, C.; Ma, W.; Zhao, J. *Phys. Chem. Chem. Phys.* **2011**, *13* (6), 1957–1969.

25. Anipsitakis, G. P.; Dionysiou, D. D. *Environ. Sci. Technol.* **2004**, *38* (13), 3705–3712.
26. Lal, M.; Rao, R.; Fang, X.; Schuchmann, H.-P. *J. Am. Chem. Soc.* **1997**, *119* (24), 5735–5739.
27. Balu, A. M.; Pineda, A.; Yoshida, K.; Campelo, J. M.; Gai, P. L.; Luque, R.; Romero, A. A. *Chem. Commun.* **2010**, *46* (41), 7825–7827.
28. Hammond, C.; Forde, M. M.; Ab Rahim, M. H.; Thetford, A.; He, Q.; Jenkins, R. L.; Dimitratos, N.; Lopez-Sanchez, J. A.; Dummer, N. F.; Murphy, D. M.; Carley, A. F.; Taylor, S. H.; Willock, D. J.; Stangland, E. E.; Kang, J.; Hagen, H.; Kiely, C. J.; Hutchings, G. J. *Angew. Chem., Int. Ed.* **2012**, *51* (21), 5129–5133.
29. Pham, A. L.-T.; Lee, C.; Doyle, F. M.; Sedlak, D. L. *Environ. Sci. Technol.* **2009**, *43* (23).
30. Garrido-Ramirez, E. G.; Theng, B. K. G.; Mora, M. L. *Appl. Clay Sci.* **2010**, *47* (3-4), 182–192.
31. Fajerwerg, K.; Debellefontaine, H. *Appl. Catal., B* **1996**, *10* (4), L229–L235.
32. Dhakshinamoorthy, A.; Navalon, S.; Alvaro, M.; Garcia, H. *ChemSusChem* **2012**, *5* (1), 46–64.
33. Lim, H.; Lee, J.; Jin, S.; Kim, J.; Yoon, J.; Hyeon, T. *Chem. Commun.* **2006**, (4), 463–465.
34. Pines, H.; Haag, W. *J. Am. Chem. Soc.* **1960**, *82* (10), 2471–2483.
35. Sposito, G. In *The Chemistry of Soils*, 2nd ed.; Oxford University Press: New York, 2008; pp 36−41.
36. Corma, A. *Chem. Rev.* **1995**, *95* (3), 559–614.
37. Ryoo, R.; Jun, S.; Kim, J. M.; Kim, M. J. *Chem. Commun.* **1997** (22), 2225–2226.
38. Wehrli, B.; Stumm, W. *Geochim. Cosmochim. Acta* **1989**, *53* (1), 69–77.
39. Sawyer, D. T.; Sobkowiak, A. *Acc. Chem. Res.* **1996**, *29* (9), 409–416.
40. Walling, C. *Acc. Chem. Res.* **1998**, *31* (4), 155–157.
41. Pang, S. Y.; Jiang, J.; Ma, J. *Environ. Sci. Technol.* **2011**, *45* (1), 307–312.
42. Gonzalez-Olmos, R.; Holzer, F.; Kopinke, F. D.; Georgi, A. *Appl. Catal., A* **2011**, *398* (1-2), 44–53.
43. Lee, H.; Lee, H.-J.; Sedlak, D. L.; Lee, C. *Chemosphere* **2013**, *92* (6), 652–658.
44. Sutton, H. C.; Winterbourn, C. C. *Free Radical Biol. Med.* **1989**, *6* (1), 53–60.
45. Baker, M. S.; Gebicki, J. M. *Arch. Biochem. Biophys.* **1984**, *234* (1), 258–264.
46. Sutton, H. C. *J. Free Radical Biol. Med.* **1985**, *1* (3), 195–202.
47. Schoonen, M. A. A.; Cohn, C. A.; Roemer, E.; Laffers, R.; Simon, S. R.; O'Riordan, T. *Rev. Mineral. Geochem.* **2006**, *64*, 179–221.
48. Vejerano, E.; Lomnicki, S. M.; Dellinger, B. *Environ. Sci. Technol.* **2012**, *46* (17), 9406–9411.
49. Kwan, W. P.; Voelker, B. M. *Environ. Sci. Technol.* **2003**, *37* (6), 1150–1158.
50. Liou, M.-J.; Lu, M.-C. *J. Hazard. Mater.* **2008**, *151* (2), 540–546.
51. Barreiro, J. C.; Capelato, M. D.; Martin-Neto, L.; Bruun Hansen, H. C. *Water Res.* **2007**, *41* (1), 55–62.

52. Pajonk, G. M. *Appl. Catal.* **1991**, *72* (2), 217–266.
53. Pierre, A. C.; Pajonk, G. M. *Chem. Rev.* **2002**, *102* (11), 4243–4265.
54. Guan, X.-h.; Chen, G.-h.; Shang, C. *J. Environ. Sci.* **2007**, *19* (4), 438–443.
55. Meier, D. M.; Urakawa, A.; Baiker, A. *Phys. Chem. Chem. Phys.* **2009**, *11* (43), 10132–10139dy..
56. Stolpe, N. B.; McCallister, D. L.; Shea, P. J.; Lewis, D. T.; Dam, R. *Environ. Pollut.* **1993**, *81* (3), 287–295.

Degradation of Trichloroethylene and Methylene Blue by a Mixture of Fe⁰ and γ-Fe₂O₃ − A Review

Y. Watanabe,[1] S. Kubuki,*,[1] and T. Nishida[2]

[1]Department of Chemistry, Graduate School of Science and Engineering, Tokyo Metropolitan University, Minami-Osawa 1-1, Hachi-oji, Tokyo 192-0397, Japan
[2]Department of Biological and Environmental Chemistry, Faculty of Humanity-Oriented Science and Engineering, Kinki University, 11-6 Kayanomori, Iizuka, Fukuoka 820-8555, Japan
***E-mail: kubuki@tmu.ac.jp.**

In this chapter, relationships between local structure and organic compounds decomposing ability of Fe^0 + γ-Fe_2O_3 mixture were introduced by applying gas chromatography (GC), ultraviolet-visible light absorption spectroscopy (UV-VIS), electrospray-ionized mass spectroscopy (ESI-MS), X-ray diffractometry (XRD) and ^{57}Fe-Mössbauer spectroscopy. Decrease in concentration of trichloroethylene (TCE) aqueous solution from 10.0 to 0.09 mg L^{-1} was observed from 10-day decomposition test using mixture of industrially produced Fe^0 (zero valent iron) and iron oxide mainly composed by γ-Fe_2O_3 with the total amount and the mass ratio of 5.0 g and 3:7, respectively. ^{57}Fe-Mössbauer spectra of iron+iron oxide mixture during the decomposition test showed decrease in the absorption area (A) of iron from 40.6 to 1.0 %, and increase in 'A' attributed to $Fe^{2.5+}O_6$ octahedra (O_h) from 15.4 to 49.2 %, indicating that iron+iron oxide mixture is converted to Fe_3O_4 caused by an oxidation of Fe^0. A consistent first order rate constant (k) of $0.30_{\pm 0.01}$ day^{-1} for oxidation of iron in the iron+iron oxide mixture and decomposition of TCE was estimated, indicating that TCE was decomposed by the oxidation from Fe^0 to $Fe^{2.5+}(O_h)O_6$ in Fe_3O_4. A precipitation

of Fe_3O_4 due to oxidation from Fe^0 to $Fe^{2.5+}(O_h)O_6$ was also observed from the decomposition test using $Fe^0+\gamma\text{-}Fe_2O_3$ (3:7) bulk mixture and 10 μmol L^{-1} methylene blue (MB) aqueous solution. The k value of MB decomposition determined to be $6.5_{\pm0.9} \times 10^{-3}$ h^{-1} becomes larger when using nanoparticles (NPs) of $\gamma\text{-}Fe_2O_3$ ($k = 1.2_{\pm0.1} \times 10^{-1}$ h^{-1}), suggesting that the increase in surface area of $\gamma\text{-}Fe_2O_3$ NPs affects the effectiveness of MB decomposing ability. It is concluded that $Fe^0+\gamma\text{-}Fe_2O_3$ mixture can be utilized for environmental purification, and organic compounds decomposing ability can be enhanced by using iron or iron oxide nanoparticles.

Introduction

Trichloroethylene (TCE) is prohibited to use because of the toxicity to the human beings and pollution to the environment. Nowadays, contamination of water and soil is caused by volatile organic compound (VOC) like TCE, toluene, benzene *etc*. In order to solve the environmental pollution caused by VOC, several detoxification methods have been developed such as adsorption by charcoal filter or remediation by microorganism (*1–4*). Metallic iron has also been recognized as an agent for the decomposition of TCE (*5, 6*), but the structural change during TCE decomposition was not revealed.

In this study, relationships between local structure and organic compounds decomposing ability of ($Fe^0 + \gamma\text{-}Fe_2O_3$) mixture were investigated by using gas chromatography (GC), ultraviolet-visible light absorption spectroscopy (UV-VIS), electrospray-ionized mass spectroscopy (ESI-MS), X-ray diffractometry (XRD) and ^{57}Fe-Mössbauer spectroscopy.

Relationship between Decomposition of Trichloroethylene and Structual Changes in Solid Mixture of Fe^0 and $\gamma\text{-}Fe_2O_3$

^{57}Fe-Mössbauer spectroscopy (nuclear resonant γ-ray absorption spectroscopy) is a powerful tool to characterize the structure of iron and iron oxide. It provides useful information about the magnetic field at the nucleus and the valence of Fe (*7*). Mössbauer spectra of the industrially produced (iron + iron oxide) mixtures with mass ratios of 0:10, 2:8, 3:7, 4:6, 5:5, and 10:0 are presented in Figure 1 (*8*). Mössbauer spectrum of the industrially produced iron oxide (Figure 1 (a)) is composed of two magnetic sextets with isomer shift (δ) of $0.32_{\pm0.01}$ mm s^{-1} and internal magnetic fields (H_{int}) of $49.6_{\pm0.1}$ T for tetrahedral (T_d) Fe^{3+}, while δ of $0.61_{\pm0.01}$ mm s^{-1} and H_{int} of $45.5_{\pm0.1}$ T for octahedral (O_h) $Fe^{2.5+}$ (*8*). The absorption area (A) of $Fe^{3+}(T_d)$ and $Fe^{2.5+}(O_h)$ was respectively analyzed to be $75.4_{\pm0.5}$ and $24.6_{\pm0.5}$ % (*8*), indicating that industrially produced iron oxide consisted of a mixture of maghemite ($\gamma\text{-}Fe_2O_3$) and magnetite (Fe_3O_4), because the absorption area ratio of $Fe^{3+}(T_d)$ and $Fe^{2.5+}(O_h)$ for regular magnetite is reported to be 1:2 (*9, 10*). The XRD patterns of $\gamma\text{-}Fe_2O_3$ and Fe_3O_4 are almost identical because both have an inverse spinel structure (*11*).Therefore, Mössbauer

spectroscopy was applied to obtain quantitative information concerning chemical environment of iron and iron oxide. A peak intensity attributed to the iron with δ and H_{int} values of $0.01_{\pm 0.01}$ mm s^{-1} and $32.6_{\pm 0.1}$ T increased with the mass ratio (Figure 1 (b)-(f)) (8). This indicates that no solid reactions occurred even though the iron and iron oxide were mixed, because the peak intensity of both iron and iron oxide components changed in accordance with the component ratio.
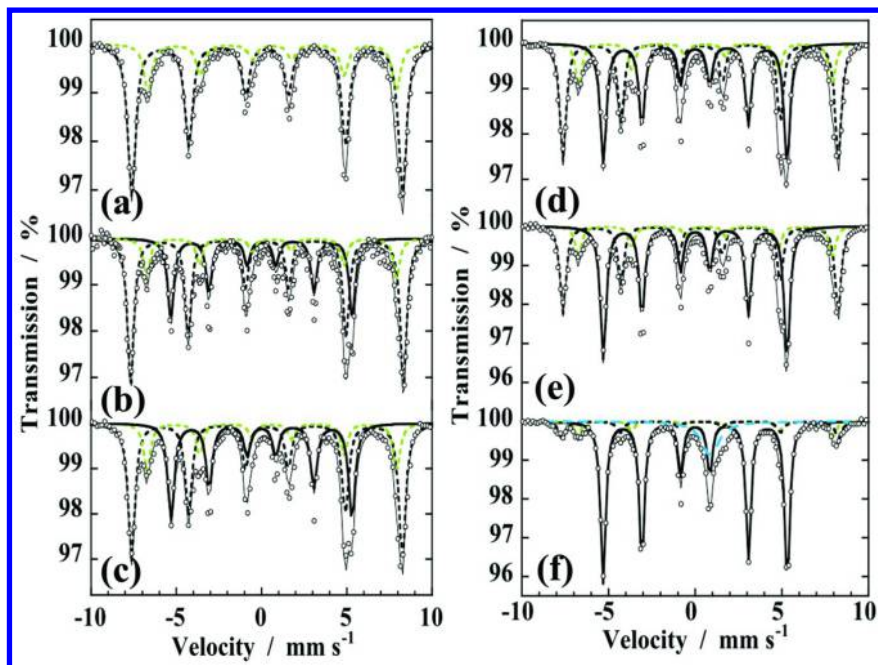
Figure 1. Mössbauer spectra of (iron + iron oxide) mixtures with mass ratios of (a) 0:10, (b) 2:8, (c) 3:7, (d) 4:6, (e) 5:5, and (f) 10:0. (Reproduced with permission from Ref. (8). 2013, Springer, Inc.)

XRD patterns of the industrially produced (iron + iron oxide) mixtures are shown in Figure 2 (8). XRD pattern of (iron + iron oxide) mixture with the ratio of 0:10 (Figure 2(a)) has sharp intense peaks at 2θ = 30.2, 35.6, 43.3, 53.6, 57.3 and 62.8° (8), showing that the industrially produced iron oxide is composed of a mixture of Fe_3O_4 (PDF No. 00-019-0629) and γ-Fe_2O_3 (PDF No. 00-039-1346). Increase in the iron content resulted in a gradual increase in the peak intensity from 84 to, 102, 159, 162 and 232 cps. at 2θ = 44.7° (Figures 2(b)-(f)) (8).
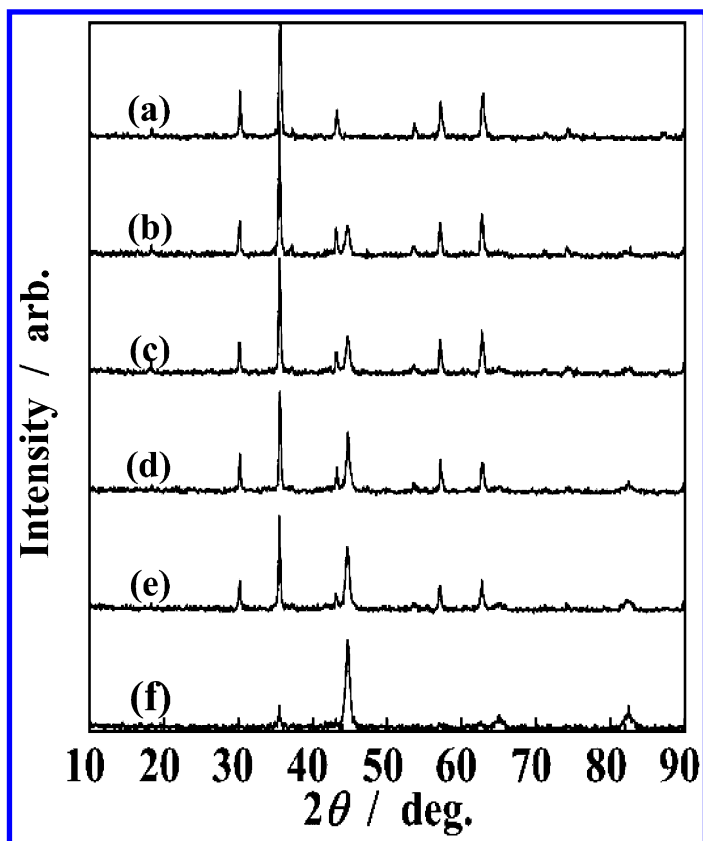
Figure 2. XRD patterns of (iron + iron oxide) mixtures with mass ratios of (a) 0:10, (b) 2:8, (c) 3:7, (d) 4:6, (e) 5:5, and (f) 10:0. (Reproduced with permission from Ref. (8). 2013, Springer, Inc.)

TCE decomposing ability was evaluated by soaking 5.0 g mixture of iron and iron oxide (γ-Fe_2O_3 + Fe_3O_4) in 200 mL of aqueous solution of TCE (Wako 208-08101) with a concentration of 10, 20, 30, 40, or 50 mg L^{-1} at 30 °C for 7 days. Gas chromatogram showed an intense peak attributed to the double bond and Cl atom of TCE at a retention time at 6.3 min. As shown in Figure 3(a), TCE concentration decreased from the initial value of 10 mg L^{-1} to 0.41, 0.52, 0.26, and 0.09 mg L^{-1} after 7-day decomposition with (iron + iron oxide) mixtures having mass ratios of 2:8, 3:7, 4:6 and 5:5, respectively (8). It should be noted that no decrease in the TCE concentration was found in the decomposition tests performed with only iron or iron oxide. A similar result was also obtained for the initial TCE concentration

of 50 mg L^{-1} (Figure 3(b)) (*8*), indicating that TCE was decomposed by the (iron + iron oxide) mixtures. A rate constant of first order reaction (*k*) can be estimated by following equation, *i.e.*,

$$C_t = C_0 \exp(-kt) \tag{1},$$

where C_t is concentration of TCE solution after *t*-day decomposition.
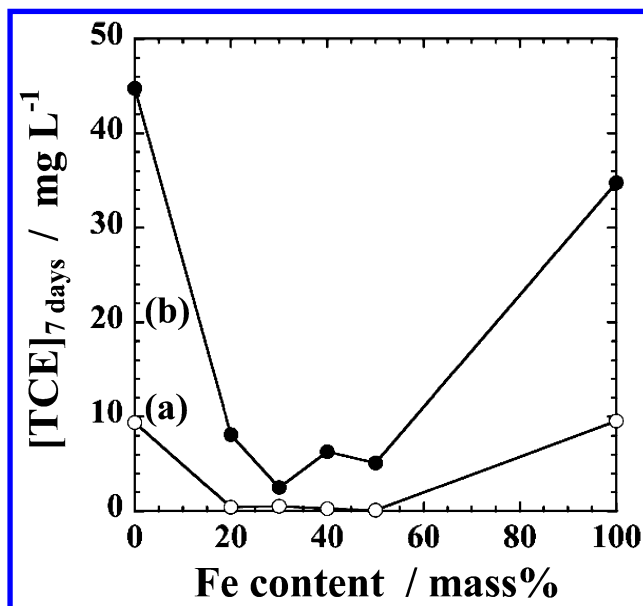
Figure 3. Decrease in TCE concentration having the initial values of (a) 10 and (b) 50 mg L^{-1} after 7-day decomposition test with various ratios of (iron + iron oxide) mixtures. (Reproduced with permission from Ref. (8). 2013, Springer, Inc.)

By using equation (1), *k* value for TCE decomposition was determined to be $0.30_{\pm 0.01}$ day^{-1} (Figure 4(d)). This value is larger than that obtained by using 3:7 mixture of reagent grade ($Fe^0 + Fe_3O_4$), *i.e.*, $k = 0.18_{\pm 0.01}$ day^{-1} (Figure 4(e)). These results suggest that γ-Fe_2O_3 with defect spinel structure and also the particle size of each component influenced the oxidation of Fe^0.

Figure 5 shows Mössbauer spectra of (iron + iron oxide) mixture (3:7) after decomposition (*8*). After decomposition for 1, 2, 3, 7, and 10 days, the '*A*' for Fe^0 respectively decreased from 40.6 to 12.6, 13.2, 3.8, 2.8 and $1.0_{\pm 0.5}$ %, while that of $Fe^{2.5+}$ (O_h) increased from 15.4 to 29.7, 36.3, 50.4, 49.1, and 49.2% at the same time (*8*). This result indicates that Fe^0 in the mixture was oxidized to $Fe^{2.5+}(O_h)$ of Fe_3O_4.
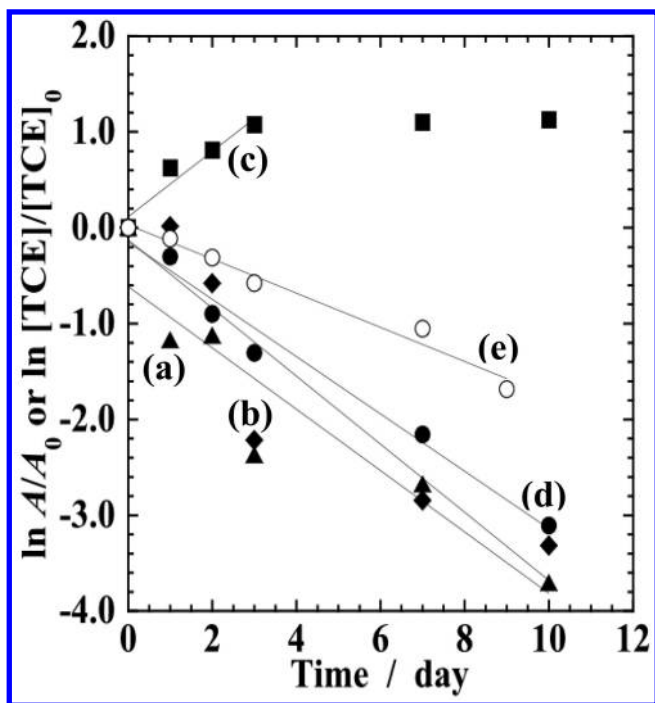
Figure 4. lnA/A₀ of (a) Fe⁰, (b) γ-Fe₂O₃ and (c) Fe₃O₄ from Mössbauer spectra vs. t, and (d) ln[TCE]/[TCE]₀ vs. t plots for decomposition tests with an (iron + iron oxide) mixture (3:7) and 10 mg L⁻¹ TCE aqueous solution. (e) ln[TCE]/[TCE]₀ vs. t plot for a decomposition test with the same conditions using the reagent grade (Fe⁰ + Fe₃O₄) mixture (3:7). (Reproduced with permission from Ref. (8). 2013, Springer, Inc.)

Relationship between Decomposition of Methylene Blue and Structual Changes in Solid Mixture of Fe⁰ and γ-Fe₂O₃

In this study, decomposing mechanism of methylene blue (MB) by (Fe⁰ + γ-Fe₂O₃) mixture was investigated. Mixture of (Fe⁰ + γ-Fe₂O₃) was prepared with Fe⁰ (Wako 097-04791, 99.9 %, φ < 45 μm) and γ-Fe₂O₃ (High Purity Chemicals No. 282965, 99 %, φ < 1 μm). Five hundred mg of (Fe⁰ + γ-Fe₂O₃) mixture with a mass ratio of 3:7 was soaked in 20 mL of 10 μmol L⁻¹ methylene blue aqueous solution (MB$_{aq}$). Decomposition test was conducted at 30 °C for 10 days.

UV-VIS spectra of MB$_{aq}$ before and after decomposition test are presented in Figure 6 (*12*). MB concentration can be determined by Lambert-Beer equation using molar absorption coefficient of 7.9×10^5 L mol⁻¹ cm⁻¹ and absorption maximum observed at 660 nm for UV-VIS spectra of MB (*13*). MB concentration decreased from 10.5 to 8.66, 5.15, 5.05, 4.70 and 4.45 μmol L⁻¹ after 0, 1, 3, 5, 7 and 10 days, respectively (*12*). By using equation (1), first order rate constant for MB decomposition (k_{MB}) was calculated to be $1.5_{\pm0.2} \times 10^{-1}$ day⁻¹ (= $6.5_{\pm0.9} \times 10^{-3}$ h⁻¹).
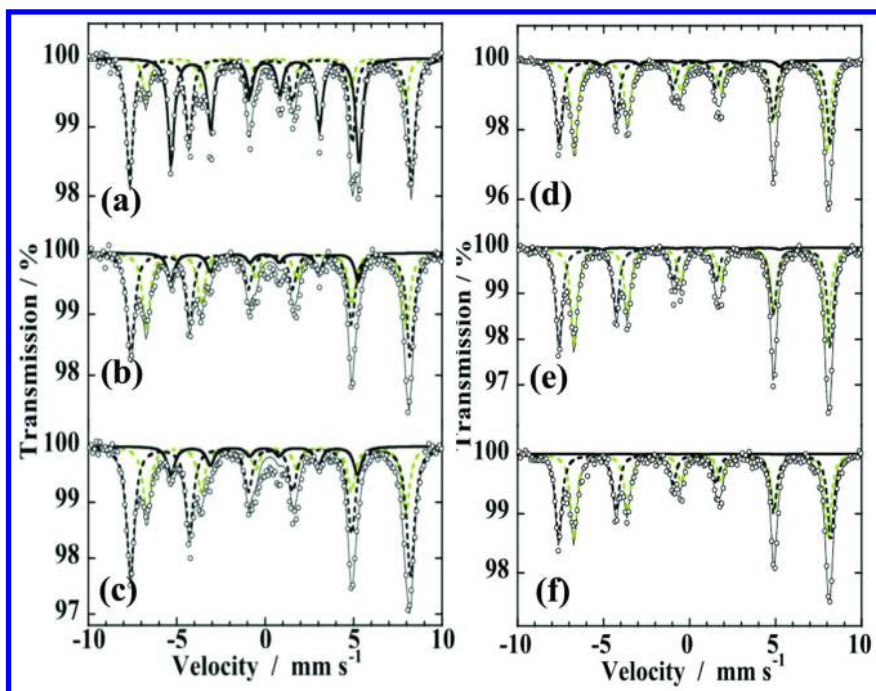
Figure 5. Mössbauer spectra of an (iron + iron oxide) mixture (3:7) after decomposition test for (a) 0, (b) 1, (c) 2, (d) 3, (e) 7, and (f) 10 days with TCE aqueous solution at an initial concentration of 10 mg L^{-1}. (Reproduced with permission from Ref. (8). 2013, Springer, Inc.)
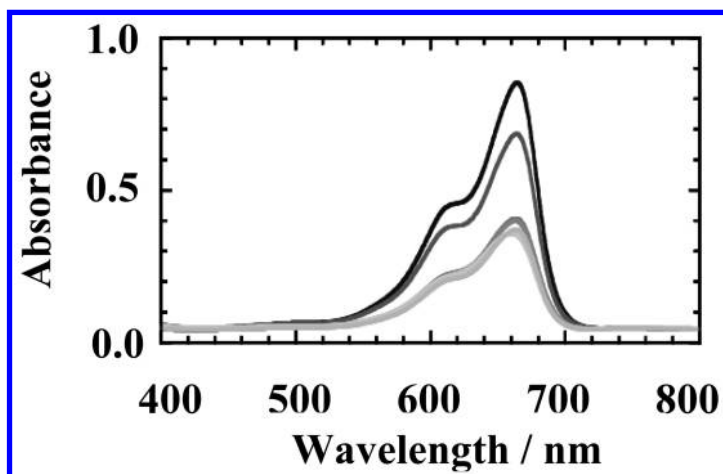
Figure 6. UV-VIS spectra of 10 μmol L^{-1} methylene blue (MB) before (top) and after 1, 3, 5, 7 and 10 day decomposition with ($Fe^0 + \gamma\text{-}Fe_2O_3$) mixture (3:7). (Reproduced with permission from Ref. (12). 2013, Springer, Inc.)

As shown in Figure 7, organic compounds of Azure A (m/z = 256), Azure B (m/z = 270) and other fractured compounds with m/z of 137, 110 and 100 could be observed from ESI-MS profiles of 10 µmolL^{-1} MB measured after decomposition test with (Fe^0 + γ-Fe$_2$O$_3$) mixture (3:7) for different time (*12*). This result suggests that MB was oxidatively decomposed by substituting –H for –CH$_3$ at the terminal position of MB.
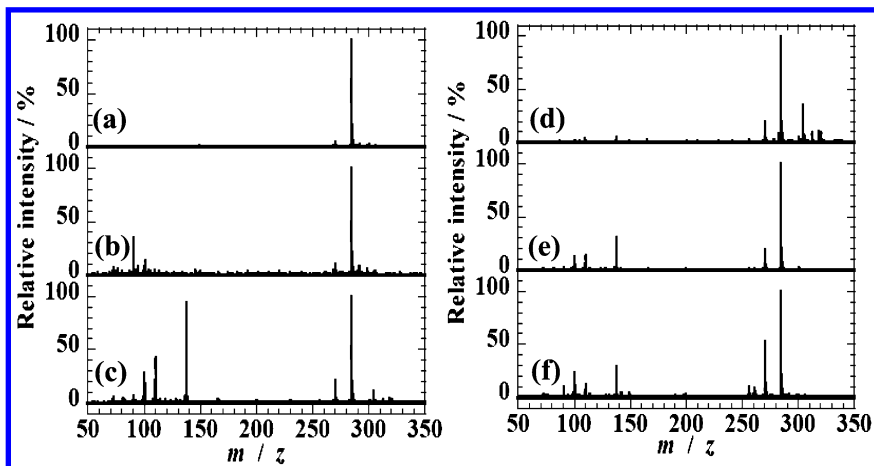
Figure 7. ESI-MS profiles of 10 µmolL^{-1} MB measured after decomposition test with (Fe^0 + γ-Fe$_2$O$_3$) mixture (3:7) for (a) 0, (b) 1, (c) 3, (d) 5, (e) 7 and (f) 10 days. (Reproduced with permission from Ref. (12). 2013, Springer, Inc.)

In Figure 8 (*12*), Mössbauer spectra of (Fe^0 + γ-Fe$_2$O$_3$) mixture (3:7) measured after the 10-day decomposition test are illustrated. Mössbauer spectrum of (Fe^0 + γ-Fe$_2$O$_3$) mixture (3:7) measured before decomposition test consists of two sextets; one is due to Fe^0 with δ of 0.00$_{\pm 0.01}$ mm s^{-1} and H_{int} of 33.0$_{\pm 0.1}$ T, and the other to γ-Fe$_2$O$_3$ with δ of 0.32$_{\pm 0.01}$ mm s^{-1} and H_{int} of 49.5$_{\pm 0.1}$ T (Figure 8 (a)) (*12*). Absorption area of Fe^0 decreased from 37.5 to 21.3, 9.7, 7.9, 7.0 and 4.5$_{\pm 0.5}$ % after decomposition of 0, 1, 3, 5, 7 and 10 days, respectively, while the absorption peak '*A*' assigned to Fe$^{+2.5}$(O_h) with δ of 0.63$_{\pm 0.01}$ mm s^{-1} and H_{int} of 45.3$_{\pm 0.1}$ T increased from 0.0 to 5.0, 13.8, 17.2, 21.0 and 22.4$_{\pm 0.5}$ % at the same time (Figure 8(b)-(f)) (*12*). In these samples, a paramagnetic doublet due to Fe^{3+} (O_h) with δ of 0.38 mm s^{-1} and D of 0.79 mm s^{-1} was observed, of which '*A*' value increased from 0.0 to 4.5, 4.6, 4.7, 4.9 and 5.0$_{\pm 0.5}$ % (*12*). These results indicate that magnetite (Fe$_3$O$_4$) and lepidocrocite (γ-FeOOH) were precipitated when (Fe^0 + γ-Fe$_2$O$_3$) mixture was reacted with MB$_{aq}$.
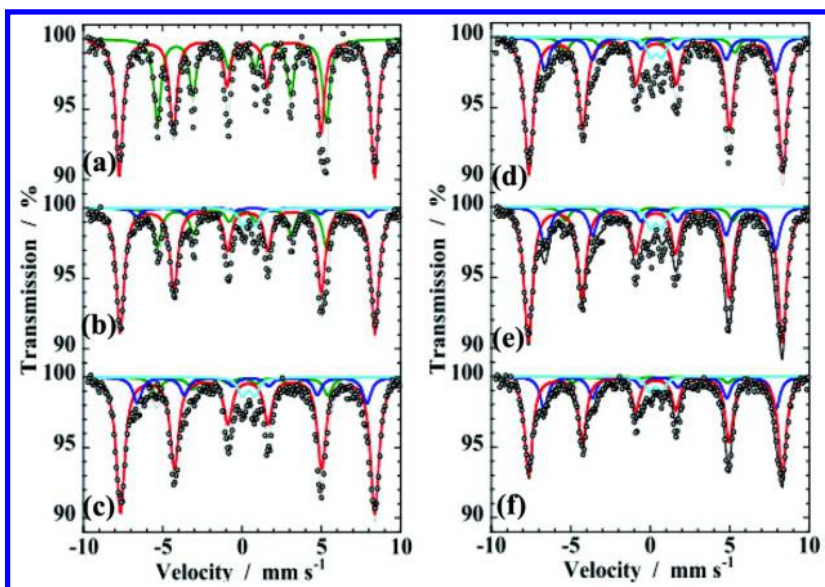
Figure 8. Mössbauer spectra of ($Fe^0 + \gamma$-Fe_2O_3) mixture (3:7) measured after decomposition test with 10 $\mu mol L^{-1}$ MB for (a) 0, (b) 1, (c) 3, (d) 5, (e) 7 and (f) 10 days. (Reproduced with permission from Ref. (12). 2013, Springer, Inc.)

Local Structure and Water Cleaning Ability of Iron Oxide Nanoparticles Prepared by Hydrothermal Reaction

In order to increase MB decomposing ability, nanoparticles (NPs) of γ-Fe_2O_3 were synthesized by hydrothermal reaction. Mixture of (bulk Fe^0 + γ-Fe_2O_3 NPs) with a ratio of 3:7 was used in decomposition test.

γ-Fe_2O_3 NPs were prepared by the following procedure (*14*). First, 1.960 g of $(NH_4)_2Fe(SO_4)_2$•$6H_2O$ (Mohr's salt) was dissolved in 7 mL of deionized water. Separately, 2.702 g of $FeCl_3$•$6H_2O$ was dissolved in 32 mL of absolute ethanol. Solution of Mohr's salt (0.714 $molL^{-1}$) was mixed with $FeCl_3$ (0.313 $molL^{-1}$) solution using a magnetic stirrer. A black precipitate appeared in the solution when 10 mL of 25 vol. % NH_3 aqueous solution was added in droplets. The resulting solution including black precipitate was transferred to an autoclave and was hydrothermally treated at 140 °C for 2 h. The black precipitate was separated from the mother liquor by centrifuging under 9000 r.p.m. for 5 min. After being washed several times with distilled water and ethanol, Fe_3O_4 NPs were dried for 24 h. γ-Fe_2O_3 NPs were obtained by annealing the synthesized Fe_3O_4 NPs at 250 °C in air for 30 min in air.

Mössbauer spectra of Fe_3O_4 NPs and $\gamma\text{-}Fe_2O_3$ NPs measured at 300 K are shown in Figure 9 (*14*). Mössbauer spectrum of Fe_3O_4 NPs is composed of two magnetic sextets with δ, H_{int} and Γ of $0.34_{\pm0.03}$ mm s^{-1}, $49.0_{\pm0.30}$ T and $1.09_{\pm0.03}$ mm s^{-1}, respectively due to $Fe^{3+}(T_d)$, and corresponding values of $0.66_{\pm0.11}$ mm s^{-1}, $44.0_{\pm0.71}$ T and $1.55_{\pm0.31}$ mm s^{-1} due to $Fe^{2.5+}(O_h)$ (*14*). Values of '*A*' for $Fe^{3+}(T_d)$ and $Fe^{2.5+}(O_h)$ were respectively determined to be 56.3 and 43.7 % (*14*), which indicates that Fe_3O_4 NPs prepared by hydrothermal reaction is not of regular type but of defective Fe_3O_4 that should be denoted as $Fe_{3-x}O_4$. Mössbauer spectrum of $\gamma\text{-}Fe_2O_3$ NPs composed of a sextet with δ, H_{int} and Γ of $0.33_{\pm0.03}$ mm s^{-1}, $46.4_{\pm0.27}$ T and $1.21_{\pm0.11}$ mm s^{-1}, respectively (*14*).
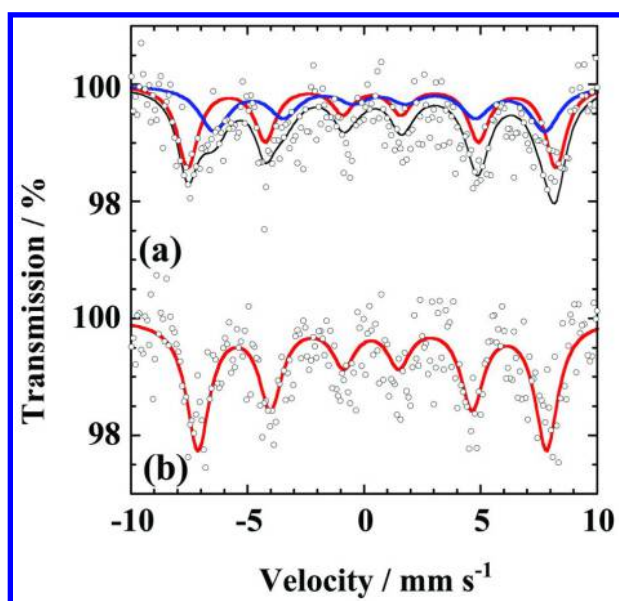
Figure 9. Mössbauer spectra of NPs of (a) $Fe_{3-x}O_4$ and (b) $\gamma\text{-}Fe_2O_3$ measured at 300 K. (Reproduced with permission from Ref. (14). 2014, Springer, Inc.)

As shown in Figure 10, XRD pattern of $Fe_{3-x}O_4$ NPs showed peaks with broad linewidth observed at $2q$ of 30.2, 35.7, 43.3, 53.7, 57.3 and 62.8 ^{o} attributed to Fe_3O_4 (PDF No. 00-039-1346) (*14*). Size of short-range ordered $Fe_{3-x}O_4$ NPs can be estimated by applying the Scherrer's formula (*15*, *16*), *i.e.*,

$$\tau = K\lambda \, / \, B \cos\Theta \qquad (2),$$

In Green Catalysts for Energy Transformation and Emission Control; Chang, et al.;

where τ, K, λ, B and Θ are size of short-range order (in nm), shape factor (= 0.849 - 1.107), wavelength of X-ray from Cu-K$_\alpha$ (0.1541 nm), FWHM and Θ at the peak (in radian), respectively. By using FWHM value of 0.44 ° obtained from (311) plane of the XRD pattern, crystallite size of Fe$_{3-x}$O$_4$ NPs was determined to be 29-37 nm. By contrast, γ-Fe$_2$O$_3$ NPs prepared by annealing of Fe$_{3-x}$O$_4$ NP at 250 °C for 30 min did not show significant difference in the crystallite size.
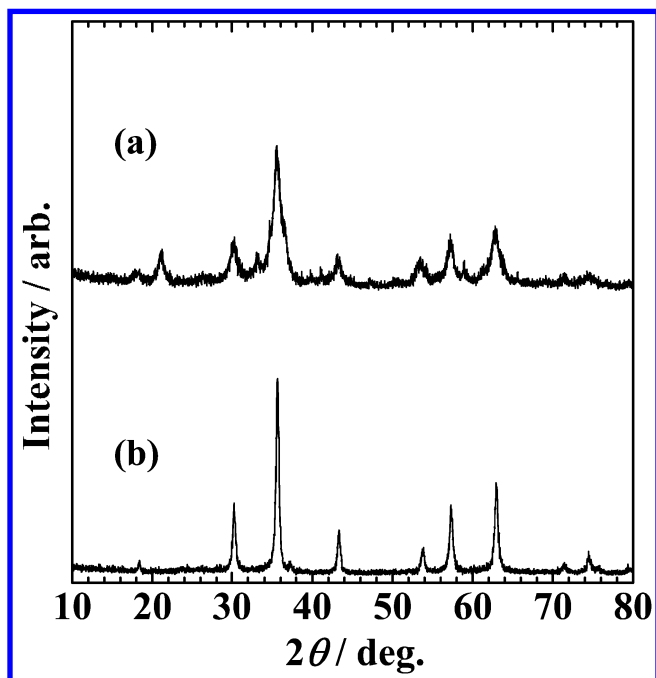
Figure 10. XRD patterns of (a) Fe$_{3-x}$O$_4$ and (b) γ-Fe$_2$O$_3$ nanoparticles. (Reproduced with permission from Ref. (14). 2014, Springer, Inc.)

Mixture (100 mg) of (bulk Fe^0 + γ-Fe$_2$O$_3$ NPs) (3:7) and 20.0 µmol L^{-1} of MB$_{aq}$ were used in 24 h decomposition test. UV-VIS spectra of MB aqueous solution recorded before and after the decomposition are shown in Figure 11 (*14*).MB concentration decreased from 19.2 to 5.9, 3.24, 1.16 and 0.95 µmol L^{-1} after decomposition of 0, 6, 12, 18 and 24 h, respectively (*14*). The first order rate constant (k_{MB}) is estimated to be $1.2_{\pm 0.1} \times 10^{-1}$ h^{-1} by using eq. (1). This value is larger than that obtained for decomposition test using (Fe^0 + γ-Fe$_2$O$_3$) bulk mixture (3:7): $6.5_{\pm 0.9} \times 10^{-3}$ h^{-1} (*12*), proving that effectiveness of MB-decomposing ability of (Fe^0 + γ-Fe$_2$O$_3$) mixture is closely related to the particle sizes of Fe^0 and γ-Fe$_2$O$_3$.
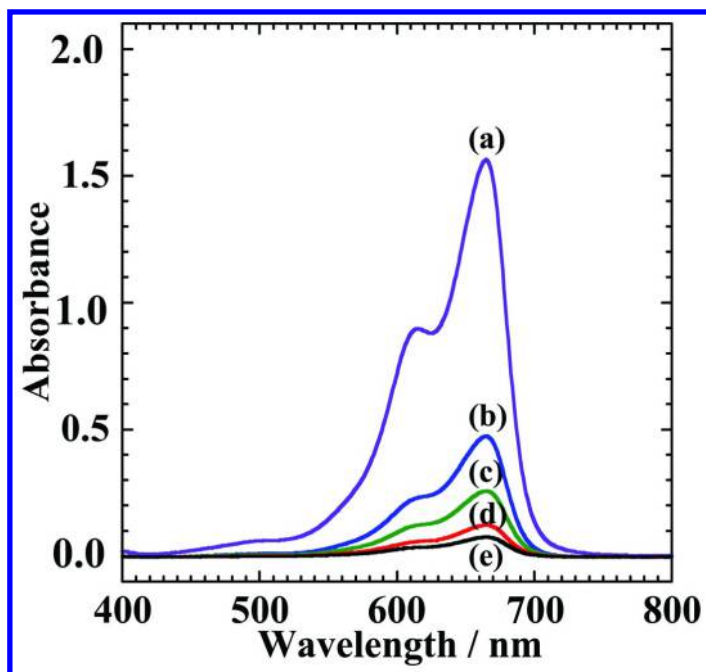
Figure 11. UV-VIS spectra of (bulk Fe^0 + γ-Fe_2O_3 NPs) mixture (3:7) measured after decomposition test with 20 $\mu molL^{-1}$ MB_{aq} for (a) 0, (b) 6, (c) 12, (d) 18 and (e) 24 h. (Reproduced with permission from Ref. (14). 2014, Springer, Inc.)

Conclusion

A Relationship was investigated between trichloroethylene (TCE) or methylene blue (MB)-decomposing ability and the structure of (Fe^0 + γ-Fe_2O_3) mixture. This chapter is summarized as follows;

1) Decomposition of TCE and MB in the aqueous solution was observed in decomposition test using (Fe^0 + γ-Fe_2O_3) mixture. During decomposition test, (Fe^0 + γ-Fe_2O_3) mixture is converted to Fe_3O_4 due to the oxidation of Fe^0 to Fe^{2+} or Fe^{3+} and by the occupation vacant octahedral site of γ-Fe_2O_3.

2) k value of MB decomposition caused by (Fe^0 + γ-Fe_2O_3) bulk mixture (3:7), $k_{MB} = 6.5_{\pm0.9} \times 10^{-3}$ h^{-1}, became larger when MB $_{aq}$ decomposition test was carried out using (bulk Fe^0 + γ-Fe_2O_3 NPs) , $k_{MB} = 1.2_{\pm0.1} \times 10^{-1}$ h^{-1}, suggesting that the increased surface area of γ-Fe_2O_3 NP affects the effectiveness of MB-decomposing ability.

It is concluded that (Fe^0 + γ-Fe_2O_3) mixture could be utilized for the environmental purification, and that organic compound-decomposing ability could be enhanced when nanoparticles were used.

References

1. Serpieri, N.; Moneti, G.; Pieraccini, G.; Donati, R.; Mariottini, E.; Dolara, P. *Urban Water* **2000**, *2*, 13–20.
2. Leahy, J. G.; Carrington, T. E.; Eley, M. H. *J. Environ. Qual.* **2004**, *33*, 1556–1561.
3. Leahy, J. G.; Tracy, K. D.; Eley, M. H. *Biotechnol. Lett.* **2003**, *25*, 479–483.
4. Rabbu, M. F.; Clarck, B.; Gale, R. J.; Ozsu-Acar, E.; Pardue, J.; Jackson, A. *Waste Manage.* **2000**, *20*, 279–286.
5. Cheng, S.; Wu, S. *Chemosphere* **2001**, *43*, 1023–1028.
6. Prommer, H.; Aziz, L. H.; Bolaño, N.; Taubald, H.; Schüth, C. *J. Contam. Hydrology* **2008**, *97*, 13–26.
7. Schwertmann, U.; Cornell, R. M. *Iron Oxides in the Laboratory*; Wiley-Vch Verlag GmbH: Weinheim, 2000; pp 27−54.
8. Kubuki, S.; Shibano, K.; Akiyama, K.; Homonnay, Z.; Kuzmann, E.; Ristić, M.; Nishida, T. *J. Radioanal. Nucl. Chem.* **2013**, *295* (1), 23–30.
9. Greenwood, N. N.; Gibb, T. C. *Mössbauer Spectroscopy*; Chapman and Hall Ltd.: London, 1971.
10. Cranshaw, T. E.; Longworth, G. In *Mössbauer Spectroscopy Applied to Inorganic Chemistry*; Long, G. J., Ed.; Plenum Press: New York, 1984; Vol. 1, Chapter 7.
11. Sun, Y.; Ma, M.; Zhang, Y.; Gu, N. *Colloids Surf., A* **2004**, *245*, 15–19.
12. Kubuki, S.; Shibano, K.; Akiyama, K.; Homonnay, Z.; Kuzmann, E.; Ristić, M.; Nishida, T. *Hyperfine Interact.* **2013**, *218* (1-3), 47–52.
13. Wakasa, M. *Magnetic field effects on the photocatalytic reaction*; Research Report of Comprehensive Research Organization; http://sucra.saitama-u.ac.jp/modules/xoonips/download.php/KP17A05-76.pdf?file_id=1427 2006; Vol. 4 (in Japanese)
14. Shibano, K.; Kubuki, S.; Akiyama, K.; Homonnay, Z.; Kuzmann, E.; Krehula, S.; Ristić, M.; Nishida, T. *Hyperfine Interact.* **2014**, *226* (1-3), 489–497.
15. Scherrer, P. *Göttinger Nachr. Ges.* **1918**, *2*, 98–100.
16. Patterson, A. *Phys. Rev* **1939**, *56*, 978–982.

Chapter 12

Ferrate(VI): A Green Molecule in Odorous Gas Treatment

Virender K. Sharma,[*,1] **Jun Ma,**[2] **Chun He,**[3] **Hyunook Kim,**[4] **and Radek Zboril**[5]

[1]**Department of Environmental and Occupational Health, School of Public Helath, Texas A&M Univeristy, College Station, Texas 77843, U.S.A.**
[2]**School of Water and Environmental Engineering, Harbin Institute of Technology, Harbin 150090, China**
[3]**School of Environmental Science and Engineering, Sun Yat-Sen University, Guangzhou, 510275, China**
[4]**The University of Seoul, Dept. of Environmental Engineering, 90 Jeonnong-dong Dongdaemun-gu, Seoul 130-743, Korea**
[5]**Regional Centre of Advanced Technologies and Materials, Departments of Experimental Physics and Physical Chemistry, Faculty of Science, Palacky University, Slechtitelu 11, 78371 Olomouc, Czech Republic**
[*]**E-mail: vsharma@sph.tamhsc.edu.**

The odorous gaseous emissions from industrial and wastewater treatment plant processes pose risk for natural ecosystem and human health. This chapter presents an assessment of the potential of ferrate(VI) ($Fe^{VI}O_4^{2-}$, Fe(VI)) to remove gaseous odor. Organosulfur compounds are usually predominate constituents of the odor and the kinetics, stoichiometry, and products of their oxidation by Fe(VI) is summarized. The second-order rate constants, k, of the oxidation reactions under alkaline conditions were in the range of $\sim 10^1$ - 10^5 $M^{-1}s^{-1}$. At a 10 mg L^{-1} K_2FeO_4 dose, half-lives of the oxidation reaction would be in seconds or less at pH 9.0. The stoichiometry of the reactions of Fe(VI) with sulfur compounds generally varied from 1:2 to 2:3 and Fe(II) and Fe(III) were the reduced products of Fe(VI). Oxygen-containing products of the sulfur compounds were formed. Examples of case studies showed the efficient removal of odorous gases by Fe(VI).

Introduction

Industrial and production processes emit waste gases, many of which cause environmental concerns at the local, regional and global scale (*1*). Airborne emissions from the processes are highly mobile and create environmental issues (*2*). The livestock production systems release airborne particulate matter, which may pose threat to the environment and ultimately to the health and welfare of animals and humans (*3*). The most common problem in lagoons is odor emission (*4*). Sulfur compounds in crude oil release sulfur oxide gases in the refining processes, which on reaction with water form sulfates and acid rain resulting in adverse effects on the environment, artifacts, and human health (*5*). Other sources of odorous emissions include municipal activities such as composting plants and wastewater treatment. The government bodies are receiving odor complaints from the nearby residential areas of wastewater treatment plants (WWTPs).

The odor emissions from WWTPs are characterized by a number of volatile odorants (Table 1) (*6*). Odorants are complex mixture of chemical compounds at ppb and ppt concentrations, which have been characterized by the gas chromatography technique (*7, 8*). Most of the emitted gases are reduced sulfur, nitrogen compounds, aldehydes, ketones, and organic acids. The dominant odorants in several odor emissions are from sulfur-containing compounds which include hydrogen sulfide (H_2S) and methyl mercaptan (CH_3SH). The daily range of CH_3SH concentration from the WWTPs was determined as 3 -14 mg m^{-3} during the spring – summer season (*9*). The CH_3SH has a very low odor threshold of ~ 0.4 ppb/v (*10, 11*). It is imperative to minimize and treat odor from the source of origin.

There are generally two treatment approaches applied to control the odor. One is dry processes, which include cold plasma, UV, thermal, and activated carbon adsorption (*10–13*). The second is wet processes such as biological (biofilters or bioscrubbers) and absorption (chemical scrubbers) (*6, 14*). In the chemical scrubbing process, odorants are oxidized rapidly in aqueous media and then oxidized by oxidants. Chlorine, hypochlorite, ozone, and hydrogen peroxide have shown potential to oxidize compounds of odorants (*15–19*). Basically, the contact time and pH are key variables to remove the compounds effectively and completely. An iron based compound in the high-valent oxidation state, commonly called ferrate(VI) ($Fe^{VI}O_4^{2-}$, Fe(VI)) can eliminate odor from sulfur and nitrogen compounds efficiently.

This chapter summarizes the role of Fe(VI) in elimination of odor in gaseous emissions using the wet-scrubber method. Initially, kinetics and products of oxidation of the compounds by Fe(VI) are presented, followed by case studies demonstrating the removal of odor in sludge and flue gas.

Ferrate(VI)

Ferrate(VI) ion contains four oxygen atoms, which are tetrahederally coordinated with the central iron atom (*20*). Sodium and potassium salts (Na_2FeO_4 and K_2FeO_4) are generally used in performing studies relevant to environmental remediation. Fe(VI) ion in alkaline solution has a characteristic

visible spectrum, which is frequently used to determine its concentration at pH 9.0 ($\varepsilon_{510\ nm}$ = 1150 M^{-1}cm^{-1}) (21). The fundamental properties of Fe(VI) ion has been recently reviewed (22–25). Ferrate(VI) has shown a significant capability as a coagulant (26–28). The final reduced by-product of Fe(VI) is a non-toxic ferric oxide/hydroxide, which is an effective coagulant for removing toxic metals and nutrients (e.g. arsenic and phosphate (29–35). Fe(VI) is also an effective disinfectant (36–41). A number of microorganisms can be treated with Fe(VI) and species that are susceptible to Fe(VI) include virus MS2 coliphage *f2*, Virus *Qβ*, and *Escherichia coli* (36, 37).

Table 1. Main Odor Descriptors for Wastewater Treatment Plants (6)

Odor descriptor	Sensorial experience	Chemical compound
Fecal/Sewer-like	- Faecal	- Skatole
	Manure	- Indole
	- Sewery	
Grassy/Woody	- Woody	- cis 3-Hexen 1-ol
	- Green/Grass	
	- Cardboard	
	- Hay	
Oxidant/Chlorinous	- Chlorinous	- Chlorine
		- Monochloramine
		- Dichloramine
Sulfide	- Decaying vegetation	- Hydrogen sulfide
	- Garlicky	- Dimethyl trisulfide
	- Rotten eggs	- Dimethylsulfide
Ammonia/Fishy	- Ammonia	- Ammonia
	- Fishy	-Trimethylamine
	- Cat urine	- 2,4 Decadienal
		- 2,4 Heptadienal
Earthy/Musty/Moddy	- Earthy/Musty	- Geosmin
	- Moldy	- 2-Methylisoborneol
		- 2,4,6 Trichloroanisole

The redox potentials of Fe(VI) ion are +2.20 V and +0.72 V in acidic and basic media, respectively (42) and has its reactivity increases as pH is decreased. Generally, most of pollutants can be removed by Fe(VI) in seconds to minutes time scales (25, 27, 43–45). Fe(VI) can effectively oxidize micropollutants such

as endocrine disruptors, and pharmaceuticals and personal care products (*23, 27, 46–50*). The following sections focuses on the oxidative conversion of sulfur by Fe(VI) in order to deordorize sludge and flue gas.

Kinectics

The rate-law for the oxidation of sulfur compounds (S) by F(VI) were found to be first-order for each reactant (eq. 1)

$$-d[Fe(VI)]/dt = k[Fe(VI)]_{tot}[S]_{tot} \qquad (1)$$

where k represents the second-order rate constant for the reaction of Fe(VI) with antibiotics, $[Fe(VI)]_{tot}$ represents the total concentration of Fe(VI) species, and $[S]_{tot}$ represents the total concentration of sulfur compounds. The second-order rate constants for the reactions of Fe(VI) with organosulfur compounds, usually found in wastewater and sludge, at pH 9.0 and 25 °C, are given in Table 2 (*44*). The rate constants vary from 5.8×10^1 to 6.0×10^5 $M^{-1}s^{-1}$ with cysteine and mercaptans displaying the highest reactivity while thioxane had the least reactivity with Fe(VI). Furthermore, it is expected that the values of k_{app} would increase with decrease in pH (*51, 51, 52*). It appears that the nucleophilicity on the sulfur atom determines the reactivity of sulfur compounds with Fe(VI) (*53*). The calculated half-lives ($t_{1/2}$) at a dose of 10 mg L^{-1} K_2FeO_4 for oxidation of organosulfur compounds were in seconds (Table 2). Oxidation of cysteine had the $t_{1/2}$ of milliseconds (Table 2). Importantly, mercaptans, which are major constituent of biosolids had values of $t_{1/2} \leq 1$ s for oxidation by Fe(VI) at pH 9.0.

Stoichiometry and Products

A few studies on the products of the oxidation of organosulfur compounds have been performed (*44*). Analysis of products suggests the transfer of oxygen atom(s) into the parent molecules to yield oxidized sulfur compounds. Also, the ratios of Fe(VI) to the various organosulfur compounds for the one oxygen-atom transfer were 0.50 and 0.67 for Fe(II) and Fe(III) as final products, respectively. In addition, different numbers of oxygen-atoms were transferred to form oxidized products. For example, the reactions of cysteine ($HSCH_2CH(NH_3^+)COO^-$) and methionine ($CH_3S(CH_2)_2CH(NH_2)COO^-$) with Fe(VI) yielded Fe(II) and Fe(III) as the reduced products of ferrate(VI), respectively (*24, 44, 54*).

$$HFeO_4^- + HSCH_2CH(NH_3^+)COO^- + H_2O \rightarrow Fe(OH)_2 +$$

$$HS(O_2)CH_2CH(NH_3^+)COO^- + OH^- \qquad (2)$$

$$2HFeO_4^- + 3CH_3S(CH_2)_2CH(NH_2)COO^- + 3H_2O \rightarrow 2Fe(OH)_3 +$$

$$3\ CH_3S(O)=(CH_2)_2CH(NH_2)COO^- + 2OH^- \qquad (3)$$
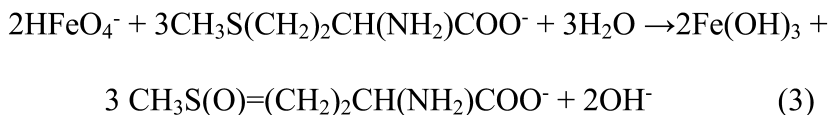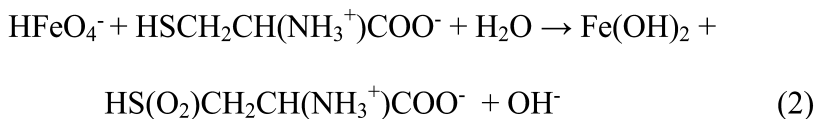
In cases, where four oxygen atoms were transferred, sulfate ion was the final oxidized product containing sulfur. This is shown in reactions (4) and (5) in which oxidation of thiourea (NH_2CSNH_2) and thioacetamide (NH_2CSCH_3) by Fe(VI) yielded sulfate ion.

$$8HFeO_4^- + 3NH_2CS\,NH_2 + 9H_2O \rightarrow 8Fe(OH)_3 +$$

$$3NH_2CO\,NH_2 + 3SO_4^{2-} + 2OH^- \qquad (4)$$

$$8HFeO_4^- + 3NH_2CSCH_3 + 9H_2O \rightarrow 8Fe(OH)_3 +$$

$$3NH_2COCH_3 + 3SO_4^{2-} + 2OH^- \qquad (5)$$
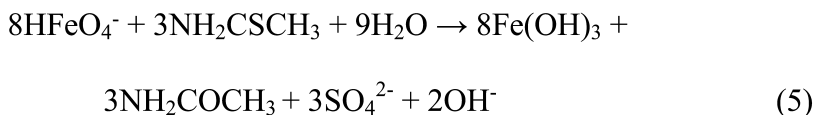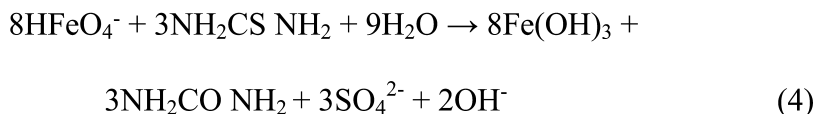
Case Studies

Methyl Mercaptan

In recent years, studies have been made to remove methyl mercaptan (CH_3SH) by *in-situ* electrochemically generated ferrate(VI) (*14*, *55*, *56*). Several parameters of the *in-situ* process were studied, which included electrolyte concentration, applied current density, and initial CH_3SH concentration in gaseous and aqueous phases. Figure 1 shows the degradation of methyl mercaptan under various conditions of current density, concentration of NaOH, and initial concentration of CH_3SH (*55*). The degradation rate was slow at low current density, but it increased linearly with the increased current density (Figure 1a). The concentration of NaOH was important in degrading CH_3SH (Figure 1b). The maximum degradation was found at 10 M. Higher concentration of NaOH might have given high yield of generated Fe(VI), but the reactivity of Fe(VI) with mercaptan decreased with the increase of the NaOH concentration. The influence of initial CH_3SH concentration on the degradation is shown in Figure 1c. The degradation rate decreased linearly with the concentration of mercaptan.

In a separate study, the second-order rate constants was determined to be $(7.91\pm0.40)\times10^2$ $M^{-1}s^{-1}$ in 10 M NaOH solution (*56*). The stoichiometry of the reaction between Fe(VI) and CH_3SH was also determined (reaction 6) (*56*).

$$14FeO_4^{2-} + 3CH_3SH + 23H_2O \rightarrow 8Fe(OH)_3 +$$

$$14H_2COCH_3 + 3SO_4^{2-} + 3CO_3^{2-}\ 16OH^- \qquad (6)$$
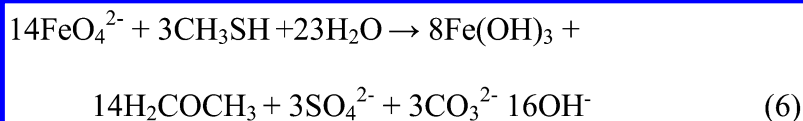
Table 2. Fe(VI) Oxidation of Sulfur-Containing Compounds at 25 °C

Compound	Molecular Formula	pH	k_{app}, $(M^{-1}s^{-1})$	$t_{1/2}$ 10 mg L^{-1} K_2FeO_4)
Cysteine	$HSCH_2CH(NH_2)COOH$	9.0	6.0×10^5	2.3 ms
2-Mercaptoethanesulfonic acid	$C_2H_6O_3S_2$	9.0	3.0×10^4	0.46 s
2-Mercaptobenzoic acid	$HOOCC_6H_4SH$	10.0	2.5×10^4	0.55 s
2-Mercaptobenzothiazole	$C_7H_5NS_2$	9.0	2.3×10^4	0.60 s
3-Mercaptopropionic acid	$HSCH_2CH_2COOH$	9.0	1.3×10^4	1.1 s
Mercaptonicotinic acid	$C_6H_5NO_2S$	9.0	1.2×10^4	1.2 s
Thioacetamide	$CH_3C(S)NH_2$	9.0	5.5×10^3	2.5 s
Thiourea Dioxide	$NH_2(SO_2)NH_2$	9.0	4.6×10^3	3.0 s
Thiourea	NH_2CSNH_2	9.0	3.4×10^3	4.1 s
Benzenesulfinate	$C_6H_5SO_2$	9.0	1.4×10^2	98.7 s
Methionine	$CH_3SCH_2CH_2CH(NH_2)COO^-$	9.0	1.3×10^2	106 s
Cystine	$(HOOCCH(NH_2)CH_2S)_2$	9.0	1.2×10^2	115 s
Diethylsulfide	$CH_3(S)CH_3$	8.0	1.0×10^2	138 s
Thiodiethanol	$OHCH_2CH_2(S)CH_2CH_2OH$	8.0	1.0×10^2	138 s
Thioxane	C_4H_8OS	9.0	5.8×10^1	238 s

(Reproduced with permission from Ref. (*53*). Copyright year 2009, the American Chemical Society.)
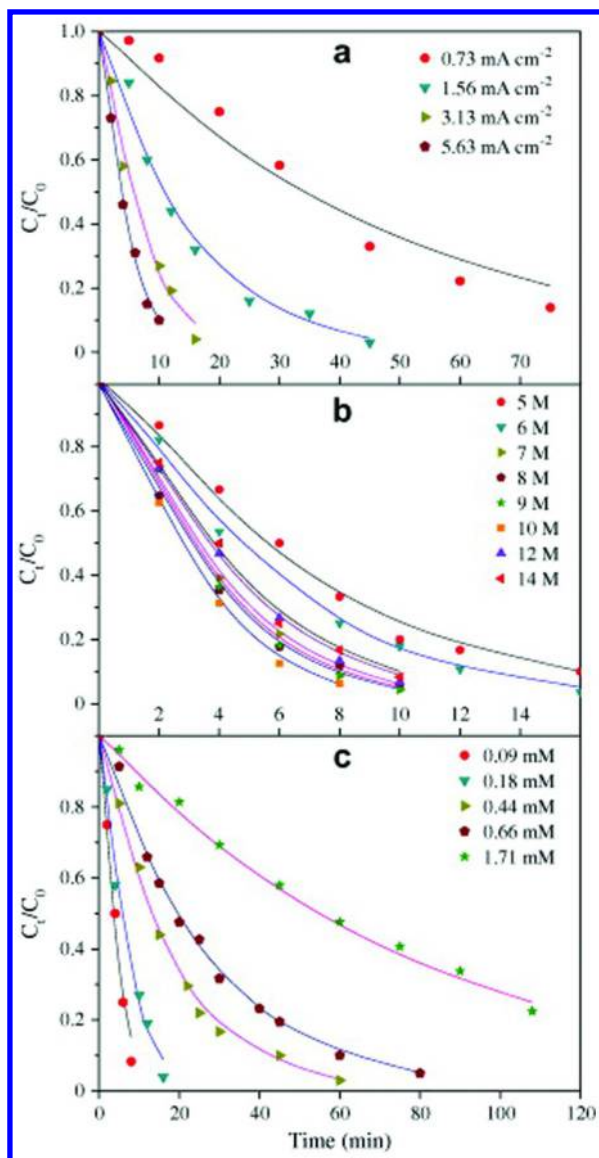
Figure 1. (a) CH₃S⁻ degradation by in-situ ferrate(VI) oxidation at different current density, fitted by the kinetic model for in situ ferrate(VI) oxidation of CH₃S⁻; (b) ~0.1 mM CH₃S⁻ degradation by IFO at different NaOH concentration with 3.13 mA cm⁻², fitted by the kinetic model for in situ ferrate(VI) oxidation of CH₃S⁻ and (c) CH₃S⁻ degradation by IFO with different initial CH₃S⁻ concentration in 14 M NaOH solution at 3.13 mA cm⁻², fitted by the kinetic model for in situ ferrate(VI) oxidation of CH₃S⁻. Lines are model fitting results. (Reproduced with permission from Ref. (55). Copyright year 2013, the Elsevier, Inc.)

Another study performed the stoichiometric experiments in the laboratory conditions at pH 9.0, which also found intermediate oxidized products (Figure 2) (*53*). The results showed sulfate was the major product (reaction 6). However, a stable intermediate was identified as methyl sulfonic acid (CH_3SO_3H). Significantly, the sum of the amount of sulfur in SO_4^{2-} and CH_3SO_3H was nearly equal to degraded sulfur from CH_3SH. A postulated mechanism suggested that the formation of radical ($CH_3S^{\bullet}$) and other intermediate species, CH_3SOH and CH_3SO_2H (*53*).
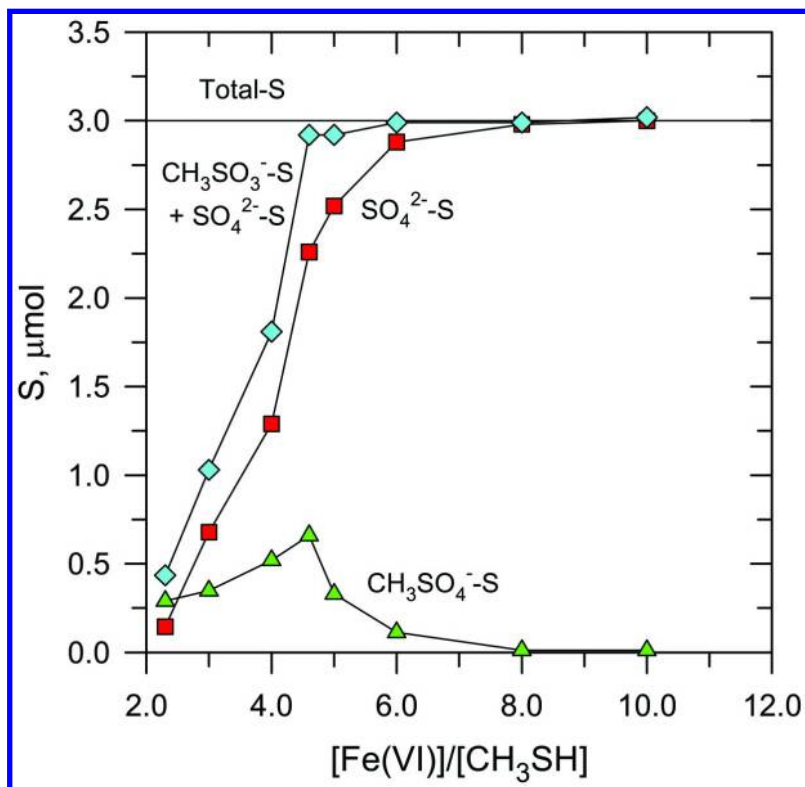
Figure 2. S formed in mercaptan oxidation by Fe(VI) as a function of [Fe(VI)]/[CH₃SH] at pH 9.0 and 25 °C. T-S stands for the theoretical value of total sulfur, SO₄²⁻-S for the formed sulfur in SO₄²⁻, CH₃SO₃⁻-S for the formed sulfur in CH₃SO₃⁻, SO₄²⁻-S + CH₃SO₃⁻-S for the total formed sulfur in SO₄²⁻ and CH₃SO₃⁻. (Reproduced with permission from Ref. (53). Copyright year 2009, the American Chemical Society.)
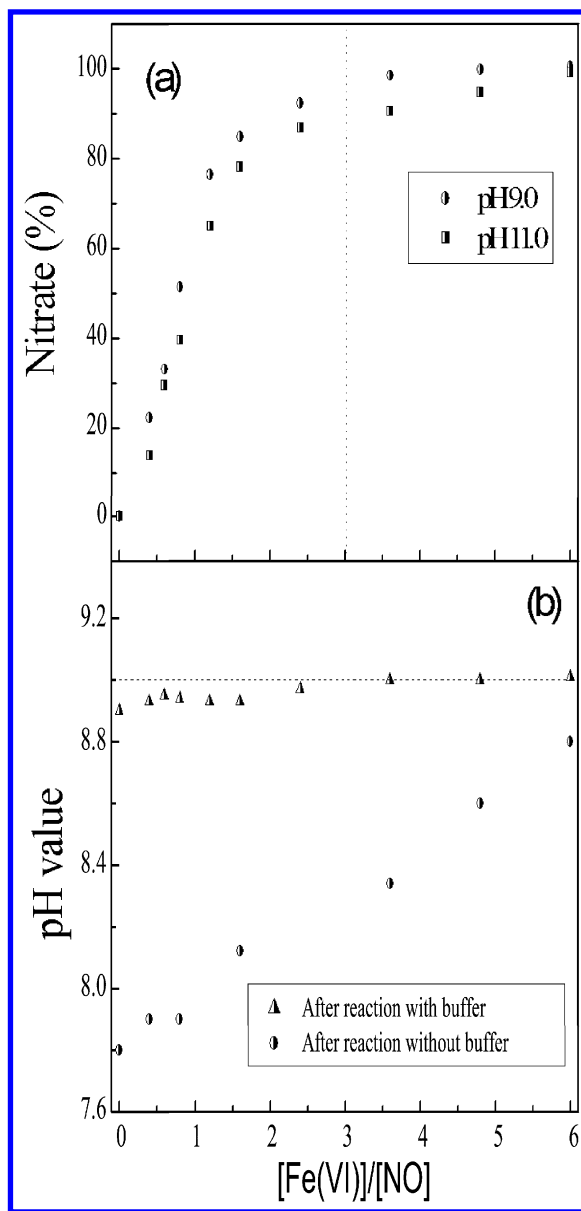
Figure 3. (a) Nitrate formed in NO oxidation by Fe(VI) as a function of [Fe(VI)]/[NO] at pH 9.0 and 25 °C, and (b) variation of pH value after reaction as a function of [Fe(VI)]/[NO] at pH 9.0 and 25 °C. (Reproduced with permission from Ref. (57). Copyright year 2011, the Royal Society of Chemistry.)
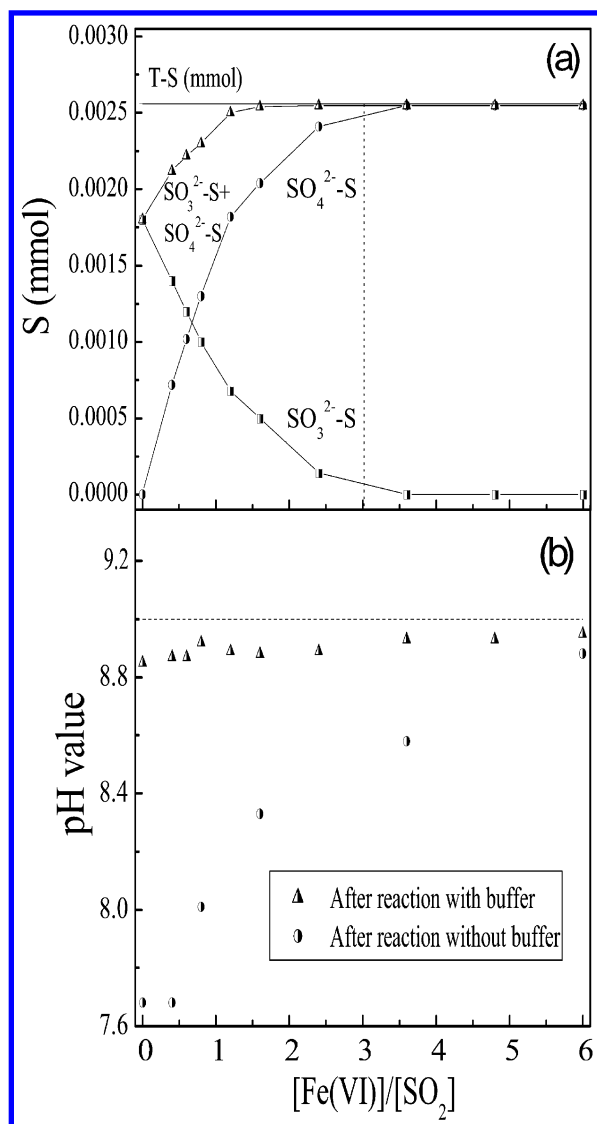
Figure 4. (a) Sulfate formed in SO_2 oxidation by Fe(VI) as a function of [Fe(VI)]/[SO_2] at pH 9.0, and (b) variation of pH value after reaction as a function of [Fe(VI)]/[SO_2] at pH 9.0 and 25 °C. T-S stands for the theoretical value of total sulfur, $SO_4^{2-}-S$ for the formed sulfur in SO_4^{2-}, $SO_3^{2-}-S$ for the formed sulfur in SO_3^{2-}, $SO_3^{2-}-S + SO_4^{2-}-S$ for the total formed sulfur in SO_4^{2-} and SO_3^{2-}. (Reproduced with permission from Ref. (57). Copyright year 2011, the Royal Society of Chemistry.)

Studies have been conducted on simultaneous removal of gaseous NO and SO_2 in flue gas (*57, 58*). Laboratory stoichiometric studies gave a ratio of 3.0 for oxidation of NO and SO_2 by Fe(VI). The oxidation of NO resulted in NO_3^- at pH 9.0 and 11.0 (Figure 3a). The formation of NO_3^- increased with increase in amount of Fe(VI) and the stoichiometric ratio of Fe(VI) to NO did not vary with pH. The influence of pH was further examined with and without buffer solution at pH 9.0 (Figure 3b). Initial pH of the reaction solution of Fe(VI) and NO without buffer was 7.8, but it increased to ~ 8.8 when a molar ratio of Fe(VI) to NO was 6.0. There was no significant change in pH when reaction solution was buffered (Figure 3b). Results of Figure 3 suggests the formation of hydroxide ion as the product of the reaction between Fe(VI) and NO. Overall, stoichiometric equation can be written as reaction (*7*).

$$3HFeO_4^- + NO + 4H_2O \rightarrow 3Fe(OH)_3 + NO_3^- + 2OH^- + 3/2O_2 \qquad (7)$$
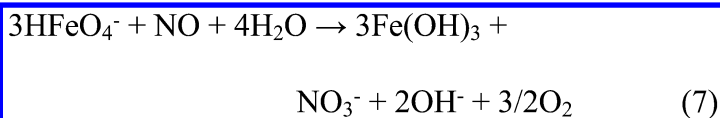
Similar set of experiments were also performed for the oxidation of SO_2 by Fe(VI) in the wet scrubber containing solution of Fe(VI) at pH 9.0 (Figure 4) (*57*). It seems SO_3^{2-} ion was the initial stable intermediate of the oxidation, which further oxidized to SO_4^{2-} ion as final oxidized product of the oxidation of SO_2 (Figure 4a). The required molar ratio of Fe(VI) to SO_2 was ~ 3.0 for complete oxidation of SO_2 (Figure 4a). The variation of pH after the oxidation of SO_2 by Fe(VI) at different molar ratios with and without buffer is shown in Figure 4b. Without buffer, the pH of the reaction solution increased from pH 7.7 to pH 8.9, however, changed in pH in buffer solution was only from 8.85 to 8.95 (Figure 4b). Based on the results of Figure 4, the stoichiometric equation can be written as reaction (*8*).

$$3HFeO_4^- + SO_2 + 7/2H_2O \rightarrow 3Fe(OH)_3 + SO_4^{2-} + OH^- + 7/4O_2 \qquad (8)$$
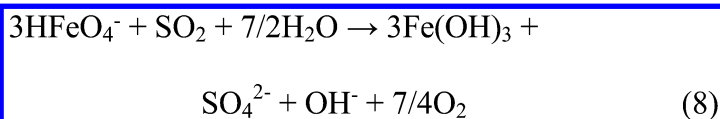
Experiments on simultaneous removal of NO and SO_2 in gaseous phase by the wet-scrubber process using with and without Fe(VI) were performed (Figure 5) (*57*). The concentrations of NO and SO_2 decreased significantly when Fe(VI) was continuously feeded (Figure 5a). The influence of the concentrations on the removal efficiency of NO and SO_2 by Fe(VI) is shown in Figure 5b. Increase in the ratios of concentrations of Fe(VI) and [NO + SO_2] showed increased removal efficiency of both NO and SO_2. At a molar ratio of more than 6.0, removal effiencies were > 90 % and 100 % for NO and SO_2, respectively.
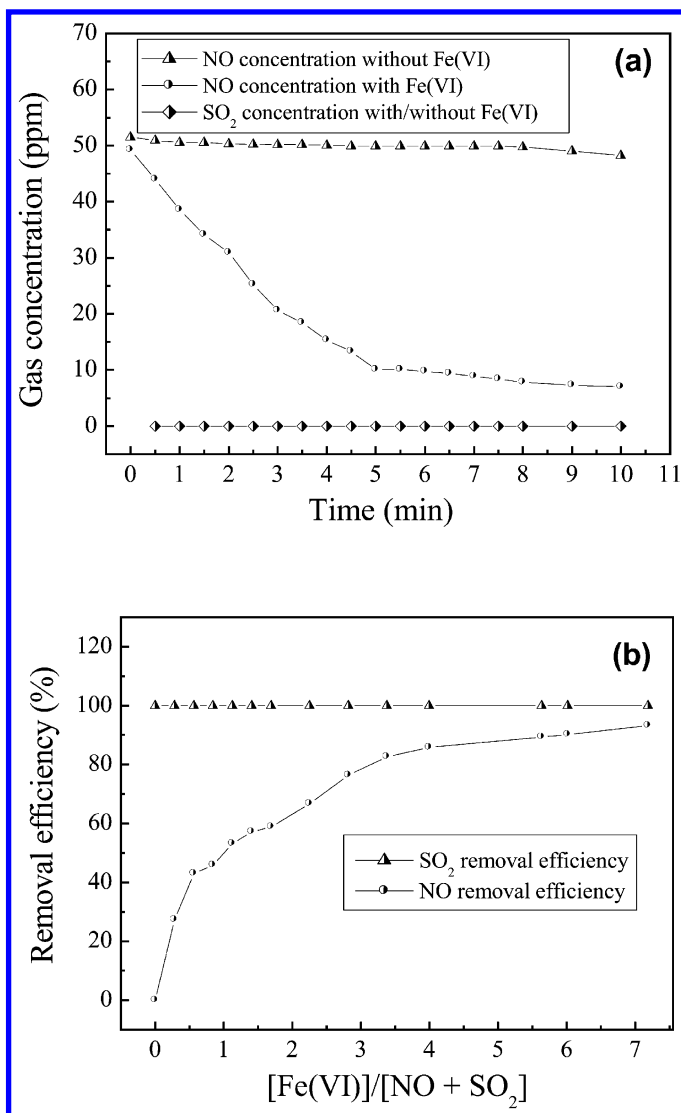
Figure 5. Simultaneous removal of NO and SO₂ in the wet scrubber without and with Fe(VI) solution ([Fe(VI)]/[NO + SO₂] = 4.0), and (b) simultaneous removal efficiency of NO and SO₂ as a function of [Fe(VI)]/[NO + SO₂]. (Reproduced with permission from Ref. (57). Copyright year 2011, the Royal Society of Chemistry.)

Conclusions

The oxidation of organosulfur compounds by Fe(VI) followed second-order kinetics in alkaline medium. The calculated half-lives of the compounds were determined to be in seconds at a dose of 10 mg K_2FeO_4 L^{-1}. Oxidation of

sulfur compounds occurred through transfer of oxygen atom(s) and different stoichiometric ratios of Fe(VI) to the compounds were found. The reduced product of Fe(VI) was mostly Fe(III), but Fe(II) was also determined in some instances. Case studies on the applications of Fe(VI) to remove mercaptan, NO, and SO_2 gases using a wet scrubber process demonstrated Fe(VI) as an effective wet-scrubber agent. Significantly, Fe(VI) could be generated *in-situ* electrochemically for potential of Fe(VI) for practical applications.

Acknowledgments

References

1. Tian, H.; Gao, J.; Hao, J.; Lu, L.; Zhu, C.; Qiu, P. *J. Hazard. Mater.* **2013**, *252-253*, 142–154.
2. Schlegelmilch, M.; Streese, J.; Stegmann, R. *Waste Manage.* **2005**, *25* (9), 928–939.
3. Cambra-López, M.; Aarnink, A. J. A.; Zhao, Y.; Calvet, S.; Torres, A. G. *Environ. Pollut.* **2010**, *158* (1), 1–17.
4. Zhang, X. L.; Yan, S.; Tyagi, R. D.; Surampalli, R. Y. *J. Environ. Manage.* **2013**, *124*, 62–71.
5. Chandra Srivastava, V. *RSC Adv.* **2012**, *2* (3), 759–783.
6. Lebrero, R.; Bouchy, L.; Stuetz, R.; Muoz, R. *Crit. Rev. Environ. Sci. Technol.* **2011**, *41*, 915–950.
7. Higgins, M. J.; Adams, G.; Chen, Y. C.; Erdal, Z.; Forbes, J. R. H.; Glindermann, D.; Hargreaves, J. R.; McEwen, D.; Murthy, S. N.; Novak, J. T.; Witherspoon, J. *Water Environ. Res.* **2008**, *80* (2), 127–135.
8. Kim, H.; Murthy, S.; McConnell, L. L.; Peot, C.; Ramirez, M.; Strawn, M. *Water Sci. Technol.* **2002**, *46*, 9–16.
9. Capelli, L.; Sironi, S.; Del Rosso, R.; Céntola, P. *Water Res.* **2009**, *43* (7), 1977–1985.
10. Bashkova, S.; Bagreev, A.; Bandosz, T. J. *Catal. Today* **2005**, *99* (3-4), 323–328.
11. Bashkova, S.; Bagreev, A.; Bandosz, T. J. *Langmuir* **2003**, *19* (15), 6115–6121.

12. Yan, N. Q.; Qu, Z.; Jia, J. P.; Wang, X. P.; Wu, D. *Ind. Eng. Chem. Res.* **2006**, *45* (19), 6420–6427.

13. Li, X. Z.; Hou, M. F.; Li, F. B.; Chua, H. *Ind. Eng. Chem. Res.* **2006**, *45* (2), 487–494.

14. Ding, L.; Liu, T. X.; Li, X. Z. *J. Chem. Technol. Biotechnol.* **2014**, *89* (3), 455–461.

15. Vilmain, J.-.; Courousse, V.; Biard, P.-.; Azizi, M.; Couvert, A. *Chem. Eng. Res. Design* **2014**, *92* (2), 191–204.

16. Biard, P. F.; Couvert, A.; Renner, C.; Levasseur, J. P. *Chemosphere* **2011**, *85* (7), 1122–1129.

17. Charron, I.; Couvert, A.; Laplanche, A.; Renner, C.; Patria, L.; Requieme, B. *Environ. Sci. Technol.* **2006**, *40* (24), 7881–7885.

18. Liu, Y.; Zhang, J.; Wang, Z. *Chem. Eng. J.* **2012**, *197*, 468–474.

19. Lin, C.-.; Chang, D. P. Y. *Water Air Soil Pollut.* **2005**, *162* (1-4), 19–35.

20. Hoppe, M. L.; Schlemper, E. O.; Murman, R. K. *Acta Crystallogr.* **1982**, *B38*, 2237–2239.

21. Luo, Z.; Strouse, M.; Jiang, J. Q.; Sharma, V. K. *J. Environ. Sci. Health, Part A: Toxic/Hazard. Subst. Environ. Eng.* **2011**, *46* (5), 453–460.

22. Sharma, V. K.; Perfiliev, Y.; Zboril, R.; Machala, L.; Wynter, C. In *Mossbauer Spectroscopy: Applications in Chemistry, Biology, Industry, and Nanotechnology*; Sharma, V. K., Klingelhofer, G., Nishida, T., Eds.; Wiley: Hoboken, NJ, 2013; pp 505−520.

23. Sharma, V. K. *Coord. Chem. Rev.* **2013**, *257*, 495–510.

24. Sharma, V. K.; Siskova, K.; Machala, L.; Zboril, R. *AIP Conf. Proc.* **2012**, *1489*, 139–144.

25. Sharma, V. K. *J. Environ. Manage.* **2011**, *92*, 1051–1073.

26. Filip, J.; Yngard, R. A.; Siskova, K.; Marusak, Z.; Ettler, V.; Sajdl, P.; Sharma, V. K.; Zboril, R. *Chem. Eur. J.* **2011**, *17* (36), 10097–10105.

27. Jiang, J. Q. *J. Chem. Technol. Biotechnol.* **2014** (89), 165–177.

28. Jiang, J.-.; Stanford, C.; Alsheyab, M. *Sep. Purif. Technol.* **2009**, *68*, 227–231.

29. Lee, Y.; Zimmermann, S. G.; Kieu, A. T.; Gunten, G. V. *Environ. Sci. Technol.* **2009**, *43*, 3831–3838.

30. Lee, Y.; Um, I.-.; Yoon, J. *Environ. Sci. Technol.* **2003**, *37*, 5750–5756.

31. Yngard, R. A.; Sharma, V. K.; Filip, J.; Zboril, R. *Environ. Sci. Technol.* **2008**, *42* (8), 3005–3010.

32. Yngard, R.; Damrongsiri, S.; Osathaphan, K.; Sharma, V. K. *Chemosphere* **2007**, *69* (5), 729–735.

33. Osathaphan, K.; Tiyanont, P.; Yngard, R. A.; Sharma, V. K. *Water Air Soil Pollut.* **2011**, *219*, 527–534.

34. Joshi, U. M.; Balasubramanian, R.; Sharma, V. K. *ACS Symp. Ser.* **2008**, *985*, 466–476 (Ferrates).

35. Jain, A.; Sharma, V. K.; Mbuya, M. S. *J. Hazard. Mater.* **2009**, *169*, 339–344.

36. Sharma, V. K. *Water Sci. Technol.* **2007**, *55* (1-2), 225–232.

37. Jiang, J. Q.; Wang, S.; Panagoulopoulos, A. *Chemosphere* **2006**, *63* (2), 212–219.

38. Sharma, V. K.; Kazama, F.; Jiangyong, H.; Ray, A. K. *J. Water Health* **2005**, *3*, 45–58.
39. Sharma, V. K.; Zboril, R.; McDonald, T. J. *J. Environ. Sci. Health, Part B* **2014**, *49* (3), 212–228.
40. Jiang, J. Q. *J. Hazard. Mater.* **2007**, *146*, 617–623.
41. Jiang, J. Q.; Lloyd, B. *Water Res.* **2002**, *36*, 1397–1408.
42. Wood, R. H. *J. Am. Chem. Soc.* **1958**, *80*, 2038–2041.
43. Casbeer, E. M.; Sharma, V. K.; Zajickova, Z.; Dionysiou, D. D. *Environ. Sci. Technol.* **2013**, *47* (9), 4572–4580.
44. Sharma, V. K.; Luther, G. W., III; Millero, F. J. *Chemosphere* **2011**, *82*, 1083–1089.
45. Sharma, V. K. *J. Environ. Sci. Health, Part A: Toxic/Hazard. Subst. Environ. Eng.* **2010**, *45*, 645–667.
46. Sharma, V. K.; Liu, F.; Tolan, S.; Sohn, M.; Kim, H.; Oturan, M. A. *Chem. Eng. J.* **2013**, *221*, 446–451.
47. Anquandah, G. A. K.; Sharma, V. K.; Panditi, V. R.; Gardinali, P. R.; Kim, H.; Oturan, M. A. *Chemosphere* **2013**, *91*, 105–109.
48. Zimmermann, S. G.; Schmukat, A.; Schulz, M.; Benner, J.; von Gunten, U.; Ternes, T. A. *Environ. Sci. Technol.* **2012**, *46* (2), 876–884.
49. Lee, Y.; von Gunten, U. *Water Res.* **2010**, *44*, 555–566.
50. Yang, B.; Ying, G. G.; Zhao, J.-.; Liu, S.; Zhou, L. J.; Chen, F. *Water Res.* **2012**, *46* (7), 2194–2204.
51. Anquandah, G.; Ray, M. B.; Ray, A. K.; Al-Abduly, A. J.; Sharma, V. K. *Environ. Technol.* **2011**, *32* (3), 261–267.
52. Sharma, V. K.; Sohn, M.; Anquandah, G.; Nesnas, N. *Chemosphere* **2012**, *87*, 644–648.
53. He, C.; Li, X.; Sharma, V. K.; Li, S. *Environ. Sci. Technol.* **2009**, *43* (15), 5890–5895.
54. Read, J. F.; Bewick, S. A.; Graves, C. R.; MacPherson, J. M.; Salah, J. C.; Theriault, A.; Wyand, A. E. H. *Inorg. Chim. Acta* **2000**, *303* (2), 244–255.
55. Ding, L.; Li, X. Z.; Lee, S. C. *Chemosphere* **2013**, *92* (10), 1301–1306.
56. Ding, L.; Liang, H. C.; Li, X. Z. *Sep. Purif. Technol.* **2012**, *91*, 117–124.
57. Xia, D.; He, C.; Zhu, L.; Huang, Y.; Dong, H.; Su, M.; Asi, M. A.; Bian, D. *J. Environ. Monit.* **2011**, *13* (4), 864–870.
58. Zhao, Y.; Han, Y.; Ma, T.; Guo, T. *Environ. Sci. Technol.* **2011**, *45* (9), 4060–4065.

Subject Index